UNIVERSITÀ DEGLI STUDI DI NAPOLI "FEDERICO II"
DIPARTIMENTO DI INGEGNERIA INDUSTRIALE

DOTTORATO DI RICERCA IN INGEGNERIA
AEROSPAZIALE, NAVALE E DELLA QUALITÀ

XXVII CICLO

TESI DI DOTTORATO

Applications of non-intrusive experimental techniques to roughness-induced transition in hypersonic flows

Francesco Avallone

Tutor
Prof. Ing. Gennaro Cardone

Coordinatore
Prof. Ing. Luigi de Luca

Marzo 2015

One more thing…

Steve Jobs

Table of Contents

Nomenclature

A	Amplitude
a_0	Speed of sound based on the storage tube conditions $[m \cdot s^{-1}]$
B, R, F	IR camera calibration constants
C	Shuttle Roughness Criteria constant
c	Speed of light $[m \cdot s^{-1}]$
C^*	Reference temperature method parameter
c_0	Speed of light in vacuum $[m \cdot s^{-1}]$
C_1, C_2	First and second radiation constant
c_d	Drag coefficient
C_f	Skin friction coefficient
C_h	Modified Stanton number
c_p	Constant pressure specific heat $[J/(Kg \cdot K)]$
c_T	Constant pressure specific heat of the particle material $[J/(Kg \cdot K)]$
D	Roughness diameter [m]
d^*	Critical throat diameter [m]
d_{cold}	Cross section diameter of the cold section of the HTFD storage tube [m]
d_{diff}	Diffraction limited diameter [px]
d_{geom}	Geometric particle image diameter [px]
d_{hot}	Cross section diameter of the heated section of the HTFD storage tube [m]
D_p	Penetration depth [m]
d_p	Particle physical diameter [m]
d_τ	Particle image diameter [px]
E	Total hemispherical emissive power $[W/m^2]$

E_b	Total black body emissive power $[W/m^2]$
$E_{b,a}$	Radiation emitted by a black body at T_a $[W/m^2]$
$E_{b,amb}$	Radiation emitted by a black body at T_{atm} $[W/m^2]$
$E_{b,obj}$	Radiation emitted by a black body at T_{obj} $[W/m^2]$
$E_{b,\lambda}$	Energy rate per body unit surface area for a given wavelength and black body temperature $[W/m^3]$
$E_{b,\lambda_1 \leq \lambda \leq \lambda_2}$	Energy flux over a certain wavelengths band $[W/m^2]$
E_t	Radiation captured by the IR camera $[W/m^2]$
$f_{\#}$	Numerical aperture
f_E	Fractional emissive power function
f_{ERR}	Global error functional in the solution of IHTP [K]
f_M	Voxel intensity in MART reconstruction [counts]
Fo_ξ	Modified Fourier number
f_s	Acquisition frequency [Hz]
f_{x_p}	Local error functional in the solution of IHTP [K]
h	Convective heat transfer coefficient $[W/(m^2 \cdot K)]$
$\mathcal{H}$	Hessian matrix
h_{aw}	Adiabatic wall enthalpy [J]
H_{coeff}	Fourier transform coefficient
h_w	Wall enthalpy [J]
I_a, I_b	Pixel intensity [counts]
$\bar{I}_a, \bar{I}_b$	Average intensity over a correlation window [counts]
k	Thermal conductivity $[W/(m \cdot K)]$
K	Non-dimensional heat flux
k_r	Roughness height [m]
$k_{r,eff}$	Effective roughness height [m]
L	Length of the HTFD storage tube [m]
L_{sep}	Separation length [m]
M_0	Magnification
M_1	Mach number in the storage tube
M_∞	Free stream Mach number
M_c	Free stream Mach number for experiments carried out on a cone
M_e	Mach number at the edge of the boundary layer
$M_{n,u}$	Normal Mach number upstream of the shock wave
M_p	Free stream Mach number for experiments carried out on a flat plate
$\dot{m}$	Flow rate $[Kg \cdot s^{-1}]$

N_g^{2cam}	Number of ghost particles for a 2-cameras system
N_g^{Ncam}	Number of ghost particles for a N-cameras system
N_p	Number of true particles
N_{pix}	Number of pixels
N_{ppp}	Particle image density
N_s	Source density
n_s	Number of samples that discretize the transient temperature
N_{TOMO}	Number of available snapshots from tomographic PIV experiments
Nu	Nusselt number
N_{VOX}	Number of voxel
N_x, N_y	Number of measurements points
n_θ	Refractive index
p_0	Free stream total pressure [bar]
P_p	Pixel pitch [m]
Pr	Prandtl number
Q	Reconstruction quality factor
q_{lam}	Theoretical wall heat flux estimated by the reference temperature method for laminar boundary layer $[W/m^2]$
q_{turb}	Theoretical wall heat flux estimated by the reference temperature method for turbulent boundary layer $[W/m^2]$
q_w	Wall heat flux $[W/m^2]$
r	Recovery factor
R	Correlation function
Re	Reynolds number $Re = (\rho U L_0)/\mu$
Re_d	Reynolds number based the relative velocity between particle and flow and on the particle diameter $Re_d = (\rho(\underline{U} - \underline{U^p})d_p)/\mu$
Re_k	Roughness Reynolds number $Re_k = (\rho_{e,r} u_{e,r} k_r)/\mu_{e,r}$
Re'_{k_r}	Scaled version of Re_{k_r}
Re_{k_r}	Reynolds number evaluated at the roughness edge $Re_{k_r} = (\rho_{k_r} u_{k_r} k_r)/\mu_{k_r}$
$Re_{k,eff}$	Effective roughness Reynolds number $Re_{k,eff} = (\rho_{e,r} u_{e,r} k_{r,eff})/\mu_{e,r}$
Re_{unit}	Unit Reynolds number $[m^{-1}]$ $Re = (\rho_\infty U_0)/\mu_\infty$
Re_x	Reynolds number based on the free stream conditions and the distance from the leading edge $Re = (\rho_\infty U_0 x)/\mu_\infty$

$Re_{x,k}$	Reynolds number based on the edge conditions at the roughness location $Re_{x,k} = (\rho_{e,r} u_{e,r} x_r)/\mu_{e,r}$
$Re_{x,t}$	Reynolds number based on the edge conditions and the transition location $Re_{xt} = (\rho_{e,t} u_{e,t} x_t)/\mu_{e,t}$
Re_{δ^*}	Reynolds number based on the edge conditions and displacement thickness at roughness location $Re_{\delta^*} = (\rho_{e,r} u_{e,r} \delta^*)/\mu_{e,r}$
Re_{θ}	Reynolds number based on the edge conditions and momentum thickness at roughness location $Re_{\delta^*} = (\rho_{e,r} u_{e,r} \theta)/\mu_{e,r}$
r_v	Vortex radius [m]
St	Stanton number
t	Time [s]
T	Temperature [K]
T^*	Reference temperature [K]
T_0	Total temperature [K]
t_0	Reference time [s]
T_∞	Free stream temperature [K]
T_a	Ambient temperature [K]
T_{atm}	Atmosphere temperature [K]
T_{aw}	Adiabatic wall temperature [K]
T_b	Absolute black body temperature [K]
T_{cold}	Temperature of the cold section of the HTFD storage tube [K]
t_d	Delay time [s]
T_{hot}	Temperature of the hot section of the HTFD storage tube [K]
T_{obj}	Temperature of a generic body [K]
t_p	Running time [s]
T_p	Particle temperature [K]
T_r	Enclosure temperature [K]
t_{start}	Start of stationary conditions in the wind tunnel [s]
$T_{t,1}$	Total temperature behind the expansion wave [K]
T_w	Wall temperature [K]
T_{wi}	Initial wall temperature [K]
$T_{w_{NUM}}$	Transient wall temperature obtained from the solution of the direct heat equation [K]
U	Flow velocity $[m \cdot s^{-1}]$
u^*	Non-dimensional particle velocity across the shock wave

u, v, w	Streamwise, spanwise and wall normal velocity components $[m \cdot s^{-1}]$
U_0	Free stream velocity $[m \cdot s^{-1}]$
u_1	Flow velocity in the HTFD storage tube $[m \cdot s^{-1}]$
U_a	Output of the IR scanner corresponding to $E_{b,a}$ [V or A]
U_{amb}	Output of the IR scanner corresponding to $E_{b,amb}$ [V or A]
u_d	Flow velocity normal component downstream of the shock wave $[m \cdot s^{-1}]$
u_e	Streamwise velocity component at the edge of the boundary layer $[m \cdot s^{-1}]$
$u_{e,r}$	Velocity ad the edge of the boundary layer at roughness location $[m \cdot s^{-1}]$
$u_{e,t}$	Velocity ad the edge of the boundary layer at transition location $[m \cdot s^{-1}]$
u_{k_r}	Flow velocity at roughness height $[m \cdot s^{-1}]$
U_{obj}	Output of the IR scanner corresponding to $E_{b,obj}$ [V or A]
U^p	Tracer particles velocity $[m \cdot s^{-1}]$
u_p	Particle velocity component normal to the shock wave $[m \cdot s^{-1}]$
U_t	Output of the IR scanner corresponding to E_t [V or A]
u_u	Flow velocity normal component upstream of the shock wave $[m \cdot s^{-1}]$
V_{swirl}	Swirl velocity $[m \cdot s^{-1}]$
W	Interrogation window size [px]
$w_{i,j}$	Weighting coefficients for MART reconstruction
x, y, z	Reference system
$x_{t,eff}$	Effective transition location [m]
x_p	Particle position [m]
x_r	Roughness location [m]
x_t	Transition location [m]
$x_{t,0}$	Smooth wall transition location [m]
x_u	Particle position upstream of the shock wave [m]
$\bar{x}$	Non-dimensional streamwise coordinate
z_0	Distance between the lens and the sensor plane [m]
Z_0	Distance between the lens and the object plane [m]
ΔL	Length of the heated HTFD storage tube [m]
Δp_{x_s}	Displacement evaluated by Snell's law [px]
$\overline{\Delta q_r}$	Reference mean spanwise amplitude of the wall heat flux $[W \cdot m^2]$

Nomenclature

$\overline{\Delta q_x}$	Mean spanwise amplitude of the wall heat flux [$W \cdot m^2$]
Δt	Time separation between camera exposures [s]
$\Delta x, \Delta y$	Image shift [px]
$\Delta x_p, \Delta y_p$	Particle image displacement [px]
δz	Depth of field [m]
Δz_0	Light sheet thickness [m]
$< u' >, < v' >, < w' >$	Streamwise, spanwise and wall normal turbulent fluctuations [$m \cdot s^{-1}$]

Greek symbols

α	Thermal diffusivity [$m^2 \cdot s^{-1}$]
α_r	Absorbed radiation fraction
α_S	Forward facing step angle [deg]
α_T	Rotation around the x axis in the camera tomographic PIV camera setup [deg]
β	Normalized bias
β_n	Noise bias [K]
β_T	Rotation around the y axis in the camera tomographic PIV camera setup [deg]
γ	Specific heats ratio
δ	Boundary layer thickness [m]
δ^*	Boundary layer displacement thickness [m]
ε_t	Total hemispherical emissivity coefficient
$\varepsilon_{\langle u' \rangle}$	Uncertainty in the estimation of the turbulent fluctuations [$m \cdot s^{-1}$]
$\varepsilon_{\bar{u}}$	Uncertainty in the estimation of the mean velocity [$m \cdot s^{-1}$]
ε_λ	Hemispherical emissivity coefficient
ϵ	Value of Re'_{k_r} at the edge of the roughness element
ϵ_M	Percentage uncertainty in the free stream Mach number
ϵ_p	Percentage uncertainty in the free stream static pressure
ϵ_T	Percentage uncertainty in the free stream static temperature
ϵ_u	Percentage uncertainty in the free stream velocity
ϵ_ρ	Percentage uncertainty in the free stream static density
θ	Boundary layer momentum thickness [m]
θ_v	Angle of view [deg]
κ	Fraction of the pixel
λ	Wavelength [m]
λ_L	Wavelength of the laser source [m]

λ_{max}	Wavelength at which the blackbody emits the maximum spectral emissive power [m]
μ	Flow dynamic viscosity [Pa · s]
μ_e	Dynamic viscosity at the edge of the boundary layer [Pa · s]
$\mu_{e,r}$	Dynamic viscosity at the edge of the boundary layer at roughness location [Pa · s]
$\mu_{e,t}$	Dynamic viscosity at the edge of the boundary layer at transition location [Pa · s]
μ_{k_r}	Free stream dynamic viscosity at roughness height [Pa · s]
μ^*	Dynamic viscosity at T* [Pa · s]
μ_∞	Free stream dynamic viscosity [Pa · s]
μ_M	Mach angle [deg]
μ_T	Relaxation coefficient for MART
ν	Frequency of the electromagnetic wave [s^{-1}]
ξ	Particle relaxation length [m]
ξ_s	Spatial frequency [m^{-1}]
ρ	Flow density [J/(Kg K)]
ρ_b	Particles bulk density [Kg/m^3]
ρ_e	Flow density at the edge of the boundary layer [Kg/m^3]
ρ_{k_r}	Flow density at the edge of the roughness [Kg/m^3]
$\rho_{e,r}$	Flow density at the edge of the boundary layer edge at roughness location [Kg/m^3]
$\rho_{e,t}$	Flow density at the edge of the boundary layer edge at transition location [Kg/m^3]
ρ_p	Particles material density [Kg/m^3]
ρ_r	Reflected radiation fraction
ρ_{rn}	Normal spectral reflectance
ρ_w	Flow density at the surface [Kg/m^3]
ρ_∞	Free stream density [Kg/m^3]
ς	Spectral absorption coefficient [m^{-1}]
σ	Normalized standard deviation
σ_B	Stefan–Boltzmann constant [$W/(m^2K)$]
σ_g	Growth rate
σ_n	Noise standard deviation [K]
τ	Particle relaxation time [s]
τ_f	Turnover time [s]
τ_r	Transmitted radiation fraction
τ_{rn}	Normal spectral transmittance
$\tau_{r\lambda}$	Transmitted radiation fraction for a given wavelength

Nomenclature

τ_T	Temperature relaxation time [s]
ϕ	Surface temperature variation with respect to the initial temperature [K]

Acronym

1D	One-dimensional
2D	Two-dimensional
3D	Three-dimensional
CCD	Charge Couple Device
DFT	Discrete fourier transform
DHE	Direct Heat Equation
FFT	Fast fourier transform
FOV	Field of View
FPA	Focal plane array
HTFD	Hypersonic Test Facility Delft
HTG	Hyperschall technologie Göttingen
IFOV	Instantaneous Field of View
IHTP	Inverse heat transfer problem
IR	Infrared
MART	Multiplicative algebraic reconstruction technique
MDTD	Minimum detectable temperature difference
MRTD	Minimum resolvable temperature
MTE	Motion tracking enhancement
MTF	Modulation transfer function
NETD	Noise equivalent temperature difference
OSP	Off-symmetry plane
OTF	Optical transfer function
PANT	Passive nosetip technology
PIV	Particle image velocimetry
PSP	Pressure sensitive paint
SCR	Shuttle roughness criteria
SP	Symmetry plane
SURF	Speed-up robust features
TKE	Turbulent kinetic energy
TL	Transition location
TOMO	Tomographic
TPS	Thermal protection system
T-S	Tollmien-Schlichting

TSP	Temperature sensitive paint

Symbols

∇^2	Laplacian
$\bar{}$	Mean value
$\underline{\quad}$	Vector
$\|\|\ \|\|$	2-norm
$\star$	Sonic conditions

Scope of the work

Measurements in the hypersonic regime are extremely challenging because of the complex flow phenomena and of the hardware limitations. The improvement of the already existing data reduction approaches coupled with the application of innovative non-intrusive experimental techniques will contribute to detect the relevant physical mechanisms behind induced laminar-to-turbulent transition.

Traditionally, laminar-to-turbulent boundary layer transition induced by roughness elements immersed in a hypersonic boundary layer was investigated by means of qualitatively flow visualizations such as oil flow (Whitehead 1969), Schlieren imaging (Jackson and Czarnecki 1960) or fluorene sublimation (Hicks and Harper 1970). However, quantitative measurements are essential when designing re-entry vehicles. For example, to measure the wall heat flux rate researchers use infrared (IR) thermography (Simeonides and Haase 1995, Tirtey et al 2011), heat flux gauges (Kumar et al 2014) or temperature sensitive paints (TSPs, Liu et al 2013). Alternatively, the wall pressure distribution is measured by pressure sensitive paints (PSPs, Yang et al 2012) or PCB sensors (Kumar et al 2014).

Even if these data are extremely useful, they do not provide information about the physical mechanisms behind transition. Therefore, detailed data of the flow field are required. To that end, physical probes (i.e. hot wires or Pitot tubes) are often used (Wheaton and Schneider 2010, Sharp and White 2014). Alternatively, high-speed flow visualizations (Danehy et al 2009, 2010, Bathel et al 2011) are performed to acquire qualitative and quantitative one-dimensional data of the flow. The necessity of non-intrusive quantitative data and the strong three-dimensionality of the flow (Iyer and Mahesh 2013, Subbareddy et al 2014) push the application of fully three-dimensional experimental techniques such as tomographic particle image velocimetry (tomographic PIV, Elsinga et al 2006).

Scope of the work is to investigate roughness-induced laminar-to-turbulent transition in hypersonic flows by means of heat flux and velocity field measurements by using IR thermography (Carlomagno and Cardone 2010) and particle image velocimetry (planar and tomographic). The working principles are carefully described in chapter 3 and 5, respectively. Even if the former is a well-established experimental technique, it is necessary to keep developing more robust data reduction approaches that are able to correct for the wind tunnel model mechanical vibrations, lateral conduction effects (relevant in presence of strong temperature gradients, de Luca et al 1993) and unsteady phenomena at the start of the wind tunnel (Cardone 2007). A data reduction technique based on the least-squares method that solves both 1D and 2D Inverse Heat Transfer Problems (IHTPs) is presented in chapter 4. Both the techniques are tested on ad hoc experimental tests performed in the Hypersonic Test Facility Delft (HTFD, chapter 2).

On the contrary, tomographic PIV has not been applied in the hypersonic regime yet. The presence of strong compressibility effects and the technical limitations such as limited optical access, aero-optical aberrations (Elsinga et al 2005), system vibrations requiring single-shot tomographic calibration (Michaelis and Wolf 2011) make its application very challenging. In chapter 5 an accurate description of the experimental procedure needed to apply tomographic PIV in the hypersonic regime, its limitations and its application to measure a laminar boundary layer on a flat plate are presented.

Finally, both the measurements techniques are applied to study induced transition by an isolated three-dimensional roughness element. First of all, the effects of the roughness geometry on the transition process are investigated by means of IR thermography in chapter 6. Then, in chapter 7 the separated region upstream of a cylindrical roughness element is investigated by means of Schlieren visualization, IR thermography and planar particle image velocimetry. The measurements provide the first experimental evidence of the complex vortex system formed upstream of the roughness element. Afterwards, in chapter 8 tomographic PIV is applied, for the first time, to study the transitional wake behind a cylindrical protuberance. A qualitatively comparison between the velocity data and the heat transfer distribution concludes the chapter. The thesis ends with conclusions and future perspectives.

Chapter 1

Introduction

1.1 Historical Background: the Origin of the Re-Entry Flight

The Space Race (1955-1972) between the Cold War rivals, United States and Soviet Union, pushed the development of the space technologies as a way to show ideological supremacy, space flight superiority and national security. Actually, the interest in high-speed flows started during the Second World War with the first supersonic rocket: the Aggregate-4 (later renamed "Vengeance Weapon" 2, V2, for military purposes). In this period, German aerospace engineers built the first supersonic wind tunnel in Peenemunde. At war's end, American, British, and Soviet scientific intelligence teams competed to capture Germany's rocket engineers along with the German rockets themselves and the designs on which they were based.

The Space Race officially started on August 2nd when the Soviet Union responded to the United States announcement to launch an artificial satellite by disclosing a similar plan. On October 4th 1957 the Soviet Union deployed the Sputnik 1 that after 3 months burned during the first re-entry in the history. After the Sputnik 1, the Sputnik 2 was launched but it was not designed for a safe re-entry. On the contrary, the first artificial satellite launched by the Unites States was able to re-entry with his guest, a monkey. Unfortunately, the parachute failed and the capsule was lost.

Some years later, in April 1961, the URSS succeeded in getting the first human into space, Yuri Gargarin, which returned safely to Earth few minutes later. The Space Race peaked on July 20th 1969 when the first human landed on the Moon with the Apollo 11 mission. The Space Race concluded on April 1972 with an agreement on the co-operative Apollo–Soyuz Test Project; in the July 1975 there was the first rendezvous in Earth orbit of a US astronaut crew with a Soviet cosmonaut crew.

The Space Race has left a legacy of Earth communications and weather satellites, and continuing human space presence on the International Space Station. It has also sparked increases in spending on education and research and development, which led to beneficial spin-off technologies.

1.2 The Hypersonic Environment

A generic rule of thumb adopted to define the flow hypersonic is that it exceeds Mach 5. This rule is rather arbitrary while it is better saying that the hypersonic regime is the one where certain physical flow phenomena become progressively more and more important as the Mach number increases (Anderson 2006). It is the regime where aerodynamics and thermodynamics meet chemistry. Indeed, the most relevant phenomena are rarefaction, high temperatures, non-ideal gas effects (dissociation and ionization), changing in the thermodynamic properties (ratio of the specific heats, γ) and catalicity at the wall surface. The consequences of the combination of such phenomena are reported in figure 1.1.

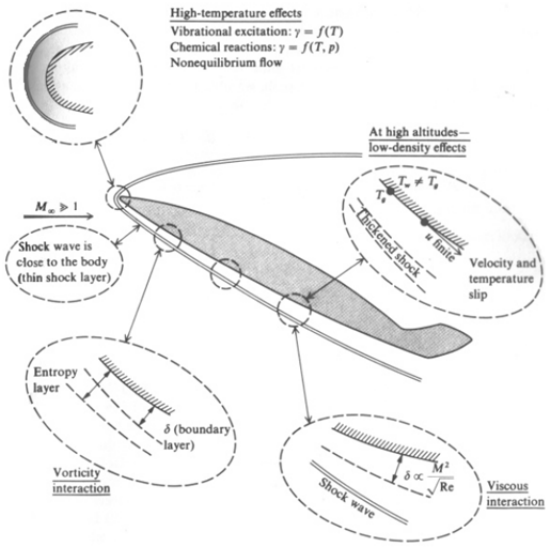

Figure 1.1. Characteristics of the hypersonic regime (from Anderson 2006).

The high temperatures present in the hypersonic regime, mainly due to the dissipation of kinetic energy in thermal energy, cause non-ideal gas effects like molecule dissociation or ionization that may change the thermodynamic properties and/or trigger the catalytic process at the wall of the vehicle. The latter causes the recombination of the dissociated species resulting in an additional increase of the wall heat transfer.

At high Mach numbers, the density across the shock becomes stronger while the thickness of the boundary layer reduces for the mass flow conservation. Furthermore, the non-linear gas effect makes the shock even thinner. The thin shock layer is the cause of the strong curvature in the blunt nose region that progressively decreases moving away. The changing in the curvature implies strong entropy gradients in a region named entropy layer. The boundary layer grows inside this strong vorticity entropy layer and is affected by it. This interaction is called vorticity interaction.

Figure 1.2. Apollo 11 capsule: the eroded thermal protection system.

Increasing the Mach number the shock moves closer to the wall because the shock wave angle becomes smaller. Furthermore, the high temperatures imply that the viscosity of the flow increases and the density decreases causing the thickening of the boundary layer. As a consequence, the shock wave and the boundary layer interact. This phenomenon is named viscous interaction.

1.3 Relevance of Transition in the Hypersonic Regime

According to the previous description, the characterization of the boundary layer state becomes a fundamental aspect in the hypersonic regime. Differently from the subsonic regime, where the state of the boundary layer influences prevalently the aerodynamic performances of the vehicle, in the hypersonic regime the state of the boundary layer is an issue when designing the thermal protection system (TPS). Indeed, in presence of a turbulent boundary layer the convective heat flux may be 3 or four times higher than in presence of a laminar boundary layer. The lack of experimental data and, consequently, of reliable methods for the accurate prediction of transition obliges engineers to use a conservative approach oversizing the thermal

protection system by reducing the allowable payload mass budget. Moreover, as for the low-speed regime, boundary layer transition affects aerodynamic performances and stability.

On the contrary, transition is widely desired in the frame of the hypersonic propulsion research for the design of scramjet engines. In this case, a turbulent boundary layer improves the overall mixing of the flow (fuel/air) and, moreover, it creates a thicker boundary layer less susceptible to the detachment caused by the adverse pressure gradients.

Roughness elements may promote boundary layer transition that may cause disastrous accidents as happened to the Columbia Space Shuttle. The prediction of induced transition by roughness elements appearing in the form of steps, joints or other patterns by ablation, thermal deformation or damage of the thermal protection system (figure 1.2) is extremely hard because the few available data do not allow understanding the basic physical aspects behind the phenomenon. This is due to the difficulties in reproducing the real flight conditions (high Mach number, high Reynolds number, high temperature, low environment noise) and in applying innovative experimental techniques in such extreme conditions (short testing time, thin boundary layer, reduced optical access, etc.).

1.4 Path to Turbulence

A general description of the road map to turbulence is necessary before going deeply in the analysis of the roughness-induced transition. A schematic of the laminar-to-turbulent boundary layer transition is reported in figure 1.3.

A nice description of the transitional process is given by Reskoto (2008)

"Process of transition for boundary layers in external flows can be qualitatively described using the following simplified scenario. Disturbances in the free stream, such as sound or vorticity, enter the boundary layer as steady and/or unsteady fluctuations of the basic state. This part of the process is called receptivity (Morkovin 1969) and although it is still not well understood, it provides the vital initial conditions of amplitude, frequency, and phase for the breakdown of laminar flow. Initially these disturbances may be too small to be measured and they are observed only after the onset of an instability. A variety of different instabilities can occur independently or together and the appearance of any particular type of instability depends on Reynolds number, wall curvature, sweep, roughness, and initial conditions. The initial growth of these disturbances is described by linear stability theory (i.e. linearized, unsteady, Navier-Stokes). This growth is weak, it occurs over a viscous length scale, and can be modulated by pressure gradients, surface mass transfer, temperature gradients, etc. As the amplitude grows, three-dimensional and nonlinear interactions occur in the form

of secondary instabilities. Disturbance growth is very rapid in this case and breakdown to turbulence occurs".

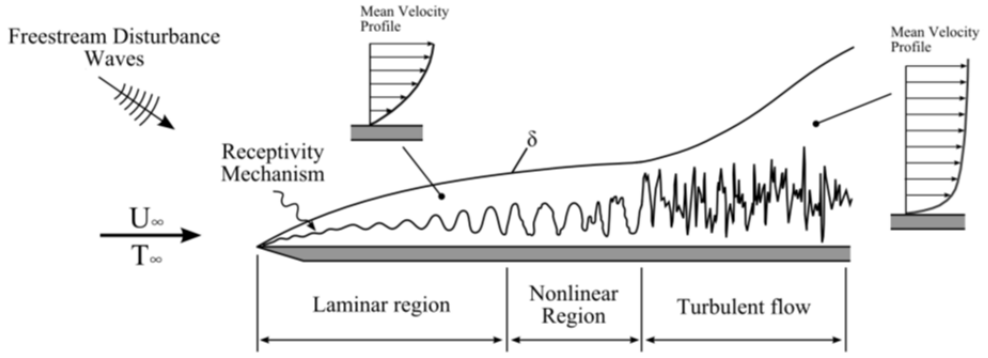

Figure 1.3. Schematic of the laminar-to-turbulent boundary layer transition (from Masutti 2013).

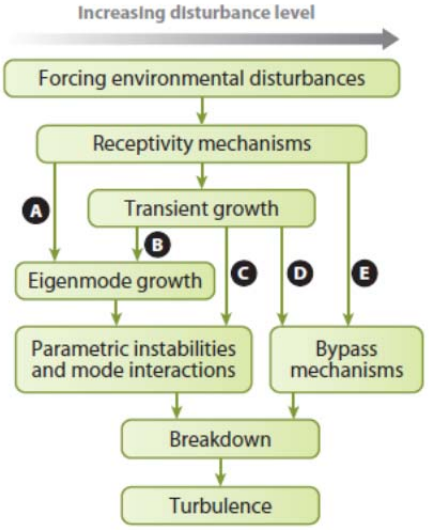

Figure 1.4. Paths to transition (from Reskoto 2008).

Until the early 1990's the laminar-to-turbulent transition process was mainly attributed to the linear amplification of the exponentially growing Tollmien-Schlichting (T-S) waves. However, transition phenomena in presence of linearly stable flow could be not explained by means of the T-S waves but better from the transient growth theory (Morkovin 1985). Following Reskoto (2008)

"Transient growth arises through the non-orthogonal nature of the Orr-Sommerfeld and Squire eigenfunctions. The largest effects come from the non-orthogonal superposition of slightly damped, highly oblique (near streamwise) T-S and Squire modes. These modes are subcritical with respect to the T-S neutral curve. The transient growth signature is essentially an algebraic growth followed by an exponential decay. Prior to this decay, they are capable of undergoing very significant growth upstream from where T-S waves are destabilized. A weak transient growth can also occur for two-dimensional or axisymmetric modes".

The transient growth theory led to the enlargement of the possible transition paths as clearly reported in figure 1.4. Morkovin et al (1994) distinguished five different paths:

A. Path A represents the path to transition that may happen in presence of low disturbance environment. It is based on the modal growth and includes transition mechanisms such as T-S waves, Görtler vortices or crossflow.
B. Path B involves the presence of the transient growth that provides higher initial amplitude to the eigenmode growth before crossing into an exponentially unstable region. Differently from the modal growth that is largest for oblique disturbances, the transient growth is largest for streamwise disturbances. How these disturbances are coupled is not still understood.
C. Path C is associated with the transient growth that arises through the non-orthogonal nature of the eigenfunctions. The largest effects come from the superposition of the slightly damped, high oblique waves of the continuous spectrum. This path may explain the many transition cases that involve bypass mechanisms.
D. Path D is characterized by a disturbance spectrum that looks like a turbulent spectrum even if the boundary layer is still laminar. It is relevant for internal flows at elevated turbulence intensity.
E. Path E represents the case of very large amplitude forcing where there is no linear regime. The resulting free-stream spectra do not resemble wind tunnel or grid turbulence spectra.

1.5 Roughness-Induced Transition

The present work focuses on the analysis of laminar-to-turbulent transition induced by three-dimensional (3D) roughness elements. As stated before, the prediction of transition is really hard because it depends on several factors: Reynolds number, Mach number, surface temperature, free stream disturbance level, geometry

and size of the roughness itself. Moreover, the impossibility to reproduce all the in-flight conditions in a same facility and the lack of real data make its comprehension even more difficult.

Roughness elements are traditionally classified in three types:

- 2D roughness: an element is assumed 2D when its characteristic length perpendicular to the flow direction and parallel to the surface (width) is one order of magnitude higher than the two other characteristic lengths. The forward facing step on an axisymmetric body is an example.
- 3D roughness: they are the most common having all the three characteristic lengths of the same order of magnitude. An isolated rivet is an example.
- Distributed roughness: in this case the flow interacts with many roughness elements randomly or uniformly distributed on the surface. The ablated TPS (figure 1.2) or rows of rivets are good examples.

The most visible effect of the presence of roughness element is to move transition forward respect to the smooth wall transition location ($x_{t,0}$) and its effectiveness mostly depends on its nature (2D, 3D or distributed), its height relative to the undisturbed boundary layer thickness and its geometry. In particular, the experiments carried out by Van Driest and McCauley (1960) showed that the influence of 2D elements is weaker than 3D elements for a given roughness height (figure 1.5). Tani (1969) gave a possible explanation of this difference

"A two-dimensional roughness element produces two-dimensional vortices which develop into a three-dimensional configuration before eventually disintegrating into turbulence. Formation of vortices with a three-dimensional configuration is considered a prerequisite to turbulence, and this explains why transition moves upstream close to the roughness element rather gradually as the stream velocity is increased. On the other hand, a three-dimensional roughness element is more straightforward in producing three-dimensional vortices, thus causing transition to move quickly upstream as soon as vortex shedding occurs at the element".

A very nice and clear description of the role of the roughness elements in promoting transition was given by Klebanoff et al (1955)

"It is observed that when transition occurs some distance from a roughness element, the alteration in the velocity profile has disappeared, leaving, however, perturbations that would not have been present in the absence of roughness. It appears, therefore, that the primary effect of the roughness is to increase the magnitude of the perturbations, probably through the unstable character of the flow behind the roughness. This argument does not hold when transition occurs at the

element, but in the case of a three-dimensional element, the development of a wedge of turbulence starting from the element evidently is not possible when the surrounding flow is below the stability limit".

However, there is no general mechanisms based theory for determining the conditions under which roughness can promote transition. In his review, Schneider (2008) discussed three scenarios on how roughness elements can promote the occurrence of transition. In the first case, the roughness element generates a wake including streamwise vorticity and a potentially unstable shear layer that may transition to turbulence. The second scenario involves the amplification of streamwise vorticity in the wake of small roughness element via instability mechanisms such as stationary crossflow, Görtler or transient growth. In the third case, the roughness element can interact with acoustic waves or other free stream disturbances to generate instability waves or precursors to instability waves via a receptivity process (King and Breuer 2001).

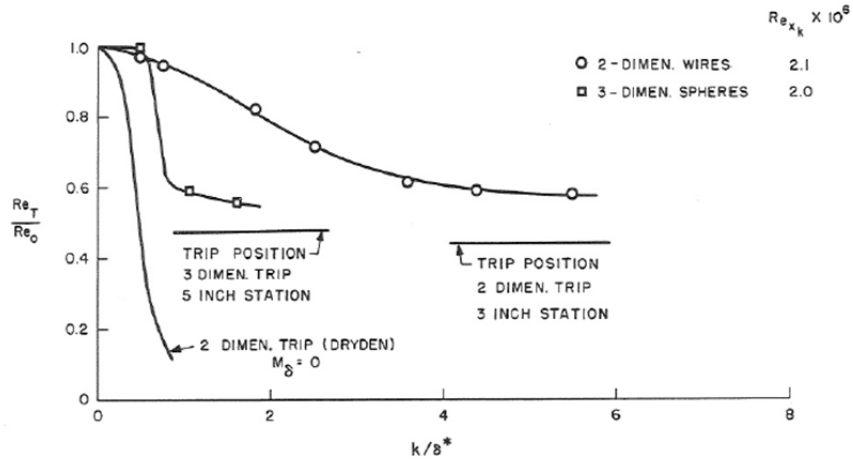

Figure 1.5. Relative effect of 2D and 3D roughness elements (from Van Driest and McCauley 1960). The experiments were carried out at Mach number at the edge of the boundary layer equal to 2.71 on a 12 inches, 10° cone.

1.5.1 Parametric Effects

The effectiveness of roughness elements on transition depends on the flow conditions (see Schneider 2008 for a comprehensive review). In particular, the Reynolds number (Re) has been recognized as being the most relevant parameter. Van Driest and Blumer (1962) studied the effect of the Reynolds number on the transition location on a 10°, 20 inches cone at zero angle of attack at edge Mach number (the Mach number at the edge of the boundary layer, M_e) equal to 2.71 (figure 1.6). They

tripped the boundary layer with an azimuthal row of 3D spherical roughness and compared the measured transition location with and without the protuberances. Curve 4 in figure 1.6 represents the transition location (x_t) as a function of the Reynolds number for the smooth wall condition. In this case natural transition occurs; the transition location moves upstream because the disturbance level into the flow increases with the Reynolds number. Differently, curves 1, 2 and 3 represent the transition location as a function of the Reynolds number in presence of spherical roughness elements. Curve 1 shows a trend that is similar to curve 4; in this case the roughness effect is negligible respect to the amplification of the free stream disturbances and the transition is said "incipient". Curve 2 represents the "critical" conditions for the roughness; the transition location moves suddenly close the roughness location. In this case the roughness element is the main cause of transition. Finally, curve 3 is almost flat and the transition is said "effective". The transition location moves as close as possible to the roughness location (dashed line in figure 1.6). In this condition the effect of free stream disturbances is negligible (Pate 1971, Casper 2011).

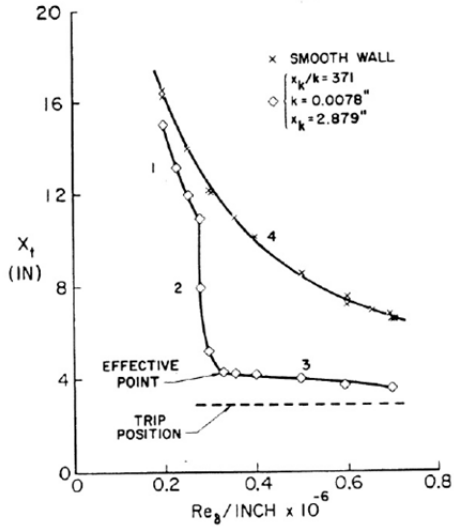

Figure 1.6. Transition location as a function of the unit Reynolds number (from Van Driest and Blumer 1962). The experiments were carried out at edge Mach number equal to 2.71 on a 20 inches, 10° cone. The boundary layer was tripped with an azimuthal row of 3D spherical roughness.

Another relevant flow parameter that influences the transition in presence of roughness elements is the Mach number. Figure 1.7 reprinted from Schneider (2008) and Morrisette et al (1969) shows a comprehensive plot of the Mach number effects on effective roughness on both flat plate and cone indicated respectively with M_p and M_c.

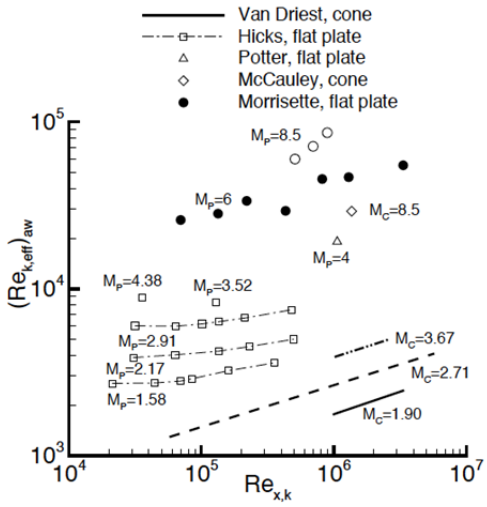

Figure 1.7. Variation of the effective roughness Reynolds number with roughness position Reynolds number and Mach number (from Schneider 2008).

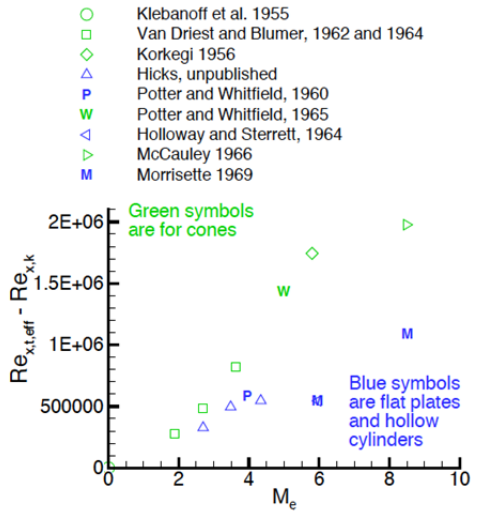

Figure 1.8. Variation with Mach number of Reynolds number based on distance from trip to transition (from Schneider 2008).

Data shows that $Re_{k,eff}$ (effective Reynolds number based on the edge conditions) increases of an order of magnitude when the Mach number at the edge of the boundary layer increases. Furthermore, it is evident that the $Re_{k,eff}$ is not constant for a given Mach number but it strongly depends on the Reynolds number based on the edge

conditions at the roughness location, $Re_{x,k}$. However, it is clear that the Mach number has a stabilizing effect on transition.

The delay in transition is very important, particularly at very high Mach numbers where even in presence of effective trips transition may occur some distance downstream of the roughness location (figure 1.8). In the figure, $Re_{x_t,eff}$ is the effective Reynolds number based on the edge conditions. Therefore, the vertical axis is the Reynolds number based on the distance from the trip to the transition location. As clearly visible, $Re_{x_t,eff} - Re_{x,k}$ increases markedly with the Mach number and it is much larger for cone than for flat plate and hollow cylinders. This phenomenon may be associated with the reduced instability of high Mach number shear layers (Schneider 2008).

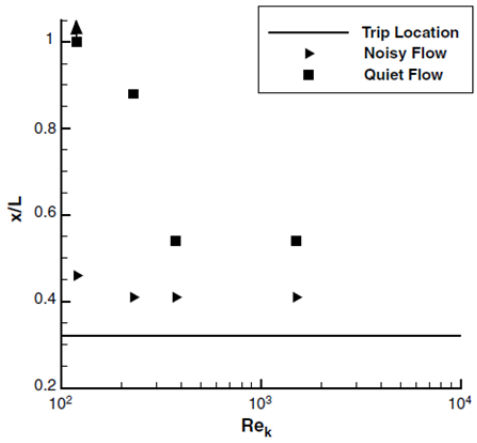

Figure 1.9. Effect of trip Reynolds number (Re_k) on the transition location. Flow over a cone at zero angle of attack and free stream Mach number equal to 6 (from Casper et al 2011).

Lastly, the effect of the wall temperature needs to be considered. Surface temperature can have a dramatic effect on transition because it changes the boundary layer properties (Van Driest and Boison 1957). In this case, the difficulties in reproducing the correct in-flight conditions are relevant: the wall-to-total temperature ratio in wind tunnels is extremely different from the expected in-flight. Furthermore, the ratio is varied by changing the wind tunnel total temperature, which also influences the noise radiated from the nozzle wall.

All the data presented in this section have been obtained from experiments conducted in conventional ground-testing facilities that are contaminated by the turbulent boundary layer normally present on the wind tunnel walls (Schneider 2001). The noise level measured in conventional facilities is usually one order of magnitude higher than the one registered during the flight and transition can occur one order of

magnitude earlier. In addition, the mechanisms of transition present in low-noise environment may be altered or even bypassed. Casper et al (2011) found that the transition location is significantly delayed when the measurements are performed in a low disturbance free stream generated by a so-called quiet wind tunnel. Furthermore, they stated that although the free stream disturbance level has a significant effect on the transition location for natural or incipient transition, it does not have a large influence when an effective trip height is reached (figure 1.9).

1.5.2 The Engineering Approach: Semi-empirical Correlations

The lack of knowledge of the physical-based mechanisms behind roughness-induced transition led to the definition of several semi-empirical correlations (see Reda 2002 for a detailed review) such as the Shuttle (Berry et al 1998) or the PANT (Wool 1975) criteria, which are calibrated using wind tunnel experiments (Berry and Horvart 2007). In general, the goal is to include the flow physics in to the correlation (e.g. the stability of the boundary layer, the effect of wall temperature) as much as possible (e.g. the transition criteria proposed by Potter and Withfield 1962 and Van Driest et al 1967). However, in practise it turns out that this is only partially possible due to the complicated flow phenomena, which requires a recalibration of the correlation for each different vehicle or roughness geometry.

In the following the Shuttle Roughness Criteria is adopted. However, for the sake of completeness the most well known correlation approaches are briefly reported.

1.5.2.1 The Shuttle Roughness Criteria

The Shuttle Roughness Criteria was developed by NASA for the Space Shuttle, X-33, X-34 and X-38 programs (McGinley et al 2006). The Shuttle roughness criteria (Berry et al 1998) is written as

$$\frac{\mathrm{Re}_\theta}{\mathrm{M}_e} = \mathrm{C}\left(\frac{\mathrm{k}_r}{\delta}\right)^{-1} \tag{1.1}$$

In the criterion, M_e is the Mach number at the edge of the boundary layer at the roughness location, Re_θ is the Reynolds number based on the edge conditions and the momentum thickness, k_r is the roughness height, δ is the boundary layer thickness and the constant C is equal or larger than 200 for critical roughness and equal or larger than 310 for effective roughness (Berry et al 2006). The correlation was obtained by comparing different dataset from experiments carried out in the same wind tunnel, at the same Mach number and wall temperature ratio. However, the value of C is dependent on the flow conditions and different values were reported in the literature over the years (Reda 2002).

1.5.2.2 The PANT Correlation for Blunt Nosetip

The PANT transition onset criterion (Wool 1975) is written as

$$\mathrm{Re}_{\theta^\star}\left(\frac{k_r}{\psi^\star\theta^\star}\right)^{0.7} = 255 \tag{1.2}$$

$$\psi^\star = 0.1B' + (1 + 0.25B')\frac{\rho_e}{\rho_w} \tag{1.3}$$

$$B' = \frac{\dot{m}}{\rho_e u_e C_h} \tag{1.4}$$

Here, values with the superscript $\star$ are taken at the sonic conditions. B' is non dimensional ablation parameter, C_h is the modified Stanton number (see equation 4.13), $\dot{m}$ is the surface ablation mass flux, ρ_e is the density at the boundary-layer edge, ρ_w is the density at the wall.

1.5.2.3 Van Driest and Blumer

Van Driest and Blumer (1967) correlates roughness-induced transition data on cones and hemispheres by plotting

$$\frac{\mathrm{Re}_{\delta^*}}{1 + 0.5(\gamma - 1)M_e^2} \tag{1.5}$$

on the abscissa versus

$$\frac{k_r/\delta^*}{1 + 700(k_r/D)} \tag{1.6}$$

on the ordinate. According to Schneider (2008) it is not certain how well this correlation would extend to other test conditions.

1.5.2.4 Potter and Whitfield

Potter and Whitfield (1962) developed a correlation for the effect of roughness on transition for blunt cones. The correlation plots

$$\sqrt{x_t - x_{t,0}} - \frac{\mathrm{Re}'_{k_r}}{\epsilon}\sqrt{\frac{x_r}{x_{t,0}}} \tag{1.7}$$

on the abscissa versus a disturbance parameter

$$\frac{\mathrm{Re}'_{k_r}}{\epsilon} \tag{1.8}$$

Here, ϵ is the value of Re'_{k_r} where $x_t = x_r$, the Re'_{k_r} is a scaled version of the Reynolds number based on the roughness height (Re_{k_r}), and $x_{t,0}$ is the smooth wall transition location. The correlation has the disadvantage of requiring the prior knowledge of the smooth-wall transition location.

1.5.2.5 Roughness Reynolds Number

The roughness Reynolds number

$$\mathrm{Re}_{k_r} = \frac{\rho_{k_r} u_{k_r} k_r}{\mu_{k_r}} \tag{1.9}$$

is evaluated by computing density, viscosity and velocity at the roughness height.

For low Mach numbers, $0 < M_e < 2$, Braslow and Horton (1958) obtained good correlation for Re_{k_r} approximately equal to 500. However, Holloway and Morrisette (1966) experimentally demonstrated that the correlation is not fully valid for higher Mach number.

1.6 Physical Mechanisms behind Roughness-Induced Transition

As clearly evident from the previous section roughness-induced transition has been extensively analysed with an engineering approach: engineers measured the transition location over different flow conditions and then they compared the experiments with in-inflight data. However, it has not been identified yet a unique correlation due to the lack of knowledge on the physical mechanisms behind roughness-induced transition. This was particularly due to available experimental technique at that time: data were mainly acquired by means of flow visualization experimental techniques such oil flow (Whitehead 1969, figure 1.10), Schlieren (Jackson and Czarnecki 1960) and fluorene sublimation (Hicks and Harper 1970). To that end, in the last years, researchers applied innovative non-intrusive techniques to visualize (Danehy et al 2009, 2010) and quantitative measure (Bathel et al 2011, Tirtey et al 2011, Kumar et al 2014) relevant flow features ahead and behind the roughness elements. The improvement in the experimental capability coupled with the availability of DNS data (Zhong and Wang 2012) will improve the knowledge of the physical mechanisms behind roughness-induced transition.

In the following a brief review of the most relevant experimental and computational works on the subject are reported.

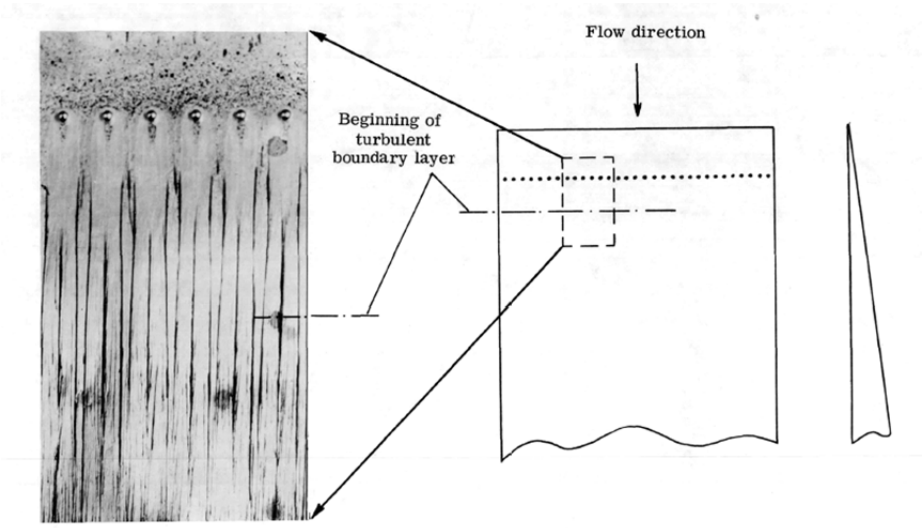

Figure 1.10. Oil Flow visualization of the flow upstream and downstream of a row of spherical elements on a flat plate. Experiments carried out at Mach number equal to 6 and k_r/δ equal to 2 (from Whitehead 1969).

1.6.1 The Separated Region Ahead of the Roughness Element

The separated region upstream of a roughness element located in a hypersonic laminar boundary layer has been of specific interest in the past due to its effect on boundary layer transition. Recently, Estruch-Samper et al (2010) and Kumar et al (2014) pointed out the importance of this region because of the presence of a localized hot spot in the region just around the protuberance. The intensity of the hot spot and its location depend on the flow conditions. Moreover, DNS data from Iyer and Mahesh (2013) and Subbareddy et al (2014) showed that the separated region upstream of the protuberances is constituted by multiple counter-rotating vortex pairs that wrap around the roughness element developing downstream as streamwise vortices.

The mechanisms of the upstream separation in presence of large compressive disturbance were clearly described by Lighthill (1953)

"A sufficiently large compressive disturbance causes separation of the boundary layer with reversed flow at the surface. In the resulting modified external flow the pressure begins to rise ahead of the separation point, and separation results there too. This upstream effect can be ascribed to the fact that a disturbance leading to a positive pressure gradient causes the boundary layer to thicken; then the boundary layer begins to curve slightly upstream and this curvature itself produces a pressure gradient in the same sense slightly upstream. Moreover, separation can also be though as constituting so large a disturbance that even in an inviscid flow it would have a

detached shock wave up to which its influence would extend. The separation point spreads upstream until the dead-air region is sufficiently slender to cause no further separation ahead of it. This happens much sooner for a turbulent boundary layer than for a laminar one, because turbulent boundary layer separates far less readily".

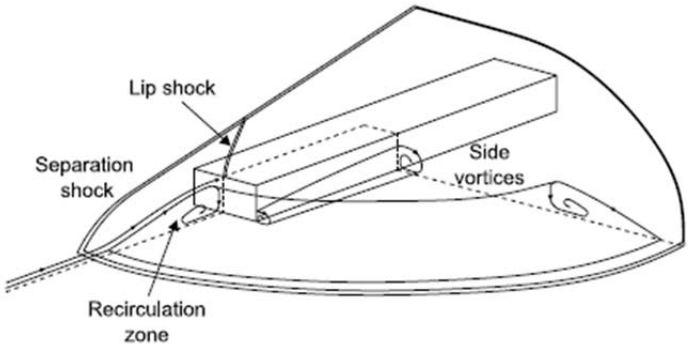

Figure 1.11. Schematic of the separated region upstream of a forward facing step (from Kumar et al 2014).

Figure 1.11 (from Kumar et al 2014) shows a simple schematic of the separated region upstream of a 3D roughness element immersed in a laminar hypersonic boundary layer. In the figure, the separation shock causes the thickening of the boundary layer; while the upper part of the boundary layer gets deflected the lower part enters the recirculation region immediately in front of the protuberance. In the separated region and just around the protuberance a local peak in the heat transfer rate is measured.

Estruch-Samper et al (2010) focused the attention on measuring the heat transfer around roughness elements located on a flat plate immersed in both a laminar and turbulent boundary layer with free stream Mach numbers ranging between 8.2 and 12.3 and unit Reynolds numbers in the range $3.35 \cdot 10^6\ \mathrm{m}^{-1} < \mathrm{Re}_{\mathrm{unit}} < 9.35 \cdot 10^6\ \mathrm{m}^{-1}$. They used thin-film gauges to measure the heat flux in the vicinity of the protuberance while further flow characteristics were identified using oil-dot and high-speed Schlieren visualizations. They investigated several forward facing steps with different protuberance deflection angles (α_S).

In presence of the separated region a system of three shock waves is formed: leading edge shock, separation shock and lip shock (figure 1.12b-f). Differently, when the recirculation region is absent the separation shock is not present (figure 1.12a). When the incoming boundary layer is laminar the separated region is more likely to occur for small protuberance angles while higher angles are necessary in case of turbulent incoming boundary layer (figure 1.13).

The heat flux measurements showed that the hot spot is present in front of the roughness elements when separation occurs. Anyway, there are cases in which the hot spot is detected on the side of the protuberances. Moreover, the hot spot intensity increases with increasing the protuberance angle because the reattachment of the separated region is more severe.

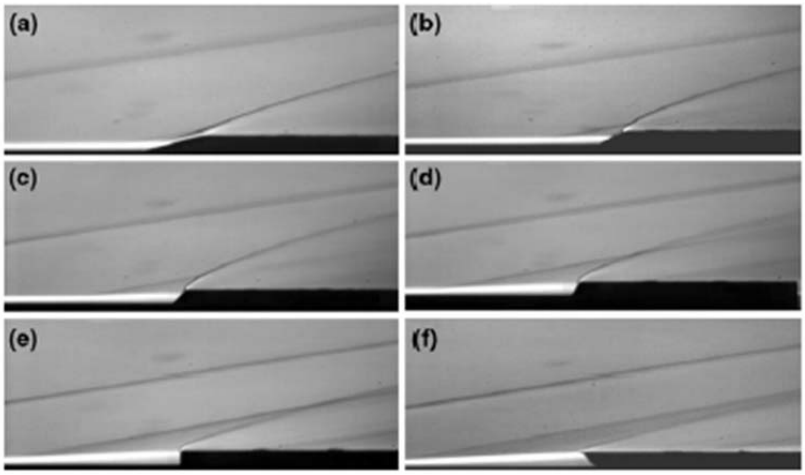

Figure 1.12. Schlieren visualization of the shock waves upstream of a protuberance located on a flat plate and immersed in a laminar boundary layer at free stream Mach number equal to 8.2 and unit Reynolds number equal to $9.35 \cdot 10^6\ m^{-1}$; (a) α_S=15°, (b) α_S=30°, (c) α_S=45°, (d) α_S=60°, (e) α_S=90°, (f) α_S=135° (from Estruch-Samper et al 2010).

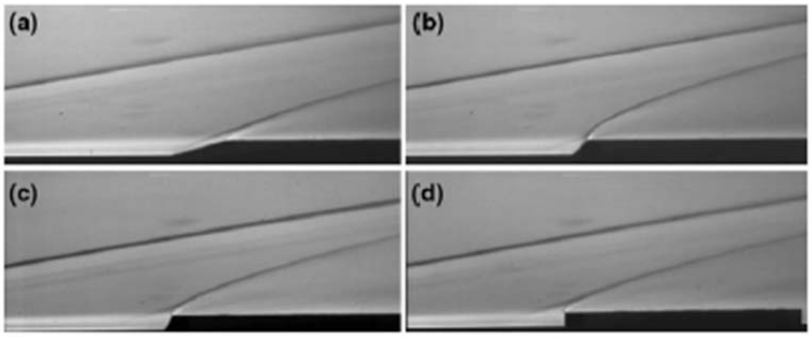

Figure 1.13. Schlieren visualization of the shock waves upstream of a protuberance located on a flat plate and immersed in a turbulent boundary layer at free stream Mach number equal to 8.2 and unit Reynolds number equal to $9.35 \cdot 10^6\ m^{-1}$; (a) α_S=15°, (b) α_S=45°, (c) α_S=60°, (d) α_S=90° (from Estruch-Samper et al 2010).

The huge amount of data collected allowed the authors to define a semi-empirical correlation able to estimate the intensity and the location of the hot spot. It is reprinted from Estruch-Samper et al (2010) in figure 1.14.

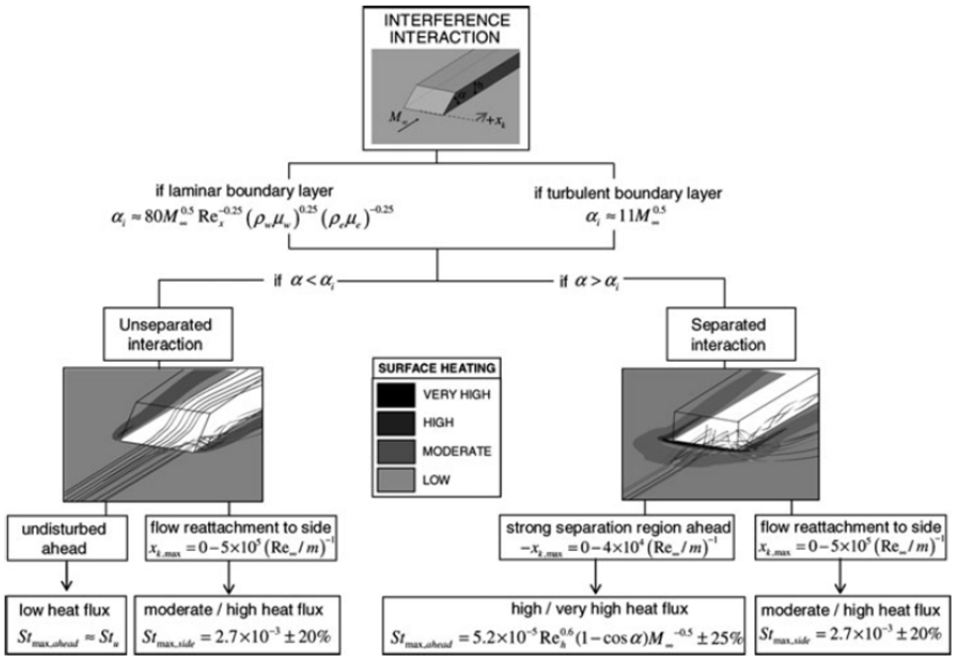

Figure 1.14. Engineering approach to predict the location and the magnitude of the highest heating in the vicinity of surface protuberances in hypersonic flows (from Estruch-Samper et al 2010).

Kumar et al (2014) found a similar shock waves' system in presence of a separated region. They carried out experiments in a shock tunnel with free stream Mach number ranging between 6 and 12. They tested forward facing steps with different protuberance deflection angles (α_S) installed both on a flat plate and a cone. Similarly to Estruch-Samper et al (2010), they measured the heat flux by means of heat flux gauges and they visualized the flow by means of Schlieren imaging. Additionally, they measured the pressure around the protuberances with PCB sensors. Finally, they compared the experimental results with numerical simulations.

From the experiments they established that the length of the separated region is approximately 10 times the roughness height (figure 1.15) when the roughness is installed on the cone while it is longer when it is located on the flat plate (approximately 11.5 times). Furthermore, increasing the roughness height an increase of the pressure upstream of the protuberance was registered. The numerical simulations confirmed the presence of a recirculation region with the formation of a vortex that wraps around the roughness element.

The structure of the flow in the separated region ahead of the roughness element is not fully clear yet. The achievements in the computations of compressible flows have shown that the upstream configuration is rather complex and it consists of multiple

counter-rotating vortex pairs (Iyer and Mahesh 2013, Subbareddy et al 2014). Similar structures were visualized by Backer (1979) and Simpson (2001) in the investigation of the junction flows at low speed.

Iyer and Mahesh (2013) performed DNS replicating the experiments carried out by Danehy et al (2009). In their computations they reported a complete analysis of the wake in front and behind a hemispherical roughness element with $k_r/\delta > 1$ at three Mach numbers (M_∞=3.37, 5.26 and 8.23). They saw that separation results in a concentration of vorticity from the boundary layer into discrete spanwise vortices.

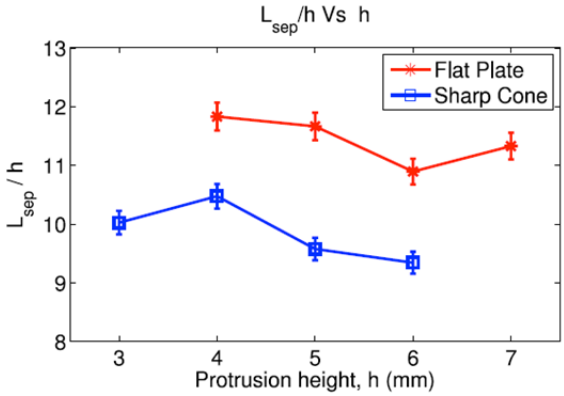

Figure 1.15. Separation length versus the protrusion height for flat plate and cone (from Kumar et al 2014).

Computations showed that a six-vortex system is produced for Mach equal to 3.37 and 5.26 (figure 1.16a-b), while a four-vortex system is present for the higher Mach number investigated (figure 1.16c). At the lower Mach number the vortices are high unsteady and their position may vary in time. In this case, the number of vortices obtained from the time averaging of the flow is different from the instantaneous one (figure 1.17a-c). Additionally, figure 1.17b and d shows that the region with high skin friction C_f appears close to the centre of the roughness while the peak in the modified Stanton number (C_h) is measured between the two vortices.

Similarly, Subbareddy et al (2014) performed a direct numerical simulation of the flow around a cylindrical element with $k_r/\delta > 1$. They replicated the experiments performed by Wheaton and Schneider (2010) in which the instability in the wake was measured by means of Pitot tube and hot wire probes in the Boeing/AFOSR Mach-6 Quiet Tunnel (BAM6QT). Subbareddy et al (2014) studied the influence of the free stream unit Reynolds number on the transitional flow pattern. They found a vortex organization similar to the one showed by Iyer and Mahesh (2013).

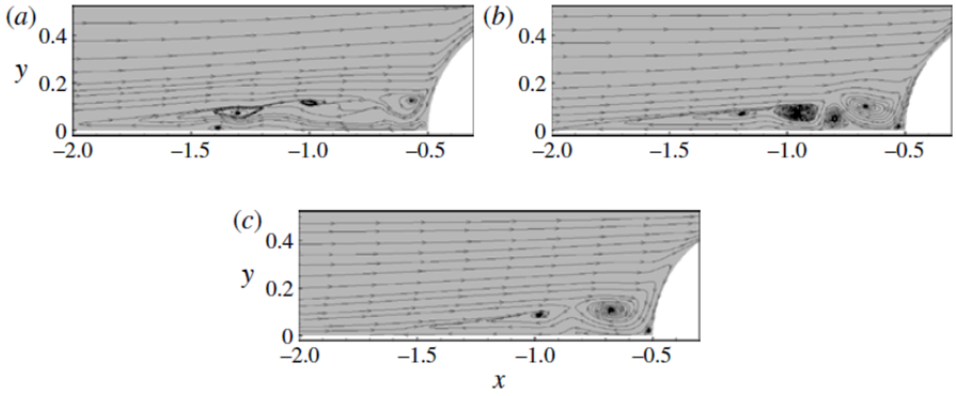

Figure 1.16. DNS streamline upstream of the spherical roughness element indicating the number of vortices; (a) M_∞= 3.37, (b) M_∞= 5.26, (c) M_∞= 8.23 (from Iyer and Mahesh 2013).

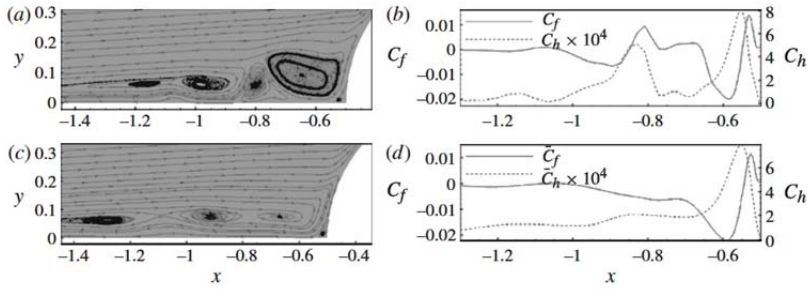

Figure 1.17. DNS streamline upstream of the spherical roughness element indicating the number of vortices at M_∞= 3-37: (a) instantaneous, (c) mean; Skin friction (C_f) and Stanton number (C_h) along the centreline for the same conditions: (b) instantaneous, (d) mean (from Iyer and Mahesh 2013).

1.6.2 The Transitional Region Downstream of the Roughness Element

The previous discussion shows that the transition region behind the roughness elements has been carefully investigated in the past. However, flow visualization techniques allowed measuring only the transition location without investigating the physical based mechanisms behind transition. To that end, in the last years, researchers applied innovative non-intrusive techniques to visualize (Danehy et al 2009, 2010) and quantitative measure (Bathel et al 2011, Tirtey et al 2011) relevant flow features behind the roughness elements.

A possible way to identify the flow structures is to look at the vortex footprints on the model surface. Flow visualization techniques are particularly useful but they do not provide quantitative data. On the contrary, measurements of the wall heat transfer rate can provide useful quantitative data that can be further used to extract information

about the most relevant flow structures. To that end, two-dimensional techniques such as IR thermography (Carlomagno and Cardone 2010) or temperature sensitive paints (Liu et al 2013, TSP) are particularly useful. For example, Tirtey et al (2011) quantitative compared different roughness geometry by means of IR thermography and oil flow visualizations. They looked at the wake features by discussing the Stanton number distribution at the wall and they proposed the K non-dimensional parameter as tool to distinguish the laminar, transitional and turbulent wake regions. They detected the formation of secondary structures moving downstream from the roughness elements (figure 1.18). Anyway, a significant scatter in the data did not permit to clearly classify the roughness effectiveness in promoting transition.

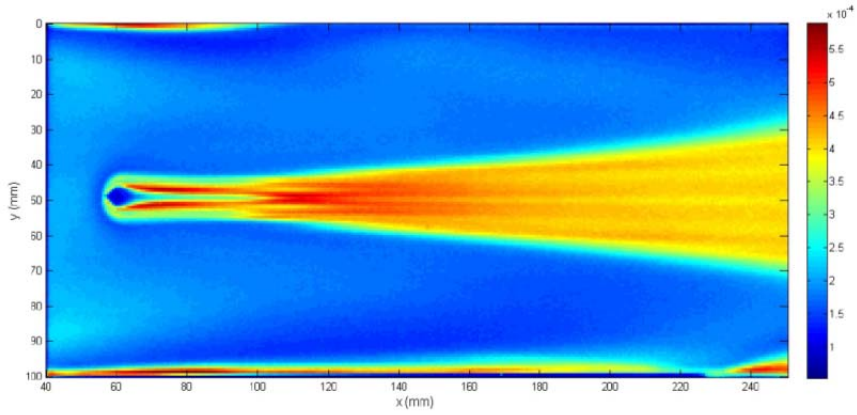

Figure 1.18. Modified Stanton number distribution of the flow past a square roughness element submerse in a laminar boundary layer at Mach number equal to 6 and unit Reynolds number equal to $2.6 \cdot 10^7$ m^{-1} (from Tirtey 2008).

However, data inside the wake are necessary. Sharp and White (2014) investigated roughness-induced transient growth on a 5° blunt cone in the Texas A&M Mach 6 Quiet Tunnel by means of Pitot tube and hot wire probes. In their experiments, they found azimuthally alternating high and low-speed streaks growing downstream of the roughness element.

The presence of physical probes may alter the flow field due to the presence of shock waves. To overtake this problem laser based techniques have been developed and applied. Danehy et al (2010) applied high-speed nitric oxide planar laser induced fluorescence (NO PLIF) to visualize the flow structures downstream of three cylindrical protuberances with different heights attached on a flat plate. They carried out the experiments in the 31-Inch Mach 10 Air Tunnel at NASA Langley Research Center, at unit Reynolds numbers ranging between $3.35 \cdot 10^6$ m^{-1} and $6.02 \cdot 10^6$ m^{-1}. The

plate angle of attack and the Reynolds number were varied to achieve desired combinations of boundary layer edge Mach number and boundary layer thickness.

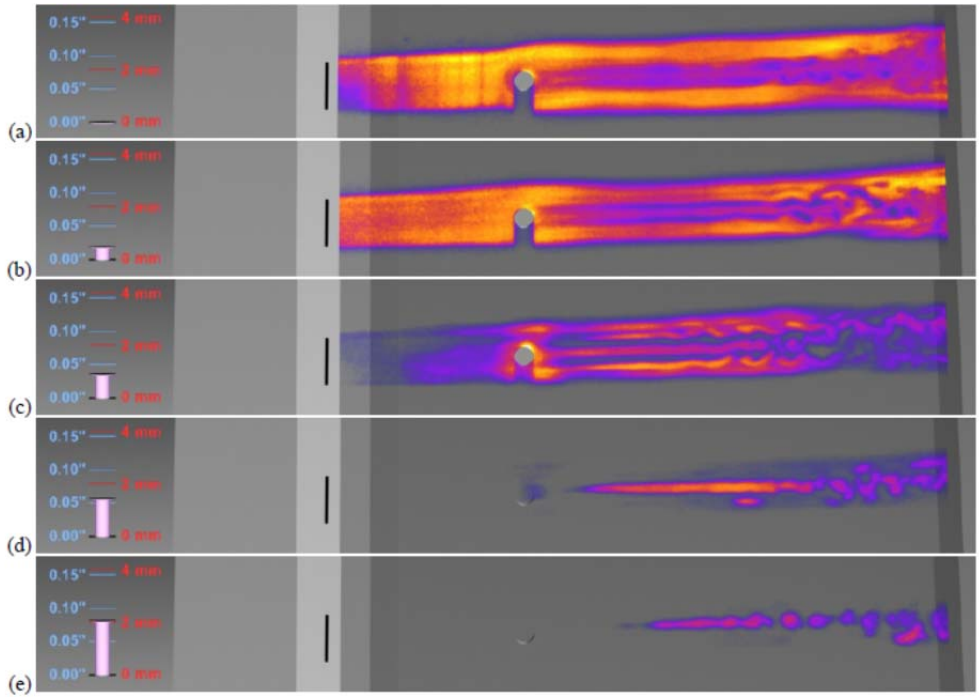

Figure 1.19. Flow past a 1 mm height cylindrical roughness element with diameter equal to 4 mm at $M_\infty = 10$. The flat plate angle of attack is 20°. The laser sheet position varies from 0 to 2 mm above the plate (a)-(e) in 0.5 mm increments (from Danehy et al 2010).

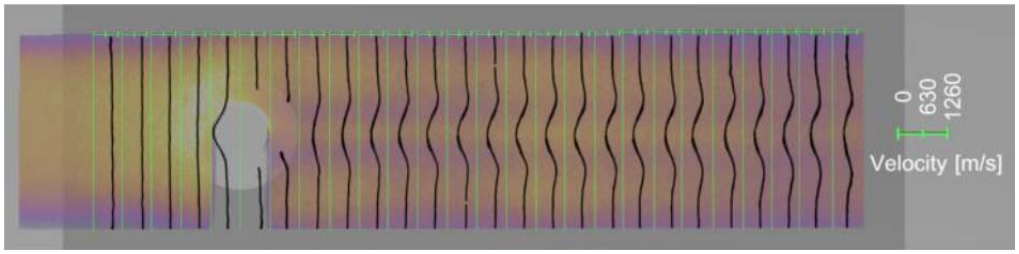

Figure 1.20. Flow past a 2 mm height cylindrical roughness element with diameter equal to 4 mm located on a flat plate at $M_\infty = 10$. The laser sheet position is 2 mm above the plate. The solid lines represent the mean velocity values out of 41 runs while the dashed line represent the 95% uncertainty in the mean velocity (from Bathel et al 2011).

They investigated the development of the wake by scanning the measurement volume in several planes parallel (plane view) and perpendicular (side view) to the flat plate while they obtained qualitative data on the wall by means of oil flow visualizations. They detected streamwise developing streaks in the wake of the

elements that were associated to streamwise vorticity. These streaks become unstable (starting from the edge of the boundary layer), oscillating with periodic structures and then they break down into irregular structures (figure 1.19).

In order to obtain quantitative measurements of the flow features Bathel et al (2011) extracted velocity measurements from NO PLIF images by generating multiple tagged lines that fluorescence as they convect downstream. Then, the axial velocity was estimated by means of a cross-correlation analysis of the horizontal shift of individual tagged lines. Bathel et al (2011) applied the technique to investigate the wake behind a 2 mm tall cylindrical protuberance with a 4 mm diameter (figure 1.20) at asymptotic Mach number equal to 10. The flow downstream of the upper and lower edge of the trip in the image is accelerated beyond the laminar flow velocity occurring upstream of the trip and on the periphery of the image downstream of the trip. As the flow progresses around the trip, the measured velocities appear to maintain the pre-trip velocity with the exception of the velocity values in the immediate wake of the trip. Downstream of the trip the velocity observed along the centreline drops to 500 m/s. In the accelerated flow region directly downstream of the top and bottom edges of the trip, the velocity exceeds 1025 m/s. However, the techniques permit to measure only the axial velocity while the flow behind the protuberances is highly three-dimensional: at this time, DNS constitutes the only complete source of information about the whole flow.

The DNS data provided by Iyer and Mahesh (2013), described in the previous section, gives relevant information about the instantaneous flow organization (figure 1.21). In particular, as expected the flow is more stable at the higher Mach number (M_∞ = 8.23, figure 1.21c) while it becomes turbulent at Mach equal to 3.37 (figure 1.21a) and 5.26 (figure 1.21b) exhibiting hairpin vortices in the wake. Furthermore, the transition location is closer to the protuberance at the lower Mach number where the roughness may be classified as effective.

They showed that the vortices formed upstream (see previous section) wrap around the protuberance and develop as streamwise vortices. Thus, the roughness wake is constitutes by couple of counter-rotating vortex pair. Their number depends on the flow conditions. The vortices across the centreline were named SP (symmetry plane) vortices while the ones away from the symmetry plane OSP (off-symmetry plane) vortices. The SP vortices have an upwash between them and the effect of the mirror vortices is to induce them to move towards each other thus strengthening the magnitude of the vertical velocity between them. On the other hand, the SP and the OSP vortices have a downwash between them; the effect of the mirror vortices is to move the vortices away from each other; in effect weakening the velocity induced between them. Based on this reasoning Iyer and Mahesh (2013) concluded that

counter-rotating vortices with a central upwash close to the wall are more likely to induce transition as compared to those with a central downwash.

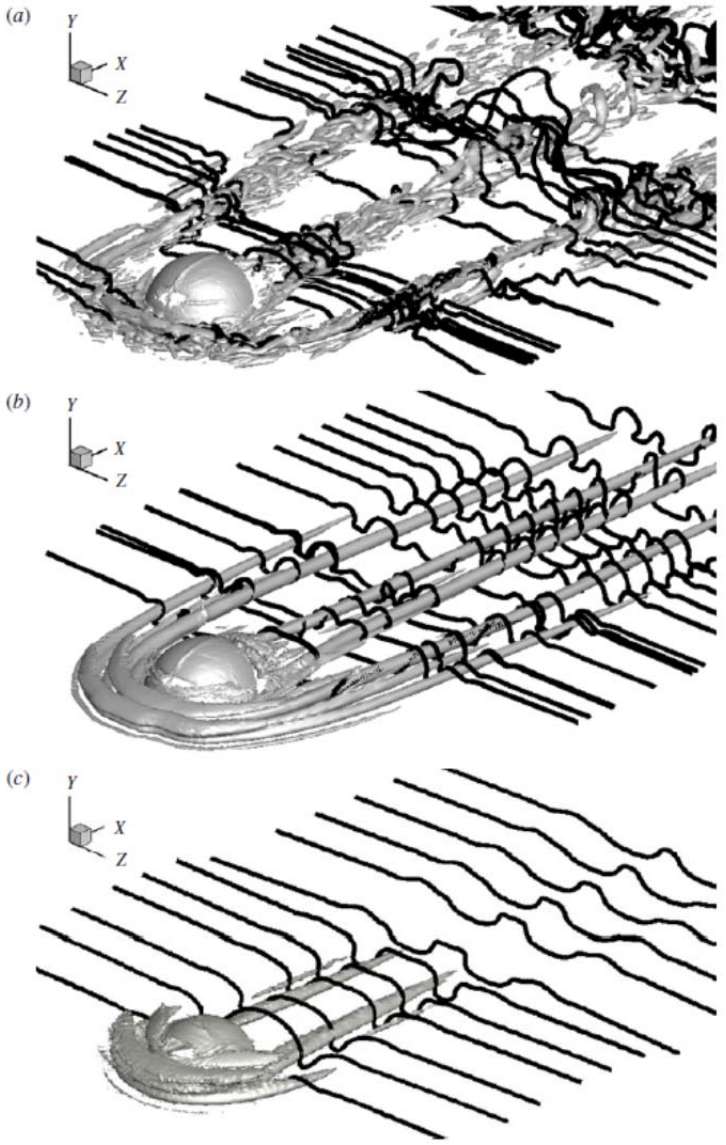

Figure 1.21. Flow past a hemispherical roughness element at Mach number equal to (a) 3.37 (b) 5.26 and (c) 8.23 (from Iyer and Mahesh 2013).

Moreover, they investigated the mean flow features by means of the Stanton number (St) distribution at the wall detecting a good correspondence between the location of the streamwise vortices and the streaks of increased St. Moving

downstream from the protuberance the uniform St distribution along the span was related to the presence of an abundance of hairpin vortices that cause the mixing of the flow. In particular, the data clearly show a strong connection between the flow features upstream of the element and the streamwise developing of the high St streaks downstream.

Similarly, Subbareddy et al (2014) performed DNS computations of the flow around a cylindrical roughness element) studied the influence of the free stream unit Reynolds number on the transitional flow pattern showing the presence of coherent hairpin-like structures only at the higher unit Reynolds number investigated (Re_{unit} = $6.56 \cdot 10^6$ m^{-1}).

These above-mentioned papers are the latest in a series of studies in which several roughness geometries have been analysed in order to investigate different transition scenarios (see for example Choudhari et al 2010, Chang and Choudari 2011).

Chapter 2

The Hypersonic Test Facility Delft (HTFD)

2.1 Historical Background: the Ludwieg Tube

The Hypersonic Test Facility Delft (HTFD, Schrijer and Bannink 2010) operates on the basis of the Ludwieg tube concept (Ludwieg 1955). Originally, Ludwieg tubes were built as low cost wind tunnels for transonic/supersonic Mach numbers. Lately, they were used as hypersonic wind tunnels (Hottner 1968) because of the long running time (0.1 to 0.2 s) and the high Reynolds number achievable (order of 5 - $50 \cdot 10^6$ m^{-1}) thank to the low free stream total temperature. Moreover, to prevent condensation the flow is heated off-line in order to reduce the energy demands and running costs.

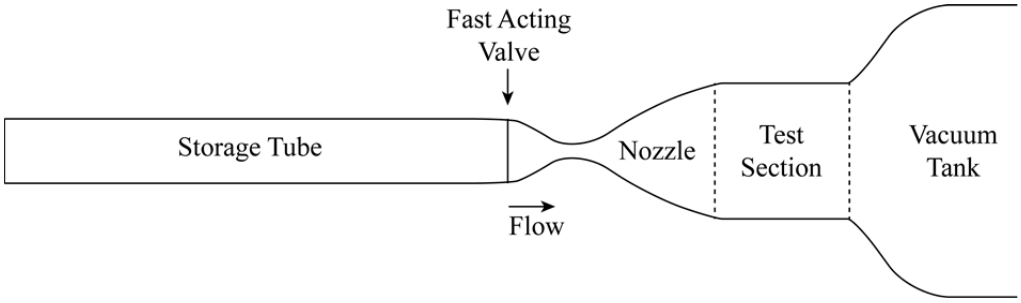

Figure 2.1. Sketch of the HTFD.

The HTFD is conceived to be a low cost flexible hypersonic wind tunnel capable of producing relatively high Reynolds numbers and a range of Mach numbers. The basic wind tunnel design was made by Hyperschall Technologie Göttingen (HTG, Friehmelt 1993) in Germany. It consists of four principal elements (see figure 2.1):

- Storage tube, where the fluid is pressurized at temperature controlled conditions.
- Conical nozzle, which is separated from the storage tube by a fast acting valve. The convergent-divergent nozzle accelerates the gas from quiescent to hypersonic conditions depending on the area ratio between the throat and test section.
- Test section, where the flow reaches the desired conditions and the wind tunnel model is located.
- Vacuum discharge tank that maintains a large pressure ratio across the nozzle in order to start and sustain the flow conditions.

When the valve opens, air flows from the storage tube through the nozzle into the test section. The expansion ratio of nozzle to test section determines the Mach number in the test section.

2.2 HTFD Ludwieg Tube Facility

The basic principles of the Ludwieg tube are reported hereafter. The theoretical estimation of the flow conditions and of the wind tunnel running time are reported together with the measurements performed to assess the performance of the facility (Schrijer 2010a, Schrijer and Bannink 2010).

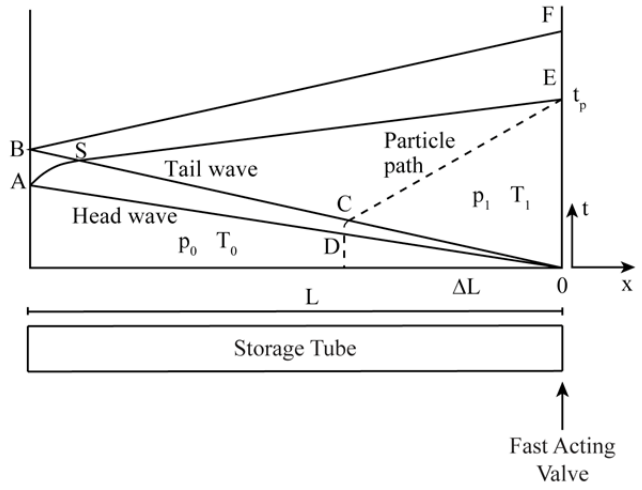

Figure 2.2. Operational principle of the HTFD.

2.2.1 Operating Principle and Facility Description

The air stored in the storage tube flows through the nozzle when the fast-opening valve is opened (figure 2.1). The valve opening is relatively quick (Wolf et al 2007)

and the process may be regarded as impulsive. Therefore, an expansion wave travels upstream into the storage tube (see with a sketch of the wave pattern in the x-t diagram in figure 2.2). The flow conditions behind the expansion wave act as reference stagnation conditions for the flow in the test section. The first and last characteristic of the expansion wave is given by OA and OSB, respectively. When the characteristics reach the end of the tube they are reflected back towards the nozzle (AE and BF) and the run ends. The running time t_p can be also seen as the time that an air particle takes to go from condition 0 to E (figure 2.2). It can be evaluated following Schrjier (2010a) as

$$t_p = \frac{L}{a_0}\frac{2}{M_1 + 1}\left(1 + \frac{\gamma - 1}{2}M_1\right)^{\frac{\gamma+1}{2(\gamma-1)}} \tag{2.1}$$

where M_1 is the Mach number in the storage tube downstream of the expansion wave, a_0 is the speed of sound based on the storage tube conditions, γ is the specific heats ratio and L is the storage tube length. M_1 depends on the tube diameter to the critical throat diameter (d^*) ratio

$$\left(\frac{d_{tube}}{d^*}\right)^2 = \frac{1}{M_1}\left[\frac{2}{\gamma + 1}\left(1 + \frac{\gamma - 1}{2}M_1^2\right)\right]^{\frac{\gamma+1}{2(\gamma-1)}} \tag{2.2}$$

Since in the HTFD the test section diameter is fixed, the free stream Mach number is set by selecting the appropriate nozzle diameter. For free stream Mach number below 9, a second nozzle is then selected for the appropriate lower free stream Mach number. However, it is the first nozzle that determines the stagnation conditions of the free stream flow. Through the expansion wave the total temperature drops according to

$$\frac{T_{t,1}}{T_0} = \frac{1 + \frac{\gamma - 1}{2}M_1^2}{\left(1 + \frac{\gamma - 1}{2}M_1\right)^2} \tag{2.3}$$

However the total temperature losses are more relevant than the one evaluated by using equation 2.3 because of the high heat transfer rate at the fast-opening valve.

As said previously, the HTFD is designed as cost optimized facility. To that end, only the section of the storage tube that contains the air used during the runs is heated. This length is computed by estimating the most upstream location of the particles that enter the test section during the run (path DCE in figure 2.2)

$$\Delta L = M_1 \frac{a_1 - u_1}{a_0} 2L \tag{2.4}$$

here, u_1 is the flow velocity in the storage tube given by

$$\frac{u_1}{a_0} = \frac{M_1}{1 + \frac{\gamma - 1}{2} M_1} \tag{2.5}$$

For the particular case of the HTFD, where the total length of the storage tube is 29 m, ΔL is estimated to be approximately 5.2 m. Therefore only the section corresponding to the first 6 m is heated.

The HTFD is also optimized in order to reduce the total length of the facility. To this purpose, the storage tube is divided into three sections: the hot tube and a cold tube split into two parts (figure 2.3). The hot tube is connected to the first cold tube by means of a bended tube. This solution allows locating the cold tube beneath the hot tube and the test section. The second cold tube is located next to and connected to the first tube by a 180° bend. Since the cold tube is located below the hot tube the problem of the natural convection is minimized.

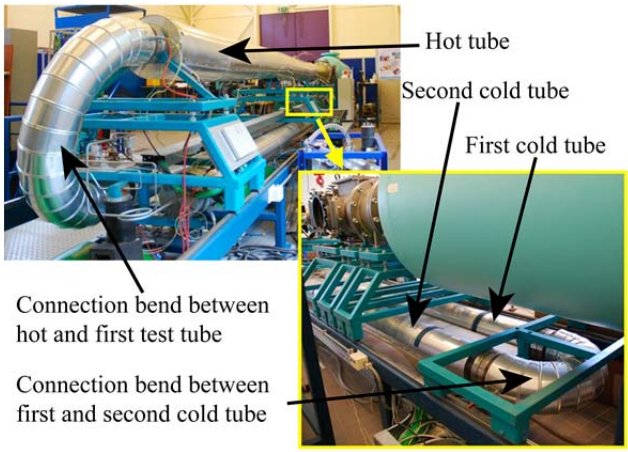

Figure 2.3. HTFD storage tube.

The discontinuity between the hot and cold sections of the storage tube may cause a reflection of the shock wave. In order to mitigate this effect it is necessary to set an appropriate temperature to the cold section for given tubes cross sections according to

$$\frac{d_{hot}}{d_{cold}} = \left(\frac{T_{cold}}{T_{hot}}\right)^{\frac{1}{4}} \tag{2.6}$$

Since the storage tube is heated at 773 K, the cold tube temperature is set at 375 K. Moreover, the high temperature in the hot section affects the specific heats ratio that is not constant because the vibrational degree of freedom cannot be neglected. For the given total temperature γ is estimated to be approximately 1.36, which is a relatively small deviation from the constant value of 1.4. Such a small difference is considered to be negligible. However, Schrijer and Bannink (2010) estimated the error in the free stream static properties by assuming γ equal to 1.4 for M_1=7 as reported in table 2.1.

Table 2.1. Percentage error in the free stream static quantities when assuming γ=1.4.

M_1	ϵ_M	ϵ_u	ϵ_T	ϵ_p	ϵ_ρ
7	-0.5	1.1	3.1	1.1	-2.0

Finally, the unsteady behaviour at the start of the wind tunnel needs to be quantified. In figure 2.4 the pressure variation with time in the storage tube is given. After approximately 25 ms a small oscillation is visible. It is caused by a small reflection coming from the temperature/cross section discontinuity. At this stage the pressure in the settling chamber is constant and the flow may be considered steady.

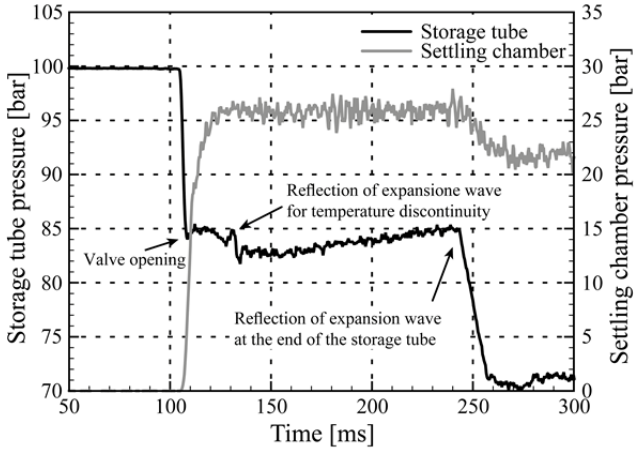

Figure 2.4. Pressure variation in time in the hot part of the storage tube and in the settling chamber (from Schrijer and Bannink 2010).

2.2.2 Nozzle Geometry and Flow Features

The HTFD is a flexible wind tunnel that be operated at different Mach numbers by changing the throat diameter.

For Mach numbers higher than 9 the throat section is directly connected to the nozzle. In order to realize Mach number lower than 9 an extra throttle nozzle is needed in order to avoid sonic condition in the smallest section of the valve. The first part of

the tandem nozzle system (figure 2.5) is a Mach 9 nozzle, which accelerates the flow to supersonic speeds after which, theoretically, it decelerates to subsonic speeds through a normal shock wave. The second throat reaccelerates the flow to the desired Mach number. The presence of the shock wave implies a loss of total pressure

$$\frac{p_0}{p_{t,1}} = \left(\frac{d_1^*}{d_2^*}\right)^2 \qquad (2.7)$$

Here p_0 is the free stream total pressure. However, pressure measurements performed by Schrijer and Bannink (2010) showed that the pressure loss is lower than expected. It was associated to the presence of a shock train in the tandem nozzle. From the equation it is evident that the loss in total pressure allows a larger critical cross section.

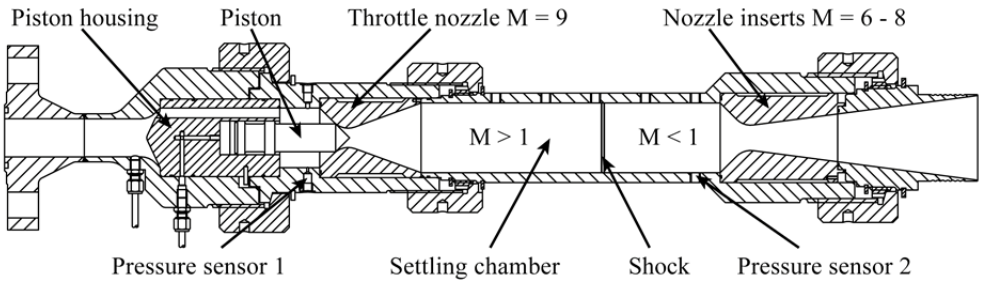

Figure 2.5. HTFD tandem nozzle section (from Schrijer and Bannink 2010).

Downstream of the throat the flow expands in a conical nozzle that, in the case of free stream flow at Mach equal to 7 is 1.18 m long. The free stream Mach number in the test section is realized by selecting the desired throat-to-test section area ratio. However, the boundary layer may influence the estimated Mach number by changing the ratio. To that end, Schrijer and Bannink (2010) measured the boundary layer at the end of the nozzle by means of planar PIV. They measured the boundary layer thickness (δ) that results to be equal to 13 mm. It implies that, for the Mach 7 nozzle, the actual free stream Mach number is equal to 6.7.

2.2.3 Free Stream Flow Characterization

When the flow enters the test section (the test section diameter is 350 mm) it continues diverging due to the outflow from the conical nozzle. Therefore, the flow will expand further and the Mach number in the test section will be higher than the obtained from the theoretical area ratio. For the Mach 7 nozzle it results in an asymptotic Mach number equal to 7.5. Moreover, the Mach number varies in the test

section along the streamwise direction due to the diverging flow field. For the Mach 7 nozzle the rate of change is $\mathrm{dM/dx} = 0.023\ \mathrm{cm}^{-1}$.

Since the test section has a cylindrical shape, a shock wave is formed at the nozzle-test section junction. For the Mach 7 nozzle it results in a theoretical shock angle of 14° with respect to the free stream direction. However, the presence of the cavity at the bottom (necessary for optical access) and a large cavity on the bottom (used to accommodate the model support) yields to a shock angle of approximately 9° and 10° at the top and the bottom, respectively. Then, the region of undisturbed flow results to be equal to $200 \times 200\ \mathrm{mm}^2$. In this region the flow divergence yields to the variation of the vertical component of the velocity of approximately 60 m/s over a distance of 200 mm in the direction normal to the free stream.

The mean velocity at the centreline is approximately 1033 m/s (figure 2.6). The data deviation from uniform flow is 0.2% (rms fluctuation within a single velocity field) while the repeatability is 0.4% (rms fluctuations with different realizations).

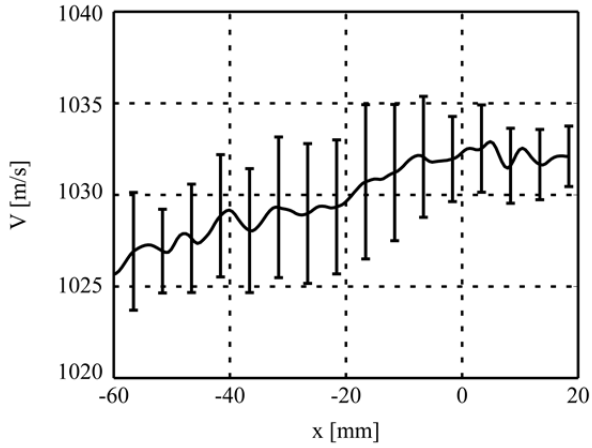

Figure 2.6. Horizontal free stream velocity profile along the test section centreline for the Mach 7 nozzle (from Schrijer and Bannink 2010).

Table 2.2. Free stream conditions for the Mach 7 nozzle configurations.

Free stream condition	Quantity
Velocity	1033 m/s
Mach number	7.5
Total Temperature	47 K
Static Temperature	579 K
Total Enthalpy	0.56 MJ/kg

The free stream conditions for the Mach 7 nozzle are summarized in table 2.2.

2.3 Experimental Configurations

Experiments are carried out at Mach number equal to 7.5 and different Reynolds numbers. The Reynolds number is varied by changing the pressure in the storage tube such that the total pressure in the settling chamber is varied between 1.7 and 2.8 MPa to select the appropriate Reynolds number. In the experiments three test conditions defined as low, medium and high Reynolds number are defined corresponding to a free stream total pressure of 1.7, 2.2 and 2.8 MPa, which yields a unit Reynolds number respectively equal to $8{\cdot}10^6$ m^{-1}, $11{\cdot}10^6$ m^{-1} and $14{\cdot}10^6$ m^{-1}. The total temperature is 579 K and the running time t_p is slightly lower than 0.1 s. The free stream flow properties are summarized in table 2.3.

Table 2.3. Free stream flow properties.

Parameter	Quantity		
M_∞	7.5		
$U_0(m/s)$	1030		
$T_0(K)$	579		
$P_0(bar)$	17	22	28
$Re_{unit}(m^{-1})$	$8 \cdot 10^6$	$11 \cdot 10^6$	$14 \cdot 10^6$

Chapter 3

InfraRed (IR) Themography

3.1 IR Thermography and the Hypersonic Regime: a dated story

The origin of infrared thermography dates back February 11th 1800 when the English physicist William Hershel (1800) discovered the thermal radiation. At the time he was trying to devise a way of cutting down the glare of looking at the sun through a telescope. He noticed that when using different coloured filters, some would let through more heat than others. This led him to devise an experiment to measure the heat given out by different colours of light. He passed sunlight through a prism to create a spectrum, and measured the heat given off at various points of the spectrum using thermometers. He discovered that there was even more heat beyond the red end of the spectrum. This was the first time that someone had shown that there was light, which was not visible to the human eye.

In the succeeding years, many physicists, among them Melloni, Kirchoff, Maxwell, Stefan, Boltzman and Planck, addressed the problem of fully understanding the properties and energy distribution of the wide spectrum of radiation.

The first infrared cameras were developed in the 1960s as offshoots of military program but without significant accuracy features. Later in the 1970s, two Swedish companies, AGA and Bosfor, with the support of the government built the first infrared scanner where the two-dimensionality of the image was achieved by rotating, or oscillating, mirrors and/or refractive elements. In the 1980s, with the development of the Focal Plane Array (FPA) the infrared cameras became effective two-dimensional transducers. The wide diffusion started in the 1990s when IR cameras based on non-cooled FPA detectors emerged (such as microbolometers).

IR thermography was used to measure, for the first time, the convective heat transfer coefficient in the hypersonic regime. Measurements were performed by using scanners operating in the middle IR band (3÷6 μm) of the infrared spectrum, at that time called the short wave IR band and now named the intermediate wavelength infrared band (see section 3.1). In particular, the AGA Thermovision 680SWB camera was employed by Thomann and Frisk (1968) to measure the temperature distribution over the surface of an elastomeric paraboloid in a hypersonic wind tunnel at free stream Mach number equal to 7. The unsteady thin film sensor was used to determine convective heat transfer coefficients, which showed a good agreement with data already obtained with different techniques and was encouraging in view of using infrared systems for heat flux measurements.

In 1976, the Arnold Engineering Development Center (AEDC) was embarked on a large-scale research program to develop IR cameras with capability to perform extensive heat transfer testing in the hypersonic regime (Bynum et al 1976). In particular, the von Karman facility was dedicated to hosting an infrared imaging system for test series that extended over a long period. Meanwhile, the infrastructure and expertise developed at AEDC were used to measure convective heating rates on a Space Shuttle model, under flow conditions prevailing in the re-entry phase, to aid in the design of the thermal protection system (Stalling and Carver 1978). Apart from heat flux evaluation, the characterization of flow field behaviour, with location of boundary layer transition to turbulence, as well as of separation and reattachment zones, constituted a subject of great interest to aerodynamicists. Consequently, huge efforts were devoted to acquiring information on the infrared cameras capability required to deal with these phenomena. In fact, IR thermography allows the evaluation of the boundary layer state both in laboratory tests (Tirtey et al 2011) as well as during flight (Brandon et al 1990).

3.2 Basic Principle of Radiation Heat Transfer

Heat transfer by radiation (or radiative heat transfer) is an energy transport mechanism that occurs by means of electromagnetic waves (Astarita and Carlomagno 2013). Since electromagnetic waves can travel in a vacuum, radiation is the only mechanism able to exchange energy between two unconnected bodies. If a medium is present in between the two exchanging bodies, the transferred energy may be partially or completely absorbed and/or reflected, or may even pass through the medium without being affected (figure 3.1).

By denoting with α_r the radiation fraction being absorbed by the body, with ρ_r the fraction being reflected by it and with τ_r the fraction being transmitted (which passes through), energy conservation requires

$$\alpha_r + \rho_r + \tau_r = 1 \tag{3.1}$$

where α_r, ρ_r and τ_r are, respectively called absorptivity, reflectivity and transmissivity coefficients of the medium under consideration. If τ_r=1, the medium is called fully transparent and this practically enables an IR scanner to view the temperature of a body without being affected by the medium. A medium can also be partially transparent, i.e. if it allows only a fraction of the transmitted energy to pass through.

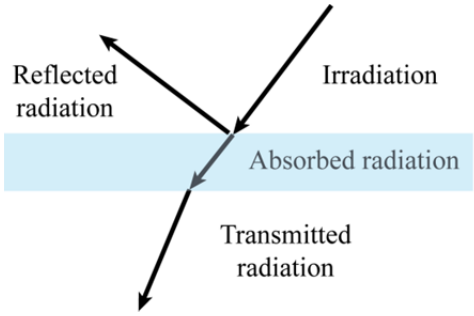

Figure 3.1. Sketch of the energy transmission, reflection and absorption through a real body.

Thermal radiation originates from all objects at a temperature above absolute zero. The wavelength λ of the electromagnetic waves that carry the energy is a function of the frequency of the wave ν and of the speed of light c

$$\lambda = \frac{c}{\nu} \tag{3.2}$$

The speed of light in a generic medium (e.g. air) is related to the speed of light in the vacuum ($c_0 = 2.998 \cdot 10^8$ m s^{-1}) through the refracted index n_θ of the medium that is usually a function of the wavelength

$$c = \frac{c_0}{n_\theta} \tag{3.3}$$

The entire electromagnetic spectrum is quite roughly divided into a number of wavelengths intervals (spectral bands) as shown in figure 3.2 where it can be seen that the thermal radiation band extends in the range $0.1\ \mu m < \lambda < 1000\ \mu m$.

In particular, when a body is at ambient temperature it radiates most of the energy in the infrared (IR) band that has wavelength comprised between 0.75 and 1000 μm. The IR is usually subdivided in four zones

- Near IR (NWIR), with radiation wavelength comprised between 0.75 and 3 μm;
- Intermediate IR or Middle IR (MWIR), with radiation wavelength comprised between 3 and 6 μm;
- Long IR (LWIR), with radiation wavelength comprised between 6 and 15 μm;
- Extreme IR (EWIR), with radiation wavelength comprised between 15 and 1000 μm.

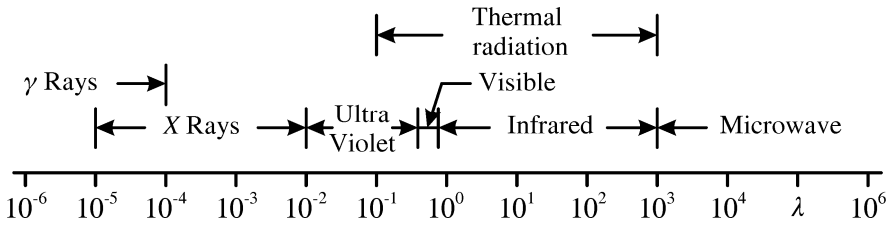

Figure 3.2. Electromagnetic spectrum. Wavelength λ is in micrometres (from Astarita and Carlomagno 2013).

3.2.1 Black Body Radiation

The blackbody is a theoretical concept that sets an upper limit to the emission of radiation in accordance with the second law of thermodynamics. It is a body that emits and absorbs the maximum possible amount of radiation in all the directions at any given temperature and wavelength (perfect radiator).

The spectral black body emissive power (the energy rate per body unit surface area for a given wavelength and black body temperature, $E_{b,\lambda}$) in vacuum is prescribed by the Planck's law of radiation (Carlomagno and Cardone 2010)

$$E_{b,\lambda}(\lambda, T_b) = \frac{C_1}{\lambda^5(e^{C_2/\lambda T_b} - 1)} \qquad (3.4)$$

where T_b is the absolute black body temperature, $C_1 = 3.742 \cdot 10^8\ \mathrm{W\,\mu m^4/m^2}$ and $C_2 = 1.439 \cdot 10^4\ \mathrm{K\,\mu m}$ are the first and the second radiation constants respectively. Equation 3.4 is plotted as a function of λ for different T_b in figure 3.3.

Following a curve in figure 3.3 the spectral emissive power is a continuous function of the wavelength that is equal to zero for $\lambda = 0$, it increases to a maximum until a certain wavelength (λ_{max} that depends on T_b) and then it decreases until it approaches to zero for $\lambda \to \infty$. For each wavelength the emitted radiation increases significantly with the T_b. Particularly, upon an increase in T_b, the position of the maximum moves towards smaller wavelength (dashed lined).

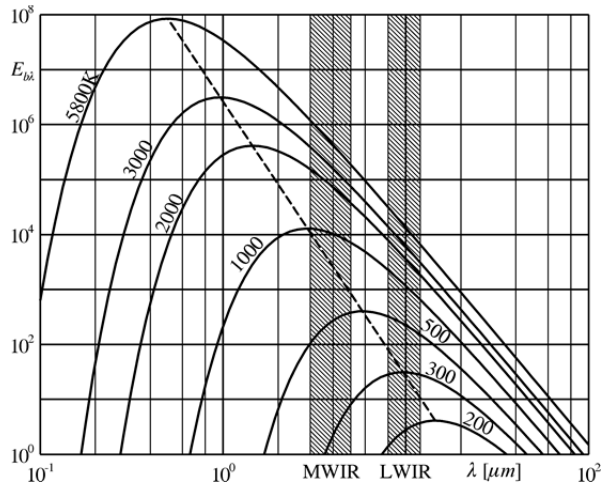

Figure 3.3. Spectral black body emissive power $E_{b,\lambda}$ in vacuum for several T_b as a function of λ (from Astarita and Carlomagno 2013).

Equation 3.4 can be differentiated with respect to λT_b setting to zero the result in order to obtain the wavelength λ_{max} at which the blackbody emits its maximum spectral emissive power for a given T_b. It is the so-called Wien's law

$$\lambda_{max} T_b = 2898 \ \mu m \ K \tag{3.5}$$

Planck's law of radiation can be integrated over the whole spectrum to obtain the Stefan-Boltzmann law that gives the total (energy flux over all wavelengths) black body emissive power E_b

$$E_b = \int_0^\infty E_{b,\lambda}(\lambda, T_b) d\lambda = \sigma_B T_b^4 \tag{3.6}$$

where $\sigma_B = 5.670 \cdot 10^{-8} \ W/(m^2 K)$ is the Stefan-Boltzmann constant. However, while making measurements with IR thermography, since infrared detectors capture only a limited band of the whole electromagnetic spectrum, a defined integral of the Planck's law is more appropriate to find the energy flux sensed by the detector in a certain band $\lambda_1 \leq \lambda \leq \lambda_2$

$$E_{b,\lambda_1 \leq \lambda \leq \lambda_2}(T_b) = \int_{\lambda_1}^{\lambda_2} E_{b,\lambda}(\lambda, T_b) d\lambda \tag{3.7}$$

By looking at the curves of figure 3.3 it can be noticed that, irrespective of the temperature of the black body, the percentage of the emissive power radiated at the wavelengths smaller than λ_{max} is about 25% of the total.

The integral in the equation 3.7 can be easily evaluated by the relationship

$$E_{b,\lambda_1 \le \lambda \le \lambda_2}(T_b) = \sigma_B T_b^4 \left(f_E(\lambda_2, T_b) - f_E(\lambda_1, T_b) \right) \qquad (3.8)$$

where f_E is the fractional emissive power function. The reader can refer to Chang and Reeh (1984) for a closed solution of the function f_E.

It is quite interesting to evaluate this fraction for the two bands most typically used by IR scanners for thermo-fluid-dynamic applications: the band of the MWIR scanners and the band of the LWIR ones. For a black body temperature of 300 K, it is found that the energy radiated in the LWIR band is about 26% of the total; while for the MWIR band this percentage is reduced to 1.3%. In this case, the LWIR band appears to have a clear advantage but, by increasing the temperature to 600 K, the MWIR band behaves a little better (23% for MWIR against 21% for LWIR).

3.2.2 Real Body Radiation

The radiation characteristics of real bodies are normally different from those of a black body. Both emitted and absorbed radiations of a black body are upper limits for real bodies that may possibly be approached only in certain spectral bands and under certain conditions. In case of real body, equation 3.1 must be considered.

A real body generally emits only a fraction E of the heat flux E_b emitted by a black body at the same temperature. Of course, this happens to be true also on a spectral basis, i.e. $E_\lambda \le E_{b,\lambda}$. In the following, for the sake of ease, E is always referred to as the total hemispherical emissive power and E_λ is the spectral hemispherical emissive power.

The spectral hemispherical emissivity coefficient ε_λ is defined

$$\varepsilon_\lambda(\lambda, T) = \frac{E_\lambda(\lambda, T)}{E_{b,\lambda}(\lambda, T)} \qquad (3.9)$$

where the real body and the black body are at the same absolute temperature.

Similarly, the total hemispherical emissivity coefficient $\varepsilon_t(T)$ is defined as

$$\varepsilon_t(T) = \frac{E(T)}{E_b(T)} \qquad (3.10)$$

Generally, the emissivity coefficient is also a function of the angle θ_v between the direction normal to the emitting surface and the direction of the emitted radiation (figure 3.4). When the last dependency does not occur, the body is called a diffuse emitter.

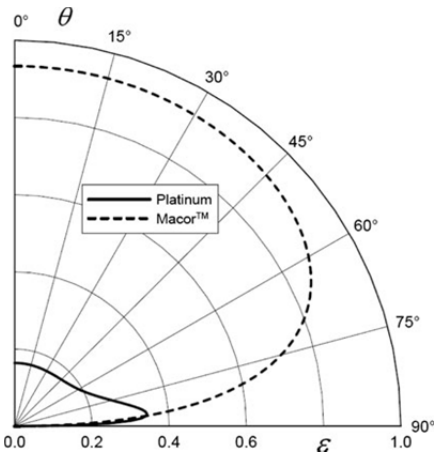

Figure 3.4. Emissivity coefficient ε_t for Macor® (8-12 μm) and platinum (2 μm) as a function of the viewing angle θ (from Carlomagno and Cardone 2010).

Bodies having their emissivity independent of θ_v are called grey bodies. Even if no real surface is truly grey over the whole electromagnetic spectrum, often a real surface can have an almost constant spectral emissivity in the used IR detector band so that, at least from a practical detection point of view, the grey hypothesis can be assumed to be satisfied.

The directional emissivity behaviour of dielectric materials is quite different from metallic ones. As shown in figure 3.4 for Macor®, dielectric materials have a quite constant and relatively high emissivity at angles θ generally less than about 60°, while they emit poorly at large angles away from normal direction. Vice versa, electric conductors (such as platinum) have usually a low emissivity, with a relative minimum in the normal direction.

3.2.3 Atmospheric Transmittance

When performing an actual measurement, the infrared scanner normally views the tested object through a medium (frequently air), which may not be completely transparent, so that part of the emitted radiation is absorbed and not captured by the scanner. In addition, the presence in the rays' path of viewing windows (such as those used in some wind tunnels or in controlled atmosphere chambers) attenuates the radiation emitted by the object and impinging on the camera lens. By focusing the attention on an air layer, the different molecules that are present in it partially absorb the thermal radiation and, as already said, they also emit, perhaps at different wavelengths.

Furthermore, particles (such as those in a gaseous suspension) may also scatter part of the incident radiation but, unless dealing with very dirty streams and/or high

viewing distances, normally this effect is negligible when performing IR measurements. Otherwise, a radiometric calibration is required.

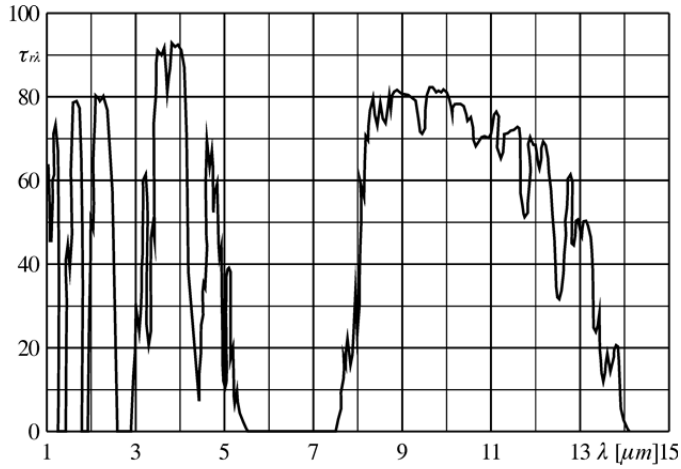

Figure 3.5. Spectral transmittance of a 1 km thick atmospheric layer in the near, middle and long infrared band as a function of λ (from Astarita and Carlomagno 2013 with data from Gebbie et al 1951).

When performing thermographic measurements it is necessary to use the two so-called atmospheric windows, which are respectively located between the visible band and about 5 μm and between 7.5 μm and 13.5 μm spectral bands. They justify the commonly adopted MWIR and LWIR bands, the former being downwards limited by the low emissive power at usual temperatures.

To emphasize the atmospheric absorption effect, in figure 3.5 the spectral transmissivity coefficient ($\tau_{r\lambda}$) of a 1 km thick standard air layer is plotted as a function of the radiation wavelength.

The significant absorptions (especially in the 5÷7.5 μm band) are essentially linked to the presence of water vapour and carbon dioxide. In particular, while in the 8÷12 μm band $\tau_{r\lambda}$ is practically constant, in the 3÷5 μm band there are a few strongly absorbed wavelengths, which if not taken into account, may produce some errors in the measurement of the object temperature.

3.3 Infrared Cameras

A very schematic sketch of the essential components of an infrared scanning radiometer is shown in figure 3.6. Thermal radiation, entering the scanner, is collected by an optical system and sent into a temperature detector that is sensible to the selected IR band. The electrical signal generated by the detector is acquired by a video frame grabber and is processed by a dedicated electronic board in order to obtain a temperature map of the scanned scene.

In the following, first the various components of an IR scanner are described with their different features. Afterwards, the parameters that characterize scanner performances are defined and discussed, including considerations on the choice of the most appropriate infrared working band. Finally, radiometric calibration of the IR scanner is examined with regard to its various facets.

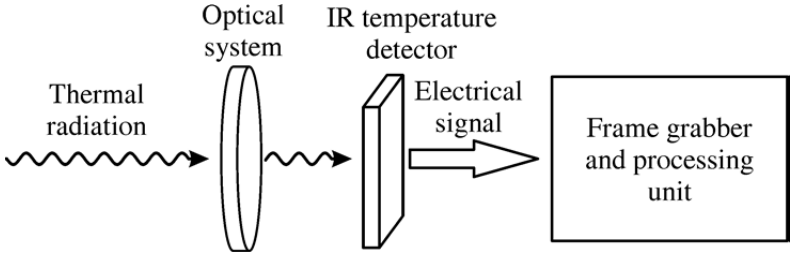

Figure 3.6. Essential component of an IR scanner (from Astarita and Carlomagno 2013).

3.3.1 Optical System

The optical system of an IR scanner is very similar to that of a camera working in the visible band. The main difference consists in the fact that the material that constitutes the optical components has to be transparent in the used infrared band. In the optical system, filters can also be introduced in order to either extend the measurable temperature range towards higher levels, to measure the temperature of a semi-transparent material or, finally, to see through the latter an object lying underneath.

As already mentioned, the lens of an IR scanner is not different from that designed for the visible part of the spectrum and is made of a number of optical elements. The substantial difference is that most of the optical glasses that are transparent in the visible band normally appear opaque in IR bands and, for this reason, particular materials must be used for lens manufacture. As a matter of fact, there are also differences between materials used in the 3÷5 μm or the 8÷12 μm band.

Typical optical materials used for general infrared applications are: for the MWIR band, silicon, sapphire, calcium fluoride, magnesium fluoride; for both the MWIR and LWIR bands, germanium, zinc selenide, zinc sulphide, sodium chloride, potassium bromide (figure 3.7). With the exception of silicon, all the above-reported materials for the MWIR band are transparent also to visible light. The same occurs for the other indicated materials with the exception of germanium. Sodium chloride is hygroscopic in nature and potassium bromide is a water-soluble material, so they have to be protected in their use yet (especially sodium chloride) they have the advantage of being relatively inexpensive.

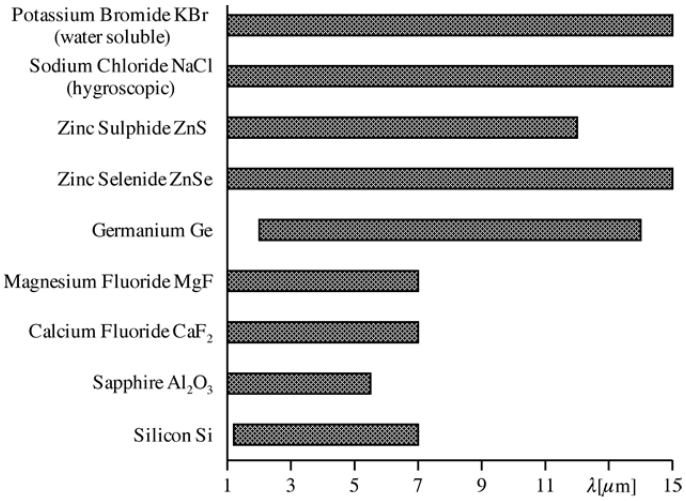

Figure 3.7. Wavelength range of transparency in the infrared for some material (from Astarita and Carlomagno 2013).

IR camera lenses are primarily made of silicon for the MWIR band and of germanium for the LWIR one. In figure 3.7, the transparency wavelength range of the most employed materials, used for the fabrication of infrared windows, is reported. Windows that have to last are often made of silicon or sapphire for the MWIR band and of germanium for the LWIR one. Even if transparent in the MWIR band, germanium is seldom used there, as it is rather expensive.

A very important design parameter of a lens system is the material refractive index. Large values of n_θ enable a larger deviation of the incident radiation and, thus, a smaller number of optical elements are needed to construct a diffraction-limited lens. However, a large refractive index produces a large reflectivity coefficient and, as a consequence, a relatively small overall transmittance.

By considering all the reflections and the overall absorption, one finally finds that the ultimate normal transmittance of the slab is equal to

$$\tau_{rn} = \frac{(1-\rho_{rn})^2 e^{-\varsigma s}}{1-\rho_{rn}^2 e^{-\varsigma s}} \tag{3.11}$$

where s is the slab thickness, ς is the spectral absorption coefficient and ρ_{rn} is the normal spectral reflectance defined as

$$\rho_{rn} = \left(\frac{n_\theta - 1}{n_\theta + 1}\right)^2 \tag{3.12}$$

If the optical material has a relatively small spectral absorption coefficient ς in the considered waveband and the slab is not too thick, by making use of equation 3.12 it is possible to rewrite equation 3.11 as follows

$$\tau_{rn} = \frac{(1-\rho_{rn})^2}{1-\rho_{rn}^2} \tag{3.13}$$

As an example, for germanium (n_θ approximately equal to 4 in the MWIR and LWIR bands), the application of previous equation leads to a normal transmissivity coefficient of about 0.47. Such a small transmittance value is not effective for IR lens making and, for this reason, normally an anti-reflection coating must be used.

The effect of a triple layer anti-reflection coating on a 2 mm thick slab of germanium is shown in figure 3.8 for the MWIR band (Cox et al 1961). From the figure, it is clear that the transmittance increases quite significantly for the coated slab and even slightly better results may be achieved with more recently developed anti-reflection coatings.

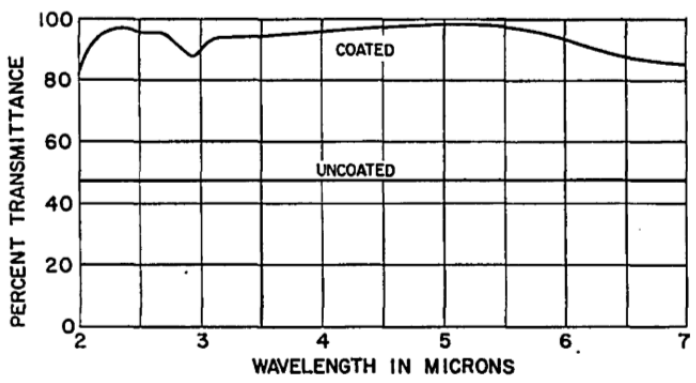

Figure 3.8. Transmittance of a 2 mm thick germanium slab with and without antireflection coating (from Cox et al 1961).

Most of the considerations discussed above apply also to viewing windows that may be necessary for measurements in confined flows, such as those in a wind tunnel with a closed test section or in a testing chamber with a controlled atmosphere.

3.3.2 IR Temperature Detectors

The temperature detector of an infrared scanner is the core device that enables one to convert the impinging radiation, within the measured infrared band, into an electrical signal. Infrared temperature detectors are normally divided into two broad

classes that differ in regard to their physical working principle: thermal detectors and photon (or photonic or quantum) detectors.

The working principle of the former class is that the incident radiation changes one of the electrical properties of the detector due to a temperature modification of the detector itself. In the latter class, the photons of the incident radiation directly interact with the electrons of the detector material.

While for the thermal detectors, the electrical response is proportional to the absorbed energy, for the photon detectors it is proportional to the number of absorbed photons that interact with the electrons.

A modern infrared temperature detector for IR cameras is formed by a two-dimensional array of sensible elements that is normally called as staring or Focal Plane Array (FPA) detector. The main technical hitch is the good uniformity of the performance of its numerous sensible elements (pixels).

3.3.3 Camera Performance

The performance of an infrared scanner is analysed in terms of thermal sensitivity, spatial resolution, acquisition frequency as well as temperature and dynamic ranges.

3.3.3.1 Thermal Sensitivity

Thermal sensitivity is generally expressed in terms of mean noise equivalent temperature difference (NETD), which is correctly defined as the time standard deviation of the random background noise averaged over all pixels of a black body scene (Levesque et al 2005). The NETD is a function of the used black body temperature and, normally, the IR scanner manufacturer provides it at ambient temperature in terms of mK.

Clearly, the thermal sensitivity decreases upon increasing the spatial frequency of the input thermal signal and for this reason it may be expressed also in terms of minimum resolvable temperature difference (MRTD), which is the minimal temperature difference of a 4-bar target detectable by the operator.

A similar index is the minimum detectable temperature difference (MDTD) for which a series of circular targets are used instead of the 4-bar one. In both cases, the low spatial frequencies limit is practically coincident with the NETD. A better measure of the influence of the spatial frequency on the thermal sensitivity is the Modulation Transfer Function (MTF), which is described in the following.

3.3.3.2 Spatial Resolution

The spatial resolution characterizes the capability of an infrared scanner to measure surface temperature of small objects or, better, to resolve temperature differences between points placed at relatively small distances.

A simplistic definition of the spatial resolution is based on the instantaneous field of view (IFOV), which is the ratio of the detector size (or pixel size for FPA) width over the lens focal length and is normally expressed in mrad. However, this is only an ideal design parameter and does not fully describe the performance of the actual IR scanner.

From a more rigorous point of view, the spatial resolution of an IR scanner has to be defined in terms of the scanner Modulation Transfer Function (MTF), which is the magnitude of the normalized complete Optical Transfer Function (OTF).

In order to understand, from a more physical point of view, the definition of spatial resolution in terms of modulation transfer function, let it be supposed that, as shown in figure 3.9, the target temperature (input signal) is a sinusoidal function of given amplitude I. For the sake of simplicity, the temperature variation is assumed to be present only along the x-direction.

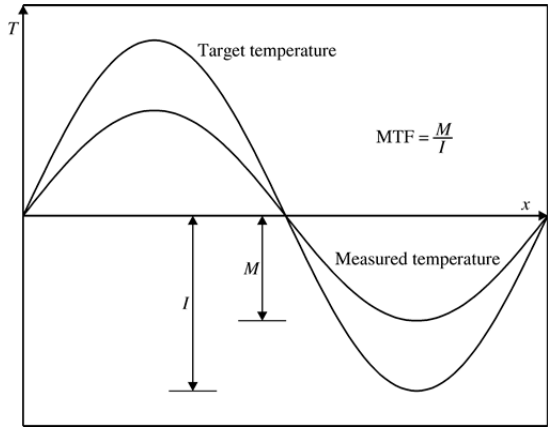

Figure 3.9. Illustration of the modulation effect.

Ideally, irrespective of the spatial frequency of the input signal, the measured amplitude should be equal to the target one but, on account of various physical phenomena including pixel size, the recorded sine wave (recorded signal) exhibits a smaller amplitude M, i.e. a modulation, which is normally a decreasing function of the signal spatial frequency. Actually, the measured sine wave may also have a different phase angle but this is not considered within this context.

For each spatial frequency, the modulation transfer function is defined as the ratio between the recorded and the input sine wave amplitudes M/I. As previously

mentioned, a source of modulation comes from the distortion and diffraction of the optical system but usually also the detector pixel dimension can play a fundamental role.

A discussion of the modulation transfer function of mechanically scanned IR systems is reported by de Luca and Cardone (1991) and of modern infrared FPA systems by Boreman (2001).

3.3.3.3 Acquisition Frequency

The acquisition frequency is an important parameter for the measurement of the convective heat transfer coefficient with unsteady heat flux sensors as well as, more generally, in transient phenomena and is mainly connected with the detector response time. Manufacturers of IR scanners normally report the rate of acquisition of a complete thermal image in terms of the number of full frames acquired per second.

3.3.3.4 Temperature and Dynamics Range

The temperature range, which can usually be measured with an IR scanner spans from −20 up to +1500°C, but it can be further extended to higher values by adequately filtering the incoming radiation. Filtering is generally performed with filters, which are grey in the used infrared band.

The intensity resolution, or dynamic range, is expressed in terms of the number of digital intensity levels the individual pixel signal is composed of. The latest generation of cameras typically provides 14 bits A/D conversion, which allows measurement of small temperature differences even in the presence of a relatively large temperature range in the viewed scene.

In any case, the temperature range is clearly limited at relatively small temperatures because of the extremely small radiative flux that impinges on the detector. Besides, since the radiative flux is a strong non-linear function of temperature, when measuring relatively large temperatures, the detector integration time must be significantly reduced or the incident radiation filtered, therefore decreasing the accuracy of the possible simultaneous measurement of lower temperatures.

3.4 Camera Calibration

The output signal of an IR scanner depends on the radiation energy that impinges on it. Then a calibration function is needed to convert the produced electrical signal into the real viewed object (target) temperature. Most modern cameras are already calibrated so that the system software is able to directly calculate the temperature; the

user does not receive the raw signal as an output but rather an exhaustive 2D map of temperatures.

Nevertheless, often a more accurate calibration, or a recalibration (e.g. in a different temperature range, smaller or larger) of the IR scanner is required. For this reason, in this section the basic information necessary to independently calibrate an infrared camera is given.

As schematically shown in figure 3.10, only a radiation flux fraction collected by the infrared scanner is actually emitted by the target. In fact, a second fraction is associated with the radiation emitted by the external ambient environment that is reflected from the target to the infrared scanner and another contribution originates from the radiation emitted by the atmosphere. Besides, it has to be pointed out that the atmosphere itself attenuates the former two fractions before they reach the IR scanner. The influence of a viewing window, which may be present in the optical path, is considered later as the same logic as applied to the atmosphere can be used and it has already been partially addressed in sub-section 3.2.3.

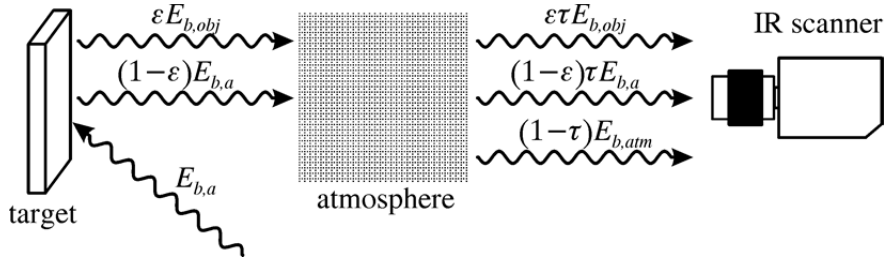

Figure 3.10. Sketch of the radiation detected by the camera.

In the most common situations, the various terms above mentioned are sufficient to describe correctly the physical phenomenon and the camera software often handles them. However, there are many situations where other contributions may arise; e.g., if stray radiation by an intense source impinges on the IR scanner, it could have a significant influence on the collected total radiation flux. In this case, the operator should identify the problem and correct it by either shielding the radiation source or, if possible, by changing the viewing direction. Besides, it is also recommended to realize around the camera an ambient environment as much isothermal as possible at a known temperature.

As previously said, the radiation flux emitted by the opaque viewed object at the temperature T_{obj} is only a fraction ε_t of the radiation emitted by a black body at the same temperature $E_{b,obj}$. By supposing that the transmissivity coefficient of the

atmosphere is τ_r the radiation emitted by the object that is collected by the used infrared scanner can be written as $\varepsilon_t \tau_r E_{b,obj}$.

If the surrounding ambient environment can be considered at a practically constant temperature T_a and its extension is large with respect to the viewed target, it is correct to assume that the surroundings behave as a black body and, thus, the radiation they emit is $E_{b,a}$.

Since the target is assumed to be opaque, its reflectivity coefficient can be pragmatically evaluated as $1 - \varepsilon_t$ and, by also considering the absorption of the atmosphere, one finds out that the radiation emitted by the surrounding ambient environment which is reflected by the target and finally collected by the infrared scanner is equal to $(1 - \varepsilon_t)\tau_r E_{b,a}$.

Similarly, by supposing that the atmosphere is at a constant temperature T_{atm} and that its emissivity has the value $1 - \tau_r$, the radiation flux that reaches the infrared scanner is evaluated to be equal to $(1 - \tau_r)\, E_{b,amb}$.

By summing up the three previously evaluated contributions, the total radiation flux E_t collected by the IR scanner turns out to be

$$E_t = \varepsilon_t \tau_r E_{b,obj} + (1 - \varepsilon_t)\tau_r E_{b,a} + (1 - \tau_r) E_{b,amb} \qquad (3.14)$$

After an internal linearization needed to compensate the possible non-linear behaviour of the temperature detector, the output signal U_t of the IR scanner becomes linearly proportional to E_t

$$U_t = \varepsilon_t \tau_r U_{obj} + (1 - \varepsilon_t)\tau_r U_a + (1 - \tau_r) U_{amb} \qquad (3.15)$$

By assuming that the output signal can be correctly approximated by a function similar to the Planck's law (IR bands are quite narrow), it is found

$$U_t = \varepsilon_t \tau_r \frac{R}{e^{B/T_{obj}} - F} + (1 - \varepsilon_t)\tau_r \frac{R}{e^{B/T_a} - F} + (1 - \tau_r) \frac{R}{e^{B/T_{amb}} - F} \qquad (3.16)$$

where the three calibration constants R, B, and F are functions of the integration time and of the characteristics of the complete infrared scanner system.

The previous equation can be easily solved for T_{obj}

$$T_{obj} = \frac{B}{\ln\left(\frac{\varepsilon_t \tau_r R}{U_t - (1-\varepsilon_t)\tau_r U_a - (1-\tau_r)U_{atm}} + F\right)} \qquad (3.17)$$

When performing measurements at relatively short distances, normally the atmospheric transmissivity coefficient can be practically put equal to 1, therefore, the terms associated with atmospheric absorption and emission may be neglected. For the sake of simplicity, this hypothesis is also assumed in the following.

If a semi-transparent window (or a mirror) is placed in the optical path, other terms, similar to that relative to the atmospheric absorption, should be included in the previous equations and both the optical characteristics of the window (mirror) and its temperature should be known.

For the determination of the calibration constants two approaches are generally followed, the first is to evaluate them before performing the real experiment and the second is based on an in situ calibration (Schulz 2000).

With the former approach, normally a black body is used as a reference object for the calibration so that the emissivity is equal to 1 and also the spurious reflections from the surrounding ambient environment can be neglected. In such a case, the black body should be put relatively close to the camera (so $\tau_r = 1$) and equation 3.17 reduces to

$$T_{obj} = \frac{B}{\ln\left(\frac{R}{U_t} + F\right)} \qquad (3.18)$$

By changing the black body temperature in the range of interest, it is possible to record the output signal from the IR scanner and then the calibration constants can be found by making a non-linear best fit of the n independent measurement points. In particular, by indicating with T_b the black body temperature, measured with a high-accuracy thermometer, the calibration constants are evaluated by varying R, B and F in order to minimize, with a standard optimization algorithm, the functional

$$\sum_{i=1}^{n}\left(T_b^i - T_{obj}^i\right)^2 \qquad (3.19)$$

3.5 Experimental Setup in the HTFD

The IR thermography measurements are performed using a CEDIP Titanium 530L IR system. The camera has a mercury cadmium telluride (MCT) quantum detector array of 320 × 256 pixels and a spectral response of 7.7÷9.3 μm. The sensor is cooled

to 77 K by a Stirling cycle and has an NETD of 25 mK. The integration time of the camera, the frame rate and the spatial resolution varies for each experiment. A 25 mm germanium objective at $f_{\#} = 2.0$ is used.

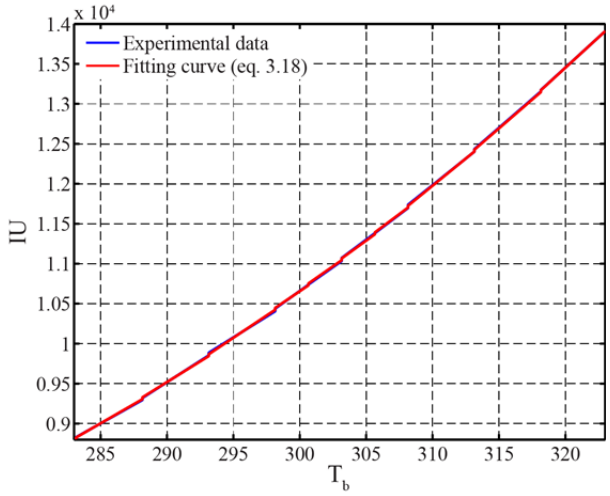

Figure 3.11. Experimental calibration.

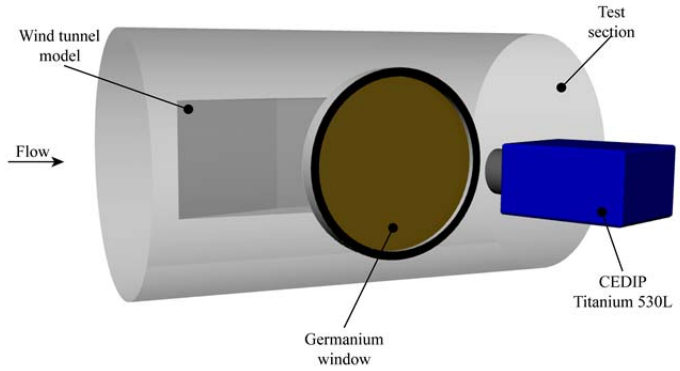

Figure 3.12. Experimental setup.

The optical access in the IR wavelength regime is provided by means of a coated germanium window that has a transmissivity of approximately 0.8 (Schrijer 2010b). The camera is calibrated using a blackbody and the germanium window is included in the calibration process to take into account the reduced transmissivity (the experimental calibration curve is reported in figure 3.11). The camera is oriented at an angle of approximately 15 degrees with respect to the germanium window to prevent

self-reflection. Furthermore, the camera is shielded from the environment using black sheets to prevent additional reflections from the background and window. A sketch of the camera setup is given in figure 3.12.

Chapter 4

Infrared (IR) Thermography Data Reduction

4.1 Introduction

The measurement of the convective surface heat transfer in high-speed flows is essential to understand physical phenomena such as boundary-layer transition, shock wave boundary layer interaction and flow separation (Liu et al 2011). When performing heat flux measurements, typically the temperature difference between the flow and the wind tunnel model is used as the driving potential. Then, from the transient surface temperature signal the convective heat flux is computed (Carlomagno and Cardone 2010). Walker and Scott (1998) categorized the data reduction procedures into three classes:

- Analytical techniques;
- Direct numerical techniques;
- Full inverse techniques.

The first class uses a closed form solution of the heat conduction equation. The approaches proposed by Cook and Felderman (1966) and Kendall and Dixon (1996) are based on the one-dimensional heat conduction equation and belong to this class (see section 4.3). Direct numerical techniques have more flexibility because they permit to include variable thermal properties for the material. Finally, the full inverse techniques (IHTP) provide maximum flexibility in the sense that they allow the solution of multidimensional problems including variable thermal properties. However a disadvantage is the increase in complexity and computational cost. Furthermore, these approaches are ill-posed since the solutions are not unique which means that they are very sensitive to changes in input data resulting from measurement and modelling errors and variation in thermal properties during the measurement time (Beck et al

1985). These effects become even more significant when dealing with high heat fluxes and large heat flux gradients such as those associated with stagnation points, shock interactions, or strong vortical structures.

The wide range of applicability of the full inverse approach has pushed the researchers on developing different techniques to solve these problems starting from the simpler case of the one-dimensional (1D) heat equation using data acquired either on the model surface or at an interior location. For example, de Luca et al (1995) and Ji et al (1997) suggested a method based on the recursive least-squares algorithm for estimating the acting time dependent heat flux. Alternatively, Scarpa and Milano (1995) reconstructed the time-dependent surface heat flux by using the Kalman smoothing technique where the initial temperature distribution and the time-temperature history were measured at an interior location. Raynaud and Bransier (1986) solved a non-linear heat equation taking into account the temperature dependence of the material characteristics using a space marching finite difference algorithm and interior temperature measurements.

In many applications, the estimation of the heat flux by means of the one-dimensional heat equation can limit the measurement accuracy. Most important, in presence of high spatial temperature gradients (i.e. those associated to strong vortical structures, de Luca et al 1992, 1993, 1995, Aymer de La Chevalerie et al 1997, Schrijer 2010b) 1D techniques underestimate the heat flux by neglecting the effects of lateral conduction. As a matter of fact, de Luca et al (1993) showed that the lateral conduction modulates the measured peak to valley temperature distribution. They proposed to use the modulation transfer function (MTF) as tool to predict the amount of modulation of the temperature signal. Recently, Schrijer (2012) showed that the estimated convective heat flux is more modulated than the temperature signal. Therefore, in presence of phenomena characterized by strong temperature gradients, it may be necessary to solve a multi-dimensional full inverse heat transfer problem. Consequently, two-dimensional transducers such as temperature sensitive paints (TSPs, Liu et al 2013) or infrared (IR) thermography (Carlomagno and Cardone 2010) are useful to measure the transient temperature in these situations. IR thermography has been widely applied in many hypersonic applications (see section 3.1): i.e. Cardone (2007) applied IR thermography for heat flux measurements in hypersonic high enthalpy wind tunnels, Gülhan et al (2008) estimated the aerothermal heating caused by jet-hypersonic crossflow interaction, and Di Clemente et al (2013) used IR measurements to validate numerical computations.

When managing IR data it must be considered that they are available in form of two-dimensional (2D) images while real surfaces used in wind tunnel applications are often not planar. According to Cardone et al (2012) it is necessary to establish a

correspondence between the observed model and the pixels of the image in order to remove optical deformations. In wind tunnel tests the position of the model and its shape are known but small oscillations, due to the low stiffness of the sting, could be present. The time history of the temperature map can be rebuilt correctly, in order to reduce the noise, by removing these oscillations that are usually in the order of a few mm. The camera calibration techniques can be classified in three types:

- Linear;
- Non-linear;
- Hybrid.

Linear techniques are fast and quite easy to implement because they neglect lens distortion (Abdel-Aziz and Karara 1971); non-linear techniques provide a rigorous and accurate modelling of the camera interior orientation and lens distortion parameters through an iterative least-squares estimation process (Brown 1971); hybrid techniques fuse linear and non-linear techniques using a linear method to recover initial approximations for the parameters and the orientation; approximations are subsequently iteratively refined (Tsai 1987, Heikkilä and Silven 1997). Examples of temperature distribution rebuilt on the three-dimensional object surface have been proposed by Le Sant (2005) and more recently by Cardone et al (2012) using the calibration method proposed by Heikkilä and Silven (1997), which takes into account lens deformations.

The solution of a multidimensional inverse heat transfer problem requires high complexity and computational cost. Ozisik and Orlande (2000) discussed several methods to solve the inverse heat conduction problem. The most well known is the conjugate gradient approach which has the advantage to solve both linear and non-linear problems in a relatively short time period. Park et al (1999) and Modenini and Schrijer (2012) applied the conjugate gradient method coupled with the adjoint equation approach. Aiming at reducing the computational cost Park et al (1999) solved the inverse problem on a reduced model. They solved a non-linear inverse problem on a square region by means of the Karhunen-Loève Galerkin procedure to estimate the time-varying strength of the heat source. The concept behind the Karhunen-Loève Galerkin procedure is that it lumps the governing transient heat conduction equation into a system of low order non-linear ordinary differential equations by the detection of empirical eigenfunctions. A different approach to solve the inverse problem is to use a recursive least-squares method. Shenefelt et al (2002) suggested a method optimal in the least-squares sense using the Duhamel's principle. The methodology requires unit pulse temperature response data. They built the system response to the unit heat pulse and they reduced the computational cost by using the singular value decomposition. They applied the technique to a one-dimensional linear problem with a time-varying

spatially constant heat source. The method is particularly suitable when the experimental data contains a large amount of noise. Yang (1998) suggested a method based on the least-squares error to solve only a linear inverse problem. The advantage of this approach is that the computation in the process only has to be done once. A disadvantage is that for non-linear problems, the analysis can be used only to compute the associated linearized equations. The computational cost of the methodology increases considerably for a large amount of measurement data.

When performing surface heat flux measurements in short duration high-speed wind tunnels one can assume that the convective heat transfer coefficient remains constant and time-independent. This assumption can be made because the surface temperature increase is relatively small with respect to the adiabatic wall temperature and thus the boundary layer characteristics do not vary. However, in some situations large temperature spatial gradients may still be present. Then, a technique that deals with the effects of the tangential conduction (it solves a multidimensional IHTP) is required. Furthermore, it should be insensitive to measurement noise (robust) and relatively fast (in order to limit the turn-around time of the experiments).

This chapter reports a full data reduction technique. The suggested approach starts with the image resection that corrects the optical deformations and reduces the measurements noise due to the model oscillations (section 4.4). Then, the heat flux rate is evaluated on the rebuilt IR images by solving an IHTP based on the least-squares method that uses the Trust Region Reflective as optimization algorithm. The inverse problem is solved for both the 1D case (section 4.5.1) and the 2D one (section 4.5.2). In the latter, the computational cost is reduced by means of the Discrete Fourier Transform. Both the 1D and the 2D solution are compared to the well-established analytical solutions (summarized for the sake of completeness in section 4.3) and experimentally validated on ad hoc test cases.

4.2 The Semi-infinite Slab Model

The heat equation with the appropriate boundary conditions is reported in equation 4.1.

$$
\begin{aligned}
k\,\nabla^2(T) &= \rho c_p \frac{\partial T}{\partial t} \\
T(x,y,z,t=0) &= T_{wi} \\
K\left.\frac{\partial T(x,y,z,t)}{\partial n}\right|_S &= q_w(x,y,t) \ \text{ and } \ T(x,y,z\in F,t) = T_{wi}
\end{aligned}
\tag{4.1}
$$

Here, k is the thermal conductivity, ρ is the density, c_p is the specific heat and T_{wi} is the initial temperature. A sketch of the problem definition is displayed in figure 4.1, where the wall S is the surface exposed to the flow and z is oriented in the wall normal direction.

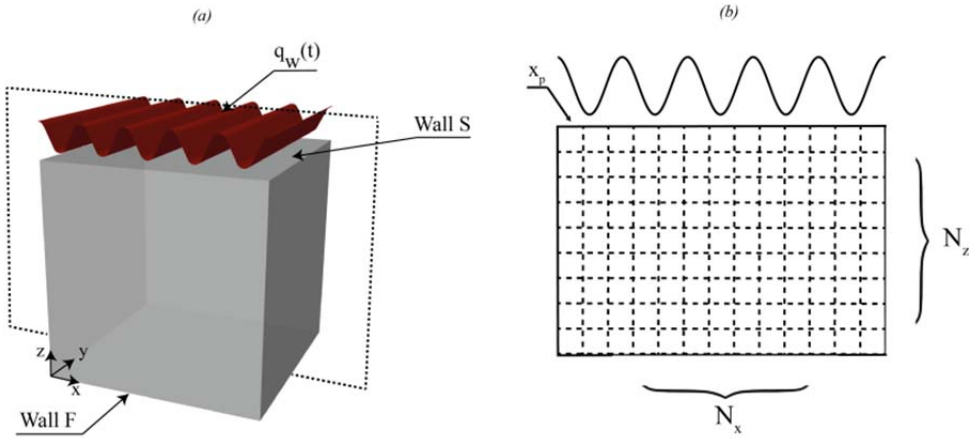

Figure 4.1. (a) Sketch of the model. Dashed line represents the investigated slice in the x − z plane that is discretized as displayed in (b).

The initial temperature distribution T_{wi} is known and it is assumed to be constant in the entire domain. The wall F is considered to be isothermal so that $T(x, y, z \in F, t) = T_{wi}$. This assumption is valid if the thickness of the material is larger than the penetration depth (Schultz and Jones 1973).

The unknown heat flux $q_w\big((x, y) \in S, t\big)$ on the surface exposed to the flow (S) in a generic point of coordinates (x, y) is defined in equation 4.2.

$$q_w\big((x, y) \in S, t\big) = h\big((x, y) \in S\big)\big(T_w\big((x, y) \in S, t\big) - T_{aw}\big) + \sigma_B \varepsilon_t (T_w^4\big((x, y) \in S, t\big) - T_r^4) \quad (4.2)$$

$q_w\big((x, y) \in S, t\big)$ depends on the convective heat transfer coefficient $h\big((x, y) \in S\big)$ which is unknown and needs to be estimated. In equation 4.2, $T_{w_{NUM}}$ is the transient wall temperature that, in the following, is obtained from the transient heat conduction equation (equation 4.1); T_{aw} is the adiabatic wall temperature that is calculated from the classical laminar or turbulent boundary layer theory (Marini 2001, Haberle and Gülhan 2007); ε_t is the total surface emissivity of the model that is assumed known either from the literature or from an experimental calibration; finally, σ_B is the Stefan–

Boltzmann constant and T_r is the enclosure temperature towards which the model radiates. In practice, in cold wind tunnel applications T_r is coincident with the ambient temperature (Gülhan et al 2008). If the temperature rise is particularly strong, some of the assumptions may be not valid: constant thermophysical properties, constant surface emissivity and time constant convective heat flux coefficient. Moreover, T_r may become object of the optimization procedure (Cardone 2007).

4.3 Analytical Solutions

In general the solution of equation 4.1 gives in a generic point $(x, y) \in S$ the temperature as a function of the location z, the time t and of the surface heat flux $q_w\big((x, y) \in S, t\big)$. However, in the current investigation the transient temperature on the wall S is measured while the heat flux rate must be evaluated. The general solution (Schultz and Jones 1973) of this inverse problem is

$$q_w\big((x, y) \in S, t\big) = \sqrt{\frac{k\rho c_p}{\pi}} \int_0^{t_p} \frac{\frac{dT_w\big((x, y) \in S\big)}{d\tau_0}}{\sqrt{t - \tau_0}} d\tau_0 \qquad (4.3)$$

Equation 4.3 reports the wall heat transfer rate as a function of the transient surface temperature. However, this form is inconvenient when managing data from real experiments since it involves the differential of the surface temperature, which may make the evaluation of the heat flux inaccurate due to the presence of noise in the measured temperature signal. According to Cook and Felderman (1966) the differential can be removed by integrating equation 4.3 by parts with the boundary condition $T_w(\tau_0) = 0$ for $(\tau_0) = 0$

$$\begin{aligned} & q_w\big((x, y) \in S, t\big) \\ & = \sqrt{\frac{k\rho c_p}{\pi}} \left[\frac{T_w\big((x, y) \in S, t\big) - T_w\big((x, y) \in S, 0\big)}{\sqrt{t}}\right] \\ & + \frac{1}{2} \int_0^{t_p} \frac{T_w\big((x, y) \in S, t\big) - T_w\big((x, y) \in S, \tau_0\big)}{(t - \tau_0)^{3/2}} d\tau_0 \end{aligned} \qquad (4.4)$$

Equation 4.4 can be rewritten in terms of the variation in the surface temperature relative to the initial temperature $\phi(t) = T_w\big((x, y) \in S, t\big) - T_w\big((x, y) \in S, 0\big)$ as follows

$$q_w\big((x,y)\in S,t\big) = \sqrt{\frac{k\rho c_p}{\pi}}\left[\frac{\phi(t)}{\sqrt{t}}\right] + \frac{1}{2}\int_0^{t_p}\frac{\phi(t)-\phi(\tau_0)}{(t-\tau_0)^{3/2}}\,d\tau_0 \qquad (4.5)$$

The numerical integration of the right side of equation 4.5 enables to determine the time varying heat flux rate. The singularity at $t=\tau_0$ introduces an error that is larger for small values of t while maintaining constant step for the integration. To that end, appropriate numerical procedures are needed (e.g. trapezii rule for integral evaluation). Cook and Felderman (1966) performed the direct numerical integration of equation 4.5 by approximating $\phi(\tau_0)$ through a piecewise linear function of the form

$$\phi(\tau_0) = \phi(t_{i-1}) + \frac{\phi(t_i)-\phi(t_{i-1})}{\Delta t}(\tau_0 - t_{i-1}) \qquad (4.6)$$

where $t_{i-1}\le\tau_0\le t_i$ ad $i=1,2,\dots,n$. Equation 4.6 can be inserted in equation 4.5 and following the algebra reported by Schultz and Jones (1973) it gives

$$\begin{aligned} q_w\big((x,y)\in S,t_n\big) = \sqrt{\frac{k\rho c_p}{\pi}}\Bigg[&\frac{\phi(t)}{\sqrt{t}} \\ &+\sum_{i=1}^{n-1}\left\{\frac{\phi(t_n)-\phi(t_i)}{\sqrt{t_n-t_i}} - \frac{\phi(t_n)-\phi(t_{i-1})}{\sqrt{t_n-t_{i-1}}}\right. \\ &\left.+2\frac{\phi(t_i)-\phi(t_{i-1})}{\sqrt{t_n-t_i}+\sqrt{t_n-t_{i-1}}}\right\} \\ &+\frac{\phi(t_n)-\phi(t_{n-1})}{\sqrt{\Delta t}}\Bigg] \end{aligned} \qquad (4.7)$$

This equation can be directly applied to a measured temperature signal to calculate the heat transfer rate. The only approximation involved is the local linearization of $\phi(t)$. An alternative approach to minimize the need for smoothing of the transient temperature signal was presented by Kendall and Dixon (1996). They solved the one-dimensional heat conduction equation with the same assumptions, initial and boundary conditions as in equation 4.1 but they considered the cumulative heat input to the model surface at time t instead of the instantaneous heating rate. It results in

$$Q_w\big((x,y)\in S,t\big)=\int_0^t q_w\big((x,y)\in S,\tau_0\big)d\tau_0 = \int_0^t \frac{T_w\big((x,y)\in S,\tau_0\big)}{\sqrt{t-\tau_0}}d\tau_0 \tag{4.8}$$

The numerical integration of equation 4.8 gives

$$Q_w\big((x,y)\in S,t_n\big) = \sqrt{\frac{k\rho c_p}{\pi}}\sum_{i=1}^{n}\frac{\phi(t_i)+\phi(t_{i-1})}{\sqrt{t_n-t_i}+\sqrt{t_n-t_{i-1}}}\Delta t \tag{4.9}$$

From equation 4.9 the wall heat transfer rate can be computed by means of the finite difference

$$q_w\big((x,y)\in S,t_n\big)=\frac{dQ_w\big((x,y)\in S,t_n\big)}{dt_n} = \frac{-2Q(t_{n-8})-Q(t_{n-4})+Q(t_{n+4})+2Q(t_{n+8})}{40(t_n-t_{n-1})} \tag{4.10}$$

4.4 Heat Flux Normalization

In the boundary layer theory the normalization of the surface heat flux is commonly performed by means of the Stanton number (St)

$$St=\frac{q_w}{\rho_\infty U_0(h_{aw}-h_w)} \tag{4.11}$$

where ρ_∞ and U_0 are the free stream density and velocity respectively, while h_{aw} and h_w are the adiabatic wall enthalpy and the wall enthalpy, respectively. Physically the Stanton number relates the convective surface heat transfer to the convected enthalpy in the free stream. With the assumption of perfect gas where $h_w = c_p T_w$ equation 4.11 can be rewritten as

$$St=\frac{q_w}{c_p\rho_\infty U_0(T_{aw}-T_w)} \tag{4.12}$$

In a short duration facility, the adiabatic wall temperature cannot be measured accurately therefore the total temperature (T_0) is often chosen as reference and a modified Stanton number (C_h) is defined

$$C_h = \frac{q_w}{c_p \rho_\infty U_0 (T_0 - T_w)} \tag{4.13}$$

As a matter of fact, following the classical definition for the adiabatic wall temperature (Simeonides 1992)

$$T_{aw} = T_\infty + r\frac{U_0^2}{2c_p} = T_\infty \left(1 + r\frac{\gamma - 1}{2} M_\infty^2\right) \tag{4.14}$$

where r is the recovery factor, T_∞ and M_∞ are the free stream static temperature and Mach number, respectively. For high Mach number equation 4.14 may be approximated by

$$T_{aw} \cong r\frac{U_0^2}{2c_p} \cong rT_0 \tag{4.15}$$

Due to the uncertainty in the recovery factor for flow condition the modified Stanton number is often used. In the following, the classical definition of the Stanton number is adopted when data are reduced by means of the 1D inverse solution because it estimates the T_{aw}. On the contrary, the 2D inverse approach does not give the T_{aw} as output and the modified Stanton number is used as non-dimensional parameter.

4.4 Image Resection

IR data obtained by an infrared camera are available in form of 2D images while the observed surfaces are often not planar. Even when model surfaces are planar (e.g. a compression ramp) optical deformations due to the angle of view must be taken into account.

To map the data from the image plane to the real world coordinate system the approach proposed by Cardone et al (2012) is adopted. The method uses a camera model that is based on a perspective projection model with a correction for lens distortion (Heikkilä 2000). The sketch of the projection perspective model is reported in figure 4.2 from Cardone et al (2012). To perform the camera calibration a target with circular dots is used. Circular dots, due to their symmetry, allow for a detection scheme that is easy to implement as well as being more robust in off-axis or rotated viewing arrangements when compared to a grid of crosses or a line grid. The target is an aluminium plate with black painted dots that have a diameter of approximately four pixels (figure 4.3). The control points (dots) are painted black in order to have high emissivity, which makes them easily detectable. The target is applied to the surface under investigation and an IR calibration image is acquired. The control points'

positions in the image are used to determine the camera calibration constants. As proposed by Heikkilä (2000), a first estimation is obtained using a linear algorithm (Abdel-Aziz and Karara 1971). The calibration constants are then found by minimizing the root mean square residual between the known image coordinates of the control points and their image coordinates computed in accordance to the camera model. The minimization process is performed with the Levenberg-Marquardt method (Marquardt 1963) where the estimation computed with the linear algorithm is used as first trial value. The first guess is obtained from a 2D direct linear transformation (Melen 1994) that considers the optical centre as the centre of the sensor. Sensor dimensions and camera focal length are given as input.

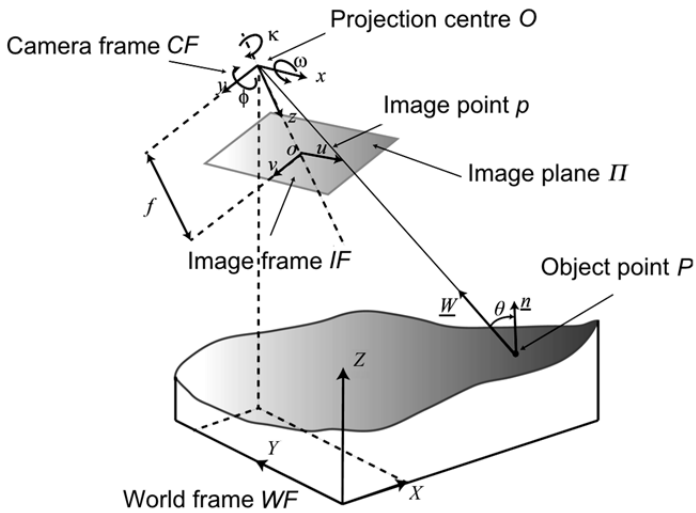

Figure 4.2. Perspective projection model (from Cardone et al 2012).

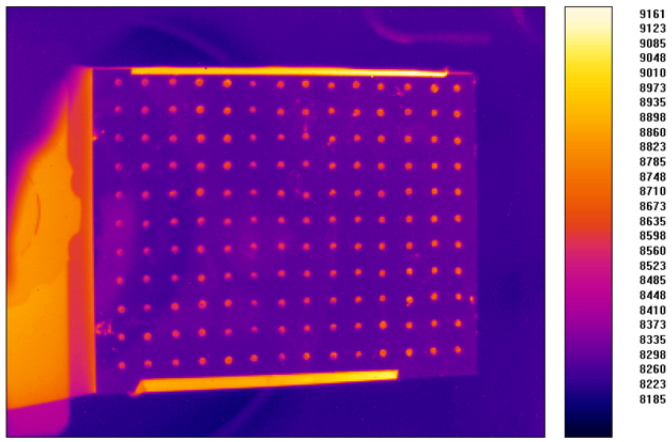

Figure 4.3. Calibration target (color-bar in Isothermal Units).

The IR images registration procedure is completed by taking into account possible model oscillations caused by resulting aerodynamic forces. This is performed to assure that the model movement does not affect the temperature history that is used in the IHTP. Since the model can be considered to be rigid, it is valid to assume that in-plane displacements are represented by 2D rigid translations while out-of-plane displacements result in image scaling.

The in-plane displacements are corrected by means of the single-step Discrete Fourier Transform (single-step DFT, Guizar-Sicairos et al 2008) with a small computation time, memory requirement and good accuracy. This method is able to register two images even if both images are scaled by a different factor.

This approach is based on two steps. The first step aims at the identification of the displacement computing the upsampled cross correlation between the image to register, $g(x,y)$, and a reference image, $b(x,y)$, by means of the Fast Fourier Transform (FFT) and locating its peak. In the first step the cross correlation peak is found to within a fraction of a pixel $1/\kappa$ with $\kappa = 2$. This initial upsampling is used to select an appropriate starting point for cross correlations that might have more than one peak of similar magnitude. The second step refines the location of the peak, to within a desired fraction of a pixel, by means of matrix multiplication of the 2D DFT (equation 4.16). The advantage of a matrix-multiply DFT results from the fact that the upsampled version of the peak location can be computed, within such a neighbourhood of the previous estimation, without the need of zero-pad $G(d,e)\,B^{*}(d,e)$. The upsampled cross correlation (by a factor $\kappa = 1000$) is computed in a 1.5×1.5 pixels neighbourhood (in units of the original pixels) about the initial estimate.

$$G(u,v) = \sum_{x,y} \frac{g(x,y)}{\sqrt{MR}} \exp\left[-i2\pi\left(\frac{dx}{M} + \frac{ey}{R}\right)\right] \qquad (4.16)$$

where M and R are the image dimensions.

The maximum displacements detected in the experimental test carried out (see section 4.5.1.2) are about 0.8 pixels in the streamwise direction while they are negligible in the spanwise direction.

The problem of the image scaling, due to out-of-plane displacements, is solved selecting “interest points” at distinctive locations in the image using the SURF (Speed-Up Robust Features) approach proposed by Bay et al (2008). It is based on the detection of the interest scale invariant points at the location where the determinant of the image Hessian matrix is maximum. Given a point x in an image I, the Hessian matrix $\mathcal{H}(x,\mathcal{s})$ in x at scale $\mathcal{s}$ is defined as follows

$$\mathcal{H}(x, s) = \begin{bmatrix} L_{xx}(x, s) & L_{xy}(x, s) \\ L_{yx}(x, s) & L_{yy}(x, s) \end{bmatrix} \tag{4.17}$$

where $L_{xx}(x, s)$ is the convolution of the Gaussian second order derivative $\frac{\partial^2}{\partial^2 x} g(s)$ with the image I in point x, and similarly for $L_{yx}(x, s)$ and $L_{yy}(x, s)$.

Once interest points are identified in each image, they are matched with a reference image (Lowe 2004) in order to identify the scale factor. Then, the rebuilt image is resized by a 2D spline interpolation. The maximum scale factor correction in the following experimental test is lower than 1%. Both registration procedures are based on matching a set of images with a reference. To perform a good cross correlation for each IR image the previous corrected image is used as a reference.

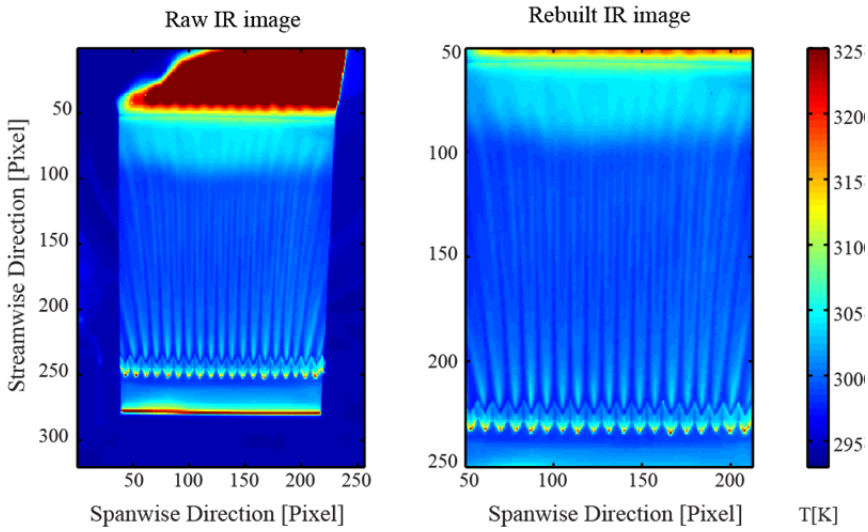

Figure 4.4. (left) An example of IR image before the calibration; (right) An example of rebuilt image after the calibration.

An example of image registration is shown in figure 4.4 where a typical raw IR image (left) and a registered one (right) are presented. The mesh spacing is chosen to be equal to the highest spatial resolution of the IR camera (region with different spatial resolution may be present in case of image distortions or oblique viewing angles), to avoid both loss of information and useless extra points. Indeed, considering that the modulation transfer function of an IR camera equipped with focal plane array detectors (Gravand et al 2014) introduces a negligible modulation of the temperature signal, the maximum measured spatial frequency of the wall temperature is close to the Nyquist frequency. In each measurement point the experimental temperature rise T_{w_M} is therefore correctly known and it consists of n temperature measurements, which

depends on the acquisition frequency of the IR system, f_s, and on the duration of test t_p.

4.5 Inverse Heat Transfer Problem

The IHTP is solved by means of a recursive least-squares approach. It works by varying the unknown parameters in order to minimize the difference between the measured temperature, $T_{w_M}(t)$, and the one generated by solving the heat equation (equation 4.1), $T_{w_{NUM}}(t)$, see equation 4.18.

$$f_{x_p}(\underline{h}) = \int_{t_{start}}^{t_p} (T_{w_M}(x_p, t, \underline{h}, T_{aw}) - T_{w_{NUM}}(x_p, t + t_d, \underline{h}, T_{aw}))dt \quad (4.18)$$

In general, the objectives of the IHTP are the discrete function $\underline{h}(x, y)$, the adiabatic wall temperature (T_{aw}) and a time delay parameter (t_d). The latter is introduced due to the presence of the wind tunnel start-up phenomena that cannot be represented by the numerical model (Cardone 2007). Indeed, during the start-up transient the convective heat transfer coefficient and adiabatic wall temperature are unsteady. Schrjier and Bannink (2010) showed that stationary flow conditions start approximately 25 ms after the valve opening by measuring the pressure variation in the settling chamber (see figure 2.4). Therefore, by introducing this delay only the temperature information after that the tunnel is properly started (t_{start}) is used.

The evolution of surface temperature on the tested body is measured by IR thermography; the image resection method presented in the previous section is applied in order to rebuild temperature maps on a regular mesh surface grid of the observed surface.

To estimate the heat flux it is necessary to set all the known values $[T_r, T_{wi}]$ and a trial value of the unknown parameters $[\underline{h}, t_d, T_{aw}]$. Then, the heat equation is solved and the parameters undergoing optimization are modified in attempt to minimize the error functional defined in equation 4.18. The optimization method is based on the solution of nonlinear least-squares problem (equation 4.19) by means of the Trust Region Reflective algorithm (Coleman and Li 1994, 1996).

$$\min_{\underline{h},t_d}\left\|f_{ERR}\left(\left[\underline{h},t_d,T_{aw}\right]\right)\right\|_2^2 = \min_{\underline{h},t_d}\left(f_1\left(\left[\underline{h},t_d,T_{aw}\right]\right)^2 + f_2\left(\left[\underline{h},t_d,T_{aw}\right]\right)^2 + \cdots + f_{N_x}\left(\left[\underline{h},t_d,T_{aw}\right]\right)^2\right) \quad (4.19)$$

In equation 4.19 $\left[\underline{h},t_d,T_{aw}\right]$ is the vector containing the parameters that are being optimized and $f_i\left(\left[\underline{h},t_d,T_{aw}\right]\right)$ is the error functional evaluated for a generic measurement point. The Trust Region approach considers the unconstrained minimization problem of equation 4.19. The basic idea is to approximate f_{ERR} with a simpler function p, which reasonably reflects the behaviour of the function f_{ERR} in a neighbourhood Z around the point in which the function is evaluated. For the sake of simplicity, in the following the point in which the function is evaluated is named h but it depends from both $\underline{h}$ and t_d for a given point. This neighbourhood is the Trust Region. A trial step s is computed by minimizing the function p over Z. This is the Trust Region sub-problem showed in equation 4.20.

$$\min_s\{p(s), s \in Z\} \quad (4.20)$$

The current point is updated to be $h + s$ if $f_{ERR}(h + s) < f_{ERR}(h)$; otherwise, the current point remains unchanged and Z, the region of trust, is shrunk and the trial step computation is repeated. The approximation of the function f_{ERR} at the point is defined by the first two terms of the Taylor approximation of f_{ERR} at h. Then, the Trust Region sub-problem is rewritten as in equation 4.21.

$$\min_Z\{{}^1/_2\ s^T\mathcal{H}s + s^Tg :\ \|Vs\| \le \Delta\} \quad (4.21)$$

where g is the gradient of f at the current point h, $\mathcal{H}$ is the Hessian matrix, V and Δ are a diagonal scaling matrix and $\|\ \|$ is the 2-norm. The subspace is determined with the aid of a preconditioned conjugate gradient method (Branch et al 1999).

To summarize the optimization procedure for a given $f_{ERR}\left(\left[\underline{h},t_d,T_{aw}\right]\right)$ an approximation function p in a neighbourhood is evaluated. Then, the procedure can be summarized as follows:

- Formulation of the two-dimensional trust-region sub-problem;
- Solve equation 6;
- If $f_{ERR}(h + s) < f_{ERR}(h)$, then $h = h + s$;

- Adjust Δ.

These four steps are repeated until convergence. The trust-region dimension Δ is adjusted or it is decreased if the trial step is not accepted $f_{ERR}(h + s) > f_{ERR}(h)$ (Sorensen 1994, Coleman and Verma 2001).

In the optimization procedure the convergence is reached if, between two subsequent iterations, both the step size Δh and $f_{ERR}(h + \Delta h) - f_{ERR}(h)$ are lower than 10^{-6}.

4.5.1 1D Inverse Heat Transfer Problem

The one-dimensional IHTP is solved by considering that the tangential conduction is negligible. In this case the time-varying heat flux is evaluated for each measurement point supposing that the heat flux in the neighbourhood does not affect it. In this context, in equations 4.18 and 4.19, h is a scalar and only three unknown parameters needs to be estimated. In particular, the T_{aw} is evaluated by assuming that it is constant for measurements points located in a certain neighborhood (e.g. the laminar region of the model surface).

In this case, to increase the rate of convergence of the solution the first attempt for each point is set equal to the solution at the neighbourhood point calculated previously.

The direct heat equation (equation 4.1) is solved using parabolic partial differential equations (Skeel and Berzins 1990). The time integration is performed using a backward approach. The spatial discretization is made evaluating the convergence in the solution of the heat equation. The typical mesh size is $2 \cdot 10^{-2}$ mm. The temperature time-history is calculated in the point corresponding to measurements in order to simplify the application of the trust region approach.

4.5.1.1 Validation on Synthetic Data

Before the data reduction technique is applied to the experimental data set, a validation on synthetic data is performed in order to identify its limits of applicability.

The validation approach can be outlined as described below. For a given running time and a prescribed heat flux (representative of the typical values encountered during the experiments), a temperature rise is generated numerically solving the direct heat equation (equation 4.1). Then, random noise with known standard deviation is added to the temperature signal to assess the influence of random measurement errors such as camera noise. This temperature rise is then given as input to the optimization routine and the inverse heat transfer problem is solved.

Although modern thermographs feature very low noise levels (for the CEDIP Titanium 530L the NETD is 25 mK at the ambient temperature see section 3.3) higher levels of noise are expected in wind tunnel experiments (Cardone 2007). Therefore, noise with standard deviation respectively equal to 0.8 K and 2 K is added and the inverse heat transfer problem is solved 2000 times in order to evaluate the statistics and infer relevant parameters. The noise standard deviation is respectively about the 7% and the 17% of the maximum temperature difference for the given temperature rise.

By considering h to be the exact value of the parameter to estimate, h_i the value of that parameter as estimated in the generic optimization i and $\overline{h} = \frac{1}{n}\sum_1^n h_i$ the average value of the total number of estimations, the normalized standard deviation is now defined as:

$$\sigma = \frac{\sqrt{\frac{1}{n}\sum_1^n (h_i - \overline{h})^2}}{\overline{h}} \tag{4.22}$$

The value of σ is a measure of the oscillations around the average in the estimation under investigation.

The same validation procedure is applied also to two analytic solutions of the heat equation: Cook and Felderman (1966) and Kendall-Dixon (1996) reported in equation 4.7 and 4.10, respectively.

The results of the validation on the synthetic dataset are reported in table 4.1. The standard deviation error is reduced by more than 25% by using the least-squares approach.

Table 4.1. Numerical validation results: noise standard deviation ($\boldsymbol{\sigma_n}$) equal to 0.8 K and 2 K.

	Trust Region Reflective	Cook and Felderman (1966)	Kendall and Dixon (1996)
$\sigma_n = 0.8$ K	0.02	0.04	0.03
$\sigma_n = 2$ K	0.06	0.10	0.08

4.5.1.2 Application on Real Experimental Data

The wind tunnel model consists of two ramps, the first ramp has a length of 150 mm and it has an angle of 5° with respect to the free stream. The second ramp is 80.9 mm long and makes an angle of 45° (figure 4.5). The span of the model is 110 mm. It is made of Makrolon® that is characterized by a relatively low thermal conductivity ($k = 0.20$ W/m K) and a high surface emissivity of $\varepsilon_t = 0.88$ (Schrijer 2010a) which make it very suitable for the application of infrared thermography. In

addition, this polycarbonate material can withstand temperatures up to 393 K without considerably changing the material properties, which is well above the maximum temperature of approximately 310 K that is reached during the experiments. To generate spanwise periodic disturbances in the boundary layer a 1.15 mm thick (k_r) zig-zag strip is attached at $x_r = 25$ mm from the leading edge of the model.

In the current experiments the material diffusivity $\alpha = 1.42 \cdot 10^{-7}$ and the maximum running time $t_p = 0.1$ s result in a penetration depth ($D_p = \sqrt{4\alpha t}$, Schultz and Jones 1973) which is equal to 0.5 mm. The small penetration depth, compared to the depth of the model at the vortex generator streamwise location (about 1 cm), allows considering valid the assumption made in equation 4.1 about the boundary condition at the far wall. The non-dimensional wavelength of the spatial heat flux variation $\chi = \lambda / D_p = 12$ is thus large than 3.5 which means that according to Schrijer (2012) the tangential conduction does not affect the measurements of the heat flux obtained by means of a 1D solution.

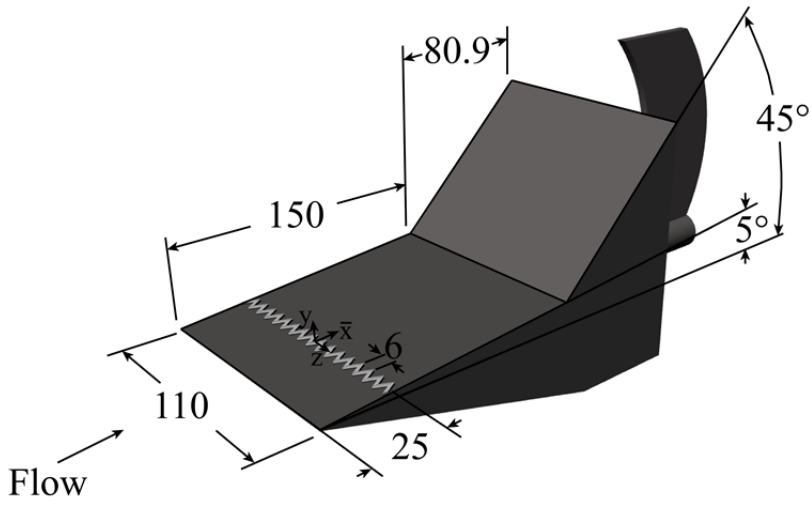

Figure 4.5. A sketch of the model used during the experimental test with the zig-zag strip puts on the model. The vortex generator height (k_r) is 1.15 mm. Dimensions are in mm.

During the measurements the IR camera (see section 3.5) is operated at the maximum frame rate $f_s = 250$ Hz while the integration time of the camera is set 340 μs.

Two shocks emanate from the vortex generator (figure 4.6). The zig-zag strip creates a local stagnation point, which deflects the flow upwards inducing a weak shock upfront of the vortex generator. In a similar fashion, a weak shock is created just downstream of the vortex generator where the flow is deflected downwards. The first

shock interacts with the leading edge shock, while the second weaker compression wave interacts with the merged separation and reattachment shock. Behind the zig-zag strip, two counter rotating vortices emanate in downstream direction. The longitudinal vortices cause a movement of low momentum fluid regions away from and high momentum fluid regions towards the wall in the upwash and downwash sections respectively (Saric 1994) and consequently spanwise heat flux oscillations.

In figure 4.4b an IR image of the flow on the first ramp is shown. As can be seen, the zig-zag strip present on the leading edge of the first ramp generates a row of streamwise vortices with a spatial frequency that is approximately equal to the distance between the teeth ($\lambda = 6\text{mm}$).

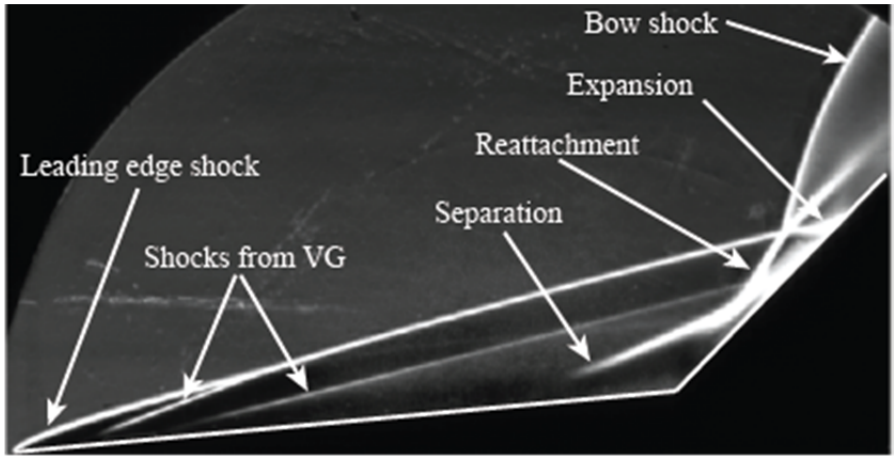

Figure 4.6. Instantaneous Schlieren image.

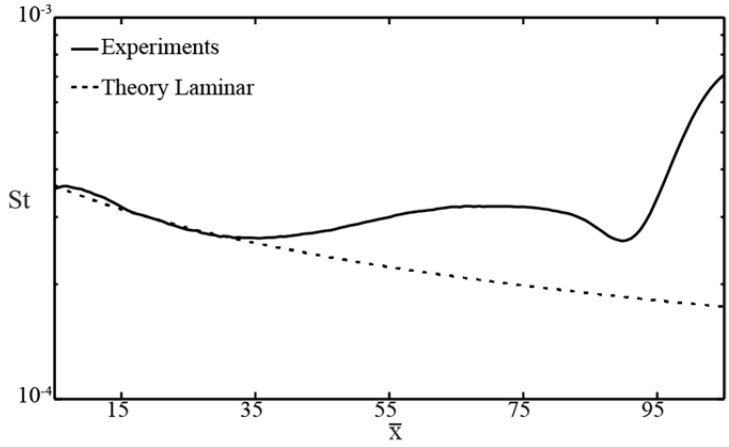

Figure 4.7. Stanton number distribution in streamwise direction (flow from the left to the right).

The measured St (figure 4.7, equation 4.11) is compared to its theoretical value, which can be computed using Reynolds analogy and the reference temperature concept (Anderson 2006)

$$St = \frac{0.41}{\sqrt{Re_x}}\sqrt{C^*} \tag{4.23}$$

$$C^* = \frac{\mu^* T_\infty}{\mu_\infty T^*} \tag{4.24}$$

$$T^* = 0.28T_\infty + 0.50T_w + T_{aw} \tag{4.25}$$

where Re_x is the local Reynold number, μ_∞ is the free stream dynamic viscosity and μ^* is the dynamic viscosity at T^*evaluated through the Southerland's formula.

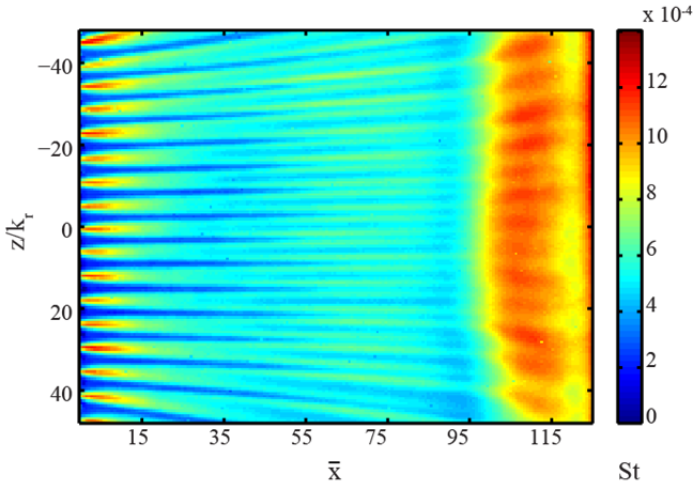

Figure 4.8. Stanton number distribution (flow from the left to the right).

Figure 4.7 shows the spanwise averaged value of the Stanton number St distribution in the streamwise direction. The origin of the coordinate coincides with the location of the element and is normalized with respect to the element height

$$\bar{x} = \frac{x - x_r}{k_r} \tag{4.26}$$

At approximately $\bar{x} = 85$ the separation of the boundary layer is detected. Downstream of the separation region there is an enhancement of the Stanton number due to the boundary layer reattachment. Here, the theoretical St distribution in the streamwise direction is compared to the experimental results starting downstream of

the zig-zag strip. Before separation occurs the flow is laminar and experimental results are in agreement with the theoretical results. The Stanton number St in presence of the vortex generator is agreeing with the theoretical laminar prediction.

In figure 4.8 the Stanton number distribution on the model surface is shown. The distribution is similar to the surface temperature map shown in figure 4.4b, which is a direct result of the governing expression for the heat flux (equation 4.1). Spanwise oscillations are clearly visible near the strip but further downstream their amplitude decreases. This is due to the increase in boundary layer thickness when moving downstream (Schrijer 2010a).

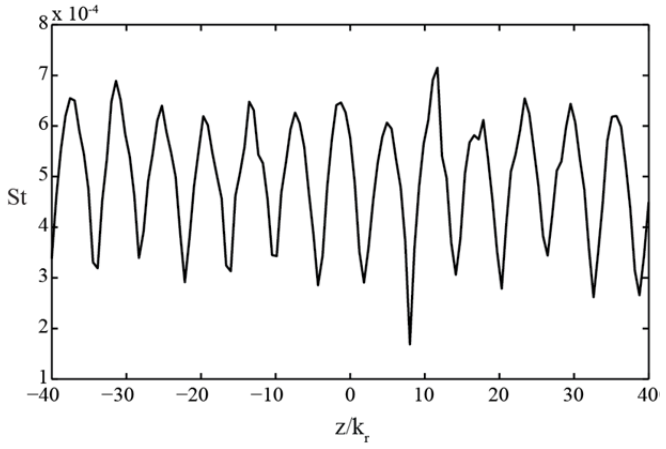

Figure 4.9. Stanton number distribution in spanwise direction at $\bar{x} = 10$.

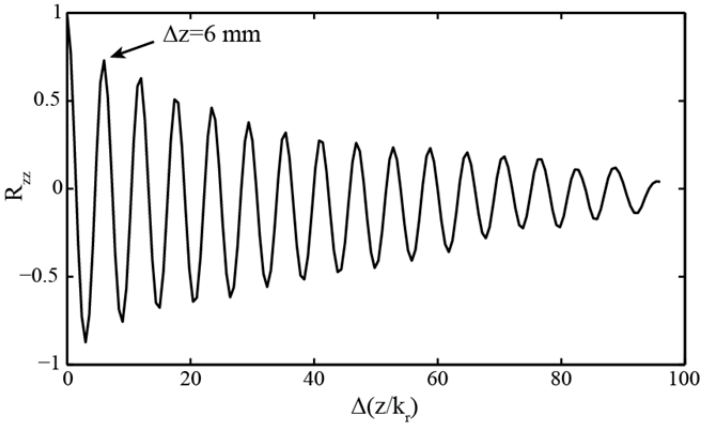

Figure 4.10. An example of spanwise correlation at $\bar{x} = 15$.

In figure 4.9 the St along the span is reported. The periodical shape, induced by the vortex generator, is clear. The spatial frequency is the same of teeth distribution. As

expected the mean value of the convective heat flux coefficient distribution is constant in the spanwise direction.

Starting from the Stanton number distribution it is possible to measure the wavelength of the spanwise vortices. In figure 4.10 an example of the autocorrelation at $\bar{x} = 15$ is shown. The obtained wavelength is 6 mm, which is equal to the spatial wavelength of the vortex generator.

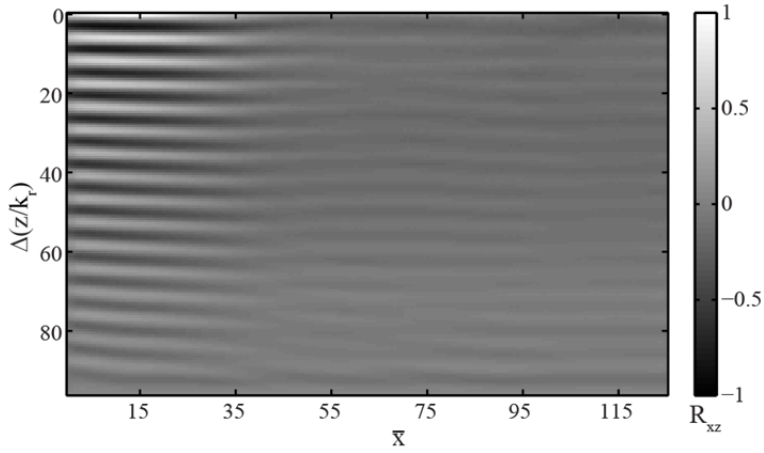

Figure 4.11. Spanwise cross correlation with the signal at $\bar{x} = 10$ for different streamwise locations.

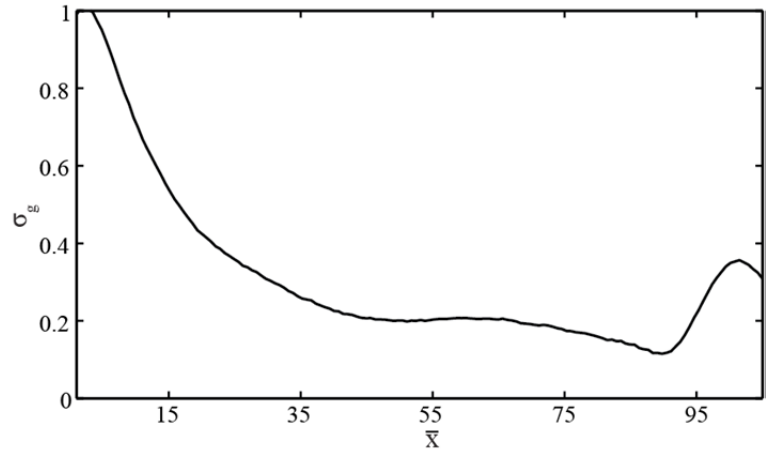

Figure 4.12. Streamwise growth rate with reference amplitude taken at $\bar{x} = 10$.

In figure 4.11 the cross correlation between the Stanton number spanwise distribution just downstream of the vortex generator ($\bar{x} = 10$) and the spanwise distribution at downstream streamwise locations is shown. It is clear that vortices are present along the 5° ramp but their amplitude decreases downstream. To quantify the

vortices growth rate, Schrijer (2010b) and Navarro-Martinez and Tutty (2005) defined it as the ratio of the mean spanwise heat flux amplitude at reattachment and separation. Here, a similar growth rate σ_g is defined as

$$\sigma_g = \frac{\overline{\Delta q_x}}{\overline{\Delta q_r}} \tag{4.27}$$

where $\overline{\Delta q_x}$ is the mean spanwise amplitude at the streamwise location $\bar{x}$ and $\overline{\Delta q_r}$ is the reference mean spanwise amplitude downstream of the vortex generator ($\bar{x} = 10$). The variation of σ_g with $\bar{x}$ is shown in figure 4.12 and it can be observed that the value decreases in downstream direction, which hints at a decrease of the strength of the vortices.

4.5.2 2D Inverse Heat Transfer Problem

In the current context, it is assumed that the influence of the tangential conduction is limited to the spanwise direction although also a more general framework can be constructed that also includes the streamwise direction. As a consequence, the IHTP is solved in the $x - z$ plane identified by the dashed line in figure 4.1a and displayed in figure 4.1b. Furthermore, the T_{aw} is not evaluated but it is estimated from the theory.

The solution of the direct heat equation is done using a finite element discretization of the domain and an implicit scheme for the time integration. The implicit scheme is unconditionally stable. For the domain discretization triangular finite elements are used (Alberty et al 1999). The domain is discretized using a number of elements on the boundary surface of the domain with the same spatial resolution of the regular mesh grid. The depth is assumed to be twice the penetration depth (Schultz and Jones 1973). In the solution of the heat equation the time step is chosen equal to the time step between two subsequent images. The grid convergence study shows that the grid has enough cells such that the solution of the heat equation is not affected.

4.5.2.1 Iterative Computational Cost Reduction

The iterative procedure outlined in the previous section is very computationally intensive due to the high spatial resolution of the data. Therefore, the amount of unknowns is reduced by applying a Discrete Fourier Transform. From the investigated domain (figure 4.1) a slice is extracted and discretized as displayed in figure 4.1b. N_x is the number of measurement points in the direction along which the temperature gradients are relevant (in this case the spanwise direction) and N_z is the number of elements in depth. In the following, it is assumed that the discrete function $\underline{h}$ is discretized in N_x elements for the sake of simplicity.

At the first step the discrete function $\underline{h}$ is represented through the Discrete Fourier Transform coefficients

$$H_{coeff}(k) = \sum_{j=1}^{N_x} h(j)\omega_N^{(j-1)(k-1)} \tag{4.28}$$

$$\omega_N = e^{(-2\pi i)/N_x} \tag{4.29}$$

$h(j)$ is the discrete signal, N_x is the length of the signal and $H_{coeff}(k)$ are the coefficients of the Fourier transform. To correctly perform the DFT the input signal must be periodic otherwise, as observed by Astarita (2008), the Gibbs phenomenon, linked to the discontinuity between the last and the first point of the input signal, may be present. To avoid this effect the input signal is duplicated using a function to join the first and the last point in way that the function and its first derivative are continuous. It is implemented by means of a third order polynomial function which stiches together the last two points and the first two points of the input signal (see Astarita 2008 for details). This procedure introduces a slight increase of number of point N used to describing signal (about +10% respect N_x).

After that, the DFT is applied to the periodic signal and the power spectral analysis is performed. Only a limited number of frequencies with power content higher than 1% of the maximum are considered to be relevant and the corresponding coefficients are taken as the parameters used in the optimization ($H_{coeff}(k)$). If all Fourier coefficients are useful, the maximum number of complex coefficients to describe signal is $N/2$. A peculiarity of this approach is that the number of required coefficients depends on the spatial frequency content of $\underline{h}$ with a strong reduction in presence of band limited oversampled signals. Furthermore, because the signal is extended by means of a low-frequency signal, this ensures that the number of Fourier coefficients is weakly increased with respect to the original signal.

Once the coefficients are identified the iterative procedure as shown in figure 4.13 is executed. The Inverse Discrete Fourier Transform (IDFT) is performed and a filtered $\underline{h}$ in the spatial domain is obtained. Then, the direct heat equation (DHE, equation 4.1) is solved, an analytical temperature rise distribution ($T_{w_{NUM}}$) is calculated and the error $f_{ERR}(\underline{h}_{coeff})$ (equation 4.18) is computed. If $f_{ERR}(\underline{h}_{coeff})$ satisfies the convergence criteria the iteration process stops. Otherwise, the coefficients are modified by means of the Trust Region Reflective algorithm and the loop is repeated until convergence is reached. An added benefit is that in addition to reducing the computational cost, the DFT also works as a filter in the iterative procedure removing the high frequency noise from the signal.

To accelerate the convergence to the solution it is important to choice a suitable first guess. In the following, the solution obtained by solving the 1D IHTP is used.

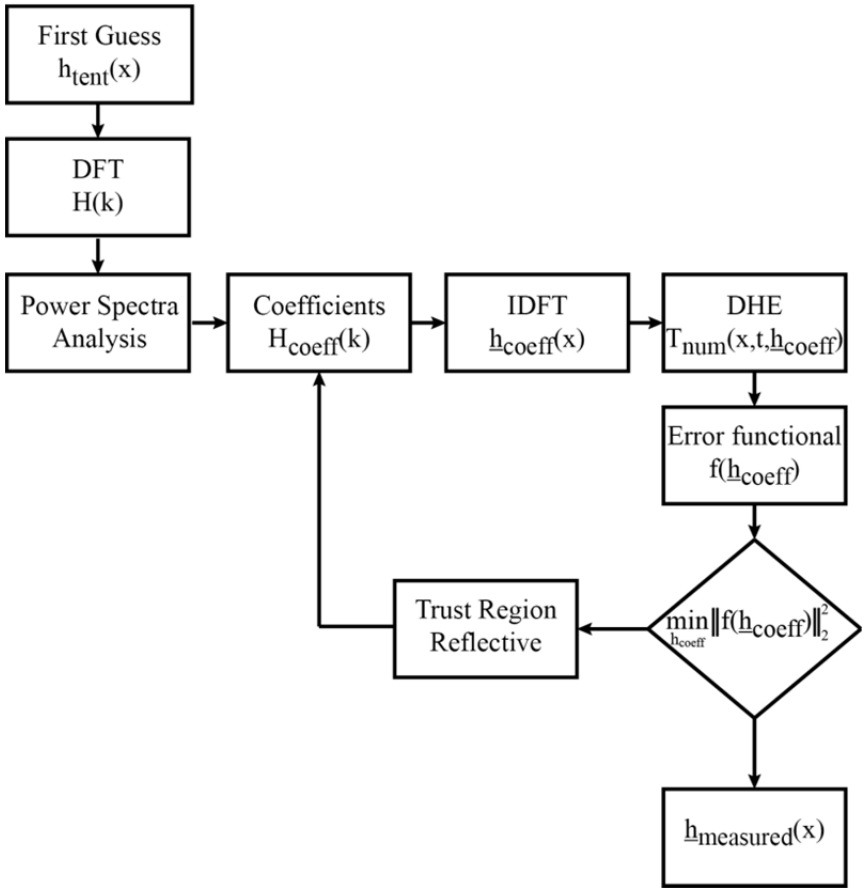

Figure 4.13. Flow chart of the 2D IHTP algorithm.

4.5.2.2 Validation on Synthetic Data

The proposed data reduction technique is first applied to synthetic data in order to evaluate the reduction in computational cost, the error introduced by the procedure itself and the sensitivity to the noise.

The validation procedure can be outlined as described below. For a given running time (t_p) and a given sinusoidal heat flux coefficient distribution $\underline{h}(x)$ an "ideal experimental" temperature rise is generated by solving the heat equation (equation 4.1) as shown in figure 4.14a assuming the delay parameter equal to zero. Hereafter random noise with a known mean value (β_n) and standard deviation (σ_n) is added to the

temperature rise to obtain the noisy temperature rise displayed in figure 4.14b. The latter is the temperature rise that is given as input to the optimization routine.

The values for $\underline{h}$ and the thermal properties used in the synthetic dataset are chosen such that the conditions are similar to those found in the experiments. The running time is $t_p = 0.2$ s and the convective heat flux coefficient distribution has a sinusoidal shape which is oversampled by a factor higher than 3 at the highest spatial frequency. The frequency of acquisition (f_s) is set equal to 70 Hz. The maximum temperature rise is $\Delta T_{wM}(x_{peak}, t = t_p, \underline{h}) = 13$ K. The exact temperature rise is perturbed with random noise characterized by:

a. $\beta_n = 0$ K, $\sigma_n = 0$ K.
b. $\beta_n = -0.1$ K, $\sigma_n = 0.1$ K;
c. $\beta_n = 0.1$ K, $\sigma_n = 0.1$ K;
d. $\beta_n = 0.2$ K, $\sigma_n = 0.2$ K;

Case a is studied in order to estimate the computational cost reduction and the error introduced by the procedure itself. The noise intensity is approximately equal to 0.7% (case b and c) and 1.4% (case d) of the maximum temperature rise. The bias in the temperature rise is introduced in order to analyse the influence of a wrong initial wall temperature in the estimation of the convective heat flux coefficient. In these cases, the exact initial wall temperature (before adding the noise) is used in the solution of the IHTP. For the statistical analysis each case is repeated $n = 1000$ times.

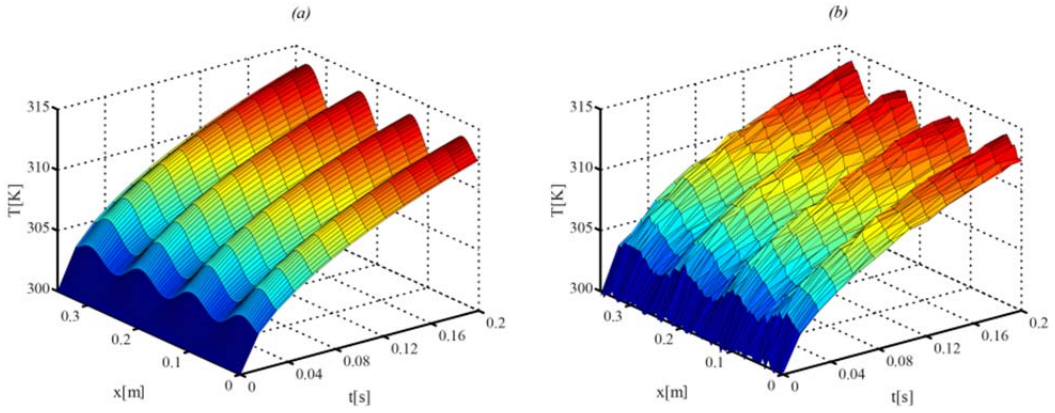

Figure 4.14. (a) Exact temperature rise $\sqrt{Fo_\xi} = 0.62$ (equation 4.30); (b) noisy temperature rise with $\sigma_n = 0.2$K.

In addition, sinusoidal convective heat flux distributions having different spatial frequencies are generated in order to simulate different rates of tangential conduction. The relevance of the tangential conduction is quantified by means of the modified

Fourier number (Fo_ξ, de Luca et al 1993) reported in equation 4.29. In the formula α is the thermal diffusivity of the sensor material, $\xi_s = 2\pi/\lambda$ is the spatial frequency, λ is the wavelength and t_p is the running time.

$$Fo_\xi = {\xi_s}^2 \alpha t_p \tag{4.30}$$

The $\sqrt{Fo_\xi}$ ranges in the interval 0.31÷2.16, which corresponds to limit conditions for which the lateral conduction is relatively unimportant and very important, respectively. As a consequence, the peak to valley temperature signal is 5 K for the lowest spatial frequency ($\sqrt{Fo_\xi} = 0.31$) while it is equal to 0.8 K for the highest case ($\sqrt{Fo_\xi} = 2.16$), resulting in a predicted temperature modulation of 2% and 80% respectively. As a result, the noise intensity added in cases b and c is approximately equal to the 2% and the 12.5% the peak to valley temperature difference for the lower and the higher spatial frequency, respectively.

The accuracy of the technique is assessed via the bias error, the random error and the modulation transfer function (MTF) reported in equations 4.31-4.34. In these equations h represents the exact value, h_i the estimated value and $\overline{h}$ the average value over the total number of estimations n (equation 4.34). The bias β (equation 4.31) quantifies the difference between the exact value and the average, the standard deviation σ (equation 4.22 and rewritten in equation 4.32 for the sake of clarity) is a measure for the oscillations around the average and the modulation transfer function (MTF, Astarita 2006) estimates the modulation of the measured signal with respect to the exact one (equation 4.32). This formulation of the MTF is sensitive to both the systematic (directly associated to the modulation) and random errors. In equation 4.33 A is the amplitude of the sinusoid, which is set equal to 100.

$$\beta = \left(\frac{\overline{h} - h}{h}\right) \tag{4.31}$$

$$\sigma = \frac{\sqrt{\frac{1}{n}\sum_1^n (h_i - \overline{h})^2}}{\overline{h}} \tag{4.32}$$

$$MTF(\lambda) = 1 - \sqrt{\frac{\sum_{i=1}^n (h_i - h)^2}{\sum_{i=1}^n \left(A\sin\left(\frac{2\pi x}{\lambda}\right)\right)^2}} \tag{4.33}$$

$$\bar{h} = \frac{1}{n}\sum_{i=1}^{n} h_i \qquad (4.34)$$

Table 4.2. Percentage of optimized coefficients vs Percentage computational time reduction.

Percentage of the optimized coefficient	Percentage reduction of the computational time
10%	97%
14%	96%
18%	91%
22%	87%
26%	83%
30%	76%

The analysis of the synthetic data starts by evaluating the computational cost reduction by varying the percentage of total Fourier coefficients used in the reconstruction of the $\underline{h}$ distribution. Table 4.2 reports the percentage of optimized coefficients versus the reduction in computational time (where the reference is the case in which all the coefficients are used) for case a. It shows that, as expected, the approach is particularly suitable in presence of band limited frequency data. When only 10% or 30% of the coefficients are used in the optimization procedure the computational time reduces with 97% and 76%, respectively.

The analysis of the synthetic dataset continues by quantifying how the measurement noise influences the estimation of the convective heat transfer coefficient. The bias (β) in the estimation of the convective heat transfer coefficient is plotted in figure 4.15a while figure 4.15b shows the standard deviation (σ). It can be immediately observed that β increases by increasing the $\sqrt{Fo_\xi}$ while the random error is almost constant for $\sqrt{Fo_\xi}$ lower than 1.6. For larger values the random error increases as well with $\sqrt{Fo_\xi}$. The bias error β is sensitive to the modulation of the signal and to the error in the estimation of the mean value. In absence of noise (case a) the inverse procedure introduces a bias lower than 0.5% for $\sqrt{Fo_\xi}$ lower than 1.6 and reaches approximately the 1% for $\sqrt{Fo_\xi} = 2.2$ due to modulation in the estimation of the sinusoidal distribution. For the test cases b, c and d the curves are shifted due to the bias noise that is added to the signal. Therefore, the temperature rise given as input to the inverse technique is biased by the noise with $\beta_n > 0$. Consequently, the measured mean convective heat flux coefficient is overestimated explaining the trend observed in figure 4.15a. The previous discussion clearly illustrates that the initial wall temperature needs to be set correctly since it can strongly bias the estimated heat flux. The random

error (figure 4.15b) increases starting from $\sqrt{Fo_\xi} = 1.6$. The increment with the spatial frequency is related to the fact that for higher $\sqrt{Fo_\xi}$ the peak to valley temperature difference is lower due to the stronger tangential conduction and the relative influence of the noise becomes more relevant lowering the overall accuracy of the result.

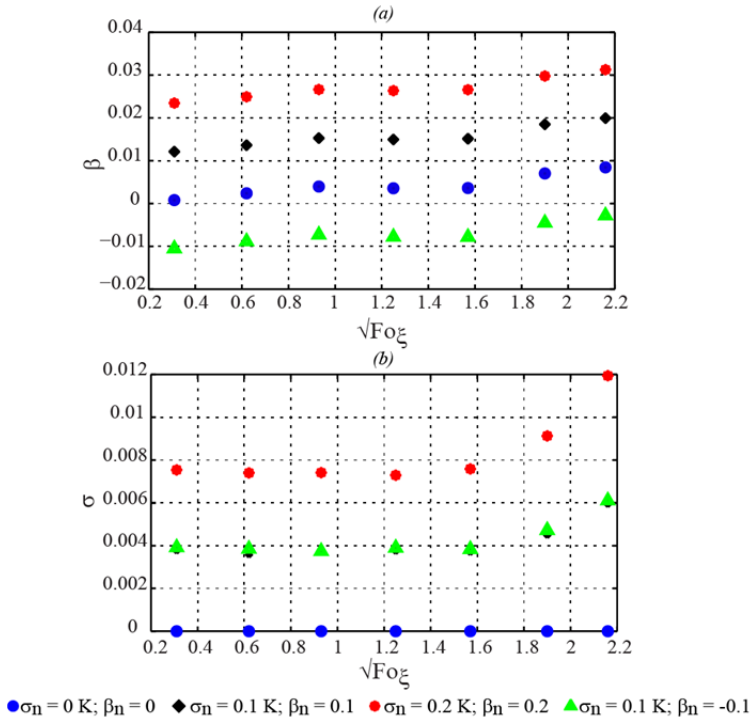

Figure 4.15. (a) Bias in the estimation of h; (b) Standard deviation in the estimation of h.

As stated before the estimated convective heat flux distribution becomes increasingly modulated for high spatial frequencies. An example is reported in figure 4.16 where the exact convective heat flux coefficient distribution and the average estimated out of 1000 samples for $\sqrt{Fo_\xi}$ equal to 0.31 (a), 0.62 (b) and 1.57 (c) are plotted. By a visual inspection of the figure it is clear that, as expected, the modulation increases for higher spatial frequencies. As a consequence, the temperature rise obtained by solving equation 4.1 using the estimated mean convective heat transfer coefficient distribution is modulated as well. The amount of modulation is estimated by means of the modulation transfer function (MTF) obtained from the synthetic data using equation 4.33. The MTF is compared with the 1D thin film sensor MTF (which form the basis for the well known Cook and Felderman 1966 approach, de Luca et al 1993) in figure 4.17a and 4.17b. Figure 4.17b shows a zoom of figure 4.17a in the range $0.85 \leq MTF \leq 1$. It is evident that the 2D inverse technique shows significantly

less modulation especially in presence of high spatial gradients (large Fourier numbers) when compared to the classical 1D thin film sensor. It can be concluded that when $\sqrt{\mathrm{Fo}_\xi}$ is higher than 1.6 the modulation starts to be relevant resulting in the reduction of the measurement accuracy (the modulation can increase up to 10% for $\sqrt{\mathrm{Fo}_\xi} = 2.2$).

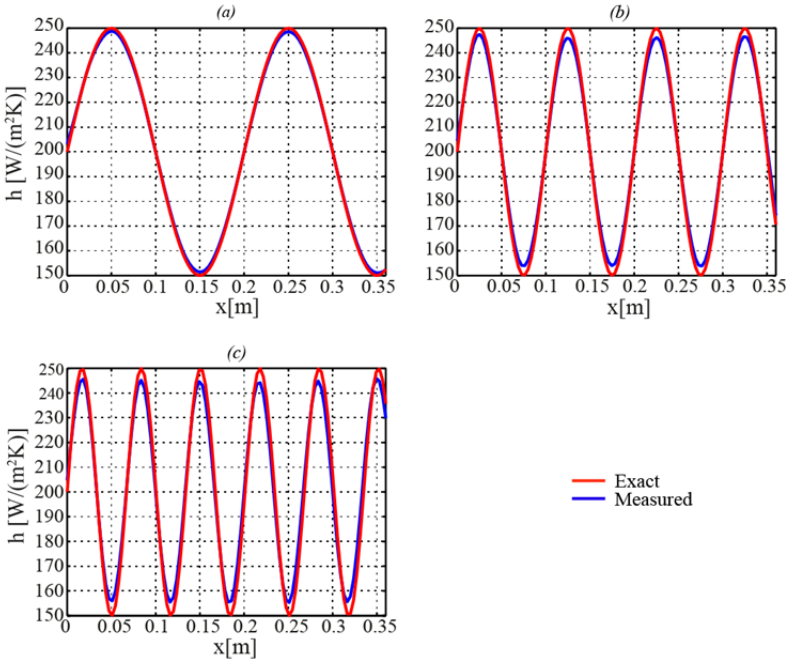

Figure 4.16. Exact convective heat flux distribution and mean estimated distribution for $\sqrt{\mathrm{Fo}_\xi}$ equal to 0.31 (a), 0.62 (b) and 1.57 (c) for case a.

The last aspect that is investigated is the influence of the time sampling frequency on the accuracy of the IHTP solution. In this case, an exact temperature rise ($\sqrt{\mathrm{Fo}_\xi} = 1, \mathrm{t_p} = 0.2\ \mathrm{s}$) is generated by using time steps of $\Delta\mathrm{t} = 0.002\ \mathrm{s}$. Then, synthetic experimental temperature signals are obtained by sampling the exact signal at different acquisition frequencies. The acquisition frequency ($\mathrm{f_s}$) range varied from 15 Hz to 80 Hz, which corresponds to a number of samples ($\mathrm{n_s}$) ranging from 3 to 16.

In figure 4.18 the bias in the estimation of the convective heat flux coefficient versus the frequency of acquisition and the number of samples is shown. At low acquisition frequencies (few samples) the inverse approach shows a relatively large bias of approximately 8% for case a. This is caused by the fact that for low acquisition frequencies, the temperature rise is very coarsely sampled and becomes approximately a step-like curve. When the discretization of the temperature signal is improved (more samples) the error goes down and it becomes almost constant from $\mathrm{f_s}$ higher than 60

Hz (12 samples) where the bias is approximately the 0.5%. Thus it can be argued that the minimum number of samples to properly discretize the temperature rise is about 13 for these conditions. It is slightly larger than the 10 samples proposed by Cook and Felderman (1966) to compute the heat flux with an error of approximately the 1%.

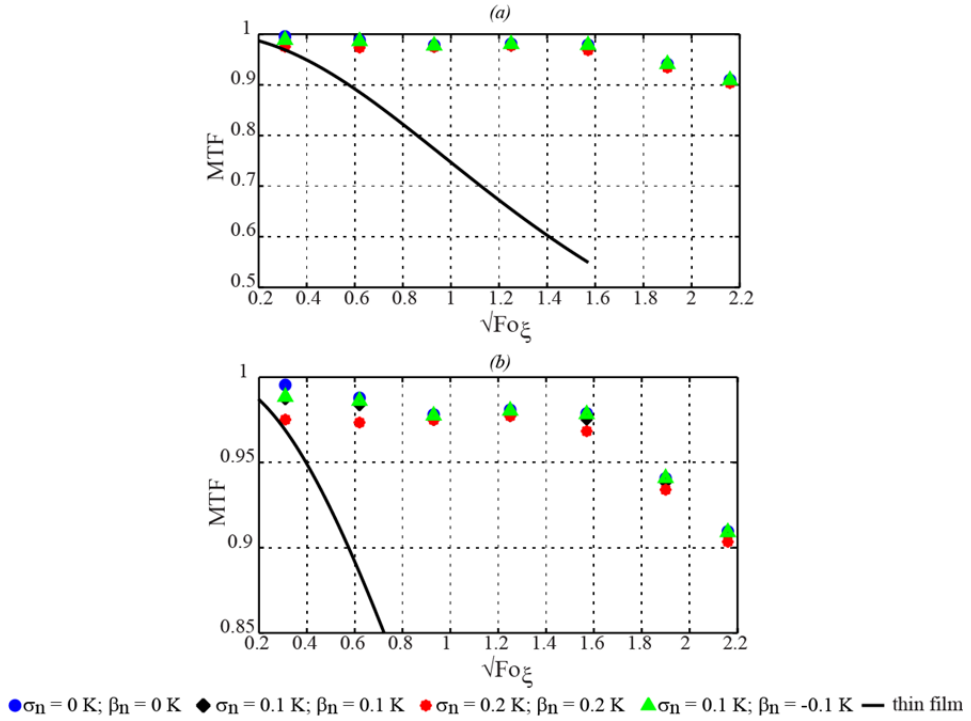

Figure 4.17. (a) MTF of the estimated temperature signal compared to the thin film sensor; (b) zoom of the MTF.

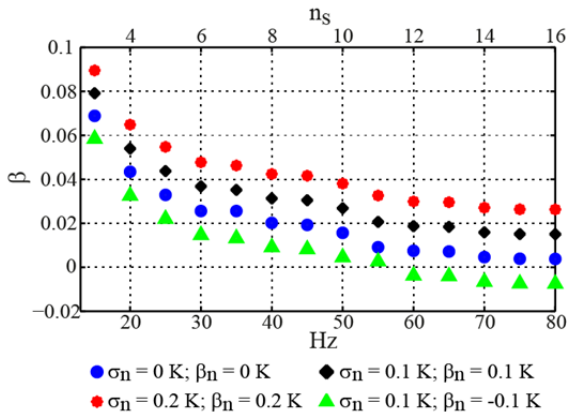

Figure 4.18. Bias in the estimation of h versus the frequency of acquisition and the number of samples.

4.5.2.3 Application on Real Experimental Data

The experiments are carried out at Mach number of 7.5 and at unit Reynolds number equal to $14 \cdot 10^6\ \mathrm{m}^{-1}$. The IR camera (see section 3.5) is operated at 200 Hz at full resolution. The exposure time is set to 400 μs. The spatial resolution is approximately 2 px/mm. Model surface temperature is typically ambient temperature at the wind tunnel start.

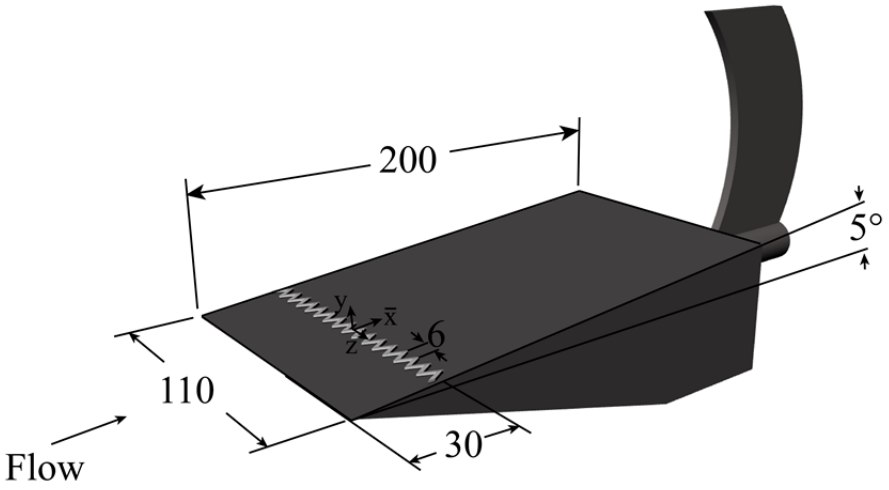

Figure 4.19. A sketch of the model used during the experimental test with the vortex generator. The vortex generator is 0.85 mm height. Dimensions are in mm.

The wind tunnel model is a planar 5° ramp, having a length of 200 mm and a width of 110 mm (figure 4.19). The experiments are conducted at zero pitch and yaw angles. The model leading edge is 50 μm and it is accurately finished to avoid leading edge instabilities. In this study streamwise vortices have been obtained by means of a zig-zag strip vortex generator. The vortex generator has a height of $k_r = 0.85$ mm and the distance between the teeth is $\lambda = 6$ mm (figure 4.19), it is positioned at $x_r = 30$ mm from the leading edge. The height compared to the boundary layer thickness is $k_r/\delta = 0.83$.

Two models are used which have different thermal properties. The anodized aluminium model has a relatively high diffusivity ($\alpha = 6.2 \cdot 10^{-6}\ \mathrm{m^2 s^{-1}}$) while the Makrolon® model has a low diffusivity ($\alpha = 1.4 \cdot 10^{-7}\ \mathrm{m^2 s^{-1}}$). Based on a maximum measurement duration of $t_p = 0.07$ s the $\sqrt{Fo_\xi}$ is equal to 0.5 and 0.1 and the predicted modulation according to de Luca et al (1993) is 0.88 and 0.98, respectively. In the current investigation the penetration depth ($D_p = 4\sqrt{\alpha t_p}$) is approximately 0.5 mm and 3 mm for the Makrolon® and the anodized aluminium model, respectively.

The assumption that the wall F is isotherm is fully valid starting from 30 mm from the leading edge where the thickness of the wind tunnel model is more than 3 times the maximum penetration depth.

The temperature maps are mapped on a rectangular regular mesh with the registration method described in 4.4 for both the Makrolon® and the anodized aluminium models. The resulting temperature maps near the end of the running time ($t = 0.07$ s) are shown in figure 4.20. The black lines represent the domain along which the heat flux is computed. By the visual inspection of the figure it is evident that the two experiments show extremely different temperature rises due to the different material properties: the maximum temperature rise for the Makrolon® model is approximately 8 K while for the anodized aluminium it is only 0.5 K.

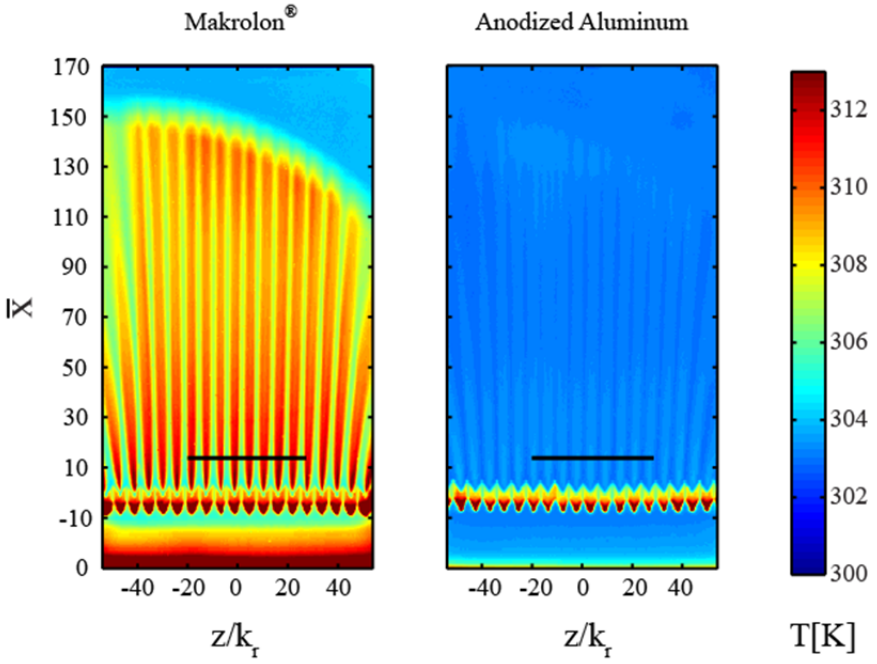

Figure 4.20. Reconstructed temperature maps for both the Makrolon® model (left) and the anodized aluminium model (right). The black lines represent the domain along which the heat flux is computed.

In the following the modified Stanton number C_h (equation 4.13) is used as non-dimensional parameter to discussion the experimental results.

The C_h measured with the proposed 2D approach is compared to the 1D C_h distribution obtained by the Cook and Felderman (1966) approach and the 1D inverse approach described in 4.5.1 (figure 4.21). The 2D solution is obtained by optimizing 24

coefficients (26% of the total) that contribute to the 95% of the total power spectral density.

The C_h measured on the Makrolon® model is reported in figure 4.21a while figure 4.21b shows the values for the anodized aluminium model. Due to its favourable thermal properties the experiment carried out on the Makrolon® model is only weakly affected by the tangential conduction (the predicted modulation is about the 2%). As a matter of fact, figure 4.21a does not show any appreciable difference between the three curves (the difference between the curve is lower than the 2%) except for some effects due to the measurement noise and the inverse techniques uncertainty. The behaviour is rather different in figure 4.21b where the modulation effect is not negligible. In this case, it is visible that the 1D solution underestimates the C_h and the measured demodulation is approximately the 10%. The correct amplitude is recovered by solving the 2D IHTP and the measured C_h starts resembling the one measured on the Makrolon® model.

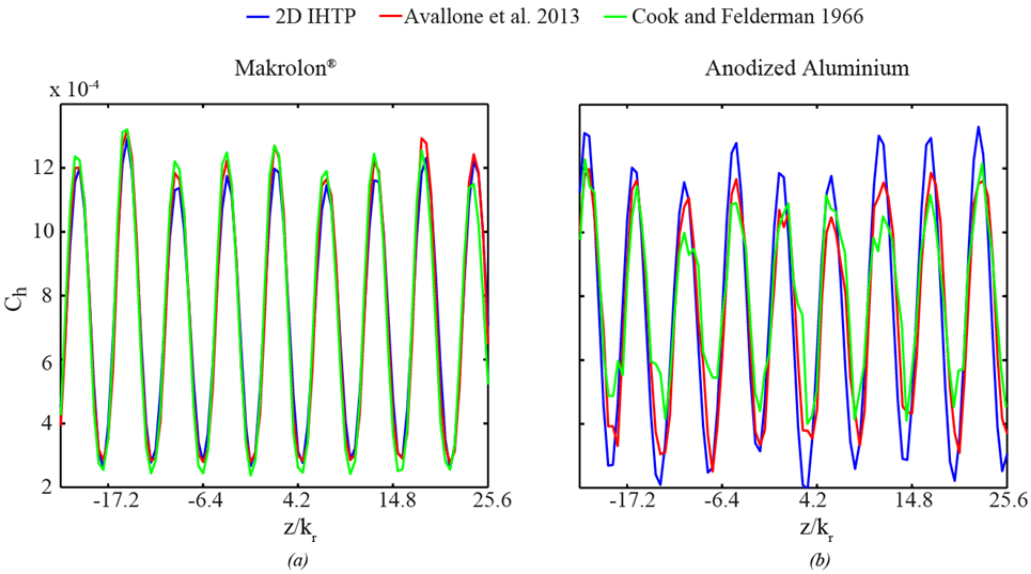

Figure 4.21. Spanwise modified Stanton number distribution along the black line shown in figure 4.20.

The experiments conducted with the anodized aluminium model permit also to analyse the effect of the measurements noise since the temperature signal is rather weak (the maximum temperature increase is only 0.5 K, which means that the noise level is almost 5%). In order to estimate the modified Stanton number by means of the Cook and Felderman (1966) analytical solution a digital low pass filter in space and time is applied to the IR images to obtain a smoother distribution. On the contrary, the inverse approach was applied on the raw IR images. It is evident that the suggested

approach is more robust in presence of noise al already demonstrated in section 4.5.1.1 for the 1D solution.

4.6 Conclusions

In this chapter a full data reduction approach is presented. In order to measure the exact heat flux the IR images are restored to remove lens distortion errors and relative displacements between the IR camera and the investigated model. Wind tunnel model mechanical vibrations are detected and corrected by means of the single-step DFT and the SURF algorithms.

Then the both the 1D and the 2D inverse heat transfer problem are solved by mean of a least-squares approach based on the Trust Region Reflective as optimization tool. The 1D data reduction technique is numerically validated and results show that, for test cases of interest, the standard deviation is lower (about the 25%) compared to the Cook and Felderman (1966) and Kendall and Dixon (1996) analytical solutions. Then the data reduction technique is applied on ad hoc experimental test in which the flow instability is generated by a zig-zag strip assembled on the leading edge of the model.

To face the problem of the tangential conduction the suggested method is extended to the 2D case. Here a way to reduce the computational cost is proposed. It is based on the detection of the most relevant coefficient of the discrete Fourier decomposition of the measured signal. These coefficients are the only ones objects of the optimization algorithm. The inverse procedure is validated on both synthetic data and real experimental data. The analysis of the synthetic data shows the effectiveness of the procedure in reducing the computational cost with band-limited data with respect to the case in which all the coefficients are optimized. In processing real experiments only 26% of the coefficients are used. Furthermore, the technique is rather insensitive to the measurement noise and the modulation is lower than 3% for $\sqrt{\mathrm{Fo}_\xi}$ up to 1.6. The data reduction technique is experimentally validated on real IR data obtained at Mach 7.5. The flow over a flat plate is perturbed by a zig-zag vortex generator installed at 30 mm from the leading edge. The experimental test confirms that the proposed data reduction presents low modulation and low sensitivity to noise.

Chapter 5

Particle Image Velocimetry (PIV)

5.1 Basic Principle of Planar PIV

Particle image velocimetry (PIV, Raffel et al 1997) is a non-invasive anemometric technique that measures the velocity field by means of tracer particles. A sketch of a basic PIV experimental setup and of the data processing is shown in figure 5.1. A basic PIV system consists of a pulsed light source collimated in a light sheet that illuminates the tracer particles within the target area (or object plane). The particles are required to be small enough to accurately track the fluid motion (for an accurate description of the tracers features see section 5.3 and Samimy and Lele 1991). The small scattering of such particles (that is proportional to the particle diameter for spherical particles according to Mie's scattering theory, Raffel et al 1997), the relatively short exposure time necessary to avoid blurring in the particles images and the necessity of a collimated light sheet led to use almost exclusively high intensity pulsed laser light sources. The light scattered by the particles is recorded on a camera oriented such that the optic axis is perpendicular to the laser sheet within alignment tolerances.

The recorded images are divided in sub-regions (often referred as interrogation windows). For each interrogation window, a velocity vector is determined using statistical methods: auto-correlation in the case of double-exposure images (Adrian and Yao 1984); cross-correlation in the case of single-exposure images (Willert and Gharib 1991). Once the particles images displacements Δx_p and Δy_p in the image plane are measured, it is possible to estimate the velocity components in the object plane according to the relation

$$\frac{u}{v} = \frac{M_0}{\Delta t}\left(\frac{\Delta x_p}{\Delta y_p}\right) \tag{5.1}$$

where u and v are the fluid velocities in the object plane, Δt is the time separation between the two pulses, and M_0 is the lateral magnification from the object plane to the image plane, taken to be constant in the absence of aberrations and misalignment of the two conjugate planes. The magnification M_0 is defined as the ratio of the image distance z_0 (distance between the lens and the sensor plane) to the object distance Z_0 (distance between the lens and the object plane).

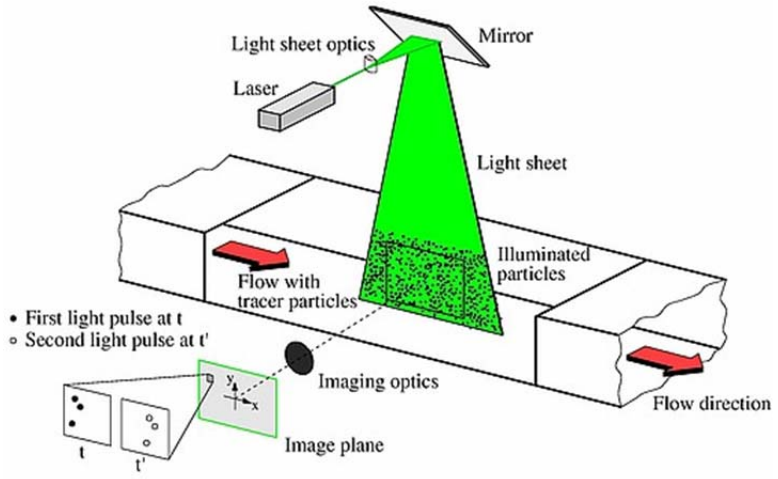

Figure 5.1. Schematic of particle image velocimetry experimental configuration and data processing (from Raffel et al 2007).

5.1.1 Particle Imaging

The particles images are formed on the sensor of the camera (in the following CCD, Charge Coupled Device, cameras are used) via a high quality lens. The particle image diameter is a function of the particles size and of the lens properties. The diameter of an imaged particle is (Adrian 1991)

$$\begin{aligned} d_\tau &\cong \sqrt{d_{geom}^2 + d_{diff}^2} \\ &= \sqrt{\left(M_0 d_p\right)^2 + (2.44 f_\#(1+M_0)\lambda_L)^2} \end{aligned} \tag{5.2}$$

where $f_\#$ is the ratio of the focal length and the aperture diameter, λ_L is the wavelength of the illuminating source, d_p is the particle physical diameter, d_{geom} is

the geometric image diameter due to magnification and d_{diff} is the diffraction-limited diameter determined by approximating the Airy disk with a Gaussian function.

The particle image diameter should be carefully set in order to improve the quality of the measurement. As a matter of fact, a smaller d_τ reduces the uncertainty in the displacement measurement (Raffel et al 2007) and guarantees strong light intensity (since the collected light scales with the inverse of the particle image area) while a bigger particle image reduces the peak-locking effect (the bias of the correlation peak towards integer pixel value, Westerweel 1993).

Considering that the light sheet has a finite thickness Δz_0, the imaged particles will be in focus only if Δz_0 is smaller than the depth of field δz, estimated as follows (Adrian 1991)

$$\delta z \cong 4.88\left(1+\frac{1}{M_0}\right)^2 f_\#^2 \lambda_L \tag{5.3}$$

The features of the recorded image depend upon the source density, defined as

$$N_s = N_{ppp}\,\Delta z_0 \frac{\pi d_\tau^2}{4M_0^2} \tag{5.4}$$

where N_{ppp} is the particles image density.

If $N_s < 1$, the probability of particles overlapping is rather small, and the image will be composed of randomly located individual spots; otherwise, since the light source is coherent, they will generate randomly oriented fringe patterns.

5.1.2 Data Processing

Once the particles images are recorded, the particle displacement is obtained by means of statistical cross correlation. The image is divided in interrogation windows. An interrogation window is selected from the recorded image and the normalized cross correlation function is computed for both the exposures

$$R(\Delta x,\Delta y) = \frac{\sum_{x,y}^{W}(I_a(x,y)-\bar{I}_a)(I_b(x+\Delta x,y+\Delta y)-\bar{I}_b)}{\sqrt{\sum_{x,y}^{W}(I_a(x,y)-\bar{I}_a)^2(I_b(x,y)-\bar{I}_b)^2}} \tag{5.5}$$

where I_a and I_b are the pixel intensities at locations x and y, W is the interrogation window size, $\bar{I}_a$ and $\bar{I}_b$ are the average image intensity within the window and Δx and Δy are the image shifts.

The cross correlation map peak provides the location of the most probable displacement of the particles present in the interrogation window. Since the diffraction-limited spot is approximately gaussian, it is reasonable to assume that the peak resulting from convolution of Gaussian signals is Gaussian as well. For this reason, among the others, a Gaussian peak interpolator is the most accurate in case of rather small particles images (Raffel et al 2007).

In order to improve accuracy and robustness an iterative approach can be used. For example, in the analysis of the planar PIV shown in chapter 7 a multi-pass algorithm with windows deformation (Huang et al 1993) and Blackman weighting windows (Astarita and Cardone 2005, Astarita 2006, 2007, 2008) is used to compute the velocity fields. For the final window size, the process is repeated iteratively in order to improve the accuracy of the image deformation (Scarano and Riethmuller 2000) and to a certain extent allows enhancing the spatial resolution of the measurement (Schrijer and Scarano 2008).

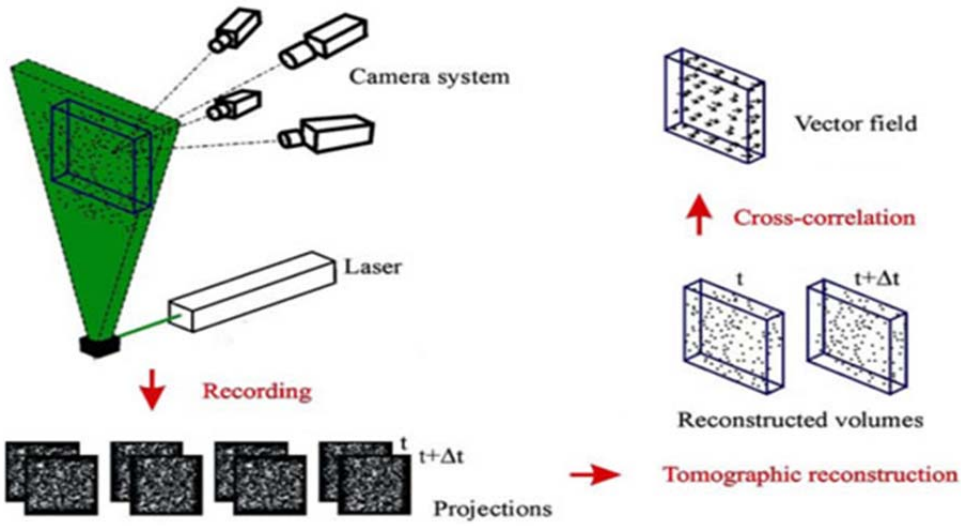

Figure 5.2. Schematic of tomographic particle image velocimetry experimental configuration and data processing (from Elsinga et al 2006).

5.2 Tomographic Particle Image Velocimetry

From the previous discussion it is evident that planar PIV provides only 4 out of 9 components of the velocity gradient tensor, thus leading to the need of assumptions to extract 3D information or possible misleading data interpretation, such as ambiguous

coherent structures identification (Discetti 2013). On the contrary, tomographic PIV (Elsinga et al 2006) measures all the 9 components of the velocity field.

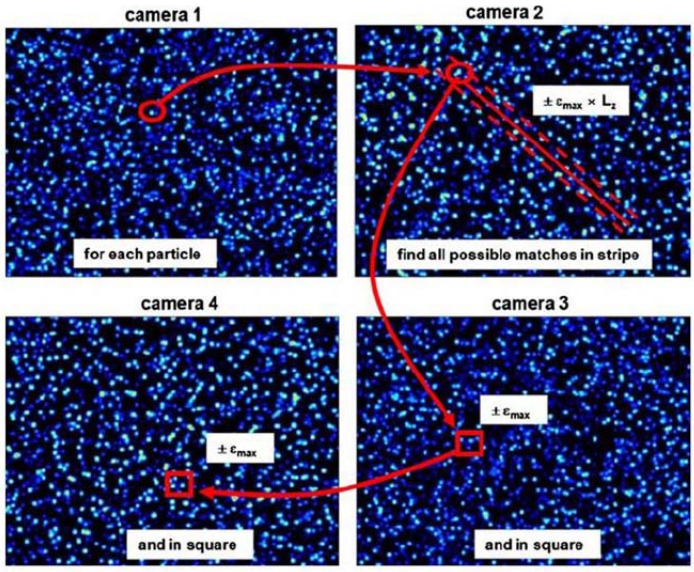

Figure 5.3. Particle triangulation procedure for the volume self-calibration (from Wieneke 2008).

The tomographic PIV relies on the reconstruction of the three-dimensional distribution of scattering objects into a control volume. The reconstruction is achieved by analysing the light intensity scattered by the particles illuminated by a pulsed light and imaged by multiple cameras from different viewing directions. The obtained light intensity field is discretized in cubic compact support functions named voxels, as they are, as a matter of fact, the 3D equivalent of the pixels. The full three components velocity field is then computed by 3D cross-correlation of the subsequent reconstructed volume. The working principle of the technique is sketched in figure 5.2.

5.2.1 Calibration

5.2.1.1 Optical Calibration

The calibration-based methods require the measurement of a mapping function, determining the correspondence $\underline{F}$ between spatial coordinates $\underline{X}$ and image coordinates $\underline{x}$.

Generally, the calibration consists in placing a target with highly contrasted markers (for example white dots on a dark background) with known physical position. The target is placed possibly in the same location of the laser sheet, and translated to sweep a volume in which the illuminated region is enclosed.

The most common mapping functions are the pinhole camera model (Tsai 1987) and the polynomial interpolating functions (Soloff 1997). In the following, the pinhole camera model is adopted. It is based on 6 extrinsic parameters (a translation vector and three Euler angles) and 6 intrinsic parameters (pixel aspect ratio; radial distortion factors of first and second order describing the distortion caused by the lenses; focal length; image coordinates intersection of the optical axis with the image plane).

5.2.1.2 Volume Self-Calibration

The volume self-calibration (Wieneke 2008) is based on the correction of the mapping functions using the actual particles. The technique consists in locating the particles on the camera images and finding the 3D position of matching particles through triangulation. The residual disparity obtained by computing the image distance between the projection of each particle and the correspondent positions on the camera images are used to correct the mapping functions (figure 5.3).

5.2.2 Volume Reconstruction

Tomography deals with the reconstruction of a m-dimensional object from a set of (m-1)-dimensional projections. A projection is defined as a line integral of the object to be reconstructed along a viewing direction. More specifically, in tomographic PIV the object is the 3D distribution of the light scattered by the tracer particles $f_M(x, y, z)$ (where x, y, z are the spatial coordinates in a 3D reference system), while the recorded intensity values on the cameras constitute the set of projections $I(X, Y)$ (where X, Y are the coordinates in the 2D camera reference system). In the case of the iterative algebraic reconstruction techniques (Herman and Lent 1976), the object is discretized as a 3D array of voxels. The line integrals of the intensity along the lines of sight are discretized as a weighted sum of the voxel intensities

$$I(X_i, Y_i) = \sum_{j=1}^{N_{vox}} w_{i,j} f_M(x_j, y_j, z_j) \qquad i = 1, \dots, N_{pix} \qquad (5.6)$$

The subscript i and j indicate the i-th pixel and the j-th voxel, respectively; N_{pix} and N_{vox} are the total number of pixels and voxels; $w_{i,j}$ is a weighting coefficient, determining the influence of the intensity of the j-th voxel on the intensity recorded on the i-th pixel. The equation 5.6 results in a system of N_{pix} linear equations with N_{vox} unknowns. The problem is underdetermined; some additional constraints can consistently reduce the dimension of the space of the solutions.

An approach to solve the equation 5.6 is the Multiplicative Algebraic Reconstruction Technique (MART, Herman and Lent 1976)

$$\left[f_M(x_j, y_j, z_j)\right]_{k+1} = \left[f_M(x_j, y_j, z_j)\right]_k \left(\frac{I(X_i, Y_i)}{\sum_{j=1}^{N_{vox}} w_{i,j}\left[f_M(x_j, y_j, z_j)\right]_k}\right)^{\mu_T w_{i,j}} \quad (5.7)$$

The subscript k indicates the iteration number, and μ_T is a relaxation coefficient, that plays a significant role in the stability of the iterative process (in MART the stability criterion is $0 < \mu_T < 2$). In both cases one iteration is completed after that the update equation has been executed for all the projections.

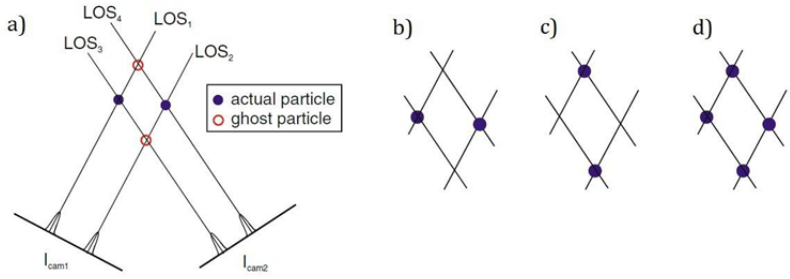

Figure 5.4. Mechanism of formation of ghost particles: (a) two particles imaged by two cameras lead potentially to two ghost particles (this is not exactly true in 3D, as the lines of sight can be non-coplanar; (b-c-d) three possible solutions of the reconstruction problem (from Elsinga et al 2011).

The intensity fields reconstructed by MART are usually affected by artefacts mainly due to the ambiguity in the estimation of the particles correct position along the line of sight. Following Novara et al (2010), the main sources of error can be bundled in three categories:

- Ghost particles (Maas et al 1993), i.e. intensity blobs forming at the intersection of line of sight carrying non-zero values, but not corresponding to the position of actual particles. The mechanism of the ghost particles formation is sketched in figure 5.4 for the simplified case of a 2D slice reconstructed by two 1D cameras. Obviously the larger is the number of particles, the larger is the number of ambiguities in the reconstruction; furthermore, the thicker is the volume, the higher is the number of positions that each true particle may occupy into the reconstructed volume, and accordingly the higher is the probability of ghost particles occurrence (Discetti 2013);
- Elongation of the reconstructed particles in the depth direction (especially when the total solid angle is too small), determining an increase of random errors in the measurement of the velocity component along the

depth. On the other hand, a large viewing angle can lead to longer line of sights, enforcing the first source of error;
- Discretization artefacts due to under-sampling, arising when the diameter of the particles to be reconstructed is below 2-3 voxels.

The first source of error can be reduced by increasing the number of cameras, reducing the seeding density (at the expense of the spatial resolution), or using high accuracy reconstruction schemes (as the MTE-MART by Novara et al 2010). The effect of the solid angle is merely geometrical, and it can be compensated only by proper orientation of the cameras. The discretization artefacts can be reduced by applying some artificial diffusion with 3D Gaussian filter (Discetti et al 2013) in the iterative process (equation 5.7).

5.2.2.1 Ghost Particles

The ghost particles constitute a severe source of error in the tomographic reconstruction.

A ghost particle is formed in every occurrence of intersection of all the lines of sight in which a particle image is present. Consider, for example, an illuminated volume of size Δx_0, Δy_0, Δz_0 and a particle image of the first camera. The particle can be located anywhere along the line of sight, whose length is approximately Δz_0 (without affecting the generality of the problem the effect of the viewing angle is neglected). The possible candidates for the matching of a single particle of the first camera on the second camera are those included in a strip with length equal to the projection of the line of sight on the second camera (it can be estimated by multiplying Δz_0 for the average magnification M_0 and dividing by the pixel pitch P_p) and width equal to the particle image diameter d_τ. The number of candidates for the matching for each particle image of the first cameras in a 2 camera system can be statistically determined by multiplying this area for the particle image density. Normalizing with the number of true particles N_p one obtains

$$\frac{N_g^{2cam}}{N_p} = N_{ppp} d_\tau \left(\frac{\Delta z_0 M_0}{P_p} \right) = \frac{4}{\pi d_p} N_s \Delta z_0 M_0 \qquad (5.8)$$

where d_p is the particle diameter (equation 5.2) and N_{ppp} is the particle image density.

The number of spurious matching is statistically determined by multiplying the particle image density N_{ppp} for the search area, which is equal to the source density N_s. This leads to the general formula for a N_{cam} system (Discetti 2013)

$$\frac{N_g^{N_{cam}}}{N_p} = \left(N_{ppp}\right)^{N_{cam}-1} d_\tau \left(\frac{\Delta z_0 M_0}{P_p}\right)\left(\frac{\pi d_\tau}{4}\right)^{N_{cam}-2} = \frac{4}{\pi d_p} N_s^{N_{cam}-1} \Delta z_0 M_0 \tag{5.9}$$

The term $(\Delta z_0 M_0)/P_p$ is the depth of the volume in voxels (provided that the resolution ratio between voxels and pixels is equal to 1), while the term $(\pi d_\tau)/4$ is the diameter of the particle image.

5.3 Particles Tracers in the Hypersonic Regime

The application of PIV fundamentally depends on the requirement that the tracer particles follow the flow field. Due to large flow accelerations present in compressible flows in the form of shock or expansion waves the inertial forces cause particle slip, which reduces the accuracy of the measurement technique in these areas (Schrijer 2010a).

The amount of particle slip, determined by the particle relaxation time depends on the particle characteristics and flow field. When the amount of particle slip is known the extent of the affected regions can be established and a possible correction strategy may be developed. Theoretical relations can be established that enable to compute the particle relaxation time (Ragni et al 2011) for given particle properties (density, size) and flow field characteristics (relative Reynolds number, relative Mach number, amount of rarefaction). However in practice it is found that the uncertainty in particle characteristics (bulk density, effective size due to agglomeration) causes large deviations from the theoretical relaxation values (Schrijer et al 2006) and that an experimental determination of the particle response is required.

5.3.1 Particle Response

In order to assess the amount of particle slip, first the behaviour of heavy particles in a gas flow is studied. The equation of motion for a particle in a (unsteady) gas flow is given by Melling (1997)

$$\frac{\pi d_p^3}{6}\rho_p \frac{d\underline{\underline{U^p}}}{dt} = -3\pi\mu d_p\left(\underline{U} - \underline{U^p}\right) + \frac{\pi d_p^3}{6}\rho\frac{d\underline{\underline{U}}}{dt} - \frac{1}{2}\frac{\pi d_p^3}{6}\rho\frac{d\left(\underline{\underline{U^p}} - \underline{U}\right)}{dt} - \frac{3}{2}d_p^2\sqrt{\pi\rho\mu}\int_{t_0}^{t}\frac{d\left(\underline{\underline{U^p}} - \underline{U}\right)}{dt'}\frac{dt'}{\sqrt{t-t'}} \tag{5.10}$$

where d_p, ρ_p and U^p are the particle diameter, density and velocity respectively while μ, ρ and U are the flow viscosity, density and velocity. The left-hand side of equation 5.10 represents the product of mass and acceleration. The right-hand side represents the forces acting on the particle. The first two right hand terms represents the viscous force and the acceleration force according to Stokes' law. The third term gives the force needed to accelerate the added mass, which, for spherical particles, equals one-half of the mass of the displaced fluid. The last term is known as the Basset force which accounts for the deviation of the flow pattern around the particle from that for steady flow (effect of history of the motion). Since the particle density exceeds the fluid density by several orders of magnitude, all right hand terms can be neglected with respect to the viscous drag. After some algebraic rearrangement the following equation results (Schrijer 2010a)

$$\frac{d\overline{U_p}}{dt} = \frac{\underline{U} - \underline{U^p}}{\tau} \tag{5.11}$$

where τ is the velocity relaxation time of a particle

$$\tau = \frac{4}{3}\frac{\rho_p d_p^2}{c_d Re_d \mu} \tag{5.12}$$

where Re_d is the Reynolds number based on d_p and $\left(\underline{U} - \underline{U^p}\right)$. Tedeschi et al (1999), reports methods that allow calculating the drag coefficient for spherical particles for a variety of flow conditions (relative Mach number, relative Reynolds number, and Knudsen number).

In compressible flow a velocity change is accompanied by a temperature change. Therefore, in addition to a velocity lag, a particle also incorporates a temperature lag. The time rate change of the particle temperature is given by Rudinger (1976)

$$\frac{\pi d_p^3}{6}\rho_p c_p \frac{dT_p}{dt} = h\pi d_p^2 (T - T_p) \tag{5.13}$$

where c_p is the thermal heat capacity of the particle material, h is the heat transfer coefficient, T_p is the particle temperature and T is the flow temperature. This equation can be rewritten in order to obtain the temperature relaxation time in a similar way as the velocity relaxation time

$$\frac{dT_p}{dt} = \frac{(T - T_p)}{\tau_T} \tag{5.14}$$

where the temperature relaxation time can be expressed as

$$\tau_T = \tau\left(\frac{1}{8}\frac{Pr\, c_d\, Re_d}{Nu}\frac{c_T}{c_p}\right) \tag{5.15}$$

Here, the Nusselt number is $Nu = (hd_p)/k$ where k is the thermal conductivity of air and c_T is the specific heat of the particle material.

5.3.2 Determination of Particle Response Time by means of Shock Wave Test

To establish the proper value of the particle time response under realistic flow conditions, experimental shock wave test are usually carried out (Tedeschi et al 1999). The trajectory of a particle over a shock wave is obtained by solving the ordinary differential equation 5.11 with the appropriate boundary conditions $u_p(t = 0) = u_u$ and $u_p(t \to \infty) = u_d$

$$u^* = \frac{u_p - u_d}{u_u - u_d} \tag{5.16}$$

where u_p is the normal particle velocity across the shock wave, u_u and u_d are the normal flow velocity component upstream and downstream of the shock (figure 5.5).

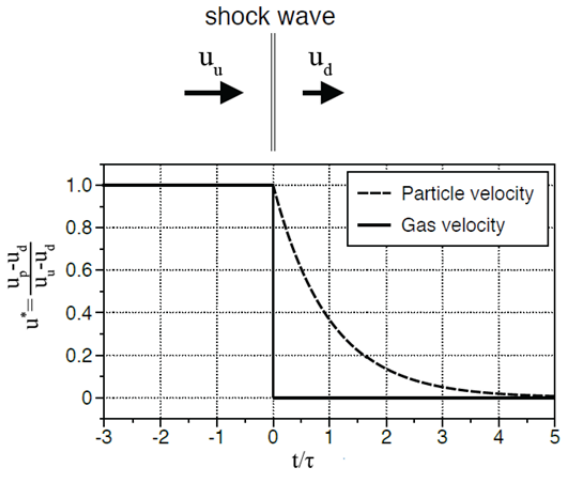

Figure 5.5. Particle response to a normal shock wave (from Schrijer 2010a)

The above solution applies to the velocity component normal to the shock wave. This expression is integrated in time to obtain the particle velocity as a function of particle position x_p with initial condition $(x_u, t_{start}) = (0,0)$

$$x_p = u_d \tau \left(\frac{u_u - u_d}{u_p - u_d} \right) + \tau (u_u - u_p) \tag{5.17}$$

For shock waves having a low normal Mach numbers $M_{n,u} \leq 1.3$ and atmospheric total temperatures $T_0 \cong 288$ K, the factor $(u_u - u_p)$ may be neglected with respect to $u_1 \left(\frac{u_u - u_d}{u_p - u_d} \right)$ and an exponential function for the relaxation length ξ may be defined

$$u^* = e^{-\frac{x_p}{\xi}} \tag{5.18}$$

At $t = \tau$ the particle is located at the position $x_p = \xi$ and $u^* = e^{-1}$, the relaxation length can be related to the relaxation time using equation 5.17

$$\xi = \tau [u_u - (u_u - u_d) e^{-1}] \tag{5.19}$$

Using the previous equation, the relaxation length can be directly obtained from the slope of the relaxation curve, measured by PIV, when displayed in a semi-logarithmic diagram

$$\frac{d \ \ln(u^*)}{dx_p} = -\frac{1}{\xi} \tag{5.20}$$

5.4 Tomographic PIV in the Hypersonic Regime

As the various numerical studies have shown (Iyer and Mahesh 2013, Subbareddy et al 2014, etc), the occurrence of transition is a highly three-dimensional process. Therefore, in order to study it more in detail and to have a good base of comparison with the state-of-the-art computations, the application of fully three-dimensional quantitative measurement techniques is a necessity. In order to realise this, tomographic particle image velocimetry is used. To date, tomographic PIV has been extensively applied to the study of boundary layers in both low speed (Elsinga and Weesterweel 2012) and high speed compressible flows (Humble et al 2009). Specifically, Sun et al (2012) studied the flow downstream of a micro ramp in a turbulent supersonic boundary layer using tomographic PIV. Applications in the hypersonic flow regime are not yet reported in literature, although Havermann et al (2002), Schrijer et al (2006) and Williams and Smits (2012) report experiments using planar PIV in hypersonic flow facilities. Schrijer et al (2006) applied planar PIV to study the flow at Mach 7 on a double compression ramp flow in the Hypersonic Test Facility Delft (HTFD). A survey of applications of PIV in the high-speed regime is given by Scarano (2008). The application of tomographic PIV in a hypersonic facility

is even more difficult with respect to planar PIV due the strong compressibility effects and the technical limitations such as limited optical access, aero-optical aberrations (Elsinga et al 2005), system vibrations requiring single-shot tomographic calibration (Michaelis and Wolf 2011). Especially the latter aspect is challenging considering the limited amount of images available for the volume self-calibration and model motion. In the following the experimental arrangement and the experimental procedure are shown.

5.4.1 Measurement Setup and Procedure

The flow is seeded with titanium dioxide (TiO_2) particles with a nominal crystal size of 50 nm (Kemira UV-TITAN L830) and with a nominal bulk density of $\rho_b = 200\ kg/m^3$. In practice, the particles tend to cluster forming porous agglomerates of approximately 400 nm (figure 5.6), which results in a particle relaxation time of $\tau = 2.5\ \mu s$ (figure 5.7, Schrijer et al 2006).

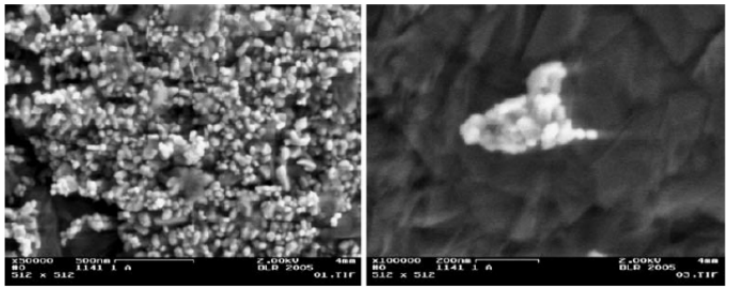

Figure 5.6. Electron microscopy images of TiO_2 particles: (left) image of a collection of particle agglomerates; (right) a single agglomerate (from Schrijer et al 2006).

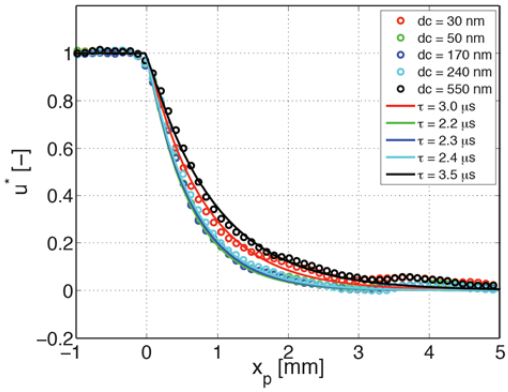

Figure 5.7. Relaxation time of TiO_2 with different nominal crystal size (from Schrijer 2010a).

In order to further reduce the relaxation time, the particles are de-hydrated as suggested by Ragni et al (2011). The tracers are introduced in the hot storage tube off-line by means of a high-pressure cyclone device. The amount of seeding injected in the storage tube is controlled by introducing it shot-wise through a successive charge-discharge of the seeded fluid in the cyclone into the hot storage tube. The single inlet port does not result in a fully uniform seeding along the storage tube and as a consequence the concentration of seeding tracers varies during the running time of the tunnel. Experiments are conducted optimizing the seeding concentration for measurements at 30 ms after valve opening.

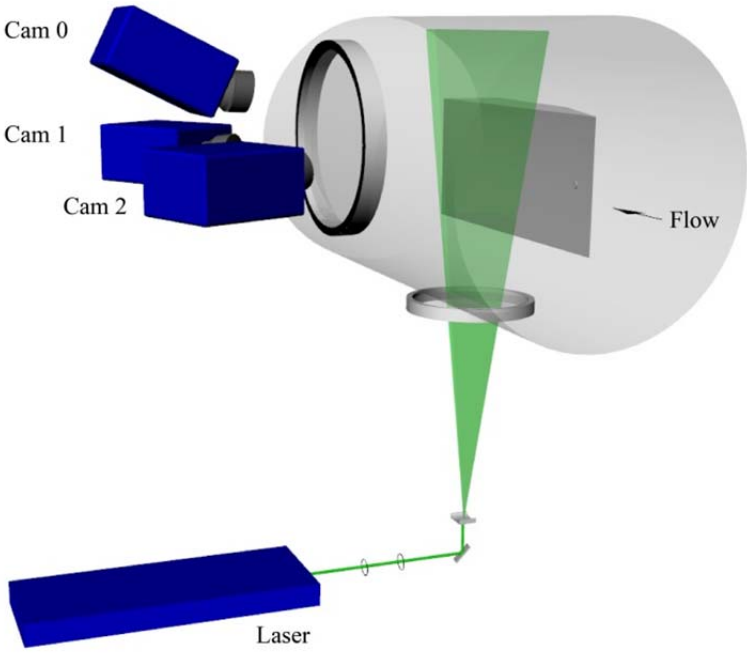

Figure 5.8. Sketch of the experimental setup.

Illumination is provided by a laser from an optical access positioned on the bottom of the test section. The duration of each laser pulse is shorter than 10 ns, which is short enough not to have particle streaks. A sketch of the experimental apparatus is shown in figure 5.8. The camera and the laser are synchronized with the wind tunnel in order to take a measurement at 30 ms after starting the wind tunnel. Due to the short running time of the wind tunnel, only one velocity measurement is obtained for each test.

The illumination and the acquisition system are synchronized with the wind tunnel by means of a LaVision programmable timing unit (PTU 9). The DAVIS 7.4 software

is used for data acquisition and DAVIS 8.1 is used for data processing (volume geometric calibration, volume self-calibration, image pre-processing, volume reconstruction and three-dimensional cross correlation). The tomographic volume calibration is performed using a LaVision Type 7 calibration plate that is translated along the depth direction in three successive steps spaced by 2 mm. The geometrical calibration is performed in the test section at ambient pressure. A three-dimensional mapping function from image-space to physical object-space is generated. This corresponds to the first step shown in the flowchart in figure 5.9.

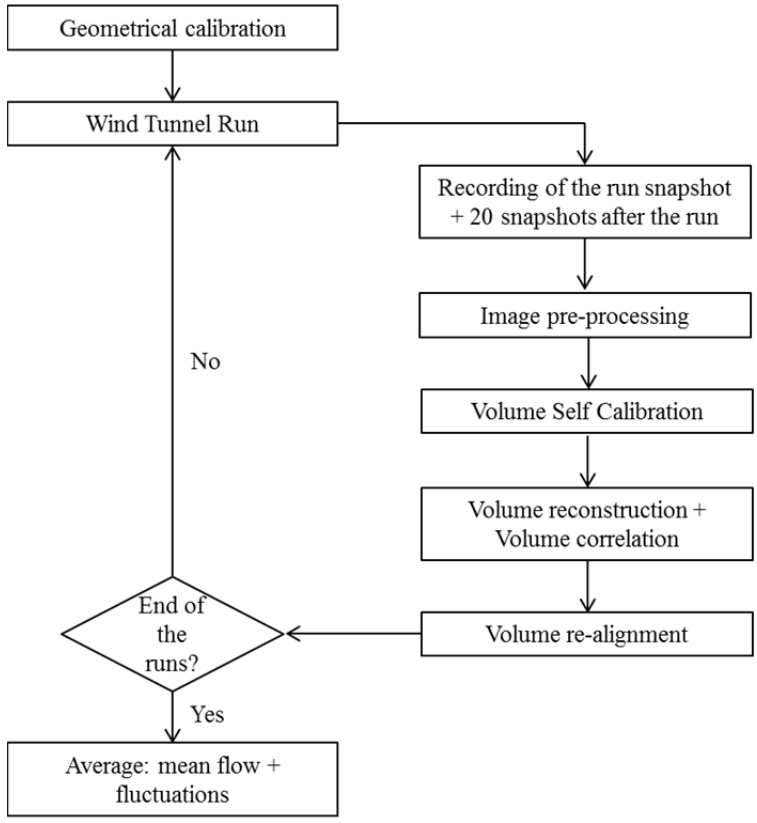

Figure 5.9. Flowchart of the experimental procedure.

For each wind tunnel run, 21 images are acquired; the first snapshot corresponds to the established flow in the test section. The subsequent 20 snapshots are recorded after the tunnel run and are used to perform the volume self-calibration in conditions of low-pressure in the test section. Before performing the volume self-calibration, the raw images (figure 5.10a) are pre-processed by subtracting the sliding minimum over 11×11 pixels in order to reduce background intensity. Furthermore, a Gaussian smoothing with a 3×3 kernel and sharpening are applied to reduce the image noise.

The raw image is shown in figure 5.10a while the resulting pre-processed image for a typical experiment in presence of a cylindrical roughness element (the experimental results are reported in chapter 8) is reported in figure 5.10b.

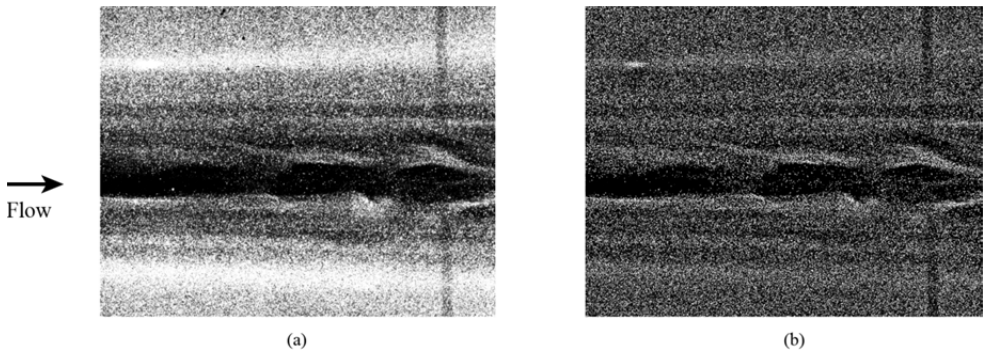

Figure 5.10. Snapshot representing the typical seeding condition during the runs from cam0 in presence of a cylindrical roughness element (see chapter 8). Raw image (a) and pre-processed image (b) for a typical experiment.

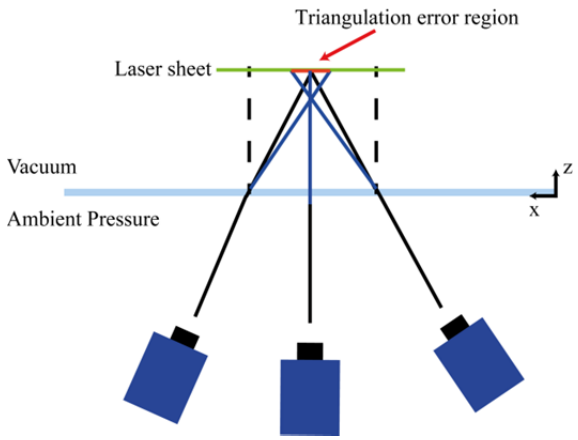

Figure 5.11. Sketch of the triangulation error due to refractive index variation (top view). In red the triangulation error region.

Light refraction has to be taken into account when an optical flow measurement technique is used in a (de) pressurized flow facility such as the HTFD. Since the conditions in the test section are close to vacuum, a different density exists between the outside and the inside of the wind tunnel. As a result, the change of refractive index coupled with oblique viewing angles affects the triangulation (see figure 5.11) to the point that it is necessary to perform the volume self-calibration under the same conditions. This is confirmed by applying Snell's law for Cam0 ($\alpha_T = 30°, \beta_T = -8°$ where α_T and β_T are the rotations around the x and z axis, respectively), which predicts a displacement as high as 0.96 pixels. To eliminate such errors, the volume self-

calibration is performed on 20 snapshots that are acquired directly after the run, when the pressure is still sufficiently low. The measured displacement due to refraction effects with respect to the geometric calibration carried out at ambient pressure is reported in figure 5.12. The initial displacement is approximately 1.6 pixels, which is reduced to less than 0.05 pixels by the self-calibration procedure. The difference between Snell's law prediction and the measured value is ascribed to additional small displacements of the imaging system during each run and to geometrical calibration errors. In view of the latter, the above procedure is repeated for each run.

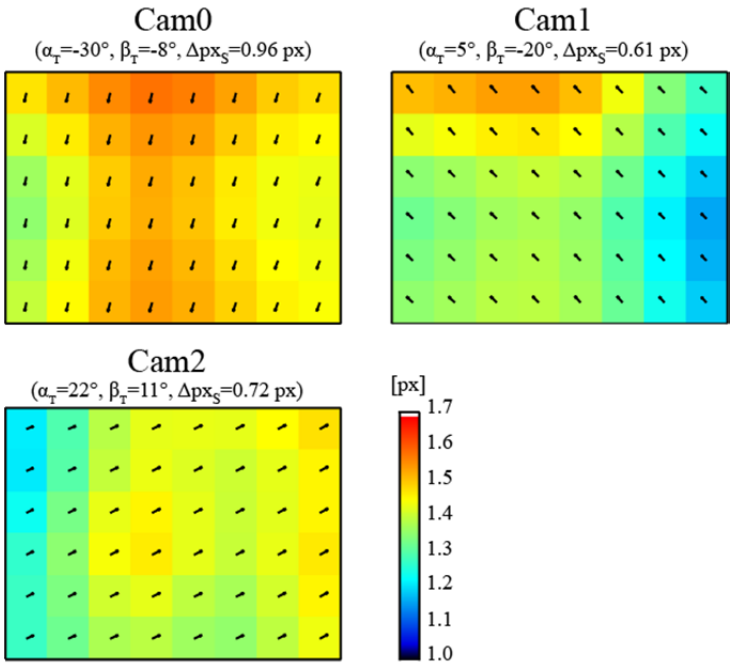

Figure 5.12. Self calibration initial displacement corrections for the three-cameras. α_T and β_T are the rotations around the x and z axis while Δpx_S is the pixel displacement evaluated by Snell's law.

The pre-processed images are reconstructed using MART (equation 5.7). To evaluate the quality of the reconstruction the particle image density is estimated by an in house code (Novara 2013). The N_{ppp} is estimated to be on average 0.03, which according to the assessment of Elsinga et al (2006) corresponds to a quality of the reconstruction (Q defined as the normalized correlation coefficient of the exact and reconstructed intensity distribution) of about 0.9. Values of Q above 0.75 are considered sufficiently high to avoid the detrimental effects of ghost particles.

To further quantify the quality of the reconstruction, a signal to noise ratio may be defined as the reconstructed particle intensity inside the illuminated area versus that reconstructed outside (Elsinga et al 2006). The reconstructed object intensity profile

along the depth for the single snapshot for a typical run is shown in figure 5.13. Comparing the average signal intensity outside and inside the laser sheet results in an average signal to noise ratio of 5. In figure 5.13 the peak located at approximately $y = 0.1$ mm corresponds to the signal coming from the model surface. In the experiments the laser sheet is oriented in such a way that it would glance the surface the model. In this way the tomographic reconstruction is able to accurately detect the position of the model surface, through the intensity peak due to impurities present on the surface. This information is used to estimate the model position and to realign all individual snapshots taking into account the small oscillations, which is of importance for the statistical analysis of the flow field.

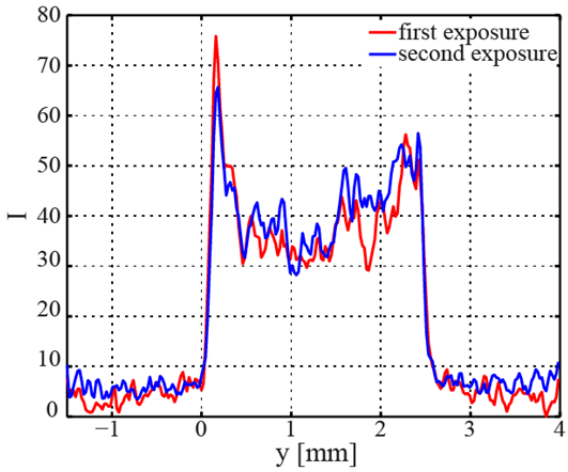

Figure 5.13. Intensity distribution of the reconstructed object along the depth direction for a single run.

5.4.3 Measurement of a Hypersonic Laminar Boundary Layer

5.4.3.1 Experimental Setup and Tomographic PIV Data Processing

The measurements are carried out at Mach number equal to 7.5, unit Reynolds number of $\mathrm{Re_{unit}} = 14 \cdot 10^6\ \mathrm{m^{-1}}$. The total pressure and total temperature are $\mathrm{p_0} = 28$ bar and $\mathrm{T_0} = 579$ K, respectively. Before the wind tunnel is started the test section and vacuum tank are evacuated to a pressure below 1 mbar.

The wind tunnel model used in the experiments is a planar 5° ramp having a length of 200 mm and a width of 110 mm (figure 5.14), it is held from the rear with a sting. The model is made out of anodized aluminium and the leading edge is accurately finished with a leading edge radius of 50 μm to avoid leading edge instabilities. The uniformity of the leading edge has been verified by measuring the undisturbed laminar boundary layer and the results do not show any spanwise inhomogeneity of the flow.

The physical domain (green region in figure 5.14) covers the range $119\ \text{mm} < x < 150\ \text{mm}$ along the streamwise direction, $-11.5\ \text{mm} < z < 11.5\ \text{mm}$ along the spanwise direction and it is 2.5 mm thick along the wall normal direction (y).

Illumination is provided by a Quantel Evergreen laser ($\text{Nd:YAG}, 200\ \text{mJ/pulse}$). The time separation between exposures is set to $\Delta t = 0.7\ \mu\text{s}$ and the laser sheet thickness is 3 mm. The particles images are recorded by three PCO Sensicam QE CCD cameras ($1376 \times 1040\ \text{pixels}, 12\ \text{bit}, 6.7\ \mu\text{m/px}$) equipped with Scheimpflug adapters and Nikon 105 mm focal length objectives set at $f_{\#} = 11$. The resulting measurement volume is $31 \times 23 \times 2.5\ \text{mm}^3$, with an average image digital resolution of $44.3\ \text{pixels/mm}$.

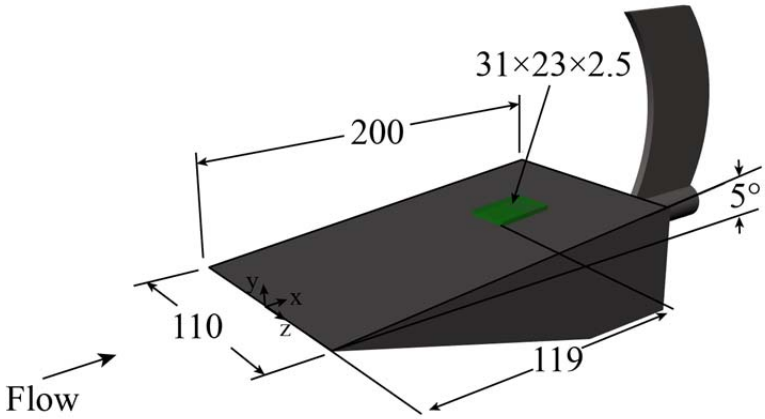

Figure 5.14. Sketch of the wind tunnel model (dimensions are in mm). The measurement domain is highlighted in green.

Table 5.1. Tomographic PIV parameters.

Parameter	Quantity
Particle image density (N_{ppp})	0.03
Measurement volume	$31 \times 23 \times 2.5\ \text{mm}^3$
Interrogation volume	$84 \times 48 \times 30$ voxels $1.89 \times 1.08 \times 0.67\ \text{mm}^3$
Interrogation volume overlap	75%
Digital resolution	44.3 pixels/mm
Vectors per field	$99 \times 143 \times 14$
Maximum displacement	$28 \times 1 \times 1$ voxels

The particles images are interrogated using a volume having a final size of $80 \times 48 \times 30$ voxels ($1.89 \times 1.08 \times 0.67\ \mathrm{mm}^3$) and an overlap factor of 75%. Non-cubic interrogation windows are chosen in order to cope with the strong velocity gradient in the wall-normal direction. Spurious vectors are removed using a median filter (Westerweel and Scarano 2005) and replaced through linear interpolation of surrounding vectors. The parameters relevant for the tomographic PIV setup are reported in table 5.1.

5.4.3.2 Experimental Results

The laminar boundary layer on the 5° ramp is examined and compared with the similarity solution for a flat plate. The measured boundary layer profile is compared to the Illingworth-Stewardson similarity solution (figure 5.15) for an adiabatic wall (Weigand 2005). The velocity profile is obtained by averaging the data over 30 snapshots. Profiles are extracted along the centreline of the model at three streamwise locations ($x = 126, 136, 146$ mm from the leading edge).

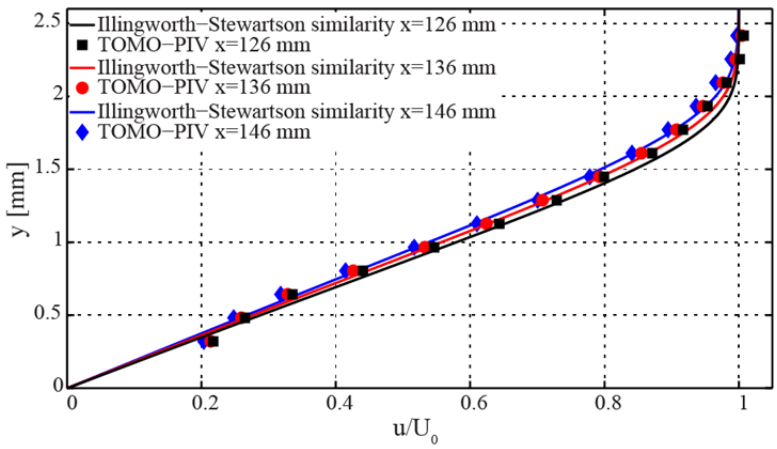

Figure 5.15. Velocity profile measured in the laminar boundary layer and comparison with Illingworth-Stewardson similarity (Weigand 2005).

The result is reported in figure 5.15 and it is clear that there is a good agreement between the measured profile and the self-similar solution. Furthermore, the boundary layer growth is correctly captured as well. Close to the wall, below 0.5 mm, the measurements deviate from the theory due to limited spatial resolution. Close to the edge of the boundary layer the curvature of the velocity profile is underestimated due to the finite size of the interrogation volume. At the edge of the boundary layer the velocity profiles return to the free stream values and collapse nicely. The average rms (estimated from the 30 available snapshots in the upper layer of the measurement domain) of the streamwise velocity component $\langle u' \rangle / U_0$ is 0.03. The causes are

measurement noise, presence of the oblique shock upstream and wind tunnel repeatability that is about 1% (Schrijer and Bannink 2010, section 2.2.3).

5.5 Conclusions

An assessment of the experimental procedure leading to the statistical characterization of the time-averaged and fluctuating velocity field is presented. The volume self-calibration technique is used with the purpose to account for index of refraction effects as well as for correcting variations from snapshot to snapshot. The measurement technique is experimentally validated by the measurement of the undisturbed laminar boundary layer growing along the plate.

Chapter 6

Investigation on the Influence of the Roughness Geometry

6.1 Experimental Setup

6.1.1 Wind Tunnel Model and Tested Configurations

The measurements are carried out at Mach number equal to 7.5. The total pressure is varied between 1.7 and 2.8 MPa to select the appropriate Reynolds number. In the experiments three test conditions defined as low, medium and high Reynolds number are defined corresponding to a free stream total pressure of 1.7, 2.2 and 2.8 MPa, which yields a unit Reynolds number of respectively equal to $8 \cdot 10^6$ m^{-1}, $11 \cdot 10^6$ m^{-1} m^{-1} and $14 \cdot 10^6$ m^{-1} (table 2.3).

A 5° ramp is used as wind tunnel model (figure 6.1). It is 200 mm long and 110 mm width and it is installed in the test section, mounted on a sting from the rear. The model is made out of Makrolon® and has a nose radius of 50 μm. The leading edge is accurately finished such that any instability (Le Duc et al 2006) is detected in the measurement of the laminar boundary layer. Makrolon® is characterized by a relatively low thermal conductivity ($k = 0.20$ W/m K) and a high surface emissivity of $\varepsilon_t = 0.88$ (Schrijer 2010a) which make it very suitable for the application of infrared thermography. In addition, this polycarbonate material can withstand temperatures up to 393 K without considerably changing the material properties, which is well above the maximum temperature of approximately 310 K that is reached during the experiments. The viewing angle with respect to the model surface is kept less than 50 degrees such that the emissivity could be regarded as constant and independent of the viewing angle (Cardone et al 2012).

Three roughness elements are investigated: two cylinders and a square like geometry, see figure 6.1 (bottom). All of the elements have a height (k_r) of 1 mm. The two cylinder shaped roughness elements have a diameter of 4 mm or 5.7 mm and they will be referred to as the small (cylS) or large (cylL) cylinder. The width of the square element is 4 mm. The roughness elements are mounted at $x_r = 30$ mm and $x_r = 60$ mm from the leading edge along the symmetry axis of the wind tunnel model. The local boundary layer properties at the location of the roughness element such as the boundary layer thickness (δ), the momentum thickness (θ), the Reynolds number based on the momentum thickness (Re_θ) and the k_r/δ ratio (ratio of the roughness height to boundary layer thickness at the roughness location) are summarized in table 6.1. These values are computed using the Blasius solution including compressibility corrections using the reference temperature concept (Anderson 2006).

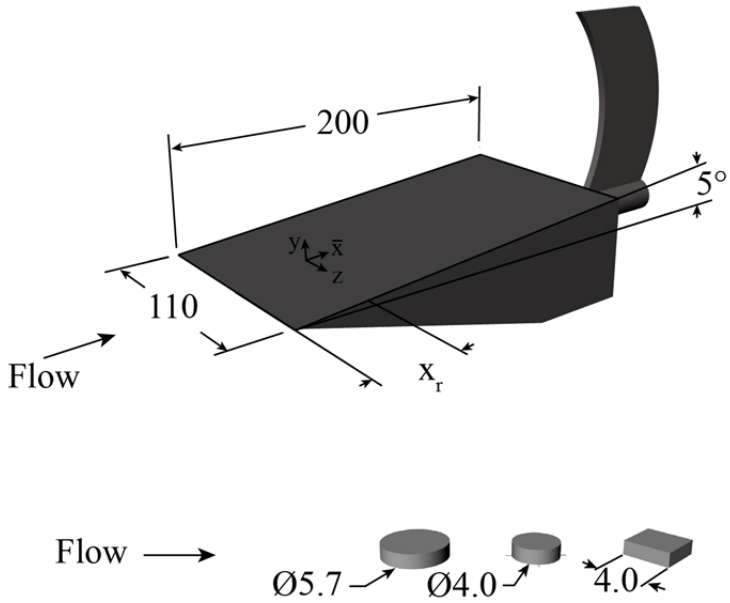

Figure 6.1. Sketch of the wind tunnel model (top) and of the roughness elements (bottom). The roughness elements are 1 mm height. Dimensions are in mm.

In order to predict whether the roughness elements are able to induce transition the Shuttle Roughness Criteria (SRC, $Re_\theta/M_e = (C(h/\delta)^{-1}$, rewritten from equation 1.1 for the sake of clarity) is used. In this criterion, M_e is the Mach number at the edge of the boundary layer at the roughness location ($M_e = 6.48$ in the current investigation) and Re_θ is the Reynolds number based on the momentum thickness (as it is reported in table 6.1). The constant C indicates the effectiveness of the element; when C is equal or larger than 200, transition occurs downstream of the element (critical roughness) while values of C larger than 310 transition occurs at the location

of the element (effective roughness, Berry et al 2006). The constant C for all tested configurations is reported in figure 6.2 (the filled symbols represents $x_r = 30$ mm while open symbols $x_r = 60$ mm); for the medium and high Reynolds numbers all roughness elements are expected to induce transition according to the criterion while for the low Reynolds number the flow does not undergo transition.

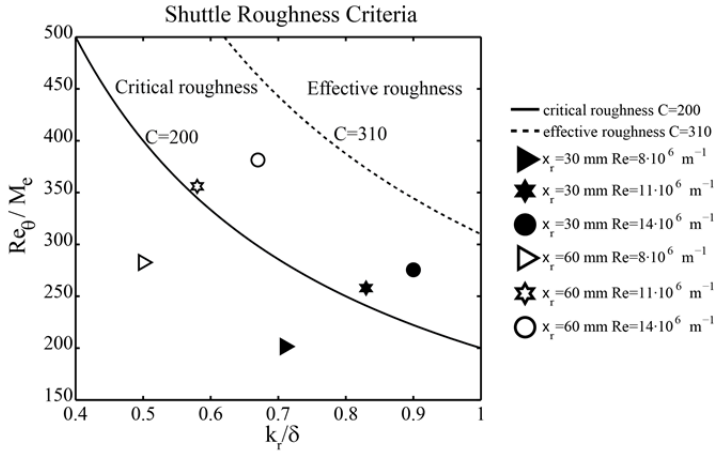

Figure 6.2. Shuttle Roughness Criteria: $C = 200, 310$ for critical and effective roughness respectively.

Table 6.1. Laminar boundary layer properties at the roughness location.

$Re_{unit}(m^{-1})$	$8 \cdot 10^6$		$11 \cdot 10^6$		$14 \cdot 10^6$	
x_r(mm)	30	60	30	60	30	60
δ(mm)	1.4	2	1.2	1.7	1.1	1.5
θ(mm)	0.17	0.24	0.15	0.21	0.13	0.18
Re_θ	1305	1830	1670	2307	1785	2450
k_r/δ	0.71	0.50	0.83	0.59	0.91	0.67

6.1.2 Measurement Technique and Data Reduction

The IR thermography measurements are performed using a CEDIP Titanium 530L IR system. The integration time of the camera is set to 200 μs and it is operated at a frame rate of 250 Hz. The obtained spatial resolution is 1.57 pixels/mm. For a sketch of the experimental setup and IR camera features see section 3.5.

The wall heat flux distribution is computed from the surface temperature signal by solving a one-dimensional Inverse Heat Transfer Problem based on the semi-infinite slab model coupled with a least-squares approach (see section 4.5.1).

The assumption of infinite slab model as isotherm is valid if the thickness of the material is larger than the penetration depth (D_p, Schultz and Jones 1973). In the current investigation the penetration depth ($D_p = 4\sqrt{\alpha t}$, where α is the thermal diffusivity equal to $\alpha = 1.4 \cdot 10^{-7}\ m^2 s^{-1}$) is approximately 0.5 mm and the assumption is fully valid starting from 15 mm from the leading edge where the thickness of the wind tunnel model is 10 times the estimated penetration depth.

According to the error analysis presented in section 4.5.1 the heat flux error associated to the inverse data reduction is less than 2%. A full error analysis (Moffat 1988) indicates that the Stanton number measurements are accurate to within 8%. It takes into account the error due to the inverse approach, the error in the quantification of the free stream flow properties, the uncertainty in the model physical properties and in the temperature measurements.

6.1.3 Heat Flux Visualization

To further visualize the heat flux distribution around and downstream of the roughness element the K value as introduced by Tirtey et al (2011) is used:

$$K = 100 \times \frac{q_w(x,z) - q_{lam}(x)}{q_{turb}(x) - q_{lam}(x)} \qquad (6.1)$$

Through K, the heat flux is normalized using the theoretical values of the laminar and turbulent heat flux (Eckert 1956). Basically a K value of 100 represents the case for which the heat flux is equal to the turbulent case while for a K value of 0 the heat flux corresponds to laminar values. In the interpretation the following conventions are introduced by Tirtey et al (2011) are adopted:

- $K < 30$: Laminar region;
- $30 \leq K \leq 70$: Transitional region;
- $K \geq 70$: Turbulent region;
- $K \geq 110$: Local structure overheating.

6.2 Experimental Results

6.2.1 Flow Field Interpretation from Heat Flux Distribution

Before starting a detailed analysis of the experimental results a general discussion about the relation between the overall flow topology and the heat flux distribution on the model surface is given here. Figure 6.3 shows a typical heat flux map around and downstream of the roughness element. In the figure the element is indicated in grey

and the $\bar{x}$ axis is oriented along the centreline. The origin of the reference system coincides with the location of the roughness element (figures 6.1 and 6.3, equation 4.26).

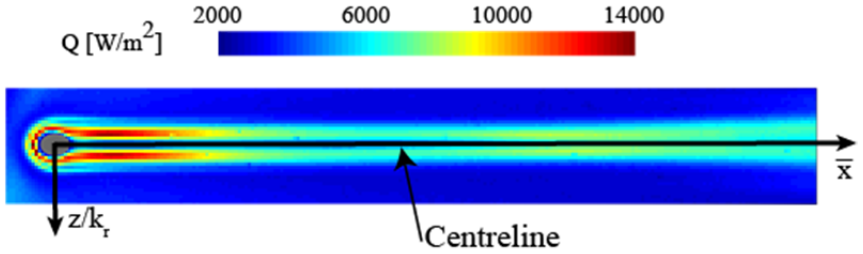

Figure 6.3. Heat flux distribution for the large cylinder positioned at $x_r = 30$ mm and $Re = 14 \cdot 10^6$ m^{-1}. The outline of the roughness elements is shown in grey.

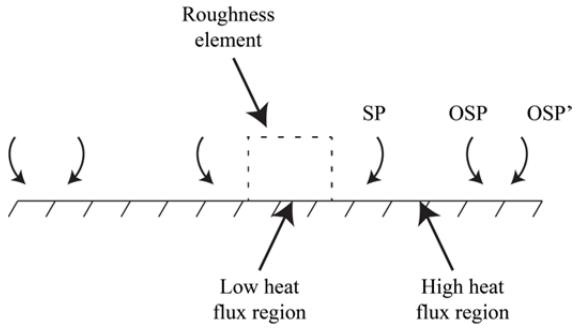

Figure 6.4. Schematic showing the nomenclature used for the streamwise vortices (SP: symmetry plane; OSP: off-symmetry plane) and the relation between the vortices and the heat flux at the centre of the roughness.

When moving in downstream direction towards the roughness element it is observed that directly upstream of the element a region characterized by an increase of the heat transfer is present. In this region the incoming laminar boundary layer separates and depending on the conditions (roughness dimensions, Reynolds number and Mach number) one or multiple vortices are formed (e.g. see the work of Iyer and Mahesh 2013 for hypersonic and Baker 1979 for subsonic flows). These vortices wrap around the element and become streamwise vortices further downstream causing the low and high heat flux streaks that are visible in figure 6.3. In the following the nomenclature adopted by Iyer and Mahesh (2013) is used, which means that the streamwise vortices that are located closest to the symmetry plane (SP) are called SP vortices and the ones located further from the symmetry plane are called off-symmetry plane (OSP) vortices (also see the sketch in figure 6.4). When progressing in downstream direction the SP vortices move closer to the symmetry plane due to the induced velocity by its image vortex and by the low-pressure region that is present in

the wake behind the element (Iyer and Mahesh 2013). Due to the rotation of the SP vortices an upwash is created near the centreline and as a consequence high momentum fluid is moved away from the wall and a local minimum in the spanwise heat flux distribution is measured along the centreline (figure 6.3). Away from the symmetry plane, a counter rotating OSP vortex pair (or two pairs OSP + OPS' depending on the conditions) is present which originates from the vortical system formed upstream. Between the SP and OSP vortices there is a central downwash (figure 6.4) with a consequent increase of the heat flux. In this case, the effect of the induced velocity is to move these vortices away from each other. When moving further downstream, the strength of these vortices decreases and as a consequence the heat transfer at the wall decreases as is clearly visible in figure 6.3.

6.2.2 Streamwise Stanton Number

The streamwise evolution of the Stanton number along the model centreline gives a first indication of how strongly the flow is affected by the roughness element. Although the centreline does not include the high heat flux regions on the side of the roughness element directly, it still provides representative information on the overall state of the flow in the wake. Figure 6.5 shows the Stanton number along the centreline versus the streamwise coordinate ($\bar{x}$, equation 4.26) for all the investigated roughness elements.

In the figures the theoretical laminar (continuous line) and turbulent (dashed line) Stanton number calculated with the reference temperature method (Eckert 1956) are plotted as a reference. For each configuration, the theoretical laminar Stanton number is compared to the streamwise profile that is measured outside of the wake to confirm that the incoming boundary layer is indeed laminar for all Reynolds numbers. For the sake of clarity, in figure 6.5 the out of wake Stanton number development is reported only for the square roughness element since the other elements yield identical results in the limit of the measurement accuracy.

When comparing the Stanton number profiles for a given roughness type for different Reynolds numbers, it can be seen that the Stanton number tends to increase with Reynolds. This can be explained by the fact that the boundary layer thickness (δ) at the roughness location becomes thinner, and therefore k_r/δ increases and the roughness becomes more effective. Following this same reasoning it can be concluded that the roughness is also more effective when it is positioned closer to the leading edge where the boundary layer thickness is smaller. However when the various roughness elements are compared for a given value k_r/δ, it is visible that the Stanton number depends both on the geometry and the frontal area of the element. This effect is especially visible when considering the high Reynolds number case (figure 6.5e and

6.5f). When comparing the square and the large cylinder, the Stanton number clearly shows a different trend when moving downstream from the element. In the range $10 < \bar{x} < 40$ the large cylinder is characterized by a Stanton number that is slightly lower than the corresponding laminar value. This effect is most probably caused by the separated region still present just behind the roughness elements. For the square a higher Stanton number is measured directly downstream of the element. Further downstream in the range $40 < \bar{x} < 70$ the Stanton numbers for the square and the large cylinder are comparable. At $\bar{x} = 70$ the Stanton number starts increasing for the large cylinder and shortly after (at approx. $\bar{x} = 80$) it increases for the square. For both elements the Stanton number slope changes, which indicates the start of the transitional boundary layer that eventually becomes turbulent where the Stanton number reaches its peak value. The transition to turbulence shows a different trend depending on the geometry: the large cylinder shows a larger slope and a higher peak when compared to the square element. Moreover, the large cylinder exhibits a higher Stanton number with respect to the turbulent reference value. These observations confirm that the geometry is a parameter that strongly influences the transition location and the local overheating.

For the small cylinder at the high Reynolds number, in the region directly downstream of the element ($10 < \bar{x} < 40$) the Stanton number is higher compared to the large cylinder and square. This suggests that the vortical structures at the edge of the roughness (SP vortices) are positioned closer to the centreline and therefore the local heat transfer is increased at this location. Furthermore, the transition to turbulence is less pronounced and the associated heat transfer pattern, represented by the s-shaped curve, has the same shape compared to the large cylinder although it reaches a lower peak value. Thus, in the present experiments both the shape and the frontal area influence the transition to turbulence. More specifically, it was found that the shape influences the transitional pattern while the frontal area influences both the transition location and the maximum value of the Stanton number. Similar observations can be made for the medium Reynolds number shown in figure 6.5c and 6.5d, where the same effects can be observed for the different roughness elements. Compared to the high Reynolds number, the medium Reynolds number has a lower maximum Stanton number when compared to the corresponding turbulent levels. For the low Reynolds number and $x_r = 30\,\text{mm}$ (figure 6.5a) the Stanton number decreases almost monotonically when moving downstream revealing that transition does not take place and the boundary layer remains laminar in the measurement area. However, the overall Stanton number is still higher than the predicted laminar one due to the presence of the streamwise vortices that influence the heat transfer at the centreline. For the lower unit Reynolds number and $x_r = 60\,\text{mm}$ (figure 6.5b) the Stanton number values in the wake centreline are almost comparable with the laminar predictions. It can be argued that the vortical structures are weak and they do not strongly influence the heat

transfer. Particularly, for the low Reynolds number transition does not take place and the Stanton number decreases when moving downstream while for the medium Reynolds number a weak increase can be detected. It suggests that in the latter case, the boundary layer is transitional but it is still far away from becoming fully turbulent.

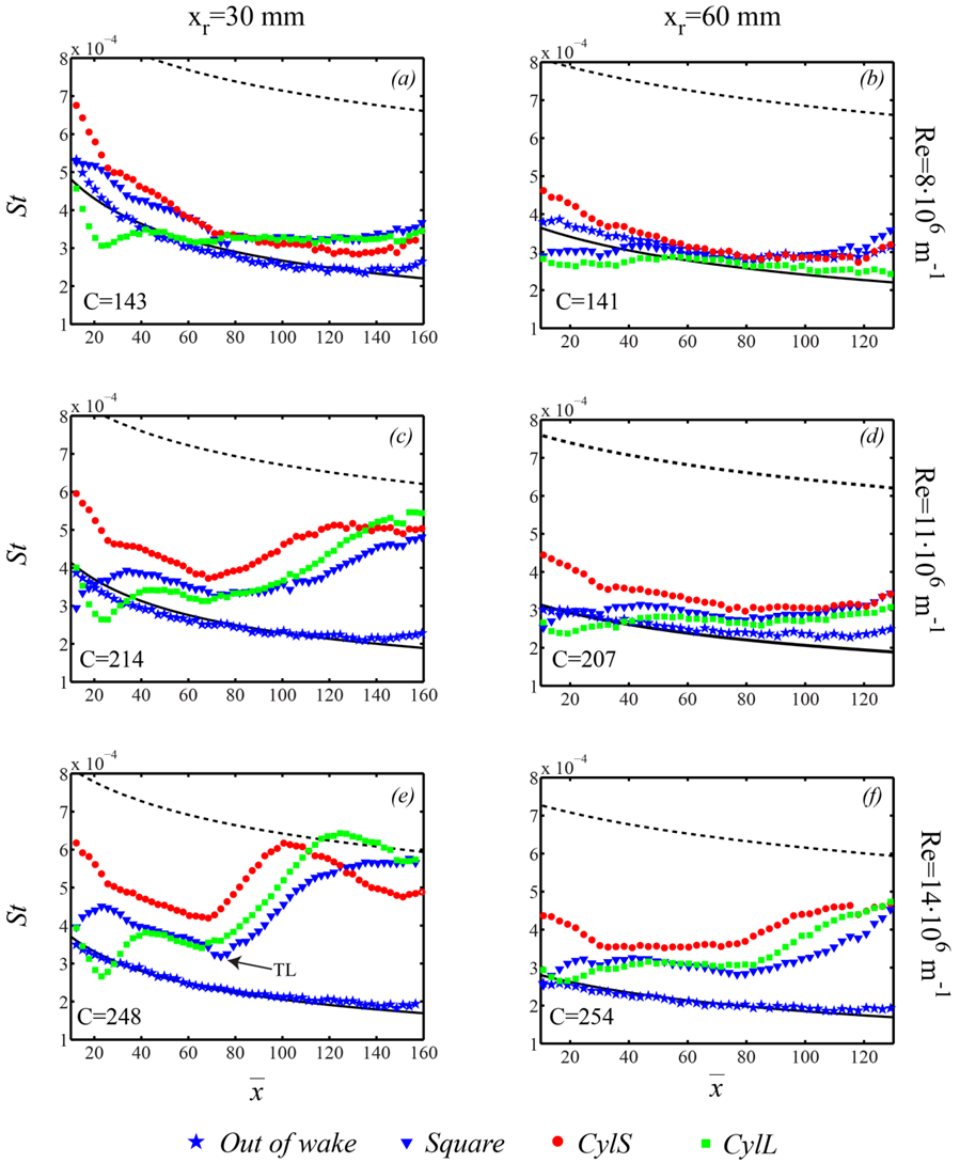

Figure 6.5. Streamwise Stanton number for $x_r = 30$ mm (a-c-e) and $x_r = 60$ mm (b-d-f). Each row displays the Stanton number for a given unit Reynolds number: $Re = 8 \cdot 10^6\ m^{-1}$ (a-b), $Re = 11 \cdot 10^6\ m^{-1}$ (c-d), $Re = 14 \cdot 10^6\ m^{-1}$ (e-f). TL indicates the estimated transition location. C is the constant evaluated from the Shuttle Roughness Criteria.

The above results agree well with the predictions obtained using the Shuttle Roughness Criteria. At low Reynolds number the roughness elements do not trip the boundary layer while at the high Reynolds number transition occurs somewhere downstream of the element so that they can be categorized as being critical, see figure 6.2. It is also interesting to highlight that the SCR predicts that the roughness is weakly effective for the medium Reynolds number when they are positioned at $x_r = 60$ mm. This is confirmed by the experiments since, for these conditions far downstream of the element a weak increase of the Stanton number is measured (figure 6.5d).

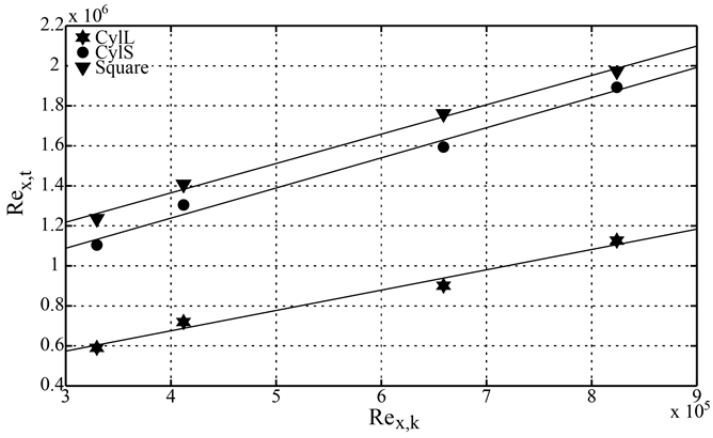

Figure 6.6. Reynolds number evaluated at the estimated transition ($Re_{x,t}$) location versus the Reynolds number evaluated at the roughness location ($Re_{x,k}$). The continuous line is a linear fit through the data points.

According to Schneider (2008), it is possible to give a clear definition of transition location but it is difficult to detect the exact location in practice. Therefore in order to quantify the transition location in the following discussion, it is defined as the point along the centreline streamwise coordinate, at which the Stanton number exhibits a local minimum followed by a rapid increase. For an example, see figure 6.5e where TL indicates the transition location. Following the suggestion by Tirtey et al (2011) the Reynolds number evaluated at the transition location is plotted versus the Reynolds number evaluated at the roughness location in order to compare the roughness element geometries and sizes. Tirtey et al (2011) reported that no clear trend could be observed between both Reynolds numbers, which they related to the large uncertainty in the measurements. For the current experiments the Reynolds number based on the transition location depends almost linearly on the Reynolds number evaluated on the roughness location, see figure 6.6. The slope of the trend line for small cylinder and the square are practically the same while the slope for the large cylinder it is slightly less, indicating that for this size and geometry the effect of the Reynolds number is reduced. Furthermore, the figure clearly shows that the large cylinder is the most effective in

tripping the boundary layer since it is located well below the others. Generally, it confirms that the cylindrical shape is more effective in perturbing the boundary layer compared to the square. It may be related to the fact that for a given frontal area the SP vortices are closer to each other just behind the roughness for the cylinder roughness element becoming even more susceptible to transition.

6.2.3 Wake Topology

IR thermography returns the 2D heat transfer map on the model surface, which helps to get a better understanding of the boundary layer topology upstream and downstream of the roughness elements. In figures 6.7 and 6.8 the K contour (as introduced in equation 6.1) is displayed for all the roughness elements at the medium and high Reynolds number for $x_r = 30$ mm and $x_r = 60$ mm respectively. The low Reynolds number results are not shown because for these conditions the roughness elements are unable to trip the boundary layer (see the discussion in the previous section). From the top to the bottom the large cylinder (figures 6.7a-b and 6.8a-b), the small cylinder (figures 6.7c-d and 6.8c-d) and the square elements (figures 6.7e-f and 6.8e-f) are plotted. In the figures the outlines of the roughness elements are shown in grey.

As was already discussed, directly upstream of the roughness element one or multiple vortices are formed depending on the flow conditions and on the roughness element geometry and dimensions. For the flow around an hemispherical bump placed in an incoming laminar boundary layer at Mach numbers 3.37, 5.26 and 8.23 Iyer and Mahesh (2013) reported that upstream of the roughness a vortex system can be formed consisting of 4 or 6 vortices depending on the Reynolds number, the Mach number and D/δ^* ratio where δ^* is the displacement thickness at the roughness location (see figure 1.16 and 1.17). The vortex configuration upstream and downstream of the roughness elements for the Mach numbers 5.26 and 8.23 as computed by Iyer and Mahesh (2013) is shown in figure 6.9. At Mach number 5.26 they detected 6 vortices upstream while at the higher Mach number only 4 vortices were found. They found a good agreement with subsonic experiments carried out by Baker (1979) for incompressible flow past a cylinder placed on a flat plate.

In order to relate the flow fields reported by Iyer and Mahesh (2013) to the present heat transfer results, the expected corresponding low and high heat flux regions are reported in figure 6.9 in red and green and by the K contour spanwise distribution. Figure 6.9a shows the result for Mach 5.26 where a 6-vortex system upstream was found, the corresponding heat flux map should show four peaks and three valleys. In figure 6.9b, where the upstream separation region is characterized by 4 vortices, only two peaks and one valley are expected. Based on these considerations it is possible to relate the upstream vortex configuration to the downstream wall heat flux distribution.

By plotting the spanwise K just behind the roughness elements (similar to the sketch in figure 6.9 right), it is possible to extract information about the system of vortices that originate from upstream. For example, a local maximum in the spanwise heat transfer profile indicates the presence of downwash between the vortex pair.

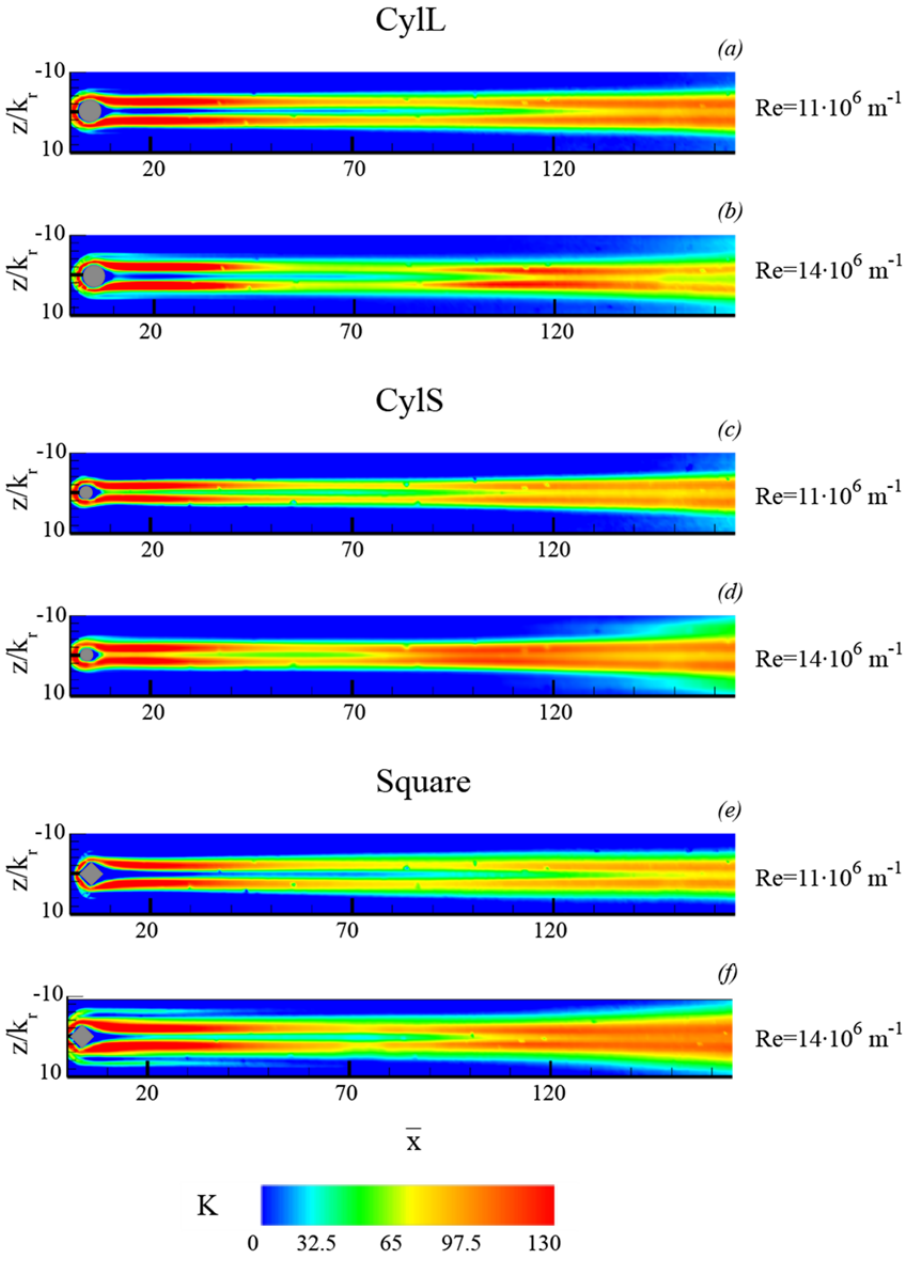

Figure 6.7. K contour for the investigated roughness elements located at $x_r = 30$ mm and at $Re_{unit} = 11 \cdot 10^6\ m^{-1}$ and $Re_{unit} = 14 \cdot 10^6\ m^{-1}$.

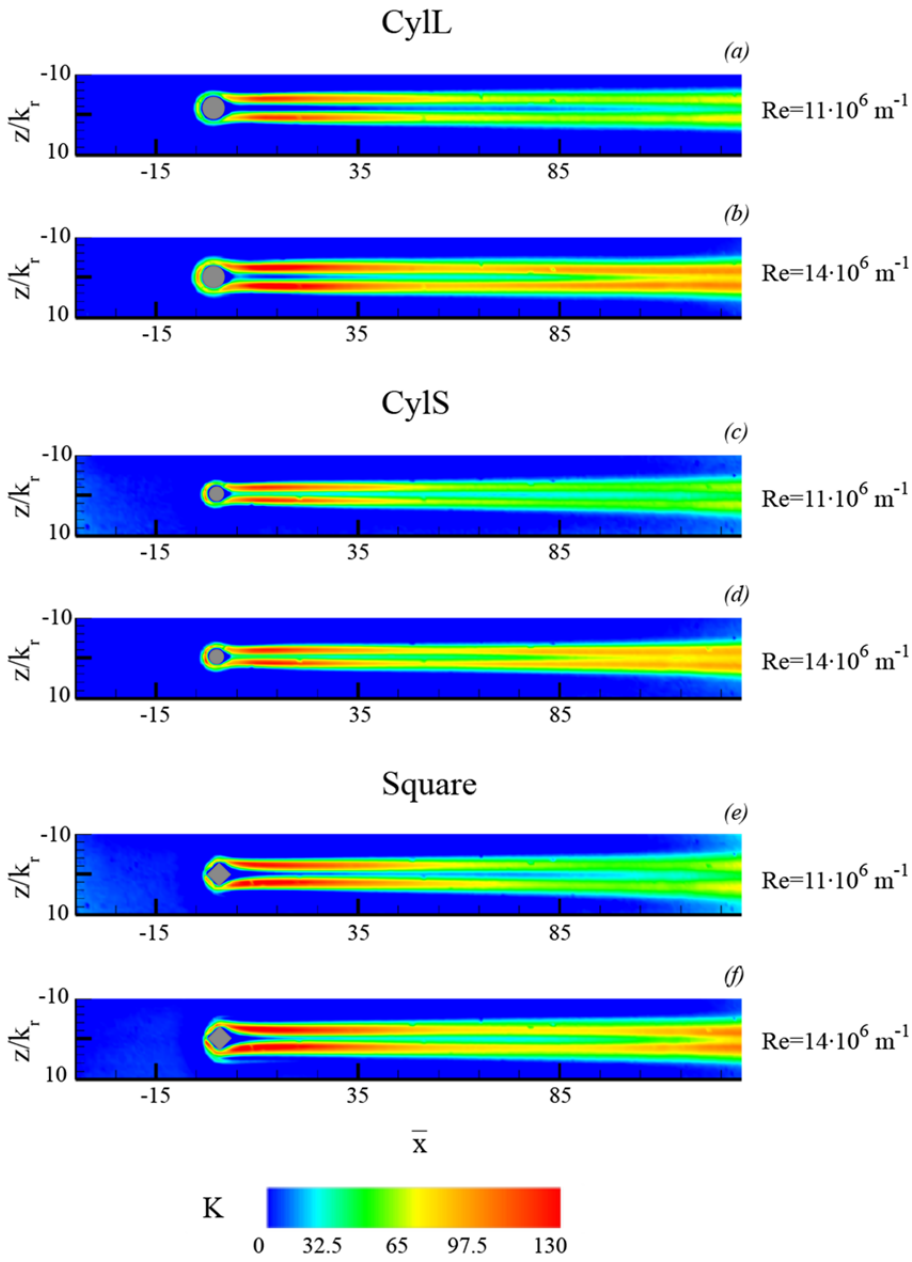

Figure 6.8. K contour for the investigated roughness elements located at $x_r = 60$ mm and at $Re_{unit} = 11 \cdot 10^6$ m^{-1} and $Re_{unit} = 14 \cdot 10^6$ m^{-1}.

The spanwise K distribution at $\bar{x} = 9$ is reported in figure 6.10 for the investigated roughness elements at the high Reynolds number. In case of the small cylinder element two peaks are found which can be associated to a 4-vortex system upstream. Looking at the small cylinder a weak trace of two secondary small peaks (z/k_r =-4.5 and z/k_r

=4.5) is visible but the K distribution along the spanwise direction is assumed to be closer to the one corresponding to figure 6.9b where only a weak effect due to secondary vortices may be present. For the square and the large cylinder elements two additional smaller but clearly visible peaks are found at approximately z/k_r = 6, 7 and z/k_r = -6, - 7 respectively, which hints at the presence of a 6-vortex system.

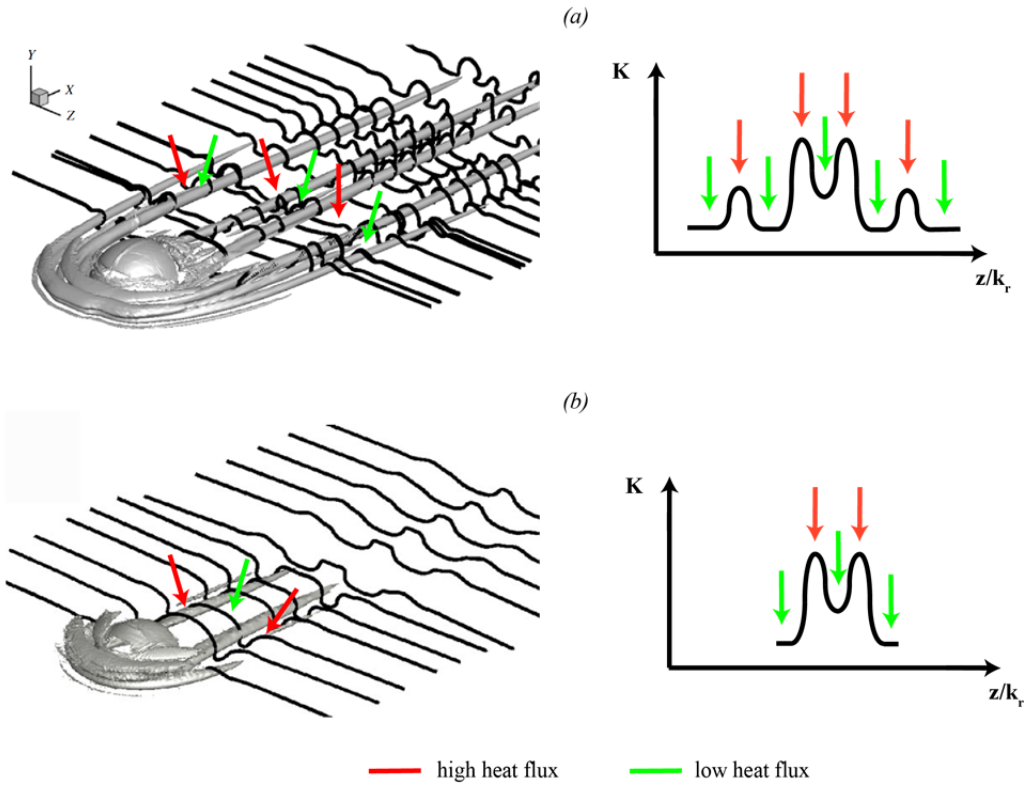

Figure 6.9. Left: isocontours of the Q criterion with instantaneous vortex lines for Mach 5.26 (a) and Mach 8.23 (b). Right: sketch of the expected heat flux distribution along the spanwise direction based on the estimated experimental spatial resolution and accuracy. Green arrows point low heat flux regions while red arrows point high heat flux regions.

With the aim to relate the system of vortices upstream of the roughness elements to the flow conditions and the roughness dimensions, the number of upstream vortices are plotted as a function of Re_D/M and $(D/\delta^*)(k_r/\delta)$ in figure 6.11. In the same figure the data reported by Iyer and Mahesh (2013) are plotted with labelled black squares. The non-dimensional parameters are chosen similarly to the parameters introduced by Baker (1979) (Re_D, D/δ^*) however with a modification based on the SRC. From the analysis of the figure it can be argued that for approximately $(D/\delta^*)(k_r/\delta) < 2$ a 4-vortex system is detected while for higher $(D/\delta^*)(k_r/\delta)$ a 6-vortex system is present. The 6-vortex system becomes stronger and more pronounced

(looking at the heat transfer footprint) for increasing $(D/\delta^*)(k_r/\delta)$. Iyer and Mahesh (2013) report that by increasing $(D/\delta^*)(k_r/\delta)$ further it even becomes unsteady.

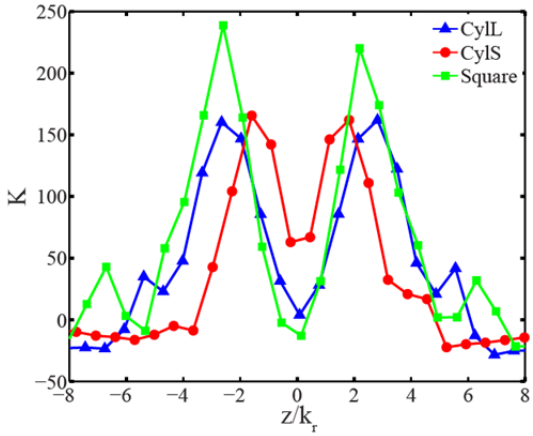

Figure 6.10. K profile at $\bar{x} = 9$ and $Re_{unit} = 14 \cdot 10^6\ m^{-1}$ for the three roughness elements positioned at $x_r = 30$ mm.

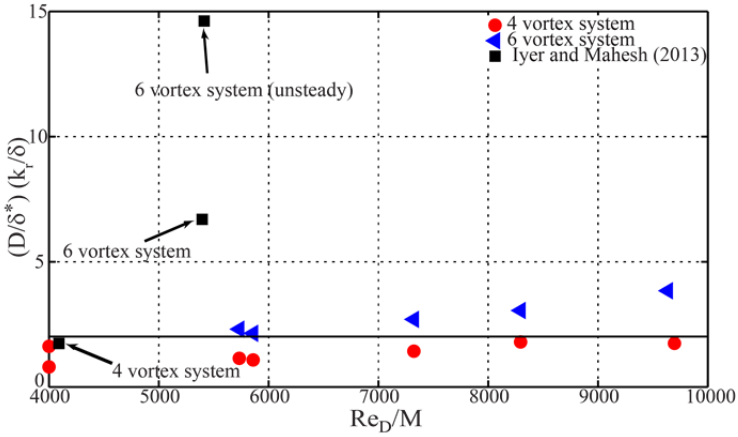

Figure 6.11. Number of vortices upstream of the roughness elements: the red circle represents 4-vortex system while the blue triangle the 6-vortex system. The black square symbol represents data obtained by the numerical simulation performed by Iyer and Mahesh (2013).

When moving downstream behind the roughness element the evolution of the streamwise vortices becomes the most relevant feature in the flow field. From figures 6.7 and 6.8 it is clear that directly behind the roughness element there is a localized region of high heat transfer that is characterized by large values of K. It is visible that when going further downstream, the streaks expand towards the symmetry plane and the K intensity decreases gradually. Following Iyer and Mahesh (2013), the reduction in the heat transfer rate can be mainly associated to the weaker SP vortices that are more susceptible to breaking down and induce transition due to the central upwash.

At a certain location, depending on the roughness geometry, position and unit Reynolds number, the flow undergoes transition (defined as the location where the slope of the Stanton number profile in the centreline increases). The onset of transition is also reflected in the heat transfer footprints of the vortical structures; first the intensity of the streaks becomes stronger when moving downstream until the boundary layer becomes turbulent and further downstream the streaks are less pronounced. The footprints of the vortices are still clear for all the investigated configurations also in the fully turbulent regions. This suggests that some coherent vortical structures are still present in the flow.

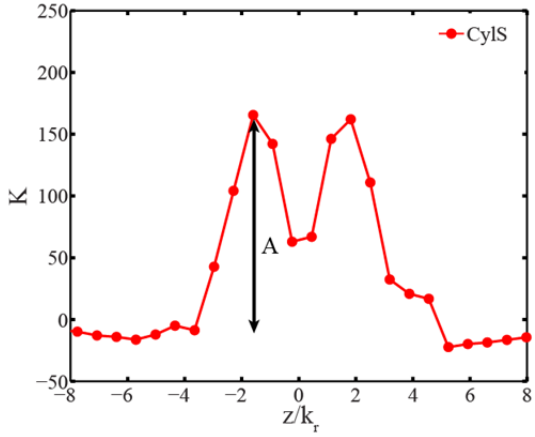

Figure 6.12. Amplitude at $\bar{x} = 9$ and $Re_{unit} = 14 \cdot 10^6\ m^{-1}$ for the small cylinder positioned at $x_r = 30$ mm.

Starting from the transition location and moving downstream the wake width increases. From figures 6.7 and 6.8 in can be inferred that the spreading angle of the wake ranges between 2° and 2.5° for all the investigated configurations. These data are in agreement with Fischer (1972) who established that the lateral turbulent spreading angle at Mach number equal to 6.5 is less than 3°.

The spanwise maximum heat transfer rate measured downstream of the roughness elements with respect to the unperturbed one is the most relevant parameter in the analysis of the mean flow since it represents the flow perturbation due to the presence of the element. To quantify the perturbation in the spanwise K distribution, the amplitude A (figure 6.12) is defined as one half of the maximum spanwise variation of K

$$A(x) = \frac{1}{2}\left(K_{max}\left(\bar{x}, \frac{z}{k_r}\right) - K_{min}\left(\bar{x}, \frac{z}{k_r}\right)\right) \qquad (6.2)$$

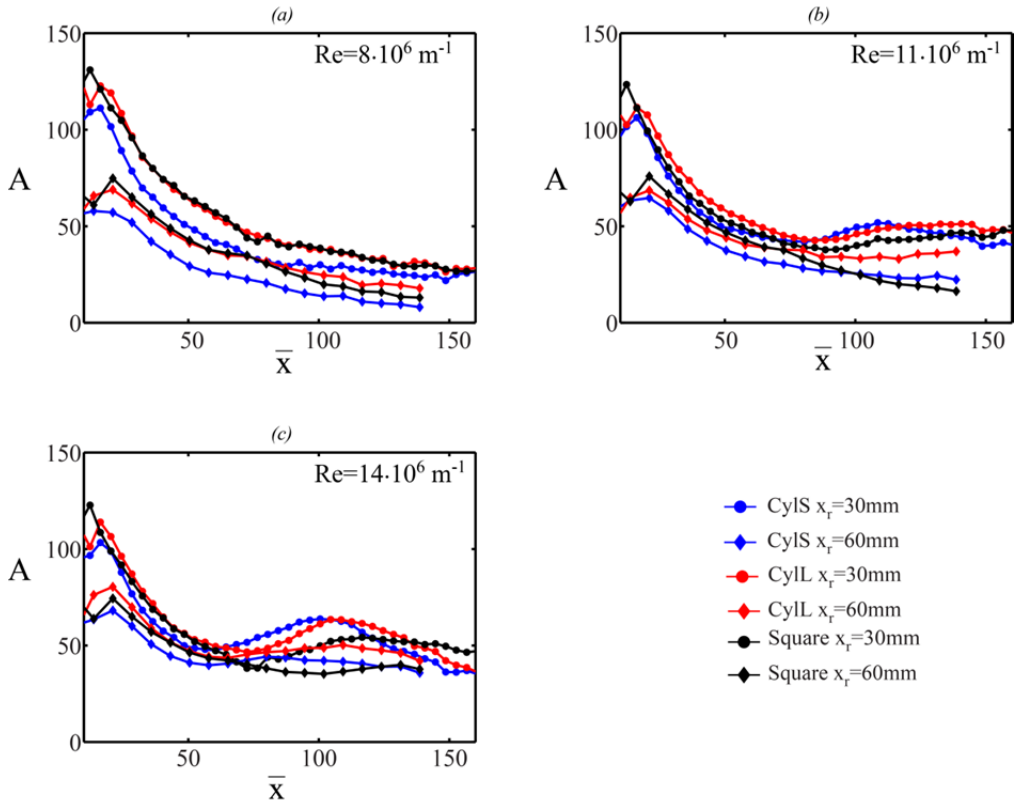

Figure 6.13. Streamwise amplitude evolution at $\mathrm{Re_{unit}} = 8 \cdot 10^6\ \mathrm{m^{-1}}$ (a), $\mathrm{Re_{unit}} = 11 \cdot 10^6\ \mathrm{m^{-1}}$ (b) and $\mathrm{Re_{unit}} = 14 \cdot 10^6\ \mathrm{m^{-1}}$ (c).

The streamwise amplitude distribution is plotted in figure 6.13 for the low (figure 6.13a), medium (figure 6.14b) and high (figure 6.14c) Reynolds number. Starting from the low Reynolds number (figure 6.13a) it is evident that the amplitude is similar for the larger cylinder and the square elements, which have the same frontal area, while it is smaller for the small cylinder. For this Reynolds number the amplitude decays monotonically for all the roughness elements. A similar behaviour for the velocity amplitude was also reported by Fransson et al (2004) who looked at subcritical roughness elements in a subsonic boundary layer. Furthermore, the elements that are located more upstream show larger amplitude for a given $\bar{x}$ and also the amplitude is larger for a larger frontal area. For the medium Reynolds number (figure 6.13b) a clear dependence on the frontal area can no longer be observed. When moving downstream the amplitude shape becomes similar for all elements in the limit of the measurement accuracy. When the flow undergoes transition an increase in Stanton number and also in K results. After the initial stages of flow development directly downstream of the element where the amplitude follows an exponential decay typical of the transient growth. This was also observed for subsonic speeds by Fransson et al (2004) and

hypersonic speeds by Sharp and White (2014) by measuring the flow velocity for distributed roughness elements. Finally the flow becomes fully turbulent and A becomes nearly constant. This can be better observed in figure 6.13c where at high Reynolds number either the roughness positioned at $x_r = 30$ mm and $x_r = 60$ mm show approximately constant values for A near the end of the measurement domain. Furthermore, roughness elements that are positioned at $x_r = 30$ mm show a region that is characterized by a downstream increase in A which is an indication of local overheating. These peaks are located upstream when compared to elements that are positioned at $x_r = 60$ mm but after that they decreases to a streamwise constant A.

6.3 Conclusions

IR thermography is applied to investigate boundary layer transition induced by discrete roughness elements placed on a flat plate in an incoming laminar boundary layer at a Mach number equal to 7.5. The IR data are analysed by solving a 1D inverse heat transfer method based on a least-squares optimization. Three roughness elements (small and large cylinder, square) that differ in shape and size are investigated at three Reynolds number in order to perform measurements for a range of k_r/δ that varies from 0.5 to 0.9. The measurements highlight that the large cylinder is more effective in tripping the boundary layer with respect to the small cylinder and the square element. From the footprints of the vortical structures just behind the roughness elements information about the system of spanwise vortices upstream of the elements are obtained that are in good agreement with DNS data that are reported in literature. Particularly, for $(D/\delta^*)(k_r/\delta) > 2$ a 6-vortex system is detected instead of 4-vortex system. Lastly, by defining the streak amplitude, A, as one half of the maximum spanwise variation of K it can be observed that the transitional and turbulent regions are characterized by A approximately constant along the streamwise direction.

Chapter 7

The Separated Region Ahead of the Roughness Element

7.1 Experimental Setup

7.1.1 Wind Tunnel Model and Tested Configurations

The measurements are carried out at Mach number equal to 7.5 and $Re_{unit} = 14 \cdot 10^6\ m^{-1}$. The total pressure and total temperature are $p_0 = 28$ bar and $T_0 = 579$ K, respectively. Before the wind tunnel is started the test section and vacuum tank are evacuated to a pressure below 1 mbar.

The wind tunnel model used in the experiments is a planar 5° ramp having a length of 200 mm and a width of 110 mm, it is held from the rear with a sting (figure 7.1). The model used for the PIV measurements and the Schlieren flow visualization is made out of anodized aluminium, while the one used for the heat flux measurements is made out of Makrolon®. Makrolon® is characterized by a relatively low thermal conductivity ($k = 0.20$ W/m K) and a high surface emissivity of $\varepsilon_t = 0.88$ (Schrijer 2010a), which make it very suitable for the application of infrared thermography. The leading edge is accurately finished with a leading edge radius of 50 μm to avoid leading edge instabilities.

A cylinder shaped roughness element with a height (k_r) of 2 mm and diameter (D) of 11.2 mm is placed at x_r = 60 mm downstream of the leading edge. At the location of the element the undisturbed laminar boundary layer thickness (δ) is approximately 1.5 mm (based on Illingworth-Stewartson transformation for a laminar boundary layer, Weigand 2005), resulting in k_r/δ equal to 1.3. The momentum thickness (θ) is 0.18 mm

and the Reynolds number based on it (Re_θ) is equal to 2450. For a summary of the undisturbed boundary layer parameters see table 7.1.

Table 7.1. Laminar boundary layer properties at the roughness location.

Parameter	Quantity
M_∞	7.5
$Re_{unit}(m^{-1})$	$14 \cdot 10^6$
$x_r(mm)$	60
$\delta(mm)$	1.5
$\theta(mm)$	0.18
Re_θ	2450
k_r/δ	1.3

In the current investigation $(D/\delta^*)(k_r/\delta) \approx 12$. Then, according to figure 6.11, a 6-vortex system is expected to be present in the upstream separated region.

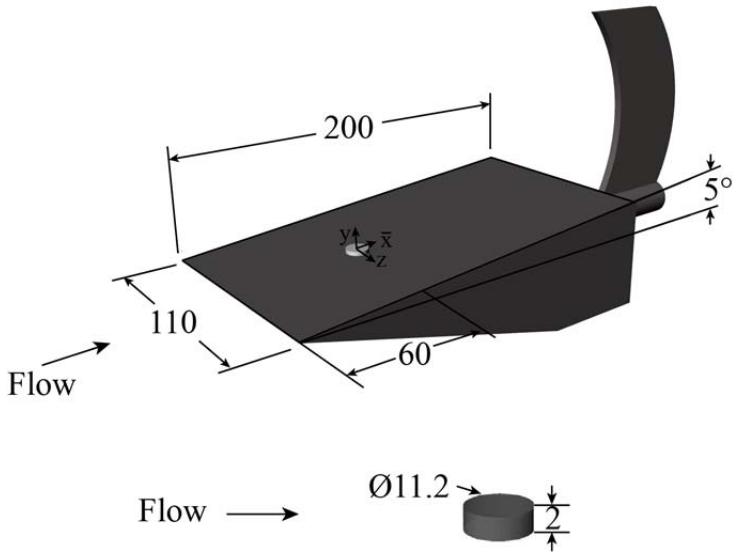

Figure 7.1. Sketch of the wind tunnel mode (top) and the roughness element (bottom). Dimensions are in mm.

7.1.2 Measurement Technique and Data Reduction

7.1.2.1 Infrared (IR) Thermography

The IR thermography measurements are performed using a CEDIP Titanium 530L IR system (see section 3.3 for the camera features). The integration time of the camera

is set to 400 μs and it is operated at a frame rate of 200 Hz. A 25 mm objective at $f_{\#}$ = 2.0 is used yielding a spatial resolution of approximately 2 pixels/mm. The heat flux is computed by solving a 1D IHTP as described in section 4.5.1.

According to the error analysis presented in section 4.5.1 the heat flux error associated to the inverse data reduction is less than 2%. A full error analysis (Moffat 1988) indicates that the Stanton number measurements are accurate to within 8%. It takes into account the error due to the inverse approach, the error in the quantification of the free stream flow properties, the uncertainty in the model physical properties and in the temperature measurements.

7.1.2.2 Planar Particle Image Velocimetry

Planar particle image velocimetry (planar-PIV) is used to map the instantaneous 2D velocity field.

The flow is seeded with Titanium dioxide (TiO_2) particles as described in the tomographic PIV experimental procedure (see section 5.4.1). Illumination is provided by a Quantel Twin BSL 200 laser (Nd:YAG, 200 mJ/pulse) from an optical access positioned on the bottom of the test section. The duration of each laser pulse is shorter than 10 ns, which is short enough not to have particle streaks. The time separation between exposures is set to Δt = 0.4 μs and the laser sheet thickness is smaller than 0.5 mm. The camera and the laser are synchronized with the wind tunnel in order to take a measurement at 30 ms after starting the wind tunnel. Due to the short running time of the wind tunnel, only one velocity measurement is obtained for each test.

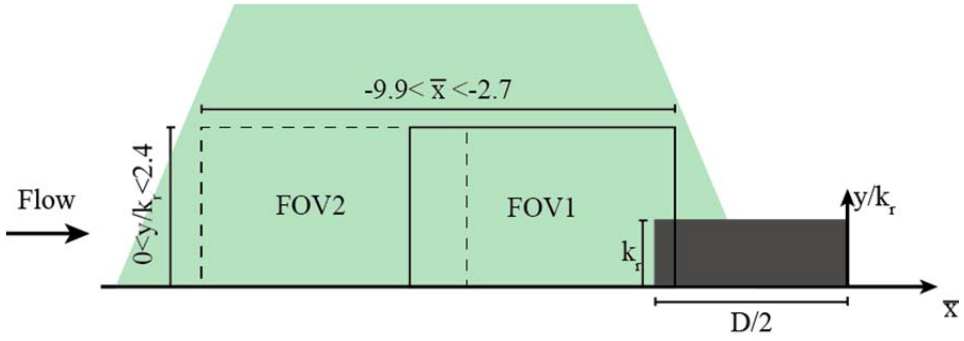

Figure 7.2. Sketch of the experimental setup and of the investigated field of view: FOV1 continuous line, FOV2 dashed line.

The particles images are recorded by a PCO Sensicam QE CCD cameras (1376 × 1040 pixels, 12 bit, 6.7 μm/px) equipped with Nikon 200 mm focal length Micro objectives set at $f_{\#}$ = 11. The average image digital resolution is 118 pixels/mm. The high spatial resolution limits the field of view dimension along the streamwise

direction. For this reason particles images for two overlapping FOVs are acquired (see figure 7.2) thus resulting in a measurement plane approximately equal to 14.4 × 4.8 mm^2. The physical domain (FOV1+FOV2) covers the range $-19.8\,\text{mm} < x - x_r < -5.4\,\text{mm}$ $(-9.9 < \bar{x} < -2.7)$ along the streamwise direction and $0\,\text{mm} < y < 4.8\,\text{mm}$ $(0 < y/k_r < 2.4)$ along the wall normal direction.

The illumination and acquisition system are synchronized with the wind tunnel by means of a LaVision programmable timing unit (PTU 9). The DAVIS 7.2 software is used for data acquisition. A multi-pass algorithm with window deformation and Blackman weighting windows (Astarita and Cardone 2005, Astarita 2006, 2007, 2008) is used to compute the velocity fields. The final interrogation window size is 24 × 32 pixels with an overlap of 75%. Spurious vectors are removed using a median filter (Westerweel and Scarano 2005) and replaced through linear interpolation of surrounding vectors.

Statistical properties of the flow are inferred from an ensemble of 100 wind tunnel runs for each FOV (and thus also image pairs).

The parameters relevant for the PIV setup are reported in table 7.2.

Table 7.2 PIV parameters.

Parameter	Quantity
Measurement plane	14.4 × 4.8 mm^2
Interrogation window	24 × 32 pixels 4.92 × 3.69 mm^2
Interrogation window overlap	75%
Digital resolution	118 pixels/mm
Vectors per field	211 × 123
Δt	0.4 μs

The uncertainty in displacement, related to the interrogation area size, is the main contribution to uncertainty in velocity. For the given particle size (approximately 3 pixels), image noise, displacement field and number of available samples the uncertainty in the mean velocity field is found to be approximately 1% while the uncertainty in the turbulent statistics is 7%.

7.1.2.3 Schlieren Flow Visualization

A Z-type Schlieren system (Settles 2001) is used so that the flow in the test section of HTFD may be qualitatively visualized. A high speed Imager Pro HS 4M (2016 × 2016 pixels, 12 bit, 11 μm/px) camera operated at a frame rate of 1 kHz with an exposure time of 10 μs is used for the video capture. The achieved spatial resolution

is approximately 13 pixels/mm. A continuous light source is used. The diameter of the pinhole is around 1 mm. A pair of concave mirrors with focal length of 2.5 m is used to generate the parallel beam of light that passes through the test section, and then refocuses at the knife-edge located in front of the high speed camera.

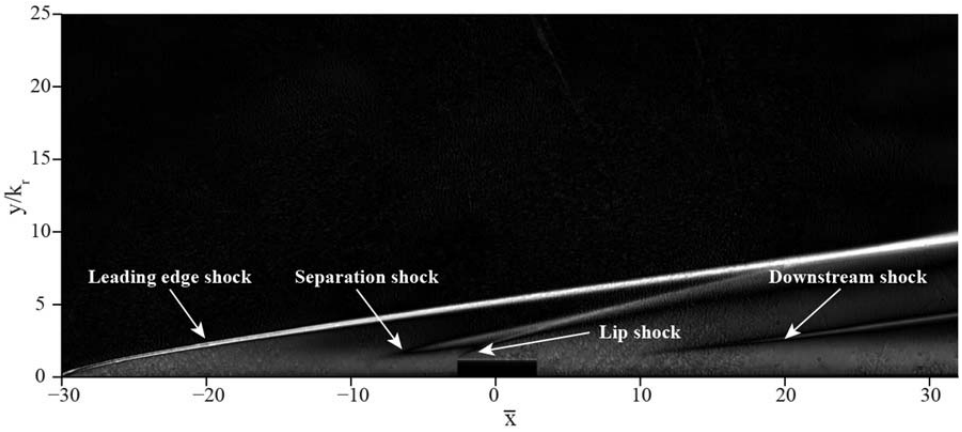

Figure 7.3. Schlieren visualization of the flow field perturbed by the cylindrical roughness element.

7.2 Experimental Results

7.2.1 Mean Flow Organization

The analysis of the mean flow field starts with the Schlieren flow visualization (figure 7.3) because it gives a first general description of the effect of the cylindrical roughness. In addition to the leading edge shock (the measured shock angle is approximately 10.5° in agreement with the theoretical prediction of 11°), there are a separation shock, a lip shock formed on the upper edge of the roughness and a last compression shock downstream of the protuberance. As a matter of fact, following Lightill (1953), the cylindrical roughness element represents a sufficient large compressive disturbance that causes the separation of the boundary layer with reversed flow at the surface. In the resulting modified external flow the pressure begins to rise ahead of the separation point, and separation results there too. This upstream effect can be partly ascribed to the fact that a disturbance leading to a positive pressure gradient causes the boundary to thicken and to curve slightly upstream. As a consequence, the pressure increases slightly upstream causing a further thickening of the boundary layer. The process repeats itself and the pressure gradient decays moving upstream. Moreover, separation constitutes a so large disturbance that causes the presence of a detached shock wave (separation shock). The separation point spreads upstream until the dead-air region is sufficiently slender to cause no further separation ahead of it. Since the region upstream of the protuberance is characterized by a recirculation

region, the roughness can be classified as supercritical (Estruch-Samper et al 2010, Kumar et al 2014).

On the front edge of the roughness element a lip shock is present. The separation shock interacts with the lip shock at approximately $\bar{x} = 2.8$ forming a lambda shaped-like shock. The compression due to the shock is followed by an expansion on the rear edge, which again is followed by a compression represented by the downstream shock (Marxen et al 2010). The expansion downstream of the roughness leads to an acceleration of the flow in the free stream. This acceleration causes the streamlines to turn towards the wall after they have been deflected away from the wall by the roughness. Finally, downstream of the roughness the downstream shock causes the streamlines to become roughly parallel to the wall again.

The downstream shock angle respect to the wall is approximately 8° confirming that the shock is weak. As a matter of fact, the shock angle is roughly in agreement with the Mach angle ($\mu_M = 8.9°$) evaluated assuming that the Mach number downstream of the roughness is equal to the one after the leading edge shock ($M_e = 6.48$). The assumption comes from the fact that the Mach number first reduces through the separation and the lip shocks and then increases due to the acceleration of the flow. However, the difference between the theoretical value and the measured one may be ascribed to the fact that the shock angle should be based on the local streamlines direction not available from the experimental data.

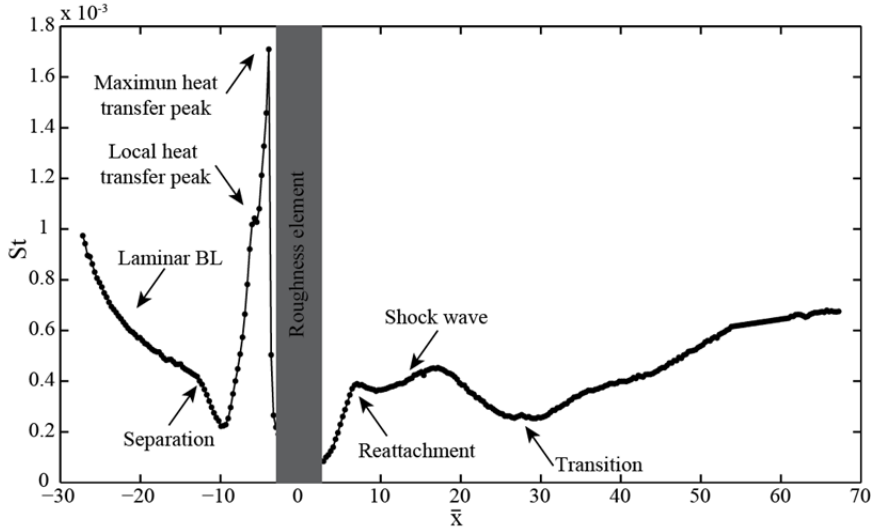

Figure 7.4. Centreline Stanton number distribution.

In order to confirm the presence of the separated region upstream of the protuberance the streamwise Stanton number along the centreline is plotted in figure

7.4. As a matter of fact, moving downstream the Stanton number first decreases, as predicted by the reference temperature method for a laminar boundary layer (Anderson 2006); afterwards, it shows a strong drop starting from approximately $\bar{x} = -12.9$ (which indicates the incipient separation region), it reaches a local minimum at $\bar{x} = -9.9$ and then it rapidly increases. Here, a first local maximum ($St = 1.05 \cdot 10^{-3}$) is measured at approximately $\bar{x} = -5.8$, while the maximum Stanton number at the centreline ($St = 1.75 \cdot 10^{-3}$) is measured at $\bar{x} = -3.9$. Then, the Stanton number suddenly decreases just upstream of the protuberance. Moving behind the protuberance, a second recirculation bubble is detected and the flow reattaches at about $\bar{x} = 6.7$ where the Stanton number exhibits a local maximum followed by a weak decrement. Then, the Stanton number increases again at $\bar{x} = 9.4$ due to the fact that the flow accelerates behind the roughness and the streamlines are deflected towards the wall. At approximately $\bar{x} = 17.4$ the streamlines are almost parallel to the model surface and the Stanton number decreases due to the boundary layer thickening, it reaches a minimum at approximately $\bar{x} = 28.1$ where transition starts and it keeps increasing until the end of the model. The wind tunnel model is not long enough to detect a fully turbulent region.

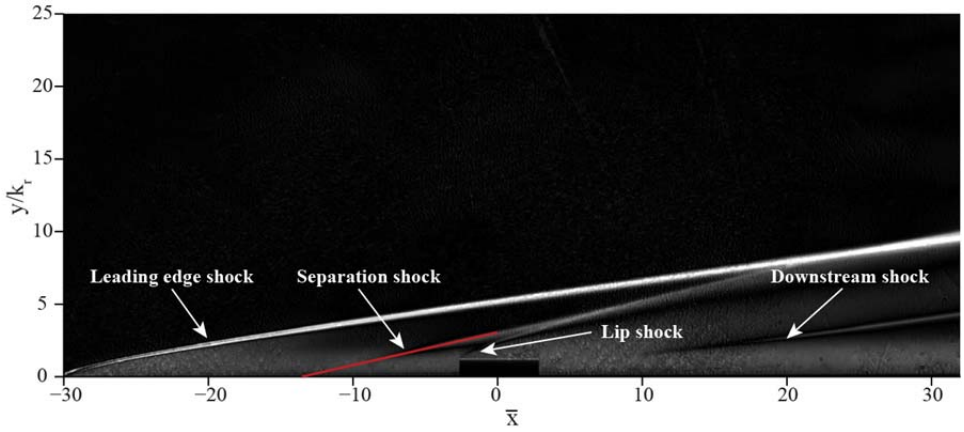

Figure 7.5. Schlieren visualization of the flow field perturbed by the cylindrical roughness element. The red line represents the extrapolation of the separation shock until the wind tunnel model.

From the previous discussion it is evident that the length of the separated region downstream of the protuberance is almost one half of the one upstream. Moreover, the length of the separated region upstream is approximately 10 times the roughness element height. These results are in agreement with the DNS data provided by Marxen et al (2010). Kumar et al (2014) provided slightly different results for the upstream separation length ($L_{sep} = 11k_r$) by looking at different supercritical protuberances by means of Schlieren flow visualizations. They obtained the separation length by extrapolating the separation shock until the wind tunnel model surface. Following the

same approach (figure 7.5) it is found that the separated region starts approximately at $\bar{x} = -13.5$ thus resulting in $L_{sep} = 10.7k_r$. The difference between the separation lengths estimated by means of the heat flux measurements and the flow visualization may be ascribed to the fact that L_{sep} is overestimated by the linear extrapolation.

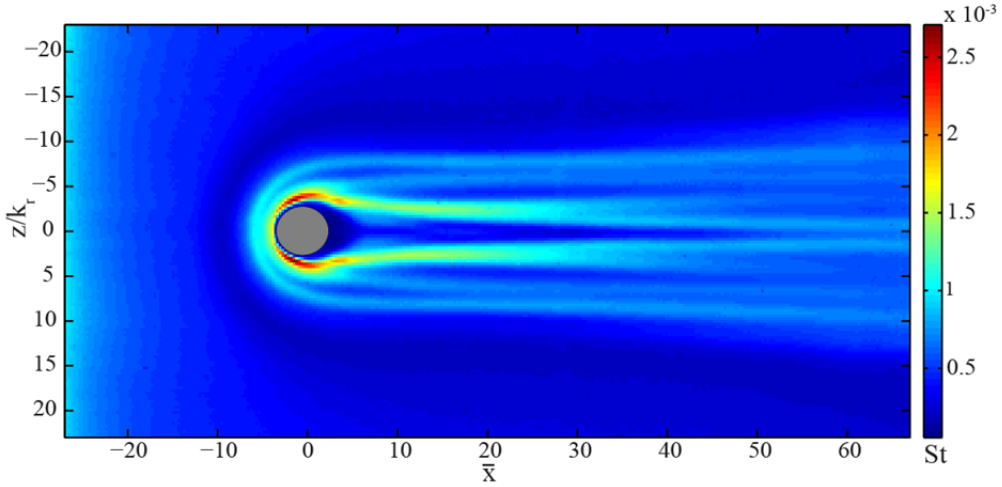

Figure 7.6. Stanton number distribution on the wind tunnel model surface.

In the separated region a complex system of vortices may be present depending on the flow conditions (figure 6.11). In the current investigation $(D/\delta^*)(k_r/\delta) \approx 12$ and a 6-vortex system is expected. This assumption is confirmed by the Stanton number distribution reported in figure 7.6 and the spanwise distribution behind the protuberance at $\bar{x} = 9$ plotted in figure 7.7. As a matter of fact, the vortex formed upstream wrap around the protuberance and develop downstream as streamwise vortices that generate alternating high and low heat flux streaks depending on the vortex rotation. In particular, six heat flux local maxima (figure 7.7) are detected that, according to figure 6.4, are created in the downwash region between two counter-rotating vortices. Moving downstream, the SP vortices split and the tracks of secondary structures are clearly detected starting from $\bar{x} = -28$. Here, the centreline Stanton number increases indicating the incipient transition, while the wake diverges. The vortices across the centreline create an upwash between them and they move towards each other moving downstream. On the contrary, when the vortices have a downwash they move away from each other. These features are extremely visible in figure 7.6 by looking at the track of the high and low Stanton number streaks. Furthermore, it can be inferred that the spreading angle of the wake is about 3.1°. This data is in agreement with Fischer (1972) who established that the lateral turbulent spreading angle at Mach number equal to 6.5 is less than 3°.

The Stanton number distribution on the wind tunnel model surface shows that the maximum heat transfer rate is present just around the protuberance according to Estruch-Samper et al (2010). For a supercritical roughness element Hung and Patel (1984) and Estruch-Samper et al (2010) stated that the maximum Stanton (St_{max}) might be present in front of the roughness along the centreline. In the current investigation the St_{max} is detected on the side at $\bar{x} = -2$ and it is approximately equal to $2.7 \cdot 10^{-3}$. This position and the intensity are well in in agreement with the engineering correlation provided by Estruch-Samper et al (2010) reported in figure 1.14.

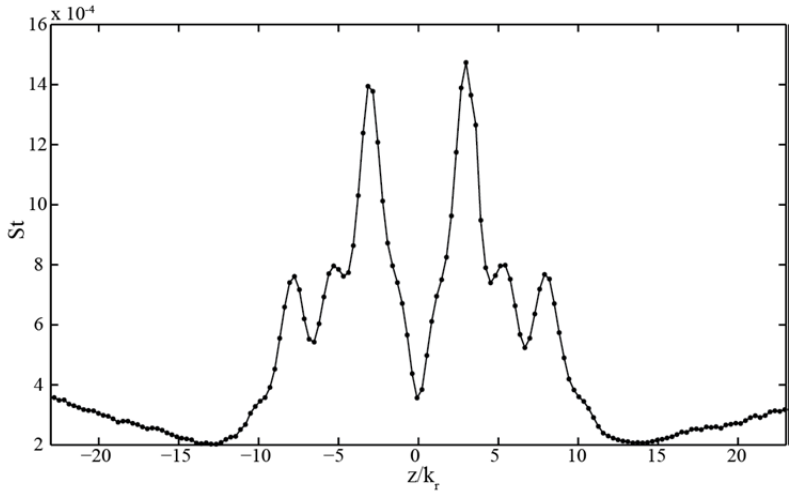

Figure 7.7. Spanwise Stanton number distribution on the wind tunnel model surface at $\bar{x} = 9$.

7.2.2 The Upstream Separated Region

The separated region upstream of the cylindrical protuberance is further investigated by means of PIV in order to describe the velocity field in the symmetry plane of the recirculation region. The mean flow field is plotted in figure 7.8 where the most relevant flow features are visualized through the streamlines.

The thickness of the separated region increases when moving from $\bar{x} = -10$ to the protuberance location ($\bar{x} = -2.8$). At $\bar{x} = -6.6$ a first counter rotating vortex pair is detected (figure 7.9). In the separated region it is expected that the vortices are almost aligned along the streamwise direction, while in the current investigation the axes of both vortices are located almost at the same streamwise coordinate. However, from the computations performed by Subbareddy et al (2014) it can be argued that, varying the flow conditions, the clockwise rotating vortex tends to get ahead of the anti-clockwise rotating one. Anyway, their disposition is such that they do not create any appreciable downwash or upwash between them thus confirming the absence of a

local heat transfer peak on the wind tunnel model surface along the centreline in figure 7.4.

Afterwards, a second pair of vortices is detected with axes at $\bar{x} = -6.2$ and -5.9 respectively. The vortex pair creates a downwash at approximately $\bar{x} = -6$ where an increase in the heat transfer is expected. As a matter of fact, in figure 7.4 a local peak of the Stanton number is detected at approximately $\bar{x} = -5.8$. The small difference between the results expected from the two experiments may be inferred to the different wind tunnel models, the small imprecision in the location of the roughness element and to the fact that the velocity data are available until $y/k_r = 0.1$.

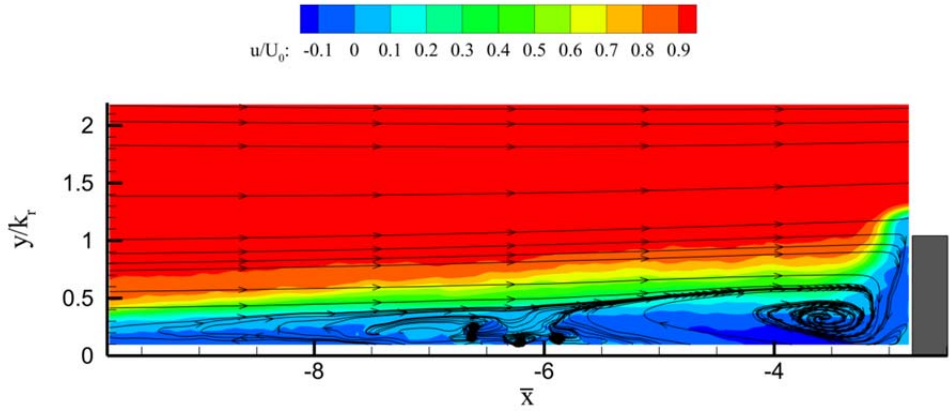

Figure 7.8. Mean velocity field measured by PIV.

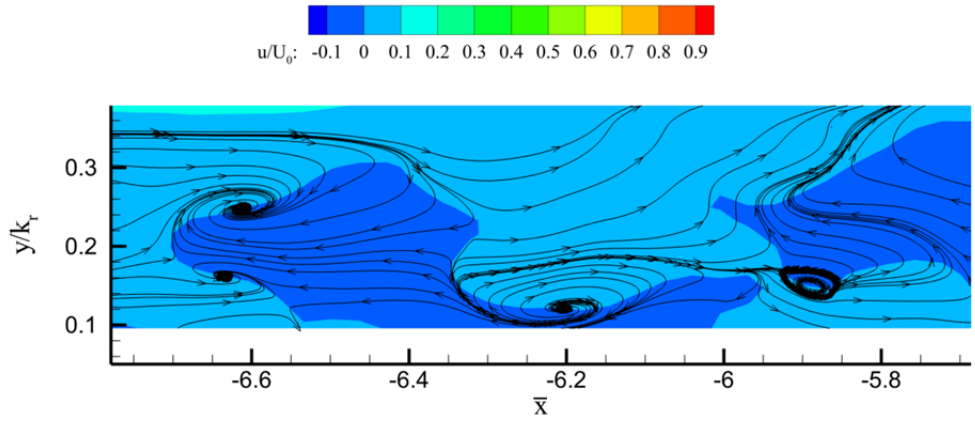

Figure 7.9. Zoom of the mean velocity field in the range $-6.67 < \bar{x} < -5.68$.

Moving closer to the roughness, the primary reattachment vortex is identified. The vortex axis is located approximately at $\bar{x} = -3.7$. The effect of this vortex is to move

high momentum fluid to the model surface causing the high heat transfer peak in the centreline Stanton number distribution (figure 7.4). The measurements suggest that the vortex comes in contact with the model surface at approximately $\bar{x} = -3.6$ while the peak in the heat transfer is measured at $\bar{x} = -3.9$. Finally, extremely close to the cylindrical protuberance a small clockwise rotating vortex is detected. In this case the spatial resolution is not enough high to correctly measure such a small structure. However, the computations performed by Subbareddy et al (2014) show the presence of this small vortex. Finally, close to the roughness location ($\bar{x} = -2.9$) a strong compression due to the lip shock (figure 7.3) formed on the front edge of the roughness element is evident.

The investigate field of view is not large enough to measure the length of the separated region. In order to estimate the separation length, the iso-line $u/U_0 = 0.05$ is extracted and plotted in figure 7.10 with a continuous line. The value of the iso-line is chosen because it allows extracting a continuous profile along the streamwise direction. As a matter of fact, due to the presence of the complex system of counter rotating vortex pairs, it is impossible to extract the continuous iso-line of the inflection points. The intersection of the linear extrapolation of the iso-line (dashed line in figure 7.10) with the model surface represents a slightly overestimation of the separation length. The linear extrapolation predicts that the separated region starts at approximately $\bar{x} = -14.3$ resulting in a separation length of approximately 11.5 times the roughness height. The estimated separation length is in agreement with the one estimated by means of the heat flux measurements and the Schlieren flow visualization in the limit of the accuracy.

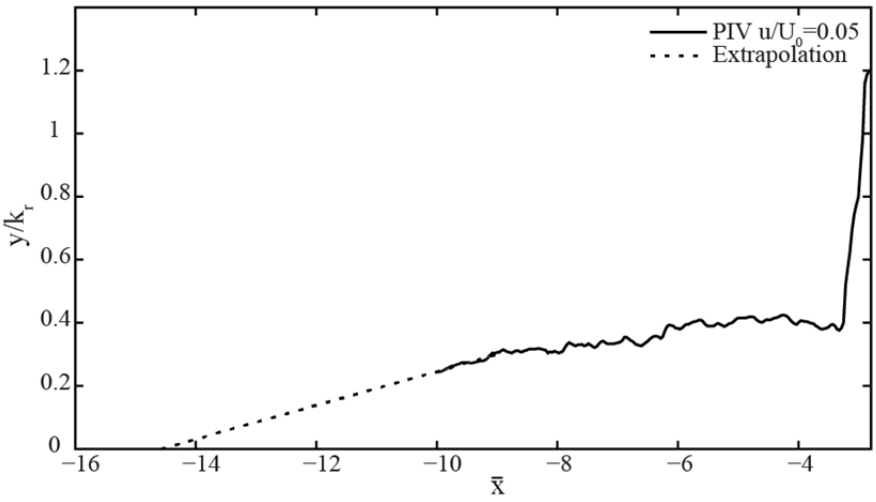

Figure 7.10. Iso-line of $u/U_0 = 0.05$ extracted from the PIV data (continuous line) and extrapolation until the model surface (dashed line).

Finally, the iso-line plotted in figure 7.10 confirms that the separated region is thicker close to the roughness location. In particular, the thickness is almost constant between $-6 < \bar{x} < -4$.

7.2.3 Turbulent Statistics

When a laminar hypersonic boundary layer interacts with a roughness element, possible sources of unsteadiness are due to the unsteady vortex system upstream, shock-induced unsteadiness and shear layer instability (Iyer and Mahesh 2013). The unsteadiness is also observed in incompressible flows (Baker 1979) and depends on the Reynolds number. When the hypersonic boundary layer comes in contact with the roughness element, a shock wave is produced at the wall-normal location corresponding to the sonic line. This shock, which is inherently unsteady, could potentially perturb the flow in the vicinity of the roughness thereby causing the flow to become unstable (Iyer and Mahesh 2013).

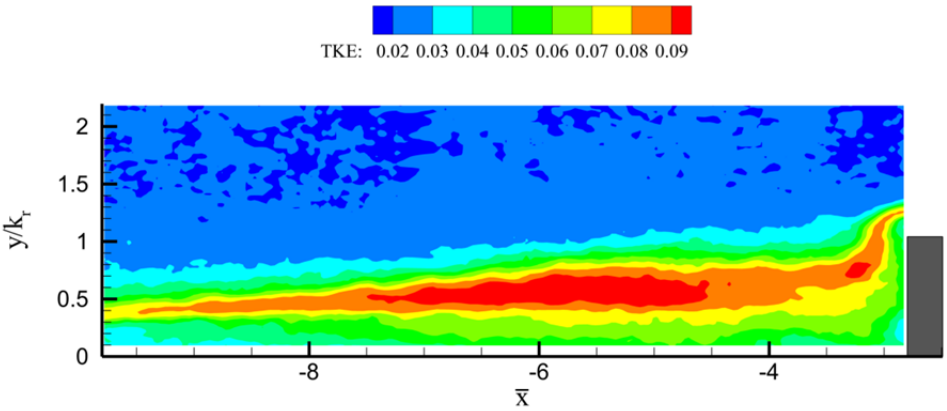

Figure 7.11. TKE distribution upstream of the roughness element.

The above source of unsteadiness are illustrated in figure 7.11 in terms of turbulent kinetic energy $\mathrm{TKE} = \left(\overline{\langle u' \rangle \langle u' \rangle} + \overline{\langle v' \rangle \langle v' \rangle}\right)/U_0^2$. The TKE distribution shows a region of high unsteadiness where the higher concentration of vortices is present. Moreover, the TKE shows a region of reduced unsteadiness close to the protuberance at almost the same location of the small clockwise rotating vortex. It suggests that here a quite steady separated region is present. This assumption may be confirmed by the low Stanton number close to the protuberance (figure 7.4),

Figure 7.12 shows the turbulent kinetic energy (TKE) profile at five upstream locations. The unsteadiness increases moving closer to the protuberance; the maximum unsteadiness (TKE=0.095) is detected approximately at $\bar{x} = -6$ (about 1D from the roughness location) and $y/k_r = 0.6$ indicating that is due to the vortices present in this

region. The shock unsteadiness, represented by the red continuous curve in the figure, is weaker and its peak (TKE=0.08) is located at approximately $y/k_r = 1.4$. In the free stream region, the estimated TKE is approximately equal to 0.02. It is caused by measurements noise and wind tunnel repeatability.

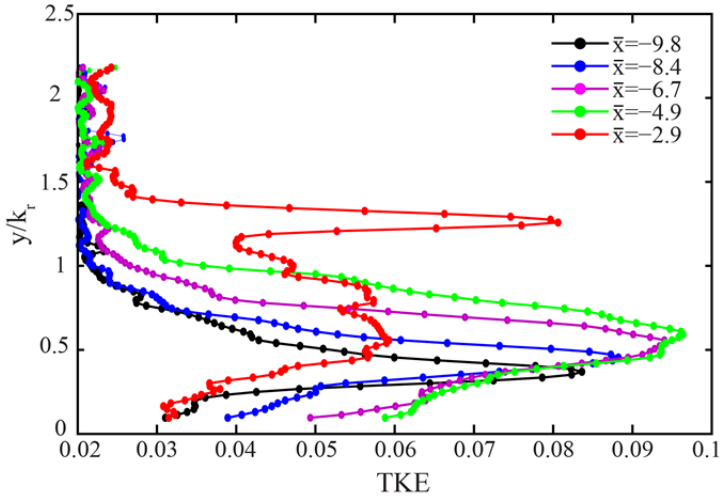

Figure 7.12. TKE profile at several streamwise locations.

7.3 Conclusions

The flow around a supercritical roughness element placed in an incoming laminar boundary layer is investigated with a particular focus on the upstream separated region.

The mean flow organization is firstly investigated by means of Schlieren flow visualization and heat transfer measurements. Data clearly show the formation of a separated region upstream through the presence of a separation shock and a local minimum in the streamwise centreline Stanton number distribution. Furthermore, the maximum heat transfer is located just around the roughness element. The velocity field measurements confirm the presence of three couple of counter-rotating vortex pairs in the recirculation region and their location is in agreement with the location of the local Stanton number maxima.

The velocity field turbulent statistics, analysed through the TKE distribution, show a region of increased unsteadiness at approximately 1 diameter from the protuberance location and it is mainly related to the high vorticity. Furthermore, the measurements confirm that the unsteadiness due to the shock wave formed just in front of the roughness is barely weak.

Chapter 8

The Wake Behind the Roughness Element

8.1 Experimental Setup

8.1.1 Wind Tunnel Model and Tested Configurations

The measurements are carried out at Mach number equal to 7.5, unit Reynolds number of $Re_{unit} = 14 \cdot 10^6\ m^{-1}$. The total pressure and total temperature are $p_0 = 28$ bar and $T_0 = 579$ K, respectively. Before the wind tunnel is started the test section and vacuum tank are evacuated to a pressure below 1 mbar.

The wind tunnel model used in the experiments is a planar 5° ramp having a length of 200 mm and a width of 110 mm (figure 8.1), it is held from the rear with a sting. The model is made out of anodized aluminium and the leading edge is accurately finished with a leading edge radius of 50 μm to avoid leading edge instabilities. The uniformity of the leading edge is verified by measuring the undisturbed laminar boundary layer and the results do not show any spanwise inhomogeneity of the flow (see section 5.4.3).

A cylinder shaped roughness element with a height (k_r) of 1 mm and diameter (D) of 4 mm (see figure 8.1) is placed at $x_r = 60$ mm downstream of the leading edge. At the location of the element the undisturbed laminar boundary layer thickness (δ) is approximately 1.5 mm (based on Illingworth-Stewartson transformation for a laminar boundary layer, Weigand 2005), resulting in $k_r/\delta = 0.67$. The momentum thickness (θ) is 0.24 mm and the Reynolds number based on the momentum thickness (Re_θ) is equal to 2450. For a summary of the undisturbed boundary layer parameters see table 8.1.

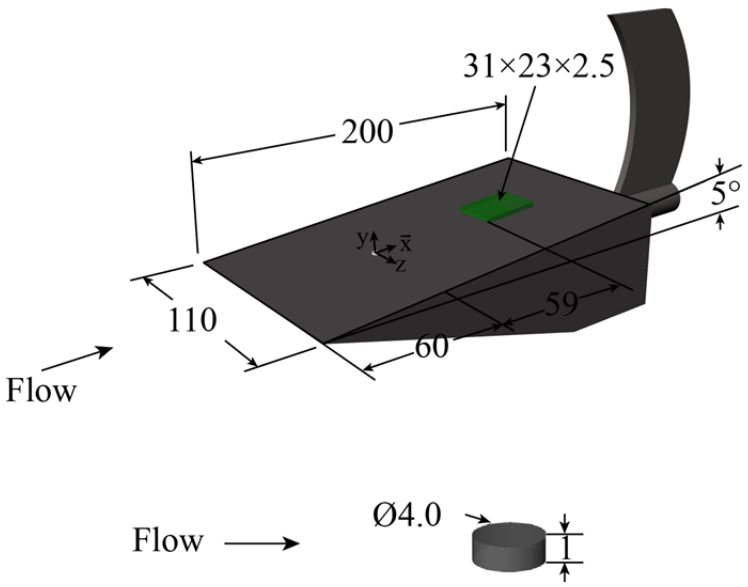

Figure 8.1. Sketch of the wind tunnel model (top) and of the roughness elements (bottom). Dimensions are in mm.

The Shuttle roughness Criteria ($Re_\theta/M_e = (C(h/\delta)^{-1}$, rewritten from equation 1.1 for the sake of clarity) is used to classify the effect of the roughness on the occurrence of transition. In the criterion, M_e is the Mach number at the edge of the boundary layer at the roughness location ($M_e = 6.48$) and the constant C is equal or larger than 200 for critical roughness (transition downstream of the element) and equal or larger than 310 for effective roughness (transition at the location of the element, Berry et al 2006). For the current conditions C has a value of $(Re_\theta\ k_r)/(\delta\ M_e) = 254$ and can therefore be classified as being critical, such that transition is expected to occur downstream of the element.

Table 8.1. Laminar boundary layer properties at the roughness location.

Parameter	Quantity
M_∞	7.5
$Re_{unit}(m^{-1})$	$14 \cdot 10^6$
$x_r(mm)$	60
$\delta_{99}(mm)$	1.5
$\theta(mm)$	0.18
Re_θ	2450
k_r/δ	0.67

8.1.2 Measurement Technique and Data Reduction

Tomographic PIV is used to map the instantaneous 3D velocity field. Statistical properties of the flow are inferred from an ensemble of 120 wind tunnel runs. The experimental procedure is clearly described in section 5.4.

The flow is seeded with Titanium dioxide (TiO_2) particles with a nominal crystal size of 50 nm (Kemira UV-TITAN L830) and with a nominal bulk density of $\rho_b = 200\ kg/m^3$. In practice, the particles tend to cluster forming porous agglomerates of approximately 400 nm which results in a particle relaxation time of $\tau = 2.5\ \mu s$ (Schrijer et al 2006).

Illumination is provided by a Quantel Evergreen laser ($Nd:YAG, 200\ mJ/pulse$) from an optical access positioned on the bottom of the test section. The duration of each laser pulse is shorter than 10 ns, which is short enough not to have particle streaks. The time separation between exposures is set to $\Delta t = 0.7\ \mu s$ and the laser sheet thickness is 3 mm. A sketch of the experimental apparatus is shown in figure 5.8. The camera and the laser are synchronized with the wind tunnel in order to take a measurement at 30 ms after starting the wind tunnel. Due to the short running time of the wind tunnel, only one velocity measurement is obtained for each test.

Table 8.2. Tomographic PIV parameters.

Parameter	Quantity
Particle image density (N_{ppp})	0.03
Measurement volume	31 × 23 × 2.5 mm^3
Interrogation volume	84 × 48 × 30 voxels 1.89 × 1.08 × 0.67 mm^3
Interrogation volume overlap	75%
Digital resolution	44.3 pixels/mm
Vectors per field	99 × 143 × 14
Maximum displacement	28 × 3 × 3 voxels

The particles images are recorded by three PCO Sensicam QE CCD cameras ($1376 \times 1040\ pixels, 12\ bit, 6.7\ \mu m/px$) equipped with Scheimpflug adapters and Nikon 105 mm focal length objectives set at $f_\# = 11$. The resulting measurement volume is $31 \times 23 \times 2.5\ mm^3$, with an average image digital resolution of $44.3\ pixels/mm$. The physical domain (green region in figure 8.1) covers the range $59 < \bar{x} < 90$ ($59\ mm < x - x_r < 90\ mm$) along the streamwise direction, $-11.5 < z/k_r < 11.5$ ($-11.5\ mm < z < 11.5\ mm$) along the spanwise direction and it is 2.5 mm thick along the wall normal direction (y).

The particles images are interrogated using a volume having a final size of $80 \times 48 \times 30$ voxels ($1.89 \times 1.08 \times 0.67\ \mathrm{mm}^3$) and an overlap factor of 75%. Non-cubic interrogation windows are chosen in order to cope with the strong velocity gradient in the wall-normal direction. Spurious vectors are removed using a median filter (Westerweel and Scarano 2005) and replaced through linear interpolation of surrounding vectors. The parameters relevant for the tomographic PIV setup are reported in table 8.2.

8.1.3 Uncertainty Analysis

The measurement errors associated to the tomographic PIV technique are the dominant component of the overall experimental uncertainty. Several factors can affect the measurement uncertainty such as the data ensemble size, cross-correlation algorithm and particle tracer response. The same approach is followed as Sun et al (2012) who performed an uncertainty analysis for a similar experiment.

The uncertainty of the average velocity depends on the magnitude of the velocity fluctuations and the size of the data set as shown in equation 8.1. The present dataset contains $N_{TOMO} = 120$ uncorrelated velocity fields and the largest velocity fluctuations are approximately 20%, which results in an uncertainty of 2%

$$\frac{\varepsilon_{\bar{u}}}{U_0} = \frac{\langle u' \rangle / U_0}{\sqrt{N_{TOMO}}} = 2\% \tag{8.1}$$

Similarly the uncertainty of the velocity fluctuations are estimated to be 7% of the maximum fluctuations

$$\frac{\varepsilon_{\langle u' \rangle}}{\langle u' \rangle_{max}} = \frac{\langle u' \rangle / U_0}{\sqrt{2N_{TOMO}}\langle u' \rangle_{max}} = 7\% \tag{8.2}$$

An additional source of random error is the cross-correlation of the digital particles images. Lynch and Scarano (2014) showed that a value of 0.5 voxels is applicable for tomographic PIV, which corresponds to 1.7% of the free stream velocity.

Another important effect is the particle tracer fidelity, quantified by the particles Stokes number. The turnover time of the typical streamwise vortices (τ_f) evaluated from the experiments is chosen as typical flow time scale, while the particle response time measured by Schrijer et al (2006) is $\tau = 2.5$ μs. The turnover time is evaluated as $\tau_f = r_v / V_{swirl} = 180$ μs where r_v and V_{swirl} are the estimated vortex radius and swirl velocity. In the current experiments, as will be shown in the next section, the radius is estimated to be 3 mm while V_{swirl} is approximately 17 m/s. The swirl velocity is taken

as the difference between the maximum and the minimum of the wall normal velocity component. The resulting particle Stokes number is 0.015, which according to the work of Samimy and Lele (1991) indicates that the tracers are able to follow the motion in the trailing vortices with negligible distortions due to slip.

8.2 Experimental Results

8.2.1 The Wake of the Roughness Element

The mean flow field (obtained from 120 uncorrelated snapshots) is investigated to infer the flow topology past the cylindrical roughness element. As discussed in section 5.4, in the averaging procedure small model oscillations or laser sheet displacements in the order of 0.2 mm are taken into account and corrected for. The residual misalignment is estimated to be less than 0.03 mm, which may be neglected in comparison to other error sources (e.g. finite size of the interrogation volume).

The resulting mean flow organization is given in figure 8.2 by showing cross flow slices at three streamwise locations $\bar{x} = 62, 72, 82$ (from top to bottom). The cross section in figure 8.2 represents the contour of the streamwise velocity on the left and the spanwise velocity on the right. Although not reported there, the measurement data shows that the mean flow organization is symmetric with respect to the centreline. This is confirmed by heat flux measurements performed in the same facility and on the same geometry (see chapter 6).

A spanwise alternation of high-speed and low-speed regions of the streamwise velocity component in combination with two pairs of counter rotating vortices characterizes the flow field. The alternating high-speed and low-speed regions distribution is presented as a characteristic flow feature in most studies and will be analysed first. It can be easily observed in figure 8.2 through the streamwise velocity contours that begin with $u/U_0 = 0.3$ near the wall and end with $u/U_0 = 0.9$ in the outer part of the measurement domain. Starting from $\bar{x} = 62$ the contours of u/U_0 show that the centreline low-speed region ($-1 < z/k_r < 1$) is characterized by an increase of the boundary layer thickness caused by the wall-normal transport of momentum by the inner pair of streamwise vortices. The low-speed region is in turn surrounded by a pair of streamwise high-speed regions corresponding to a reduced thickness of the boundary layer. The high-speed region on the left extends from $z/k_r = -1$ to $z/k_r = -3.5$. From $z/k_r = -3.5$ to $z/k_r = -5$ a region of increased boundary layer thickness is observed. From $z/k_r = -5.5$ the boundary layer is unperturbed and the boundary layer profile starts resembling the laminar one. The wake expands along the spanwise direction moving downstream ($\bar{x} = 72, 82$) where the undisturbed boundary layer starts at $z/k_r = -6$ and -6.5, respectively.

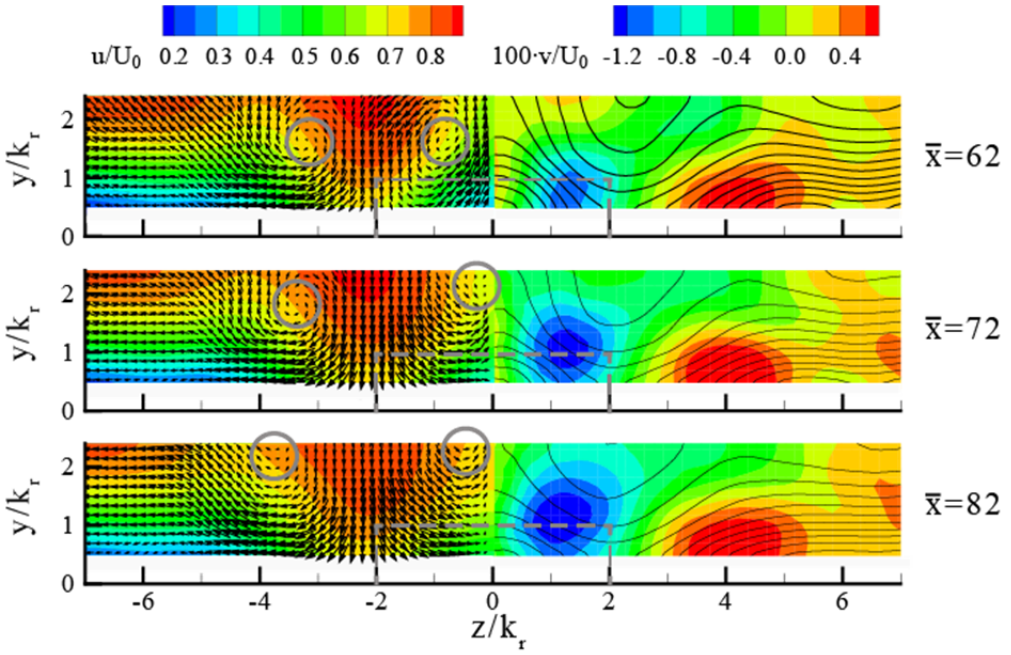

Figure 8.2. Time averaged velocity distribution in the spanwise wall-normal plane. Streamwise (left) and spanwise (right) velocity component contours at $\bar{x} = 62, 72, 82$ from top to bottom. Projected vectors on the y-z plane (left). On the right the isolines of u/U_0 start from 0.3 near to wall and end at 0.9. The grey dashed lines represent the projection of the cylinder in the y-z plane, while grey circles highlight the core of the streamwise vortices.

Two pairs of counter rotating vortices (one for each side) are clearly identified from the projected vectors in the y-z plane in figure 8.2 (left). At the upstream location ($\bar{x} = 62$) the inner pair of counter rotating vortices is located at $y/k_r = 1.75$ and the separation between the two vortices' axes is 0.5D, where D is the cylinder diameter. The outer pair of streamwise vortices is located at the same height ($y/k_r = 1.75$) while the separation between the vortices' axes is 1.75D. These vortices lift up from the wall at different rates when moving downstream. The inner pair of vortices lifts up faster than the outer ones and they move towards the centreline. Consequently, the low speed region across the centreline separates from the rest of the boundary layer as also reported by Choudhari et al (2010). On the other hand, the outer vortex pair tends to move away from the centreline going from $z/k_r = 3.5$ at $\bar{x} = 62$ to $z/k_r = 4$ at $\bar{x} = 82$. Therefore, it can be argued that the high-speed streamwise region broadens.

In figure 8.3 the isosurfaces of the streamwise vorticity (ω_x) are visualized. Red represents counter-clockwise while blue indicates clockwise rotation. The two pairs of counter rotating vortices are clearly visible and they may be associated with the horseshoe vortex system that originates near the front of the roughness element, which was observed in the computations of Iyer et al (2013). The outer pair of vortices

remains strong along the measurement domain while the inner pair shows a reduced intensity when moving downstream, which can be partly explained by their upward motion. They intensity starts decreasing at approximately $\bar{x} = 80$, as clearly visible from the contour of the streamwise vorticity at $y/k_r = 1.5$ in figure 8.3.

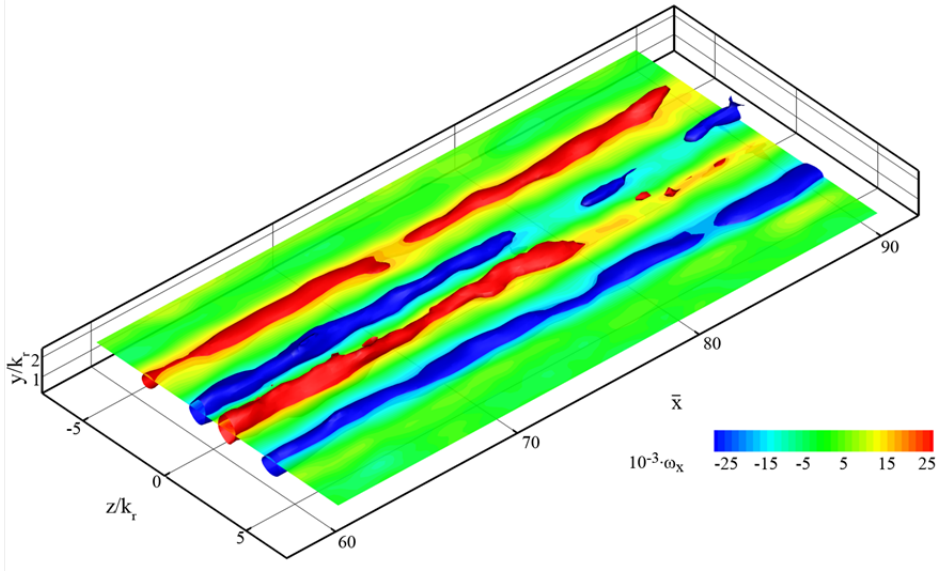

Figure 8.3. Slice of the streamwise vorticity (ω_x) at $y/k_r = 1.5$ with iso-surfaces of ω_x (red represents clockwise and blue counter clockwise rotation).

Figure 8.4a displays several spanwise profiles of the streamwise velocity component at a wall normal height $y/k_r = 0.5$. Starting at the centre plane ($z/k_r = 0$), the wake of the element results in a defect of streamwise velocity. Moving away from the centre plane, the inner vortices induce a downwash motion associated with a pronounced increase of streamwise momentum at approximately $z/k_r = 2$. The streamwise velocity decreases again moving away from the centre, with a secondary small peak (at $z/k_r = 6.5$) ascribed to a weaker downward motion induced by outer vortices. The primary peak velocity slightly increases when moving downstream and moves towards the centre of the wake reducing the velocity deficit at $y/k_r = 0.5$. As a matter of fact, the local maximum for $\bar{x} = 61$ is located at $z/k_r = 2.2$ but that the overall maximum is at $\bar{x} = 90$ and $z/k_r = 2$. The first local maximum occurs at a spanwise location that coincides with the location of the edge of the cylinder. Moving downstream, the outer velocity peak, located at $z/k_r = 6.5$, tends to disappear.

A more detailed analysis of the velocity deficit reduction is performed following the work of Fransson et al (2004). They define the streak amplitude (A), see figure

8.4a, as one half of the maximum spanwise variation of the streamwise velocity component normalized by the free stream velocity:

$$A(\bar{x}) = \frac{1}{2}\max_{z/k_r}\left(\frac{u}{U_0}\left(\bar{x}, 0 < \frac{z}{k_r} < 2\right)\Big|_{max} - \frac{u}{U_0}\left(\bar{x}, 0 < \frac{z}{k_r} < 2\right)\Big|_{min}\right) \quad (8.1)$$

The stream amplitude is displayed in figure 8.4b and it decreases when moving downstream and away from the wall. Considering that in figure 8.4a the velocity peak remains almost constant, the decrease in streak amplitude A can be primarily ascribed to the reduction in velocity deficit in the centre of the low-speed region. At $\bar{x} = 80$, where the vortices from the inner pair become less strong (also see figure 8.3), the A profile shows a plateau.

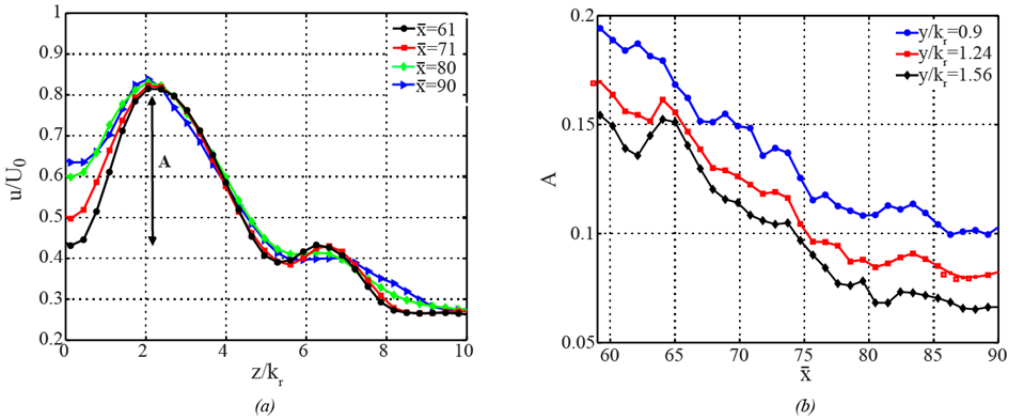

Figure 8.4. (a) Spanwise distribution of the streamwise velocity profile at $y/k_r = 0.5$; (b) Amplitude distribution along the streamwise direction for three different distances from the wall.

In figure 8.5a the boundary layer profile at four spanwise locations ($z/k_r = 0, 2, 5, 10$) and the self-similar boundary layer profile at $\bar{x} = 75$ are shown. The slope of the boundary layer increases moving from $z/k_r = 10$ (out of wake) to $z/k_r = 2$ (high-speed region) and then decreases again at the centreline. The high-speed region features a velocity close to that of the free stream until $y/k_r = 1.6$ suggesting that the boundary layer thickness is reduced by approximately 24% with respect to the undisturbed case, where free stream conditions are reached at $y/k_r = 2.1$. At the centreline ($z/k_r = 0$) the streamwise velocity is still far away from the free stream velocity. In figure 8.5b the evolution of the centreline streamwise velocity profile at three streamwise locations is displayed. The perturbed boundary layer is compared to

the self-similar solution. It shows that when moving downstream from the roughness element the streamwise velocity away from the wall increases.

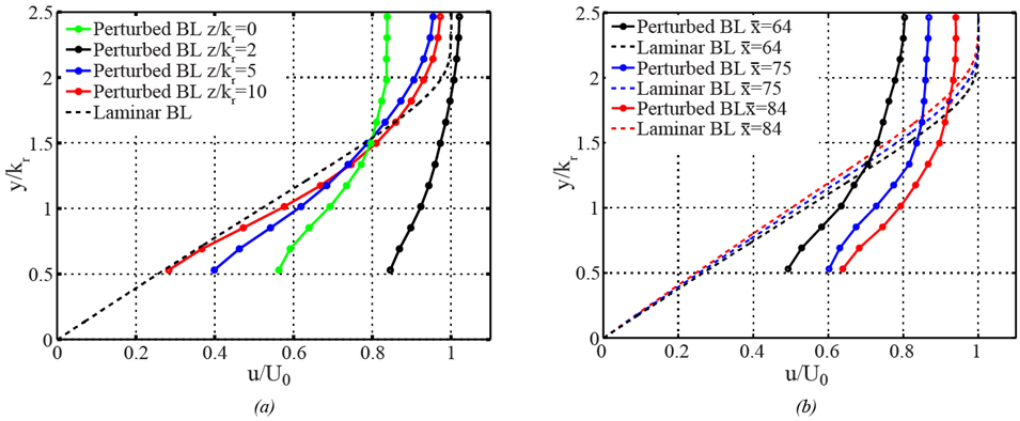

Figure 8.5. (a) Boundary layer profile at $\bar{x} = 75$ from the leading edge; (b) Centreline boundary layer profile.

8.2.2 Turbulent Statistics

The statistical turbulent flow properties are investigated in terms of streamwise velocity fluctuations. The contours of $< u' > /U_0$ at three streamwise cross sections ($\bar{x} = 62, 75$ and 86) are plotted in figure 8.6. In the wake region at the most upstream location ($\bar{x} = 62$) the fluctuations across the wake centreline are about equal to $0.15U_0$ and almost constant along the wall normal direction. Two peaks with intensity equal to $0.21U_0$ are measured near the bottom of the investigated domain. The distance between the peaks is about 0.5D suggesting that they are related to the inner pair of streamwise vortices following to the previous discussion. Moving downstream ($\bar{x} = 75$) these peaks move closer to the centreline and they finally merge at $\bar{x} = 86$. The intensity of the peaks is approximately constant moving downstream from the roughness element. On the other hand, fluctuations associated to the outer pair of counter rotating vortices become stronger when moving downstream.

The fluctuations of the streamwise velocity component feature a region of increased activity at the centre plane. Furthermore, a pronounced increase of the velocity fluctuations is observed at the wall and specifically below the streamwise vortices (both vortex pairs). On the contrary, the high-speed regions exhibit reduced fluctuations with intensity comparable to that measured in the laminar boundary layer. Observing the instantaneous spatial distribution of particle tracers (figure 5.10), an undulation of the interface is noticed. The latter may indicate that the shear layer that encompasses the wake with the main streamwise vortex pair undergoes oscillations due to Kelvin-Helmholtz type vortices. Such behaviour has been observed in a number of

other studies (Sun et al 2012, Lu et al 2010, among others). However, the occurrence of such vortices could not been detected in the present experiments, mostly due to the limited spatial resolution.

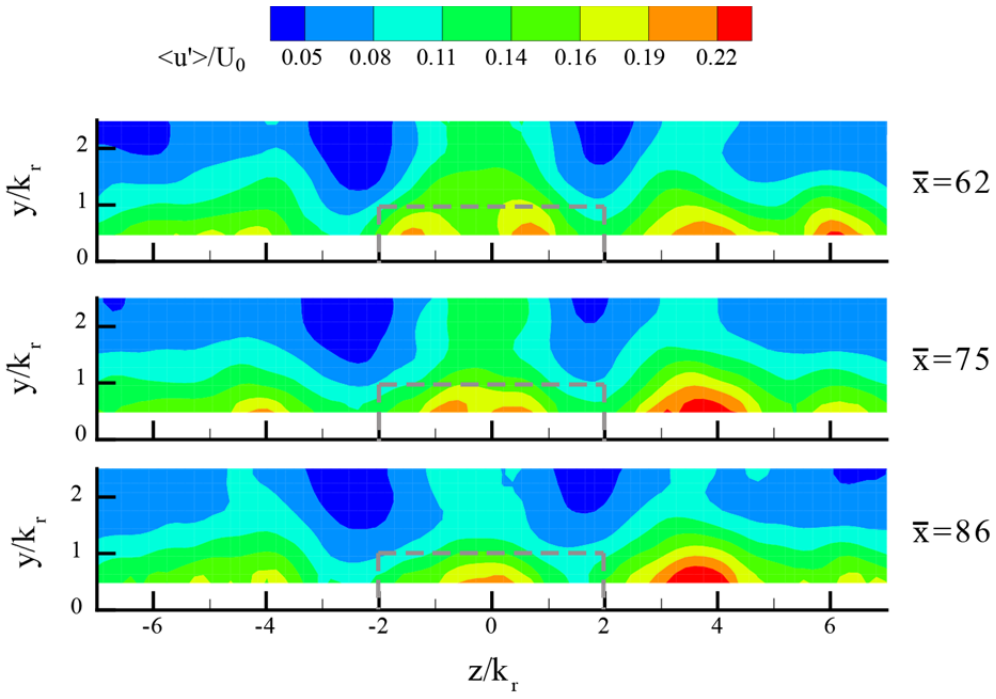

Figure 8.6. RMS fluctuations of streamwise velocity in the wall normal spanwise plane at streamwise locations $\bar{x} = 62, 75$ and 86.

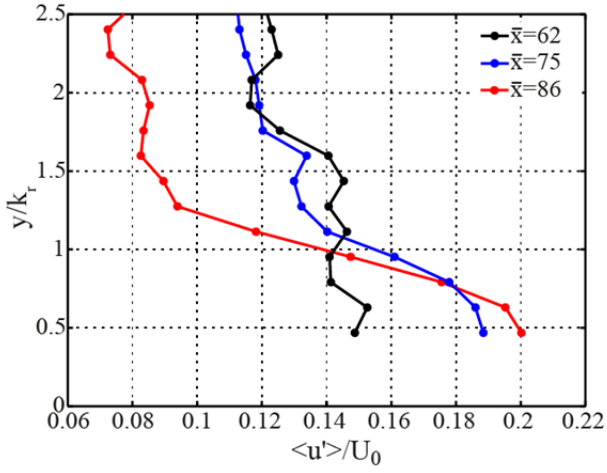

Figure 8.7. $< u' > /U_0$ at the centreline at three streamwise locations $\bar{x} = 62, 75$ and 86.

Figure 8.7 displays wall normal profiles of streamwise velocity RMS fluctuations. The profiles are selected along the centreline at three streamwise locations $\bar{x} = 62, 75$ and 86. The strongest fluctuations are concentrated in the near wall region, which agrees with the numerical simulation performed by Subbareddy et al (2014) for a wake that does not show strong transitional features. They report a peak close to the wall with similar trend as reported in figure 8.7. In particular, moving downstream it is evident that the RMS intensity decreases for y/k_r higher than 1. Such reduction may be due to the effect of the counter rotating vortices move out of the measurement domain. For $0.5 < y/k_r < 1$ the intensity of the fluctuations at $\bar{x} = 75$ looks comparable to those at $\bar{x} = 86$ while close to the wall the fluctuations are stronger at $\bar{x} = 86$.

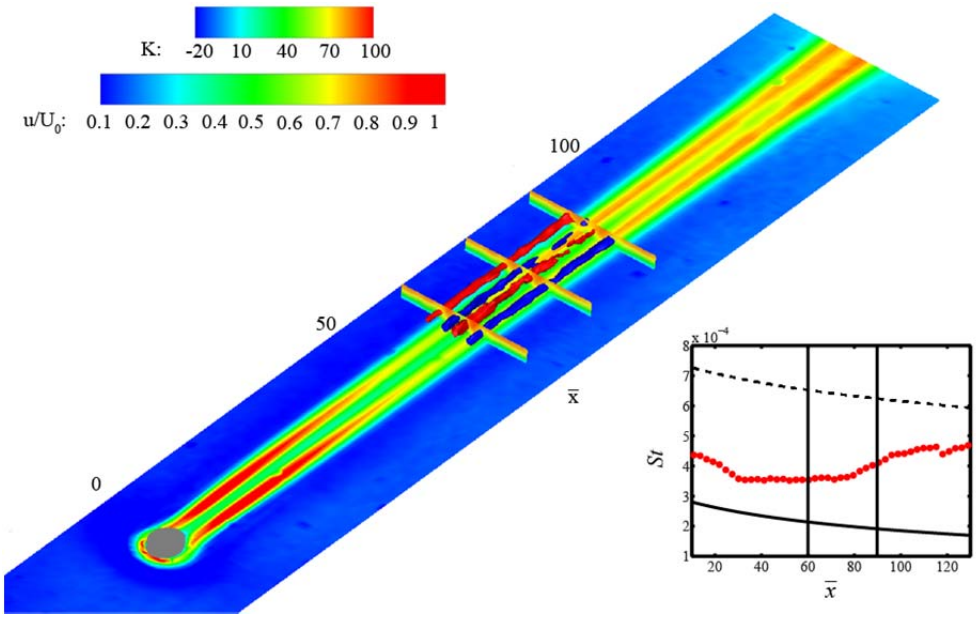

Figure 8.8. Heat transfer distribution and flow topology for the small cylinder positioned at $x_r = 60$ mm and at $Re_{unit} = 14 \cdot 10^6\ m^{-1}$. On the bottom the K contour is displayed. Three spanwise slices are contoured by the streamwise velocity. Iso-surfaces are contoured by the streamwise vorticity (red represents clock-wise rotation while blue represents anti-clockwise rotation). On the bottom right the centreline streamwise Stanton number is shown.

8.3 Qualitative Comparison with IR Thermography

The qualitative comparison between the two measurements (figure 8.8) confirms that along the centreline a pair of counter-rotating SP vortices are present in combination with a region characterized by a low heat transfer while the high heat transfer streaks are generated from the downwash between the SP and the OSP vortices. In particular, figure 8.4b that starting from approximately $\bar{x} = 80$ the

streamwise velocity amplitude distribution becomes constant. It may be associated to the fact that the streamwise SP vortices were partly moving out from the measurement domain. However, approximately at the same location the centreline Stanton number discussed in chapter 6 shows an increase suggesting that it can be also partly associated to some transitional features.

8.4 Conclusions

Tomographic PIV is used to study the wake of an isolated roughness element submerged in a hypersonic boundary layer in Mach 7.5 flow. The perturbed boundary layer shows two pairs of counter rotating vortices and an associated system of low and high-speed regions, which are consistent with the hypothesis of a horseshoe vortex generated in front of the roughness and a second vortex pair inducing a downwash. The streamwise velocity fluctuations are most pronounced in proximity of the vortices, indicating that their position may be subject to large-scale oscillations. The present study does not still allow determining further statistical properties such as Reynolds shear stresses and wavenumber spectra, which will be necessary to study the onset and growth of unstable waves leading to flow transition.

Conclusions and Perspectives

In this thesis, quantitative non-intrusive experimental techniques (infrared thermography, planar and tomographic particle image velocimetry) are developed and applied to study transition induced by an isolated roughness element located in an incoming hypersonic laminar boundary layer.

In the first part of the thesis, a technique that reduces the noise in the transient temperature history due to the wind tunnel model mechanical vibrations is presented. It is based on the distinction between the wind tunnel model out-of-plane (represented by the wind tunnel model scaling in the IR images) and the in-plane displacements (represented by rigid translation of the wind tunnel model in the IR images). These displacements are corrected by means of the Speed-Up Robust Features and the single-step Discrete Fourier Transform, respectively.

Then, a data reduction technique that solves multidimensional Inverse Heat Transfer Problems starting from the measured transient temperature history is proposed. It is based on the least-squares approach and it uses the Trust Region Reflective Algorithm as optimization tool. The method is extremely stable even if in presence of strong noise intensity. The high computational cost is reduced by detecting the most powerful coefficients of the Discrete Fourier Transform of the unknown signal. These coefficients are the objects of the optimization algorithm. The technique is validated by means of both synthetic and experimental data. The validation confirms that the computational cost sensibly reduces with band-limited data and it is stable even in presence of high tangential conduction rate.

With the aim of investigating the physical mechanisms leading to transition, tomographic PIV is applied for the first time to hypersonic flows. It represents a break-through in the investigation of boundary layer transition.

An assessment of the experimental procedure leading to the statistical characterization of the time-averaged and fluctuating velocity field is presented. The

volume self-calibration technique is used with the purpose to account for index of refraction effects as well as for correcting mechanical vibrations present between several snapshots. The measurement technique is experimentally validated by measuring the undisturbed laminar boundary layer growing along the plate.

Further developments of the techniques are still necessary with a particular focus on the tracer particles. On going preliminary study on nanostructured aluminium tracers (characterized by a lower response time with respect to the conventional TiO_2 tracers, Ghaemi et al 2010) aims at injecting these particles in the high-pressure vessel by means of a gas-booster.

In the last part of the thesis, roughness-induced transition is investigated by means of the developed non-intrusive experimental techniques.

A first characterization of the flow field upstream and downstream of three-dimensional roughness elements placed in an incoming boundary layer is obtained by means of heat flux measurements. These measurements are used to detect the transition location, the influence of the geometry on the transitional pattern and to estimate the vortex structures formed upstream. More specifically, it is found that the shape influences the transitional pattern while the frontal area influences both the transition location and the maximum value of the Stanton number. Furthermore, experiments confirm that the vortices formed across the centreline are most susceptible to break down to turbulence due to their interaction. A first characterization of the upstream separated region is obtained by looking at the footprints of the vortical structures just behind the roughness elements. Particularly, for $(D/\delta^*)(k_r/\delta) > 2$ a 6-vortex system is detected instead of 4-vortex system. Lastly, by defining the streak amplitude, A, as one half of the maximum spanwise variation of K, it has been observed that the transitional and turbulent regions are characterized by A approximately constant along the streamwise direction.

For a given configuration, the wall heat transfer distribution is compared with the three-dimensional velocity field measured be means of tomographic PIV. The qualitative comparison between the two measurements confirms that along the centreline a pair of counter-rotating vortices is present in combination with a region characterized by low heat transfer. On the contrary, high heat transfer streaks are generated from the downwash between the SP and the OSP vortices. The perturbed boundary layer shows two pairs of counter rotating vortices and an associated system of low and high-speed regions, which are consistent with the hypothesis of a horseshoe vortex generated in front of the roughness. The streamwise velocity fluctuations are most pronounced in proximity of the vortices, indicating that their position may be subject to large-scale oscillations.

Finally, the flow ahead of a supercritical roughness element placed in an incoming laminar boundary layer is investigated by means of planar particle image velocimetry. The velocity field measurements confirm the presence of the expected 6-vortex system in the recirculation region and the vortices locations are in agreement with the local Stanton number local maxima obtained from the heat flux measurements. The velocity turbulent statistics, analysed through the TKE distribution, show an increased unsteadiness in the region with the highest vorticity concentration (at approximately 1 diameter from the protuberance location). Furthermore, the measurements confirm that the unsteadiness due to the shock wave formed just in front of the roughness is barely weak.

The measurements presented in the thesis represent a first step to understand roughness induction transition in the hypersonic regime. Comparison with other innovative experimental techniques (such as PLIF) and computations are still necessary for a complete comprehension of the phenomena.

References

Abdel-Aziz YI, Karara HM (1971). Direct linear transformation from comparator coordinates into object space coordinates in close range photogrammetry. Proceedings of the Symposium on Close-Range Photogrammetry, Urbana-Champaign, Illinois (USA), 28 July-1 August,1-18.

Adrian RJ (1991). Particle-imaging techniques for experimental fluid mechanics. Annual Review of Fluid Mechanics, 23: 261-304.

Adrian RJ, Yao CS (1984). Development of pulsed laser velocimetry (PLV) for measurement of fluid flow. Proceedings of the 8th Biennial Symposium on Turbulence, Rolla, Missouri (USA), 170–186.

Alberty J, Carstensen C, Funken SA (1999). Remarks around 50 lines of Matlab: short finite element method implementation. Numerical Algorithms, 20(2-3): 117-137.

Anderson D (2006). Hypersonic and high-temperature gas dynamics, Second Edition. American Institute of Aerodynamics and Astronautics, Reston, VA (USA).

Astarita T (2006). Analysis of interpolation schemes for image deformation methods in PIV: effect of noise on the accuracy and on the spatial resolution. Experiments in Fluids, 40(6): 977-987.

Astarita T (2007). Analysis of weighting windows for image deformation methods in PIV. Experiments in Fluids, 43(6): 859-872.

Astarita T (2008). Analysis of velocity interpolation schemes for image deformation methods in PIV. Experiments in Fluids, 45(2): 257-266.

Astarita T, Cardone G (2005). Analysis of interpolation schemes for image deformation methods in PIV. Experiments in Fluids, 38(2): 233-243.

Astarita T, Carlomagno GM (2013). Infrared thermography for thermo-fluid-dynamics. Berlin Heidelberg, New York (USA).

Aymer De La Chevalerie D, Fonteneau A, De Luca L, Cardone G (1997). Goertler vortices in hypersonic flow: the ramp problem. International Journal of Experimental Thermal and Fluid Science, 15(2): 69-81.

Baker CJ (1979). The laminar horseshoe vortex. Journal of Fluid Mechanics, 95(2): 347-367.

Bathel BF, Danehy PM, Inman JA, Jones SB, Ibey CB, Goyne CP (2011). Velocity profile measurements in hypersonic flows using sequentially images fluorescence-based molecular tagging. AIAA Journal, 4(9): 1883-1896.

Bay H, Ess A, Tuytelaars T, Van Gool L (2008). Speeded-up robust features (SURF). Computer Vision and Image Understanding, 110: 346-359.

Beck JV, Blackwell B, St. Clair CR (1985). Inverse heat conduction: ill-posed problems. John Wiley and Sons Inc., New York, NY (USA).

Berry SA, Bouslog SA, Brauckmann GJ, Caram JM (1998). Shuttle orbiter experimental boundary-layer transition results with isolated roughness. Journal of Spacecraft and Rockets, 35(3): 241-248.

Berry SA, Hamilton HH, Wurster KE (2006). Effect of computational method on discrete roughness correlations for shuttle orbiter. Journal of Spacecraft and Rockets, 43(4): 842-852.

Berry SA, Horvart TJ (2007). Discrete roughness transition for hypersonic flight vehicles. Proceedings of the 45th AIAA Aerospace Sciences Meeting and Exhibit, Reno, Nevada (USA), 8 – 10 January, AIAA 2007-0307.

Boreman GD (2001). Modulation transfer function in optical and electronic optical system. SPIE, Bellingham, WA (USA).

Branch MA, Coleman TF, Li Y (1999). A subspace, interior, and conjugate gradient method for large-scale bound-constrained minimization problems. SIAM Journal of Scientific Computing, 21(1): 1-23.

Brandon JM, Manuel GS, Wright RE, Holmens BJ (1990). In-flight flow visualization using infrared imaging. Journal of Aircraft, 27(7): 612-618.

Braslow AL, Horton EA (1958). Effects of surface roughness on transition. Proceedings of the NACA Conference on High-Speed Aerodynamics, NASA-TM-X-67639, 439-450.

Brown DC (1971). Close range camera calibration. Photogrammetric Engineering, 37(8): 855-866.

Bynum DS, Hube FK, Key CM, Dyer PM (1976). Measurement and mapping of aerodynamic heating in VKF tunnel B with an infrared camera. AEDC TR 76-54.

Cardone G (2007). IR heat transfer measurements in hypersonic plasma flows. Quantitative Infrared Thermography Journal, 4(2): 233-251.

Cardone G, Ianiro A, dello Ioio G, Passaro A (2012). Temperature maps measurements on 3D surfaces with infrared thermography. Experiments in Fluids, 52(2): 375-385.

Carlomagno GM, Cardone G (2010). Infrared thermography for convective heat transfer measurements. Experiments in Fluids, 49(6): 1187-1218

Casper KM, Johnson HB, Schneider SP (2011). Effect of freestream noise on roughness-induced transition for a slender cone. Journal of Spacecraft and Rockets, 48(3): 406-413.

Chang CL, Choudari MM (2011). Hypersonic viscous flow over large roughness elements. Theoretical and Computational Fluid Dynamics, 25(1-4): 85-104.

Chang SL, Rhee KT (1984). Blackbody radiation functions. International Communications in Heat and Mass Transfer, 11(5): 451-455.

Choudhari M, Li F, Wu M, Chang C-L, Edwards J, Kegerise M, King R (2010). Laminar turbulent transition behind discrete roughness elements in a high-speed boundary layer. Proceedings of the 48th AIAA Aerospace Sciences Meeting including the New Horizon Forum and Aerospace Exposition, Orlando, Florida (USA), 4 - 7 January, AIAA 2010-1575.

Coleman TF, Li Y (1994). On the convergence of reflective newton methods for large-scale nonlinear minimization subjects to bounds. Mathematical Programming, 67(1-3): 189-224.

Coleman TF, Li Y (1996). An interior trust region approach for nonlinear minimization subject to bounds. SIAM Journal of Optimization, 6(2): 418-445.

Coleman TF, Verma A (2001). A preconditioned conjugate gradient approach to linear equality constrained minimization. Computational Optimization and Applications, 20(1): 61–72.

Cook WJ, Felderman EJ (1966). Reduction of data from thin-film heat-transfer gages: a concise numerical technique. AIAA Journal, 4(3): 561-562.

Cox JT, Hass G, Jacobus F (1961). Infrared filters of antireflected Si, Ge, InAs and InSb. Journal of the Optical Society of America, 51(7): 714-718.

Danehy PM, Bathel B, Ivey C, Inman JA, Jones SB (2009) NO PLIF study of hypersonic transition over a discrete hemispherical roughness element. Proceedings of the 47th AIAA Aerospace Sciences Meeting including the New Horizon and Aerospace Exposition, Orlando, Florida (USA), 5 - 8 January, AIAA 2009-0394.

Danehy PM, Ivey CB, Inman JA, Bathel BF, Jones SB, McCrea AC, Jiang N, Webster M, Lempert W, Miller J, Meyer T (2010) High-speed plif imaging of hypersonic transition over discrete cylindrical roughness. Proceedings of the 48th AIAA Aerospace Sciences Meeting including the New Horizon and Aerospace Exposition, Orlando, Florida (USA), 4 - 7 January, AIAA 2010-703.

de Luca L, Cardone G (1991). Modulation transfer-function cascade model for a sampled IR imaging system. Applied Optics, 30(13): 1659-1664.

de Luca L, Cardone G, Aymer de la Chavalerie D (1993). Goertler instability of a hypersonic boundary layer. Experiments in Fluids, 16(1): 10-16.

de Luca L, Cardone G, Aymer de la Chavalerie D (1995). Viscous interaction phenomena in hypersonic wedge flow. AIAA Journal, 3(12): 2293-2298.

de Luca L, Cardone G, Carlomagno GM, Aymer De La Chevalerie D, Alziary De Roquefort T (1992). Flow visualization and heat transfer measurement in hypersonic wind tunnel. Experimental Heat Transfer, 5(1): 65-79.

Di Clemente M, Rufolo G, Ianiro A, Cardone G (2013). Hypersonic test analysis by means of aerothermal coupling methodology and IR thermography. AIAA Journal, 51(7): 1755-1769.

Discetti S (2013). Tomographic particle image velocimetry. Development and applications to turbulent flows. PhD thesis, University of Naples “Federico II”.

Discetti S, Natale A, Astarita T (2013). Spatial filtering improved tomographic PIV. Experiments in Fluids, 54:1505.

Eckert E (1956). Engineering relations for heat transfer and friction in high-velocity laminar and turbulent boundary-layer flow over surface with constant pressure and temperature. Transaction ASME, 78(6): 1273-1283.

Elsinga GE, Scarano F, Wieneke B, van Oudheusden BW (2006). Tomographic particle image velocimetry. Experiments in Fluids, 41(6): 933-947.

Elsinga GE, van Oudheusden BW, Scarano F (2005). Evaluation of aero-optical distortion effects in PIV. Experiments in Fluids, 39(2): 245-256.

Elsinga GE, Westerweel J (2012) Tomographic-PIV measurement of the flow around a zigzag boundary layer trip. Experiments in Fluids, 52(4): 865-876.

Elsinga GE, Westerweel J, Scarano F, Novara M (2011). On the velocity of ghost particles and the bias errors in tomographic piv. Experiments in Fluids, 50(4): 825-838.

Estruch-Samper D, MacManus DG, Stollery JL, Lawson NJ, Garry KP (2010). Hypersonic interference heating in the vicinity of surface protuberances. Experiments in Fluids, 49(3): 683-699.

Fischer MC (1972). Spreading of a turbulent disturbance. AIAA Journal, 10(7): 9757-9959.

Fransson JH, Brandt L, Talamelli A, Cossu C (2004) Experimental and theoretical investigation of the nonmodal growth of steady streaks in a flat plate boundary layer. Physics of Fluids, 16(10): 3627-3638.

Friehmelt H, Koppenwallner G, Muller-Eigner R (1993). Calibration and first results of a redisegned Ludwieg expansion tube. Proceedings of the AIAA/DGLR 5th International Aerospace Planes and Hypersonics Technologies Conference, Munich, Germany, 30 November - 3 Decembe, AIAA 93-5001.

Gebbie HA, Harding WR, Hilsum C, Pryce AW, Roberts V (1951). Atmospheric Transmission in the 1 to 14 μm region. Proceedings of the Royal Society of London A, 206(1084): 87-107.

Ghaemi S, Schmidt-Ott A, Scarano F (2010). Nanostructured tracers for laser-based diagnostics in high-speed flows. Measurements Science and Technology, 21: 105403.

Gravrand O, Baier N, Ferron A, Rochette F, Berthoz J, Rubaldo L, Cluzel R (2014). MTF issues in small-pixel-pitch planar quantum IR detector. Journal of Electronics Material, 43(8): 3025-3032.

Guizar-Sicarios M, Thurman ST, Fienup JR (2008). Efficient subpixel image registration algorithms. Optics Letters, 33(2): 156-158.

Gülhan A, Schutte G, Stahl B (2008). Experimental study on aerothermal heating caused by jet-hypersonic crossflow interaction. Journal of Spacecraft and Rockets, 45(5): 891–899.

Haberle J, Gulhan (2007). International flowfield investigation of a hypersonic inlet at Mach 6 with bleed. Journal of Propulsion and Power, 23(5): 1007-1017.

Havermann M, Haertig J, Rey C, George A (2002). Application of particle image velocimetry to high-speed supersonic flows in a shock tunnel. Proceedings of the 11th

International Symposium on Application of Laser Technology to Fluid Mechanics, Lisbon, Portugal, 8 – 11 July.

Heikkilä J (2000). Geometric camera calibration using circular control points. IEEE Transaction on Pattern Analysis and Machine Intelligence, 22(10): 1066-1077.

Heikkilä J, Silven O (1997). A four-step camera calibration procedure with implicit image correction. Proceedings of the 1997 Conference on Computer Vision and Pattern Recognition, San Juan, Argentina, 11-17 June, 1106-1112.

Herman GT, Lent A (1976). Iterative reconstruction algorithms. Computers in Biology and Medicine, 6(4): 273-294.

Hicks RM, Harper WRJr (1970). A comparison of spherical and triangular boundary-layer trips on a flat plate at supersonic speeds. NASA, TM-X-2146.

Holloway PF, Morrisette EL (1966). Roughness effects on boundary-layer transition for blunt-leading edge-plates at Mach 6. NASA Technical Note, TN-D-3517.

Hottner T (1968). Der rohrwindkanal der aerodynamichen versuchsanstalt göttingen. Technical Report, AVA-68A-77.

Huang HT, Fiedler HE, Wang JJ (1993). Limitation and improvement of PIV, part II. Particle image distortion, a novel technique. Experiments in Fluids, 15(4-5): 263-273.

Humble RA, Elsinga GE, Scarano F, van Oudheusden BW (2009) Three-dimensional instantaneous structure of a shock wave/turbulent boundary layer interaction. Journal of Fluid Mechanics, 622: 33-62.

Hung F, Patel D (1984). Protuberance interference heating in high-speed flow. Proceedings of the AIAA 19th Thermophysics Conference, Snowmass, Colorado (USA), 25 - 28 June , AIAA 84-1724.

Iyer PS, Mahesh K (2013). High-speed boundary-layer transition induced by a discrete roughness element. Journal of Fluid Mechanics, 729: 524-562.

Jackson MW, Czarnecki KR (1960). Investigation by Schlieren technique of methods of fixing fully turbulent flow on models at supersonic speeds. NASA, TN-D-242.

Ji CC, Tuan PC, Jang HY (1997). A recursive least-squares algorithm for on-line 1-D inverse heat conduction estimation. International Journal of Heat and Mass Transfer, 40(9): 2081-2096.

Kendall DN, Dixon WP (1996). Heat Transfer Measurements in a hot shot wind tunnels. Transaction on Aerospace and Electronic Systems, 3(4): 596-603.

King RA, Breuer KS (2001). Acoustic receptivity and evolution of two-dimensional and oblique disturbances in a Blasius boundary layer. Journal of Fluid Mechanics, 432: 69-90.

Klebanoff P, Schubauer G, Tidstrom, K (1955). Measurements of the effect of the two-dimensional and three-dimensional roughness elements on boundary layer transition. Journal of Aeronautical Sciences, 22(11): 803–804.

Kumar CS, Singh T, Reddy KPJ (2014). Investigation of the separated region ahead of the three-dimensional protuberances on plates and cones in hypersonic flows with laminar boundary layer. Physics of Fluids, 26: 126101.

Le Duc A, Sesterhenn J, Friedrich R (2006). Instabilities in compressible attachment-line boundary layers. Physics of Fluids, 18: 044102.

Le Sant Y (2005). An image restoration method for infrared measurements. Quantitative Infrared Thermography Journal, 2(2): 207-222.

Levesque P, Brémond P, Lasserre JL, Paupert A, Balageas DL (2005). Performance of FPA IR cameras and their improvement by time, space and frequency data processing. Part I: Intrinsic characterization of the thermographic system. Quantitative InfraRed Thermography Journal, 2(1): 97-112.

Lighthill MJ (1953). On boundary layers and upstream influence. I. A comparison between subsonic and supersonic flows. Proceedings of the Royal Society of London A, Mathematical and Physical Sciences, 471(1130): 344-357.

Liu T, Wang B, Rubal J, Sullivan JP (2011). Correcting lateral heat conduction effect in image-based heat flux measurements as an inverse problem. International Journal of Heat and Mass Transfer, 54(5-6): 1244-1258.

Liu T, Ward CAC, Rubal J, Sullivan JP, Schneider SP (2013). Heat flux measurements with temperature-sensitive paint in Mach-6 quiet tunnel. Journal of Spacecraft Rockets, 50(2): 282-293.

Lowe DG (2004). Distinctive image features from scale-invariant keypoints. International Journal of Computer Vision, 60(2): 91–110.

Lu FK, Pierce AJ, Shich Y (2010). Experimental study of near wake of micro vortex generators in supersonic flow. Proceedings of the AIAA 40th Fluid Dynamics conference and Exhibit, Chicago, Illinois, 28 June - 1 July, AIAA 2010-4623.

Ludwieg H (1955). Der rohrwindkanal. Zeitschrift für Flugwissenschaften, 3(7): 206-216.

Lynch KP, Scarano F (2014). Experimental determination of tomographic PIV accuracy by a 12-camera system. Measurements Science and Technology, 25: 084003.

Maas HG, Gruen A, Papantoniou D (1993). Particle tracking velocimetry in three-dimensional flows. Experiments in Fluids, 15(4-5): 133-146.

Marini M (2001). Analysis of hypersonic compression ramp laminar flows under sharp leading edge conditions. Aerospace Science and Technology, 5(4): 257-271.

Marquardt D (1963). An algorithm for least-squares estimation of nonlinear parameters. SIAM Journal of Applied Mathematics, 11(2): 431-441.

Marxen O, Iaccarino G, Shaqfeh ESG (2010). Disturbance evolution in a Mach 4.8 boundary layer with two-dimensional roughness-induced separation and shock. Journal of Fluid Mechanics, 648: 435-469.

Masutti D (2013). Ground testing investigation of hypersonic transition phenomena for a re-entry vehicle. PhD thesis, Delft University of Technology, The Netherlands.

McGinley CB, Berry SA, Kinder GR, Barnwell M, Wang KC, Kirk BS (2006). Review of orbiter flight boundary layer transition data. Proceedings of the 9th AIAA/ASME Joint Thermophisics and Heat Transfer Conference, San Francisco, California (USA), 5-8 June, AIAA 2006-2921.

Melen T (1994). Geometrical modelling and calibration of video cameras for underwater navigation. PhD thesis, Norwegian Institute of Technology, Norway.

Melling A (1997). Tracer particles and seeding for particle image velocimetry. Measurement Science and Technology, 8: 1406-1416.

Michaelis D, Wolf CC (2011) Vibration compensation for tomographic PIV using single image volume self calibration. Proceeding of the 9th International Symposium on Particle Image Velocimetry, Kobe, Japan, 21-23 July.

Modenini D, Schrijer FFJ (2012). Heat transfer measurements in a supersonic wind tunnel through inverse temperature data reduction to a backward facing step. Quantitative InfraRed Thermography Journal, 9(2): 209-230.

Moffat RJ (1988). Describing the uncertainties in experimental results. Experimental Thermal and Fluid Science, 1(1): 3-17.

Morkovin M (1969). On the many faces of transition. Proceeding of the Symposium on Viscous Drag Reduction, Dallas, Texas (USA), 24 – 25 September, 1-31.

Morkovin M (1985). Bypass transition to turbulence and research desiderata. Lewis Research Center Transition in Turbines, NASA, 161-204.

Morkovin M, Reshotko E, Herbert T (1994). Transition in open flow system. A reassessment. Bullettin of American Physical Society, 39(9): 1882.

Morrisette EL, Stone DR, Whitehead JrAH (1969). Boundary-layer tripping with emphasis on hypersonic flows. Proceedings of the Symposium on Viscous Drag Reduction, Dallas, Texas, 24 – 25 September, 33-51.

Navarro-Martinez S, Tutty OR. Numerical simulation of Gortler vortices in hypersonic compression ramps. Computers & Fluids, 34(2): 225-247.

Novara M (2013) Advances in tomographic PIV. PhD Thesis, TU Delft, The Netherlands.

Novara M, Batenburg KJ, Scarano F (2010). Motion tracking-enhanced MART for tomographic PIV. Measurement Science and Technology, 21: 035401.

Ozisik MN, Orlande HRB (2000). Inverse heat transfer: fundamentals and applications. Taylor & Francis, New York, NY (USA).

Park HM, Chung OY, Lee JH (1999). On the solution of inverse heat transfer problem using the Karhunen-Loève Galerkin method. International Journal of Heat and Mass Transfer, 42(1): 127-142.

Pate SR (1971). Measurements and correlations of transition Reynolds numbers on sharp slender cones at high speeds. AIAA Journal, 9(6): 1082-1090.

Potter JL, Withfield JD (1962). Effects of slight nose bluntness and roughness on boundary layer transition in supersonic flows. Journal of Fluid Mechanics, 12(4): 501-535.

Raffel M, Willert CE, Wereley ST, Kompenhans J (2007). Particle image velocimetry. A practical guide. Second Edition. Springer-Verlag, New York (USA).

Ragni D, Schrijer FFJ, van Oudheusden BW, Scarano F (2011). Particle tracer respose across shocks measured by PIV. Experiments in Fluids, 50(1): 53-64.

Raynaud M, Bransier J (1986). A new finite-difference method for the non-linear inverse heat conduction problem. Numerical Heat Transfer, 9(1): 27-42.

Reda DC (2002). Review and synthesis of roughness-dominated transition correlations for reentry applications. Journal of Spacecraft and Rockets, 39(2): 161-167.

Reshotko E (2008). Paths to transition in wall layers. advances in laminar-turbulent transition modeling, Von Karman Lecture Series, EN-AVT-151-12.

Rudinger G (1976). Flow of solid particles in gases. Technical Report, AG-222, AGARD.

Samimy M, Lele SK (1991). Motion of particles with inertia in a compressible free shear layer. Physics of Fluids, 3(8): 1915.

Saric WS (1994). Görtler vortices. Annual Review of Fluid Mechanics, 26: 379-409.

Scarano F (2008) Overview of PIV in supersonic flows. Topics in Applied Physics, 112: 445-463.

Scarano F, Riethmuller ML (2000). Advances in iterative multigrid PIV images processing. Experiments in Fluids, 29(7): 51-60.

Scarpa F, Milano G (1995). Kalman smoothing technique applied to the inverse heat conduction problem. Numerical Heat Transfer, 28(1): 79-96.

Schneider SP (2001) Effects of high-speed tunnel noise on laminar-turbulent transition. Journal of Spacecraft and Rockets, 38(3): 323-333.

Schneider SP (2008). Effects of roughness on hypersonic boundary-layer transition. Journal of Spacecraft and Rockets, 45(2): 193-209.

Schrijer FFJ (2010a). Experimental investigation of re-entry aerodynamic phenomena - Development of non-intrusive flow diagnostics in a Ludwieg tube. PhD thesis, Technological University Delft, The Netherlands.

Schrijer FFJ (2010b). Investigation of Görtler vortices in a hypersonic double compression ramp flow by means of infrared thermography. Quantitative Infrared Thermography Journal, 7(2): 2012-215.

Schrijer FFJ (2012). Unsteady data reduction techniques for QIRT: consideration of temporal and spatial resolution. Proceedings of the 11th Quantitative InfraRed Thermography Conference, Naples, Italy, 11 - 14 June ,QIRT 2012-317.

Schrijer FFJ, Bannink WJ (2010). Description and flow assessment of the Delft hypersonic Ludwieg tube. Journal of Spacecraft and Rockets, 47(1): 125-133.

Schrijer FFJ, Scarano F (2008). Effect of predictor-corrector filtering on the stability and spatial resolution of iterative piv interrogation. Experiments in Fluids, 45(5): 927-941.

Schrijer FFJ, Scarano F, van Oudheusden BW (2006). Application of piv in a mach 7 double-ramp flow. Experiments in Fluids, 41(2): 353-363.

Schultz DL, Jones TV (1973). Heat-transfer measurements in short duration hypersonic facilities. NATO Advisory Group for Aerospace Research and Development, AGARD - AG - 165.

Schulz A (2000). Infrared thermography as applied to film cooling of gas turbine components. Measurement Science and Technology, 11: 948-956.

Settles GS (2001). Schlieren and shadowgraph techniques: visualization phenomena in transparent media. Springer Verlag, New York (USA).

Sharp NS, White EB (2014). Roughness induced transient growth on a hypersonic blunt cone. Proceedings of the AIAA 52nd Aerospace Sciences Meeting, National Harbor, Maryland (USA), 13 - 17 January, AIAA 2014-0432.

Shenefelt JR, Luck R, Taylor RP, Berry JT (2002). Solution to inverse heat conduction problems employing singular value decomposition and model-reduction. International Journal of Heat and Mass Transfer, 45(1): 67-74.

Simeonides G (1992). Hypersonic shock wave boundary layer interactions over compression corners. PhD thesis, von Karman Institute, Belgium.

Simeonides G, Haase W (1995). Experimental and computation investigations of hypersonic flow about compression ramps. Journal of Fluid Mechanics, 283: 17-42.

Simpson RL (2001). Junction flows. Annual Review of Fluid Mechanics, 33: 415-443.

Skeel R D Berzins M (1990). A method for the spatial discretization of parabolic equations in one space variable. SIAM Journal on Scientific and Statistical Computing, 11(1): 1–32.

Soloff SM, Adrian RJ, Liu ZC (1997). Distortion compensation for generalized stereoscopic particle image velocimetry. Measurement Science and Technology, 8: 1441-1454.

Sorensen DC (1994). Minimization of large scale quadratic function subject to an ellipsoidal constraint. Technical Report, Dept. of Computational and Applied Mathematics, Rice University, TR 94-24.

Stalling DW, Carver DB (1978). Infrared and phase-change paint measurements on the space shuttle orbiter. AEDC-TSR-78-V13.

Subbareddy PK, Bartkowicz MD, Candler GV (2014). Direct numerical simulation of high-speed transition due to an isolated roughness element. Journal of Fluid Mechanics, 748: 848-878.

Sun Z, Schrijer FFJ, Scarano F van Oudheusden BW (2012). The three dimensional flow organization past a micro-ramp in a supersonic boundary layer. Physics of Fluids, 24(5): 0551051-05510522.

Tani I (1969). Boundary-layer transition. Annual Review of Fluid Mechanics, 1: 169-196.

Tedeschi G, Gouin H, Elena M (1999). Motion of tracer particles in supersonic flows. Experiments in Fluids, 26(4): 288-296.

Thomann H, Frisk B (1968). Measurements of heat transfer with an infrared cameras. International Journal of Heat and Mass Transfer, 11(5): 819-826.

Tirtey SC (2008). Characterization of a transitional hypersonci boundary layer in wind tunnel and flight conditions. PhD Thesis, Universite Libre de Bruxelles, Belgium.

Tirtey SC, Chazot O, Walpot L (2011). Characterization of hypersonic roughness-induced boundary-layer transition. Experiments in Fluids, 50(2): 407-418.

Tsai RY (1987). A versatile camera calibration technique for high accuracy 3D machine vision metrology using off-the shelf TV camera and lenses. IEEE Journal of Robotics Automation, 3(4): 323-344.

Van Driest E, Blumer CB (1962). Boundary-layer transition at supersonic speeds-Three Dimensional Roughness Effects (Spheres). Journal of Aerospace Science, 29(8): 909-916.

Van Driest ER, Blumer CB, Wells CSJr (1967). Boundary layer transition on blunt bodies - Effects of roughness. AIAA Journal, 5(10): 1913-1915.

Van Driest ER, Boison JC (1957). Experiments on boundary layer at supersonic speeds. Journal of Aeronautical Sciences, 24(12): 885-899.

Van Driest ER, McCauley WD (1960). The effect of controlled three-dimensional roughness on boundary layer transition at supersonic speed. Journal of Aeronautical Sciences, 27(4): 261-271.

Walker DG, Scott EP (1998). Evaluation of Estimation Methods for High Unsteady Heat Fluxes from Surface Measurements. Journal of Thermophysical Heat Transfer, 12(4): 543-551.

Weigand B (2005). Analytical methods for heat transfer and fluid flow problems. Springer Verlag, New York (USA).

Westerweel J (1993). Digital particle image velocimetry - Theory and application. PhD Thesis, Delft University of Technology, The Netherlands.

Westerweel J, Scarano F (2005). Universal outlier detection for PIV data. Experiments in Fluids, 39(6): 1096-1100.

Wheaton BM, Schneider SP (2010). Roughness-induced instability in a laminar boundary layer at Mach 6. Proceedings of the 48th AIAA Aerospace Sciences Meeting

including the New Horizon and Aerospace Exposition, Orlando, Florida (USA), AIAA 2010-1574.

Whitehead AHJr (1969). Flowfield and drag characteristic of several boundary-layer tripping elements in hypersonic flow. NASA, TN-D-5454.

Wieneke B (2008). Volume self-calibration for 3D particle image velocimetry. Experiments in Fluids, 45(4): 549-556.

Willert CE, Gharib M (1991). Digital particle image velocimetry. Experiments in Fluids, 10(4): 181-193.

Williams OJ, Smits AJ (2012) Application of PIV to the measurement of hypersonic turbulence. Proceedings of the 16th International Symposium of Laser Techniques to Fluid Mechanics, Lisbon, Portugal, 9-12 July.

Wolf T, Estorf M, Radespiel R (2007). Investigation f the starting process in a ludwieg tube. Theoretical and Computational Fluid Dynamics, 21(2): 81-98.

Wool MR (1975). Final summary report, passive nosetip technology (PANT) program. SAMSO, TR-75-250.

Yang CY (1998). Solving the two-dimensional inverse heat source problem through the linear least-squares error method. International Journal of Heat Mass and Transfer, 41(2): 393-398.

Yang L, Erdem E, Zare-Behtash H, Kontis K, Saravanan S (2012). Pressure-sensitive paint on a truncated cone in hypersonic flow at incidences. International Journal of Heat and Fluid Flow, 37: 9-21.

Zhong X, Wang C (2012). Direct Numerical simulation on the receptivity, instability and transition of hypersonic boundary layer. Annual Review of Fluid Mechanics, 44: 527-561.

List of Publications

Journal

Avallone F, Greco CS, Ekelschot D (2013). Image resection and heat transfer measurements in hypersonic flows. Quantitative InfraRed Thermography Journal, 10(2): 188-206.

Avallone F, Ye Q, Schrijer FFJ, ScaranoF, Cardone G (2014). Tomographic PIV investigation of roughness induced transition in a hypersonic boundary layer. Experiments in Fluids, 55(11): 1852.

Avallone F, Discetti S, Astarita T, Cardone G. Convergence enhancement of single-pixel PIV with symmetric correlation. Experiments in Fluids, 56(4): 71.

Avallone F, Greco CS, Schrijer FFJ, Cardone G. A low computational cost inverse heat transfer technique for convective heat transfer measurements in hypersonic flows. Experiments in Fluids. In press.

Under review:

Avallone F, Schrijer FFJ, Cardone G. Experimental investigation on induced transition by isolated roughness elements in hypersonic flows. Physics of Fluids.

Conference

Avallone F, Greco CS, Ekelschot D (2012). 2D Inverse heat transfer measurements by IR Thermography in hypersonic flows. 11th PEGASUS-AIAA Student Conference, Poitiers, France, April 11-13.

Avallone F, Greco CS, Ekelschot D (2012). 2D Inverse heat transfer measurements by IR Thermography in hypersonic flows. 11th Quantitative InfraRed Thermography, Naples, Italy, June 11-14, QIRT 2012-367.

Avallone F, Schrijer FFJ, Cardone G (2013). IR thermography measurements on roughness induced transition. Bulletin of the America Physical Society, Pittsburgh, Pennsylvania (USA), 24 – 26 November, 58(18).

Avallone F, Schrijer FFJ, Cardone G (2014). IR thermography investigation on roughness induced transition in high-speed flows. 12th Quantitative InfraRed Thermography, Bordeaux, France, 7 – 11 July, QIRT 2014-143.

Avallone F, Ye Q, Schrijer FFJ, Scarano F, Cardone G (2014). Tomographic PIV investigation of roughness induced transition in a hypersonic boundary layer. 17th International Symposium on Application of Laser Techniques to Fluid Mechanics, Lisbon, Portugal, 7 – 11 July.

Avallone F, Correale G (2015). Efficiency of energy deposition of a ns-DBD. 10th Pacific Symposium on Flow Visualization and Image Processing, Naples, Italy, 15-18 June.

Submitted

Crispo CM, Greco CS, Avallone F, Vitale L, Cardone G (2015). Stereo PIV measurements on circular and chevron synthetic jet. 11th International Symposium on Particle Image Velocimetry, Santa Barbara, California (USA), 14-16 September.

Avallone F, Ragni D, Schrijer FFJ, ScaranoF, Cardone G (2015). PIV-based study of a cylindrical roughness element in a hypersonic laminar-boundary layer. 11th International Symposium on Particle Image Velocimetry, Santa Barbara, California (USA), 14-16 September.

Workshop

Avallone F, Schrijer FFJ, Cardone G (2014). IR thermography investigation on roughness induced transition. Workshop on Hypersonic Boundary Layer Transition, DLR Gottinga, Germany, 12 July.

Avallone F, Schrijer FFJ, Scarano F, Cardone G (2014). IR thermography and Tomographic PIV measurements on roughness induced transition in hypersonic flows. NATO meeting NATO STO-WG Hypersonic Laminar Turbulent Transition, Colorado Springs, Colorado (USA), 3 - 4 April.

Acknowledgements

Foremost, I would like to express my sincere gratitude to my supervisor Prof. Gennaro Cardone for his valuable guidance, scholarly inputs and consistent encouragement I received throughout the research work. A person with an amicable and positive disposition, Gennaro has always made himself available to clarify my doubts despite his busy schedules. Thank you Gennaro, for all your help and support. I hope that we will continue collaborating in the coming years.

I sincerely thank Prof. Tommaso Astarita for the insightful discussions. Thank you for always replying to my phone calls. I thank Prof. Giovanni Carlomagno for the experiences and the knowledge that he transmitted me during the nice conversations we had.

I would like to thank Prof. Ferry Schrijer, Prof. Fulvio Scarano and all the people of the High Speed Laboratory for hosting me twice at Delft University of Technology. Thank you for the discussions and the continuous support. I really appreciate your hospitality and I always felt as being part of the group.

I warmly thank all my colleagues and friends that I met at the University of Naples. Particularly, I wish to thank Carlo Greco, a loyal friend since we met as undergraduate. I will never forget all the nice conversations that we had about our future and the morning “press review”. I hope we will keep in touch. I would like to thank Giuseppe Ceglia, Gioacchino Cafiero, (Prof.) Andrea Ianiro, (Prof.) Stefano Discetti, Giusy Castrillo, Cuono Massimo Crispo, Simone Boccardi, Gianluigi Tufano, Roberto Opromolla and Stefano Rocco for the many enjoyable moments that we shared together during these years.

A special thank goes to all the people that I met in Delft. In particular, I would like to thank (Prof.) Daniele Ragni for helping me during my crazy experiments.

A special thank goes to my friends Wentò, Nello, Niglio, Gabriele, Maria Vittoria, Angela, Piero and all the others for all the enjoyable time that we have since we met several years ago. Thank you for being part of my life.

Lastly, but most important, a special thank goes to my family, which supported me in reaching this goal. I thank my father and my mother for continuously supporting all the decisions that I made during these years. Finally, I would like to thank my sister Elena and I wish her good luck for her future.